Separation of eddy turbulence and wave turbulence in rotating or stratified flows

H. Lam

Numéro d'ordre NNT: 2021LYSEC50 Année: 2021

THÈSE de DOCTORAT DE L'UNIVERSITÉ DE LYON
opérée au sein de **L'ÉCOLE CENTRALE DE LYON**

ÉCOLE DOCTORALE MEGA
Mécanique, Energétique, Génie civil et Acoustique

Spécialité: Mécanique des fluides

Soutenue le 14/12/2021 par

Henri Lam

Separation of waves and eddies in rotating or stably stratified flows

---

Devant le jury composé de:

F. S. Godeferd	Directeur de Recherche, CNRS	Directeur de thèse
A. Delache	Maître de conférences, Université de Saint-Étienne	co-Directeur de thèse
C. P. Caulfield	Professeur, University of Cambridge	Rapporteur
M. K. Verma	Professeur, IIT Kanpur	Rapporteur
A. Naso	Chargée de recherche, CNRS	Examinatrice
S. Galtier	Professeur, École polytechnique	Examinateur/Président
R. Marino	Chargé de recherche, CNRS	Invité
B. Favier	Chargé de recherche, CNRS	Invité
A. Maffioli	Maître de conférences, École Centrale de Lyon	Invité

Acknowledgements

First, I want to thank my two supervisors. Alexandre have been very involved in this thesis and have helped me a lot. He coded some nasty and complicated part of the program, helped me with mathematic formalism and came with a bunch of crazy and innovative ideas. Fabien also played an important role in this thesis. He helped me to be more rigorous and improve my English. All questions I asked him always found a clear and understandable answer. I am thankful to them for these nice and challenging 39 months.

Second, I thank Andrea Maffioli. Andrea was a postdoc under the supervision of Alexandre and Fabien when I started my PhD (and now he is "maitre de conférence"). My PhD thesis can be understood as the continuation of the work of Andrea. Thus, Andrea explained to me all he did during his post doc and this has helped me a lot. For example, the forcing he implemented was very clear and used extensively for my PhD.

Third, I thank the different members of the jury. Thanks to the two referees (C. P. Caulfied and M. K. Verma) for their reports and relevant remarks. Thanks to A. Naso, S. Galtier, R. Marino, B. Favier and A. Maffioli for their relevant question in the PhD defence. A special thank to M. K. Verma and R. Marino who modified their schedule so that the PhD defence could be held in December.

Fourth, I would like to thank the different computing facilities that have allowed me to run my numerical simulation. At the start of my PhD I was using Newton and everything worked really well. This is of course due to the work of Laurent and Anne (among others) who did a marvellous job at maintaining Newton all year around. For the last two years of my PhD, I have been using mostly the supercomputer Jean-Zay at Idris and again, everything worked well, thanks to the people working at Idris (I don't have any names though...).

Finally, I would like to thank all the PhD, postdocs and students that helped me and shared some good moments in and out of the lab. Here is a list of them: Cenk, Aleksandr, Juan, Haining, Zecong, Aurelien, Majid, Ahmed, Wesley (N'Nankou), Tong, Ryo, Jerome, Smail, Aloualid, Nelson, Etienne, Mathieu, Hasan... I also thank all the permanent people at the lab LMFA.

Last but not least, I would like to thank my family and my friends ("Team Ehpad", "Les Leprechauns du 75", ...) for the good times during the PhD. I especially thank "Bichette" for these nice and refreshing times during the PhD and my parents for their support and indefectible help before and during the PhD.

Contents

List of Figures

List of Tables

Abbreviations

IGW	**I**nternal **G**ravity **W**aves
IW	**I**nertial **W**aves
VSHF	**V**ertically **S**heared **H**orizontal **F**low
GM	**G**eostrophic **M**ode
HIT	**H**omogeneous and **I**sotropic **T**urbulence
FFT	**F**ast **F**ourier **T**ransform

Operators

$\bar{}$	Complex conjuguate
$\hat{}$	Space Fourier domain
$\tilde{}$	Space and time Fourier domain
$[\hat{f}(\mathbf{k},t),\hat{g}(\mathbf{k}',t)] \equiv \frac{1}{T}\int_T \hat{f}(\mathbf{k},t)\overline{\hat{g}(\mathbf{k}',t)}\delta_{\mathbf{k}-\mathbf{k}'}\mathrm{d}t$	Average inner product in time
$<\hat{f},\hat{g}>=\sum_{\mathbf{k}}\mathrm{Re}[\hat{f}(\mathbf{k},t),\hat{g}(\mathbf{k},t)]$	Energetic content
$<\hat{f},\hat{g}>_K=\sum_{\substack{\mathbf{k}\\ \lvert\mathbf{k}\rvert=K}}\mathrm{Re}[\hat{f}(\mathbf{k},t),\hat{g}(\mathbf{k},t)]$	Energetic content on a sphere of radius K

Nomenclature

$\mathbf{u} = (u_x, u_y, u_z)$	velocity
u^p	poloidal velocity
u^t	toroidal velocity
b	buoyancy field
p	pressure
$\mathbf{g}$	vertical gravity
$\mathbf{c} = (c_x, c_y, c_z)$	advective velocity
$\mathbf{k} = (k_x, k_y, k_z)$	wavevector
P	forcing power
$\mathbf{v}_g$	group velocity
$\mathbf{v}_\Phi$	phase velocity
N	Brunt-Väisälä frequency
T_u	kinetic transfer
T_b	potential transfer
$T_{u\to b}$	kinetic to potential transfer
E_u	kinetic energy
E_b	potential energy
F_u	kinetic forcing
F_b	potential forcing
ω	angular frequency
ω_r	dispersion relation (for stratified or rotating flows)
ω_c	dispersion relation advected with sweeping effect
ω_f	forcing frequency
θ	angle of $\mathbf{k}$ against the horizontal plane

n_g	number of grid points in one direction
Ω	rotation rate
η	Kolmogorov scale
Γ	mixing coefficient
ν	kinematic viscosity
χ	thermal viscosity
ρ	density
ε_b	potential dissipation
ε_u	kinetic dissipation
ε	total dissipation
F_α	added viscosity

Abstract

We propose a new separation technique of internal gravity waves (resp. inertial waves) and eddies in stratified (resp. rotating) turbulence. The separation is based on the dispersion relation of waves modified by the advection of a vertically sheared horizontal flow (resp. the geostrophic mode) called sweeping effect. Different regimes are studied with a low Froude number $Fr \ll 1$ (resp. Rossby number $Ro \ll 1$) but with a varying buoyancy Reynolds number Re_b (resp. inertial Reynolds number Re_I). We observe that the distribution of energy between waves and eddies follow the Fr (resp. Ro) number. We establish the evolution equations for the waves and eddies parts separately. Generally, we observe a large transfer of energy from waves to eddies. We also observe in the rotating case that it is mostly waves that transfer energy to the geostrophic mode. A few inverse cascades are observed for particular types of transfers. The dissipation and mixing due to waves and eddies against the different parameters are calculated. Finally, 2D velocity fields are decomposed into their wave and eddy parts.

Keywords Turbulence, stratification, rotation, mixing, dissipation, transfer, energy, waves, eddies.

Résumé

Nous développons une nouvelle technique de séparation des ondes internes de gravité (resp. des ondes inertielles) et tourbillons dans des écoulements turbulents stratifiés (resp. en rotation). Cette séparation est basée sur la relation de dispersion des ondes modifiée par l'advection d'un écoulement cisaillé (resp. du mode géostrophique) appelée effet sweeping. Différents régimes sont étudiés à bas nombre de Froude $Fr \ll 1$ (resp. nombre de Rossby $Ro \ll 1$) mais avec un nombre de Reynolds de flottaison Re_b (resp. nombre de Reynolds d'inertie Re_I) variable. Nous observons que la répartition d'énergie entre les ondes et les tourbillons dépend fortement du nombre de Fr (resp. du nombre de Ro). Nous définissons l'équation d'évolution de l'énergie pour les ondes et tourbillons séparément. De manière générale, on observe un large transfert d'énergie des ondes vers les tourbillons. Dans le cas en rotation, on observe que c'est principalement les ondes qui alimentent le mode géostrophique. Quelques cascades inverses sont observées pour certains types de transferts. La dissipation et le mélange dûs aux ondes et tourbillons sont aussi calculés. Enfin, les vitesses des ondes et des tourbillons sont séparément visualisées dans des plans de coupe 2D.

Mots clefs Turbulence, stratification, rotation, mélange, dissipation, transfert, énergie, ondes, tourbillons.

Chapter 1

Introduction

1.1 Where do IGW and IW occur?

Internal Gravity Waves (IGW) exist in stratified flows, where the density varies with height in a stable stratification (heavy fluid below light fluid). This type of flow is encountered in the atmosphere and ocean where density varies with altitude. It is possible to observe waves with the help of clouds as shown in figure 1.1. Hence, they can be very important in the dynamics of the weather and climate which require modelling

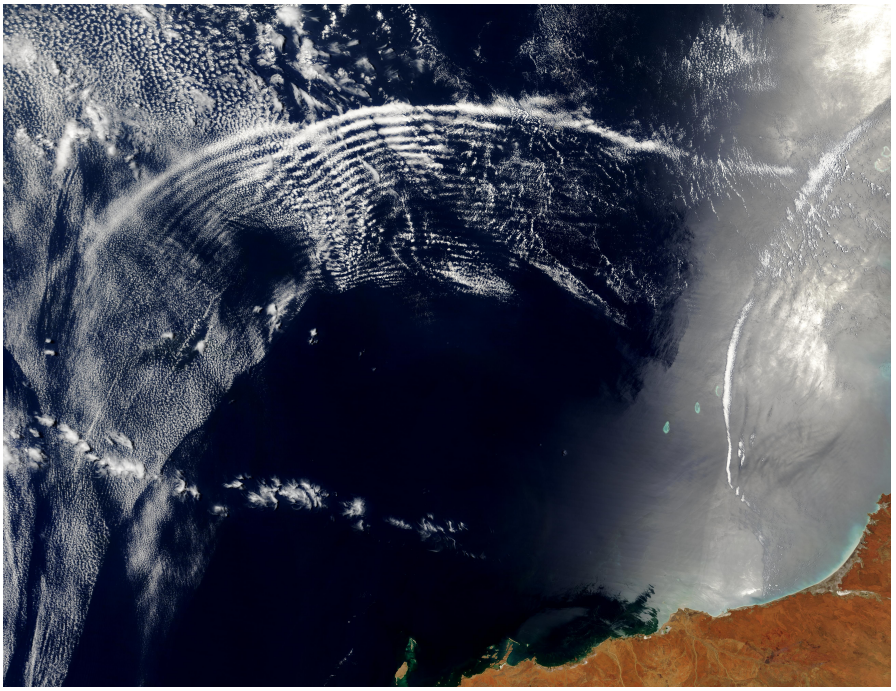

FIGURE 1.1: Example of atmospheric gravity waves (source: Jacques Descloitres, MODIS Rapid Response Team, NASA/GSFC)

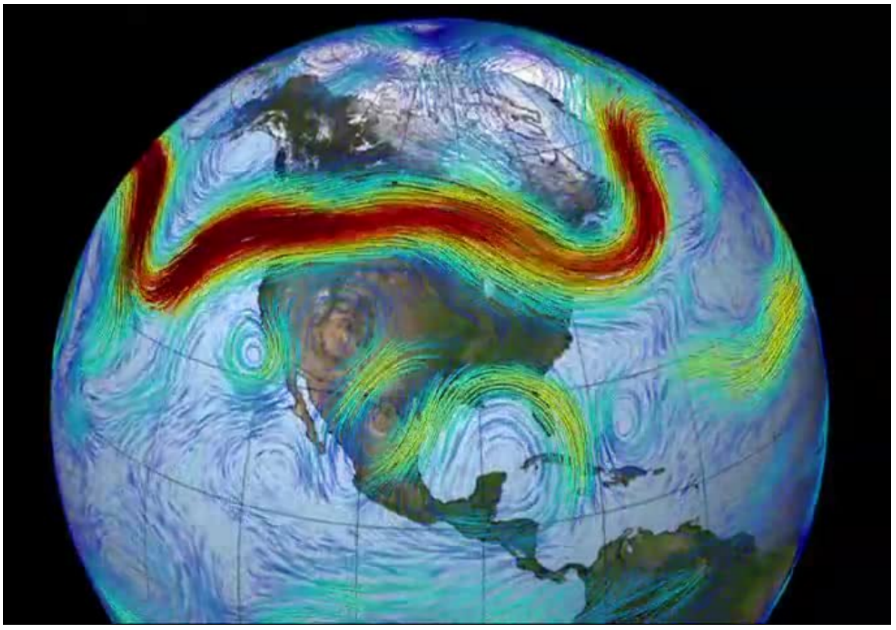

FIGURE 1.2: Visualisation of the polar jet stream. Faster winds are in red and slower winds are in blue (source: NASA's Goddard Space Flight Center)

of the atmosphere and ocean. For example the 2001 IPCC report explains that random internal waves are one of the most important processes driving ocean mixing [136]. Furthermore, this report claims that the uncertainty over the parameterization of the ocean mixing is probably small for a few decades on climate's projection but considerable for larger time scale. While the understanding of the ocean mixing has increased, there is still uncertainties that could influence the thermal expansion of the ocean [31], the climate model performance, or the accuracy of the simulation in the Indian and Atlantic tropical oceans [47].

Similarly Inertial Waves (IW) exist in rotating flows. This type of flow is particularly studied for planetary cores. They also take place in the atmosphere or ocean and in this case they are called Rossby waves [115]. Different types of inertial waves exist, for example, planetary Rossby waves are created with a variation of the Coriolis force with latitude and topographic Rossby waves exist in a rotating fluid with a variable depth [80]. They are linked to the formation and behaviour of the jet stream (associated to Rossby waves) which influences a lot the weather and climate on Earth [134]. An example of the polar jet stream is displayed in figure 1.2.

It is possible to trap and visualize in a wave attractor the movement of IGW as in Brouzet et al. [20], Maas et al. [88] and the movement of IW as in Brunet et al. [21]. Waves can also be observed in the atmosphere. It is particularly the case during an eclipse [32, 95] because when the moon hides the sunlight it suddenly changes the radiation that the atmosphere receives, which is assimilated as a forcing and results in the creation of

waves. The velocities linked to these waves are very close to an ellipse shape [32]. For example, in Colligan et al. [32], plotting the zonal wind velocity in the x axis and the meridional wind velocity in the y axis after an eclipse, an ellipse shape is recovered which can be understood as the imprint of atmospheric gravity waves.

1.2 How do they manifest?

It can be obscure to understand how waves behave inside a fluid. Indeed, we are much more used to "seeing" the waves (such as the surface waves on the ocean) or "listening" to the waves (such as sound waves). Yet, it is possible to obtain a global understanding of an IGW movement inside a fluid as shown in figure 1.3. When a parcel of fluid of density ρ_1 goes to a heavier fluid environment ρ_2, it is quite obvious that a force will occur on the parcel of fluid to move it to a lower density environement ρ_3. Then the parcel of fluid of density ρ_1 has a higher density than its environment and it is pushed downward again. However this movement is not perfectly vertical as the flow is incompressible. The incompressibility of the flow creates also some horizontal velocities.

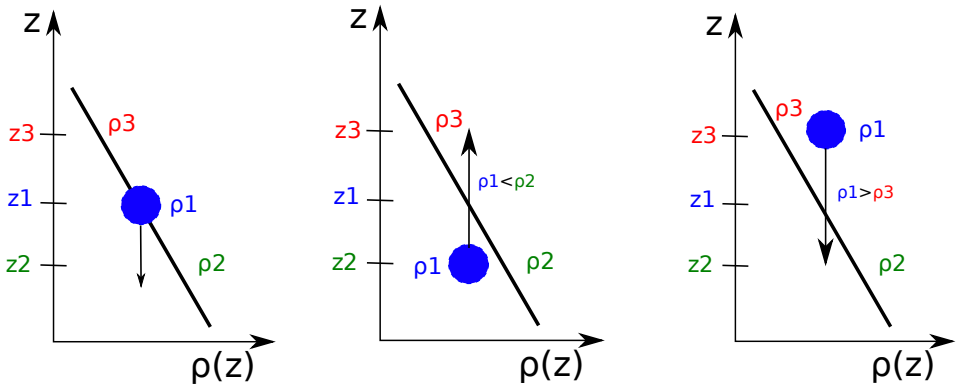

FIGURE 1.3: Representation of the movement of IGW in a stratified flow.

In the case of rotating turbulence the mechanism of IW movement is somehow more complicated. IW appear in a rotating frame because of the Coriolis force $-2\boldsymbol{\Omega} \times \mathbf{u}$ (see figure 1.4). When a parcel of fluid moves at a velocity field $\mathbf{u}_1$, the Coriolis force creates a force $\mathbf{F}_1$ on it. This induces a new velocity on the parcel of fluid $\mathbf{u}_2$ and a new force $\mathbf{F}_2$. By repeating this phenomenon for $\mathbf{u}_3$ and $\mathbf{u}_4$, we obtain a parcel of fluid that oscillates like a wave. Again, this velocity field is not purely two dimensional and vertical components of velocity also exist due to incompressibility.

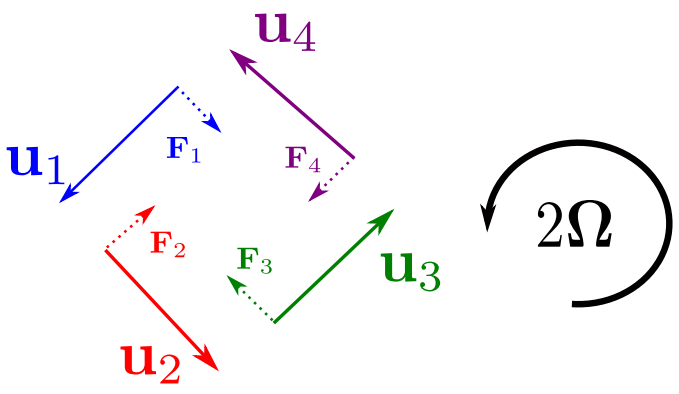

FIGURE 1.4: Representation of the movement of IW in a rotating flow.

1.3 Why do we need to separate waves and eddies?

When a flow is strongly stratified or rotating, waves can dominate the overall structure of the flow. If the amplitude of the waves is small, we are in the weak wave turbulence regime. The non-linearity can be ignored compared to the stratified or rotating term and it is possible to derive an analytical solution for this kind of flow [120]. If the amplitude of the waves is large, waves interact due to the non-linear term and we recover the strong wave turbulence regime [110].

When the flow is barely stratified or barely rotating, one can ignore the stratified and rotating term and, far from boundaries, one recovers the classical result of 3D homogeneous and isotropic turbulence (HIT) summarized in Frisch [48]. Despite not knowing an analytical solution for HIT, this type of flow is well known and has been the subject of numerous articles. Furthermore, 2D flows have also been extensively documented as in Boffetta and Ecke [14], Kraichnan and Montgomery [70], Tabeling [137].

Added complexity arises in between those two cases, when the stratified or rotating terms are important but do not dominate the flow. In this case, the eddy dynamics cannot be studied individually from the wave dynamics as they are entangled with one another. Furthermore, waves can create eddy turbulence [11, 44] and conversely, eddy turbulence can create waves [107, 150]. Hence, it is useful to separate the waves and eddies to better understand how they interact with one another and to observe their dynamics individually. This is the objective of this thesis.

The manuscript is organised as follows. The first chapter presents the equation for rotating and stratified flows. It shows the properties of IGW and IW. The effect of large structure on the wave's characteristics is also presented. The second chapter presents a new technique to extract the 3D wave field and the 3D eddy field in a turbulent flow.

The fourth and fifth chapters show new physical results obtained from our wave/eddy separation technique for stratified or rotating flows.

Chapter 2

Waves in Flows

In this chapter, we sum up the relevant properties of Internal Gravity Waves (IGW) and Inertial Waves (IW) encountered in stratified or rotating flows.

2.1 Equations for a stratified fluid

We start by the computation of the different sets of equations used in this thesis. In the case of a stratified flow, the Navier-Stokes equations are

$$\rho(\partial_t \mathbf{u} + \mathbf{u} \cdot \boldsymbol{\nabla}\mathbf{u}) = -\boldsymbol{\nabla} p + \mu \boldsymbol{\nabla}^2 \mathbf{u} + \rho \mathbf{g} \tag{2.1}$$

$$\boldsymbol{\nabla} \cdot \mathbf{u} = 0 \tag{2.2}$$

$$\partial_t \rho + \mathbf{u} \cdot \boldsymbol{\nabla}\rho = \chi \boldsymbol{\nabla}^2 \rho. \tag{2.3}$$

The dynamical variables used here are defined as $\mathbf{u} = (u_x, u_y, u_z)$ the velocity vector, p the pressure term, ρ the density, μ the dynamic viscosity, χ the thermal diffusivity and $\mathbf{g}$ the vertical gravity.

Compare to the full Navier-Stokes equation for compressible flow, the Boussinesq approximation assumes that only variations of density linked to gravity are important [15]. This is the case in flows where variations of density are small but where the flows is driven by a strong buoyancy force. The other terms where the density is involved neglect its variation. As a result, the equation of continuity (mass conservation) can be simplified as an incompressible flow (2.2) and lead to a simplified equation in (2.1). The fluctuations of density in the inertial term can also be neglected and the density

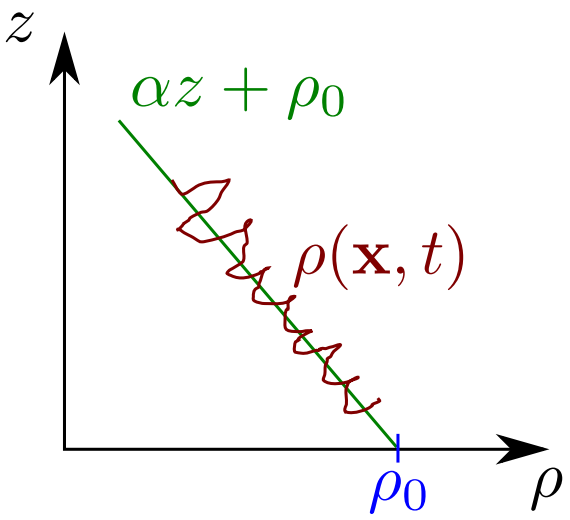

FIGURE 2.1: Decomposition of the buoyancy field $\rho(\mathbf{x}, t)$ with a linear background density field $\rho_0 + \alpha z$.

field follows an advection-diffusion equation (2.3). The density field can be linked to the temperature or concentration of a species as the salt in the ocean.

The density $\rho(\mathbf{x}, t)$ can be considered with a linear background density field variation $\rho_0 - \alpha z$ and a density fluctuation $\rho'(\mathbf{x}, t)$ (see figure 2.1), where α is the spatial average gradient of density $\alpha = |d\rho/dz|$. Furthermore, only small variations of density are allowed ($\rho' \ll \rho_0$). The density field is:

$$\rho(\mathbf{x}, t) = \rho_0 - \alpha z + \rho'(\mathbf{x}, t). \tag{2.4}$$

By injecting equation (2.4) into equations (2.1) and (2.3), the Navier-Stokes equations in the Boussinesq approximation become:

$$\begin{aligned} \rho_0(\partial_t \mathbf{u} + \mathbf{u} \cdot \boldsymbol{\nabla}\mathbf{u}) &= -\boldsymbol{\nabla} p + \mu \boldsymbol{\nabla}^2 \mathbf{u} + (\rho_0 - \alpha z + \rho')\mathbf{g} \\ \boldsymbol{\nabla} \cdot \mathbf{u} &= 0 \\ \partial_t \rho' + \mathbf{u} \cdot \boldsymbol{\nabla}\rho' + \alpha u_z &= \chi \boldsymbol{\nabla}^2 \rho'. \end{aligned} \tag{2.5}$$

The term ρ_0 disappears from the advection-diffusion equation as it is constant. Furthermore, as the Boussinesq approximation states that the buoyancy variations are only important in the terms linked to gravity, the fluctuation of density ρ' and the linear term αz are neglected in the inertial part of the equation of momentum in (2.5).

In a flow at rest, $-\boldsymbol{\nabla} p + (\rho_0 - \alpha z)\mathbf{g} = 0$. The pressure term can also be rewritten using the linear background of density field. The new pressure term p' becomes:

$$p' = p + (-\rho_0 z + \frac{\alpha}{2} z^2) g + cste. \tag{2.6}$$

We multiply the advection equation (2.3) by g/ρ_0 and we define $b = -\frac{\rho' g}{\rho_0}$. We also introduce the Brunt-Väisälä frequency $N = \sqrt{\alpha g/\rho_0}$. Hence, the Navier-Stokes equations become:

$$\begin{aligned} \partial_t \mathbf{u} + \mathbf{u}\cdot\boldsymbol{\nabla}\mathbf{u} &= -\frac{1}{\rho_0}\boldsymbol{\nabla}p' + \frac{\mu}{\rho_0}\boldsymbol{\nabla}^2\mathbf{u} + b\mathbf{n} \\ \boldsymbol{\nabla}\cdot\mathbf{u} &= 0 \\ \partial_t b + \mathbf{u}\cdot\boldsymbol{\nabla}b + N^2 u_z &= \chi\boldsymbol{\nabla}^2 b. \end{aligned} \tag{2.7}$$

Then, we non-dimensionalise the equations (2.7) using a characteristic time T and a characteristic length scale L. The new dimensionless variables are written with a subscript 'd':

$$\mathbf{u} = L/T\,\mathbf{u}_d, \quad t = T t_d, \quad p' = \rho_0 (L/T)^2 p_d, \quad \boldsymbol{\nabla} = \boldsymbol{\nabla}_d/L, \quad N = N_d/T. \tag{2.8}$$

By inserting the dimensionless variables (2.8) into equations (2.7), and dropping the subscript 'd' we get:

$$\begin{aligned} \partial_t \mathbf{u} + \mathbf{u}\cdot\boldsymbol{\nabla}\mathbf{u} &= -\boldsymbol{\nabla}p + \nu\boldsymbol{\nabla}^2\mathbf{u} + b\mathbf{n} \\ \boldsymbol{\nabla}\cdot\mathbf{u} &= 0 \\ \partial_t b + \mathbf{u}\cdot\boldsymbol{\nabla}b &= -N^2 u_z + \chi\boldsymbol{\nabla}^2 b \end{aligned} \tag{2.9}$$

where $\nu = \frac{\mu T}{\rho L^2}$ and can be understood as the inverse of the Reynolds number. As the Reynolds number describes the effect of the viscosity, ν will be associated to the kinematic viscosity in this thesis. Equations (2.9) are the set of equations for stratified cases that will be used in this thesis.

2.2 Equations for a rotating fluid

We derive the set of equations used in the rotating case. We start by writing the Navier-Stokes equations in the inertial frame:

$$\begin{aligned} \partial_t \mathbf{u} + \mathbf{u}\cdot\boldsymbol{\nabla}\mathbf{u} &= -\frac{1}{\rho}\boldsymbol{\nabla}p + \frac{\mu}{\rho}\boldsymbol{\nabla}^2\mathbf{u} \\ \boldsymbol{\nabla}\cdot\mathbf{u} &= 0. \end{aligned} \tag{2.10}$$

The velocity field in the rotating frame $\mathbf{u}_r$ is linked to the velocity field in the absolute frame (non rotating frame) $\mathbf{u}$ as shown in figure 2.2. The equation that links these two

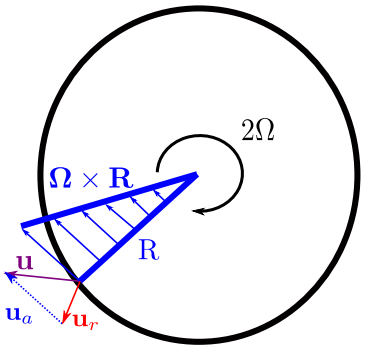

FIGURE 2.2: Velocity fields $\mathbf{u}_r$ and $\mathbf{u}_a$ in the rotating frame and velocity field $\mathbf{u}$ in the Cartesian frame.

velocities is

$$\mathbf{u} = \mathbf{u}_r + \boldsymbol{\Omega} \times \mathbf{R} = \mathbf{u}_r + \mathbf{u}_a \tag{2.11}$$

where $\mathbf{u}_a = \boldsymbol{\Omega} \times \mathbf{R}$ is the rotating velocity, $\mathbf{R}$ is the distance to the axis of rotation and $\boldsymbol{\Omega}$ is the rotation rate (see figure 2.2).

In the rotating frame, the Navier-Stokes equations become:

$$\begin{gathered} \partial_t \mathbf{u}_r + \mathbf{u}_r \cdot \boldsymbol{\nabla} \mathbf{u}_r = -\frac{1}{\rho}\boldsymbol{\nabla} p - \boldsymbol{\Omega} \times (\boldsymbol{\Omega} \times \mathbf{R}) - 2\boldsymbol{\Omega} \times \mathbf{u}_r + \frac{\mu}{\rho}\boldsymbol{\nabla}^2 \mathbf{u}_r \\ \boldsymbol{\nabla} \cdot \mathbf{u}_r = 0. \end{gathered} \tag{2.12}$$

In a flow at rest, the rotating velocity $\mathbf{u}_a$ is linked to the pressure field p_a by the equation $\frac{1}{\rho}\boldsymbol{\nabla} p_a + \boldsymbol{\Omega} \times (\boldsymbol{\Omega} \times \mathbf{R}) = 0$. Furthermore, the centrifugal term can be rewritten $\boldsymbol{\Omega} \times (\boldsymbol{\Omega} \times \mathbf{R}) = -\boldsymbol{\nabla}(\frac{1}{2}\Omega^2 R^2)$. Therefore, the pressure term can include the centrifugal term as well. This new pressure term p_r is

$$p_r = p - \frac{\rho}{2}\Omega^2 R^2. \tag{2.13}$$

The Navier-Stokes equations with rotation retain only the Coriolis term $-2\boldsymbol{\Omega} \times \mathbf{u}$ and become:

$$\begin{gathered} \partial_t \mathbf{u}_r + \mathbf{u}_r \cdot \boldsymbol{\nabla} \mathbf{u}_r = -\frac{1}{\rho}\boldsymbol{\nabla} p_r - 2\boldsymbol{\Omega} \times \mathbf{u}_r + \frac{\mu}{\rho}\boldsymbol{\nabla}^2 \mathbf{u}_r \\ \boldsymbol{\nabla} \cdot \mathbf{u}_r = 0. \end{gathered} \tag{2.14}$$

Again, we non-dimensionalise equation (2.14) against a characteristic time T and a characteristic length scale L. The new dimensionless variables are written with a subscript 'd':

$$\mathbf{u}_r = L/T\mathbf{u}_d, \quad t = Tt_d, \quad p_r = \rho(L/T)^2 p_d, \quad \boldsymbol{\nabla} = \boldsymbol{\nabla}_d/(L), \quad \boldsymbol{\Omega} = \boldsymbol{\Omega}_d/T. \tag{2.15}$$

By inserting the dimensionless variables in equation (2.15) into equation (2.14), and dropping the subscript d we obtain:

$$\begin{aligned} \partial_t \mathbf{u} + \mathbf{u} \cdot \boldsymbol{\nabla} \mathbf{u} + \boldsymbol{\nabla} p &= -2\boldsymbol{\Omega} \times \mathbf{u} + \nu \boldsymbol{\nabla}^2 \mathbf{u} \\ \boldsymbol{\nabla} \cdot \mathbf{u} &= 0 \end{aligned} \tag{2.16}$$

where ν is defined similarly to the stratified case. Equations (2.16) are the set of equations for rotating cases that will be used in this thesis.

2.3 Navier-Stokes equations for rotating and stratified flows

The Navier-Stokes equations in both rotating and stratified cases are presented in equation (2.17). The stratified equation is written under the Boussinesq approximation, when the variation in density is taken into account only in the direction of gravity z. It is studied both analytically and by numerical simulations:

$$\begin{aligned} \partial_t \mathbf{u} + \boldsymbol{\omega} \times \mathbf{u} &= -\boldsymbol{\nabla} p + \nu \boldsymbol{\nabla}^2 \mathbf{u} + \mathbf{n} b - 2\boldsymbol{\Omega} \times \mathbf{u} + \mathbf{F}_u \\ \boldsymbol{\nabla} \cdot \mathbf{u} &= 0 \\ \partial_t b + \mathbf{u} \cdot \boldsymbol{\nabla} b &= -\chi \boldsymbol{\nabla}^2 b - N^2 \mathbf{n} \cdot \mathbf{u} + F_b, \end{aligned} \tag{2.17}$$

with $\boldsymbol{\omega} = \boldsymbol{\nabla} \times \mathbf{u}$ and $\boldsymbol{\omega} \times \mathbf{u} = \mathbf{u} \cdot \boldsymbol{\nabla} \mathbf{u} - \frac{1}{2} \boldsymbol{\nabla} u^2$. Note that the gradient term $\frac{1}{2} \boldsymbol{\nabla} u^2$ is not written in equation (2.17) because it is inserted in the modified pressure field $p = p' - u^2/2$ similarly to equation (2.13).

We sum up the different dynamical variables used in this thesis, they are defined as $\mathbf{u} = (u_x, u_y, u_z)$ the velocity vector, $\boldsymbol{\omega} = \boldsymbol{\nabla} \times \mathbf{u}$ the vorticity, p the modified pressure term, b the negative fluctuation of density around the mean constant gradient N^2, $\mathbf{n}$ the vertical unit vector along the stratification and the physical parameters are ν the kinematic viscosity, $\mathcal{X}$ the thermal diffusivity, Ω the rotation rate and N the Brunt-Väisälä frequency. $\mathbf{F}_u = (F_{u_x}, F_{u_y}, F_{u_z})$ and F_b are different forcings that vary depending on the case and is explained for each simulation (see sections 2.6.2.2, 2.7.1, 4.2.1 for example). All equations and parameters are dimensionless by reference to length and scale as shown for example in equations (2.8) and (2.15).

While it is possible to consider a rotating and stratified flow at the same time, in this thesis we only consider either flow separately, a purely stratified flow (without the Coriolis term $-2\boldsymbol{\Omega} \times \mathbf{u}$) or a purely rotating flow (without density variations).

2.4 Craya-Herring frame

Equations (2.17) can be rewritten using the spatial Fourier transform denoted by $\hat{}$ with $\mathbf{k}$ a wavevector. For example the spatial Fourier transform of the velocity vector $\mathbf{u}(\mathbf{x}, t)$ is

$$\hat{\mathbf{u}}(\mathbf{k}, t) = \frac{1}{2\pi^3} \int_0^{2\pi} \mathbf{u}(\mathbf{x}, t) e^{-\mathrm{i}\mathbf{k}\cdot\mathbf{x}} d^3x. \tag{2.18}$$

The flows that we are using are incompressible ($\boldsymbol{\nabla} \cdot \mathbf{u} = 0$) meaning that in the spatial Fourier domain the velocity field is perpendicular to the wavevector ($\mathbf{k} \cdot \hat{\mathbf{u}}(\mathbf{k}) = 0$). This suggests a new frame of reference called Craya-Herring frame (see figure 2.3). In this new frame the velocity field is perpendicular to the wave vector [63, 120]. This new frame is different from the classical Cartesian frame and permits the reduction of the velocity field from three components to only two components. The new polar spherical coordinates are the toroidal component $\mathbf{e}^t$, the poloidal component $\mathbf{e}^p$ and the radial component $\mathbf{e}^r$. They are unit vectors of the so-called Craya-Herring frame $(\mathbf{e}^t, \mathbf{e}^p, \mathbf{e}^r)$ and are defined using the vertical unit vector $\mathbf{e}^z$ as:

$$\mathbf{e}^r = \mathbf{k}/k, \quad \mathbf{e}^t = \mathbf{e}^r \times \mathbf{e}^z, \quad \mathbf{e}^p = \mathbf{e}^r \times \mathbf{e}^t. \tag{2.19}$$

In this frame of reference, the velocity vector $\hat{\mathbf{u}}$ in Fourier space is perpendicular to the wavevector $\mathbf{k}$ as the flow is incompressible ($\boldsymbol{\nabla} \cdot \mathbf{u} = 0$ or $\mathbf{k} \cdot \hat{\mathbf{u}} = 0$). As a result, the new velocity field in Fourier space can be defined with only two components, the toroidal velocity $\hat{v}^t$ and poloidal velocity $\hat{v}^p$:

$$\hat{\mathbf{u}}(\mathbf{k}) = \hat{v}^t \mathbf{e}^t + \hat{v}^p \mathbf{e}^p \tag{2.20}$$

Note that this particular frame is ill-defined when the angle θ done between the wavevector $\mathbf{k}$ and the horizontal plane is $\theta = \pm\pi/2$, or when the horizontal wavenumber $k_h = 0$ as both the toroidal and poloidal components can be in any direction. For the particular point $k_h = 0$, we can set the velocity $\hat{u}_x$ to be equal to the toroidal velocity $\hat{u}^t$ and the velocity $\hat{u}^y$ to be equal to the poloidal velocity $\hat{u}^p$ (or the inverse).

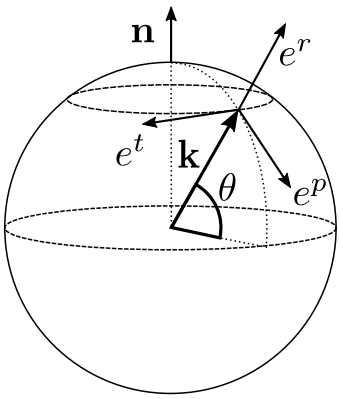

FIGURE 2.3: The polar-spherical frame of reference linked to $\mathbf{k}$ in spectral space, also named Craya-Herring frame. Unit vectors are toroidal $\mathbf{e}^t$, poloidal $\mathbf{e}^p$, radial $\mathbf{e}^r$.

2.4.1 Dispersion relation for internal gravity waves

From equations (2.9), we will compute the dispersion relation of IGW that links a spatial statistic (an angle) to a time statistic (a frequency). To do so, we first remove the non-linear terms. Indeed, IGW are plane-wave solutons of the linearised Navier-Stokes equations. Without non-linear terms, the Navier-Stokes equations in the Boussinesq approximation of equations (2.9) are:

$$\partial_t \mathbf{u} + \boldsymbol{\nabla} p - \nu \boldsymbol{\nabla}^2 \mathbf{u} = \mathbf{n} b \tag{2.21}$$

$$\boldsymbol{\nabla} \cdot \mathbf{u} = 0 \tag{2.22}$$

$$\partial_t b - \chi \boldsymbol{\nabla}^2 b = -N^2 \mathbf{n} \cdot \mathbf{u}. \tag{2.23}$$

Taking the divergence of (2.21) one finds the Poisson equation

$$\boldsymbol{\nabla}^2 p = \boldsymbol{\nabla} \cdot \mathbf{n} b. \tag{2.24}$$

The spatial Fourier transform of equations (2.21) and (2.24) yields:

$$\partial_t \hat{u}_i + (\mathrm{i} k_i \hat{p} - n_z \delta_{iz} \hat{b}) + \nu k^2 \hat{u}_i = 0 \tag{2.25}$$

$$\hat{p} = -\mathrm{i} \frac{k_z}{k^2} \hat{b}. \tag{2.26}$$

Combining equations (2.25) and (2.26) one obtains:

$$\partial_t \hat{u}_i + (\frac{k_i k_z}{k^2} - n_z \delta_{iz}) \hat{b} + \nu k^2 \hat{u}_i = 0. \tag{2.27}$$

The buoyancy b has been projected on a plane perpendicular to $\mathbf{k}$ by applying the projector operator $P_{ij} = \delta_{ij} - \frac{k_i k_j}{k^2}$. This operator projects any term to make them

perpendicular to $\mathbf{k}$.

Taking the spatial Fourier transform of equation (2.23) and multiplying by the unit vector $\mathbf{k}/k$, the buoyancy term becomes:

$$\partial_t \hat{b}\frac{\mathbf{k}}{k} + \chi k^2 \hat{b}\frac{\mathbf{k}}{k} = -N^2 \hat{u}_z \frac{\mathbf{k}}{k}. \tag{2.28}$$

Projecting equations (2.27) and (2.28) on the Craya-Herring frame, one therefore gets a new, simpler set of kinematic equations:

$$\begin{aligned} \partial_t \hat{v}^t + \nu k^2 \hat{v}^t &= 0 \\ \partial_t \hat{v}^p + \cos\theta \hat{b} + \nu k^2 \hat{v}^p &= 0 \\ \partial_t \hat{b} - N^2 \cos\theta \hat{v}^p + \chi k^2 \hat{b} &= 0. \end{aligned} \tag{2.29}$$

The angle θ is the angle between the wavevector $\mathbf{k}$ and the horizontal plane (see figure 2.3). By taking the Fourier transform in time of equations (2.29) and writing $\tilde{}$ the Fourier transform in space and time of the components, we get:

$$\begin{aligned} \mathrm{i}\omega \tilde{v}^t + \nu k^2 \tilde{v}^t &= 0 \\ \mathrm{i}\omega \tilde{v}^p + \cos\theta \tilde{b} + \nu k^2 \tilde{v}^p &= 0 \\ \mathrm{i}\omega \tilde{b} - N^2 \cos\theta \tilde{v}^p + \chi k^2 \tilde{b} &= 0 \end{aligned} \tag{2.30}$$

where, for example, the Fourier transform in time of component $\hat{v}^t(\mathbf{k}, t)$ is:

$$\tilde{v}^t(\mathbf{k}, \omega) = \int \hat{v}^t(\mathbf{k}, t) e^{-\mathrm{i}\pi\omega t} dt. \tag{2.31}$$

By removing the diffusive terms ($\nu = \chi = 0$), and merging the last two equations in (2.30), we obtain an equation for the poloidal term (which is similar for buoyancy):

$$(N^2 \cos^2\theta - \omega^2)\tilde{v}^p = 0 \tag{2.32}$$

We expect a non-null solution for $\tilde{v}^p$. Hence, equation (2.32) is possible if and only if the dispersion relation for internal gravity waves in stratified flows is satisfied [82]:

$$\omega_r = \pm N \cos\theta. \tag{2.33}$$

A particularity of the dispersion relation (2.33) is that it does not depend on the length of the wavevector $\mathbf{k}$ but only on its direction and on the stratification strength N. This

is not the case for other types of waves such as capillary waves.

If the viscous term is kept with a Prandtl number $Pr = \nu/\chi = 1$ then the solution of equation (2.30) is:

$$\omega = \pm N \cos\theta + \mathrm{i}\nu k^2. \tag{2.34}$$

From the plane wave solution $e^{\mathrm{i}(\mathbf{k}\cdot\mathbf{x}+\omega t)}$, replacing the angular frequency ω by its value in equation (2.34), the effect of the viscous term is only a damping of the wave amplitude of the form $e^{-\nu k^2 t}$.

2.4.2 Dispersion relation for inertial waves

To compute the dispersion relation of IW, we remove the non-linear term in the rotating Navier-Stokes equations computed in (2.16). The new set of equations is:

$$\partial_t \mathbf{u} + \boldsymbol{\nabla} p - \nu \boldsymbol{\nabla}^2 \mathbf{u} = -2\boldsymbol{\Omega} \times \mathbf{u} \tag{2.35}$$

$$\boldsymbol{\nabla} \cdot \mathbf{u} = 0. \tag{2.36}$$

Taking the divergence of (2.35)

$$\boldsymbol{\nabla}^2 p = \boldsymbol{\nabla} \cdot (-2\boldsymbol{\Omega} \times \mathbf{u}), \tag{2.37}$$

the spatial Fourier transform of (2.35) and (2.37) is

$$\partial_t \hat{\mathbf{u}} + (\mathrm{i}\mathbf{k}\hat{p} + 2\boldsymbol{\Omega} \times \hat{\mathbf{u}}) + \nu k^2 \hat{\mathbf{u}} = 0 \tag{2.38}$$

$$\hat{p} = \mathrm{i}\frac{2\mathbf{k} \cdot (\boldsymbol{\Omega} \times \hat{\mathbf{u}})}{k^2}. \tag{2.39}$$

Combining (2.38) and (2.39):

$$\partial_t \hat{\mathbf{u}} + 2\left(-\frac{\mathbf{k} \cdot (\boldsymbol{\Omega} \times \hat{\mathbf{u}})}{k^2}\mathbf{k} + \boldsymbol{\Omega} \times \hat{\mathbf{u}}\right) + \nu k^2 \hat{\mathbf{u}} = 0. \tag{2.40}$$

The rotation terms are projected perpendicular to $\mathbf{k}$ with the projector operator $P = \delta_{ij} - \frac{k_i k_j}{k^2}$.

Projecting equation (2.40) onto the Craya-Herring frame, the velocity field can now be written with only two components:

$$\begin{aligned} \partial_t \hat{v}^t - 2\Omega \sin\theta \hat{v}^p + \nu k^2 \hat{v}^t = 0 \\ \partial_t \hat{v}^p + 2\Omega \sin\theta \hat{v}^t + \nu k^2 \hat{v}^p = 0. \end{aligned} \tag{2.41}$$

By taking the Fourier transform in time of equations (2.41), we obtain

$$\begin{aligned} i\omega \tilde{v}^t - 2\Omega \sin\theta \tilde{v}^p + \nu k^2 \tilde{v}^t = 0 \\ i\omega \tilde{v}^p + 2\Omega \sin\theta \tilde{v}^t + \nu k^2 \tilde{v}^p = 0. \end{aligned} \tag{2.42}$$

By removing the viscous term ($\nu = 0$), and merging the two equations in (2.42), we obtain an equation for the poloidal velocity (which is similar for the toroidal velocity):

$$(4\Omega^2 \sin^2\theta - \omega^2)\tilde{v}^p = 0 \tag{2.43}$$

We expect a non-null solution for $\tilde{v}^p$. Hence, equation (2.43) is possible if and only if the dispersion relation for inertial waves in rotating flows is satisfied:

$$\omega_r = \pm 2\Omega \sin\theta. \tag{2.44}$$

Again, the dispersion relation written in equation (2.44) does not depend on the value of the wavevector $\mathbf{k}$ but only on its direction and on the rotation strength 2Ω.

If the viscosity ν is kept, then the solution of equation (2.42) is:

$$\omega = \pm 2\Omega \sin\theta + \mathrm{i}\nu k^2. \tag{2.45}$$

Similarly to the stratified case, the viscous term can be understood as a damping term of the wave amplitude.

2.4.3 Phase and group velocities

The phase velocity $\mathbf{v}_\Phi$ and group velocity $\mathbf{v}_g$ of waves can be calculated from the dispersion relation ω_r (equations (2.33) and (2.44)). They are written:

$$\mathbf{v}_\Phi = \mathbf{k}\omega_r/k^2 \quad \text{and} \quad \mathbf{v}_g = \nabla_{\mathbf{k}}(\omega_r) = \begin{pmatrix} \frac{\partial \omega_r}{\partial k_x} \\ \frac{\partial \omega_r}{\partial k_y} \\ \frac{\partial \omega_r}{\partial k_z} \end{pmatrix}. \tag{2.46}$$

The phase velocity can be understood as the propagation of phase crest, where $\mathbf{k}\cdot\mathbf{x} + \omega_r t = cste$ [115]. According to [115], the crest of constant phase $\phi = \mathbf{k}\cdot\mathbf{x} + \omega_r t =$ constant, propagates perpendicularly to the wavevector $\mathbf{k}$ since $\boldsymbol{\nabla}_{\mathbf{x}}\phi = \mathbf{k}$ with a phase velocity $\mathbf{v}_\Phi = \omega_r \mathbf{k}/k^2$. It propagates with a phase velocity $\mathbf{v}_\Phi$ parallel to $\mathbf{k}$ if $\omega_r < 0$ and anti-parallel to $\mathbf{k}$ if $\omega_r > 0$. On Figure 2.4, we plot the four possibilities (the four quadrants Q_1, Q_2, Q_3, Q_4) of the propagation of the crest of phase in the plane (θ, ω) according to the sign of θ and ω.

The group velocity (the envelope of the wave) is the velocity at which the energy is propagated. The dispersion relation, the phase velocity and group velocity can be rewritten as in Jause-Labert [66] for rotating flows:

$$\omega_r = \pm 2\Omega \frac{k_z}{k}, \quad \mathbf{v}_\Phi = \pm 2\Omega \frac{k_z}{k^2}\mathbf{k}, \quad \mathbf{v}_g = \pm 2\Omega \frac{\mathbf{k}\times(\mathbf{e}^z \times \mathbf{k})}{k^3}. \tag{2.47}$$

For stratified flows, the dispersion relation, the phase velocity and group velocity can be written as in Davidson [35]:

$$\omega_r = \pm N \frac{k_h}{k}, \quad \mathbf{v}_\Phi = \pm N \frac{k_h}{k^2}\mathbf{k}, \quad \mathbf{v}_g = \pm N \frac{k_z \mathbf{k}\times(\mathbf{k}\times\mathbf{e}^z)}{k^3 k_h}. \tag{2.48}$$

From equations (2.47) and (2.48), it is obvious that the group velocity is perpendicular to the phase velocity ($\mathbf{v}_g \perp \mathbf{v}_\Phi$) for waves in both stratified and rotating flows [115].

2.5 Direct Numerical Simulation method

The non-dimensional Navier-Stokes equations are solved using an in-house pseudo-spectral code in FORTRAN 90 and parallelized with MPI. This code have been already used in the research group for many papers [2, 38, 72, 73, 92, 140]. The equations are solved on a 3D 2π-periodic box and on a uniform grid space in the three directions. The number of points in each direction is n_g, so that each DNS is computed with n_g^3 points. The Navier-Stokes equations are computed in the 3D spatial Fourier domain using the P3DFFT library [116] but the non-linear terms are computed in the physical domain

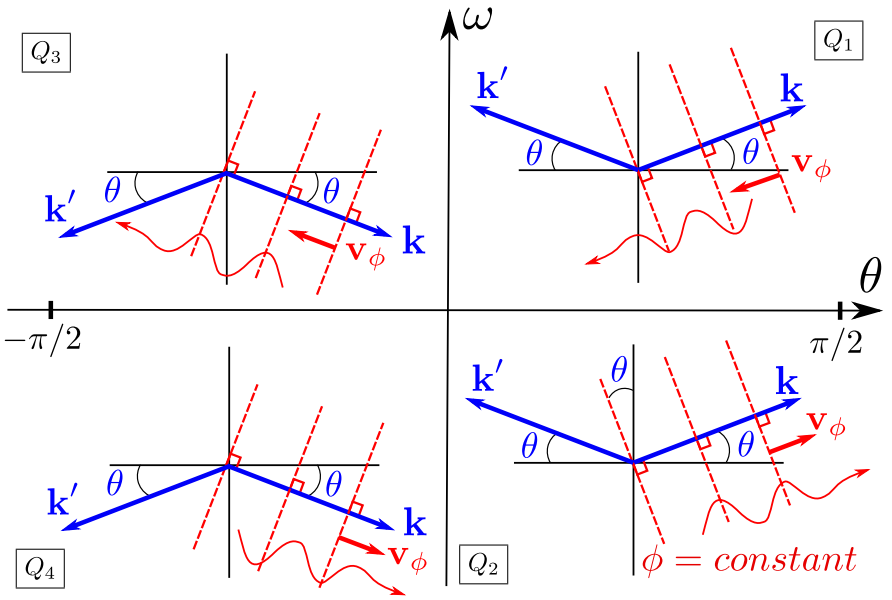

FIGURE 2.4: Diagram representing the four possibilities Q_1, Q_2, Q_3, Q_4 of the propagation of the crest of constant phase $\phi = \mathbf{k}\cdot\mathbf{x} + \omega_r t =$ constant in the plane (θ, ω_r) (see text for explanation). We also introduce $\mathbf{k}' = (-k_x, -k_y, k_z)$ as the horizontal opposite of $\mathbf{k}$ and sharing the same angle θ.

to reduce the computational cost. The phase shifting method is used, resulting in a truncated term at $k_{max} = \sqrt{2}n_g/3$ [28]. The numerical time integration is done using a third-order Adams-Bashforth scheme [72].

2.6 Space-time analysis of the flow

As shown in the equations (2.44) and (2.33), the waves experience a natural relationship between the spatial component θ and the time component ω. In order to use this link, we need to analyse the flow in space and in time.

2.6.1 Numerical technique for space-time analysis

In the experimental work done by Yarom and Sharon [147], a new method has been implemented to calculate the spatio-temporal energy against the angular frequency ω a variable related to time, and the angle between the wave vector $\mathbf{k}$ and horizontal plane θ, a variable related to space. This was also done in numerical works [75] and in an experiment with wave attractor [34]. A similar technique was also implemented where the energy was calculated against the frequency ω and the wavenumber k [41]. More recently, this technique have been refined to calculate the density of energy against ω, θ and k [72, 92].

We explain here how the space-time statistics are computed to link the direction of propagation θ — a spatial variable — to the frequency ω — a time variable in a varying range of wavenumber k. This is done by calculating the time-dependent angular-dependent spectral density of kinetic energy. To do this, the wave vector space is first decomposed into several elementary cones with an angle θ with respect to the horizontal plane and a length k (see Figure 2.5). Due to the θ angle discretization, the elementary cone is a thin volume where all wave vectors $\mathbf{k}$ have an angle $\theta(\mathbf{k}) \in I_\theta = [\theta - \Delta\theta, \theta - \Delta\theta]$.

To compute the energy into this elementary cone, we decompose the computation into four steps:

1. each elementary cone that contains a wave vector $\mathbf{k}$ with an angle $\theta(\mathbf{k}) \in I_\theta$, is divided into sub-volumes by selecting the scale $k = |\mathbf{k}|$. Then, all the velocity vectors are summed over the sub-volume in a local average of velocity $\hat{\mathbf{U}}(\theta, t, k) = \sum_{\theta(\mathbf{k}) \in I_\theta, |\mathbf{k}|=k} \hat{\mathbf{u}}(\mathbf{k}, t)$.
2. The Fourier transform in time of that new variable is computed as $\tilde{\mathbf{U}}(\theta, \omega, k) = FFT\left[\hat{\mathbf{U}}(\theta, t, k)\right]$.
3. The spectral density of kinetic energy is recovered in a (θ, ω) plane for a range of scales between k_1 and k_2 that is a set of sub-volumes:

$$E(\theta, \omega, k_1 \leq k \leq k_2) = \sum_{k_1 \leq k \leq k_2} E(\theta, \omega, k) = \sum_{k_1 \leq k \leq k_2} |\tilde{\mathbf{U}}(\theta, \omega, k)|^2. \tag{2.49}$$

4. The total spectral density of kinetic energy into an elementary cone, regardless of scale k, can be computed as a summation over all sub-volumes:

$$E(\theta, \omega) = \sum_{0 \leq k \leq k_{max}} E(\theta, \omega, 0 \leq k \leq k_{max}) \ , \tag{2.50}$$

where $\hat{\mathbf{u}}$ is obtained from DNS. It is also possible to apply the same algorithm on the separate components of the velocity field ($\hat{u}_x$, $\hat{u}_y$, $\hat{u}_z$) and on the buoyancy field $\hat{b}$.

When the numerical simulation contains only waves, one should observe a peak of energy density that follows the dispersion relation curve defined by equations (2.33) or (2.44) in the (θ, ω) plane (as illustrated in Figure 2.7b).

2.6.2 Saint Andrew's cross for stratified flow: a benchmark

In order to test our method to compute the density of energy against (θ, ω), we compare the theoretical solution against the numerical simulations in the following.

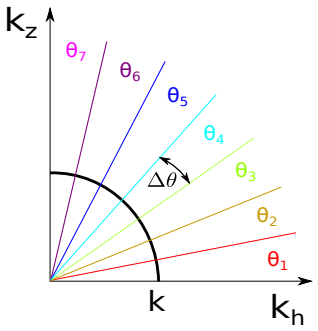

FIGURE 2.5: Decomposition of the Fourier space in elementary "cones" containing wavevectors $\mathbf{k}$ with given wavenumber amplitude k, and θ within discretized intervals between 0 ($k_z = 0$) and $\pi/2$ ($k_h = 0$) as done in Teaca et al. [138].

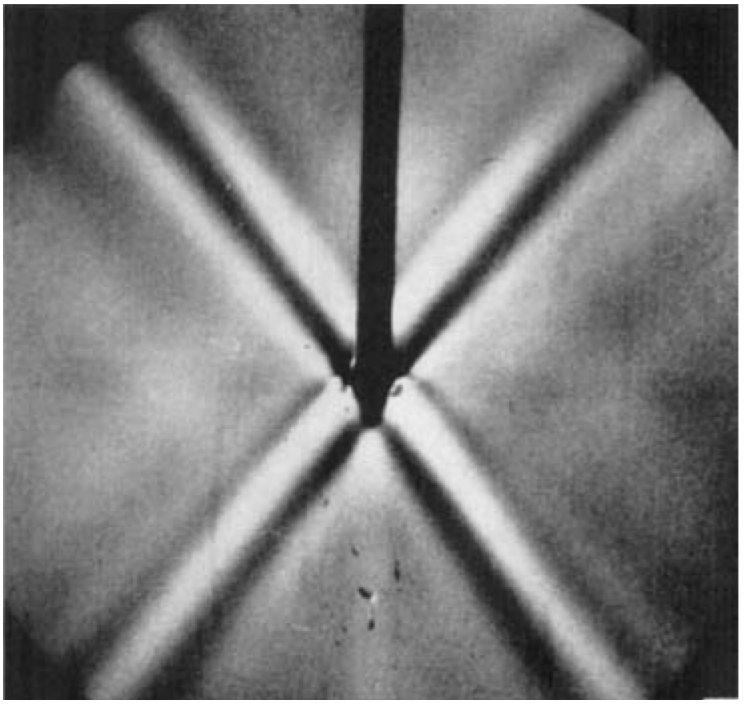

FIGURE 2.6: Example of a Saint Andrew's cross obtained experimentally from an oscillating cylinder in a stably stratified flow (reproduced from Mowbray and Rarity [103]).

When an oscillation inside a stratified or rotating flow at a regular frequency ω_f occurs, it is possible to observe the propagation of waves at the frequency of the forcing and for a particular angle θ. Hence, a saint Andrew's cross appear which is named so, because the propagation of waves at the angle θ creates a shape very similar to the saint Andrew's cross. An example of this Saint Andrew's cross in a stably stratified flow is visible in an experiment done by Mowbray and Rarity [103] and in a numerical simulation in figure 2.7a. The Saint Andrew's cross can be created in a stratified or rotating flow by oscillating a cylinder at a regular frequency in it [43] or by directly forcing the flow to oscillate as done in this thesis. Its main advantage is to propagate IGW or IW in only four directions. As waves are localized in space, it allows the visualization of the phase and group velocities directly in the flow.

2.6.2.1 Analytical solution

We derive the analytical solution of a stratified flow forced on the buoyancy term by an oscillating point at frequency ω_f. From the Navier-Stokes equations in Boussinesq approach projected in the Craya-Herring frame (see equations (2.29)), we add a pointwise sinusoidal forcing on the buoyancy term:

$$\partial_t \begin{pmatrix} \hat{v}^p \\ \hat{b} \end{pmatrix} + \begin{pmatrix} 0 & \cos\theta \\ -N^2\cos\theta & 0 \end{pmatrix} \begin{pmatrix} \hat{v}^p \\ \hat{b} \end{pmatrix} = \begin{pmatrix} 0 \\ \sin(\omega_f t) \end{pmatrix} \tag{2.51}$$

where $\hat{v}^p$ is the corresponding solution for the poloidal component of velocity.
Denoting $\omega_r = N\cos\theta$ and by writing the set of equations (2.51) against only the buoyancy term $\hat{b}$, one gets:

$$\partial_t^2 \hat{b}(t) + \omega_r^2 \hat{b}(t) = \omega_f \cos(\omega_f t) \tag{2.52}$$

The solution of this equation is the sum of the homogeneous and of a particular solution:

$$\hat{b}(t) = \begin{cases} C\cos(\omega_r t) + D\sin(\omega_r t) + \dfrac{\omega_f \cos(\omega_f t)}{\omega_r^2 - \omega_f^2} & \text{if } \omega_r^2 - \omega_f^2 \neq 0 \\ C\cos(\omega_r t) + D\sin(\omega_r t) + \dfrac{t}{2}\sin(\omega_f t) & \text{if } \omega_r^2 - \omega_f^2 = 0. \end{cases} \tag{2.53}$$

Using the initial conditions $\hat{b}(t=0) = 0$ and $\partial_t \hat{b}(t=0) = 0$, the solution of this equation is

$$\hat{b}(t) = \begin{cases} \omega_f \dfrac{\cos(\omega_f t) - \cos(\omega_r t)}{\omega_r^2 - \omega_f^2} & \text{if } \omega_r^2 - \omega_f^2 \neq 0 \\ \dfrac{t}{2}\sin(\omega_f t) & \text{if } \omega_r^2 - \omega_f^2 = 0. \end{cases} \tag{2.54}$$

Applying the time Fourier transform on (2.54) in the case $\omega_r^2 - \omega_f^2 \neq 0$, the solution for the buoyancy is

$$\tilde{b}(\mathbf{k}, \omega) = \frac{\omega_f}{\omega_r^2 - \omega_f^2} \left[\frac{\delta(\omega - \omega_f) + \delta(\omega + \omega_f)}{2} - \frac{\delta(\omega - \omega_r) + \delta(\omega + \omega_r)}{2} \right] \tag{2.55}$$

and similarly for the poloidal velocity component, the solution at $\omega_r^2 - \omega_f^2 \neq 0$ is

$$\tilde{v}^p(\mathbf{k}, \omega) = \frac{\cos\theta}{\omega_r^2 - \omega_f^2} \left[\frac{\omega_f}{\omega_r} \frac{\delta(\omega - \omega_r) + \delta(\omega + \omega_r)}{2i} - \frac{\delta(\omega - \omega_f) + \delta(\omega + \omega_f)}{2i} \right]. \tag{2.56}$$

A peak of energy is obtained in the equations (2.55) and (2.56) for $\omega = \pm\omega_f$ and for $\omega = \pm\omega_r$ representing respectively the forcing frequency and the dispersion relation frequency. The equations diverge for $\omega_f = \pm\omega_r$ because the calculation is done for an inviscid case. When viscosity is added, the solution is a lot more complicated but the

denominator is not only composed of the difference between ω_f^2 and ω_r^2 but also by the viscous term (see Annexe A). Hence the solution does not diverge but reaches a peak of finite value. In numerical simulations, where the viscosity is set very low but not null, the solution does not diverge as well when $\omega_r^2 - \omega_f^2 \simeq 0$ (see section 2.6.2.2).

2.6.2.2 Numerical simulation

We test here the statistical characterization of waves by a simple benchmark consisting of a single wave propagation in a Saint Andrew's cross pattern, as in experiments [82]. The flow forcing produces only waves and is examined from its initial condition at rest. Several forcing possibilities exist to create either a single isolated wave or several superimposed ones. The forcing term is introduced in the linearized Navier-Stokes equations in the Boussinesq approximation: the non-linear terms $\boldsymbol{\omega} \times \mathbf{u}$ and $\mathbf{u} \cdot \boldsymbol{\nabla} \mathbf{b}$ are removed from equations (2.17), likewise in the numerical simulation. For this benchmark, the forcing F_b is only imposed in the buoyancy equation, so that $\mathbf{F}_u = 0$. We choose a point forcing localized in physical space (as in section 2.6.2.1), of the form:

$$F_b = \delta_x \sin(\omega_f t) \tag{2.57}$$

with $\omega_f = 0.3$. This forcing implemented only in the buoyancy equation of system (2.17) ensures that the incompressibility condition is maintained for the velocity field. The function δ_x is the Dirac function. In the Fourier space, it means that all wavenumbers are forced even though there is more energy for high wavenumbers.

The resolution of the numerical simulation is $n_g = 128$ in each direction meaning that the box solved contains a total number of $n_g^3 = 128^3$ points. We assume negligible viscous diffusion so that $\nu = 10^{-7}$, and the Brunt-Väisälä frequency is $N = 1$. We recall that all parameters are written non-dimensional against time and space (see equations (2.8) and (2.15)), thus no dimensions are written when the parameters are set. As expected, we observe in Figure 2.7 the propagation of waves according to an angle θ set by ω_r such that $\omega_r = N \cos\theta$. Figure 2.7a shows the distribution of the vertical velocity components, and the same pattern could be observed in the buoyancy field. The spatio-temporal analysis is then applied using 1000 fields separated by a time step $\Delta t = 0.5$. The total time span is therefore $79.6 T_N$ where the $T_N = 2\pi/N$ is the Brunt-Väisälä period. Upon computing the space-time statistics of energy density $E(\theta, \omega)$ according to equation (2.50), the energy distribution in the (θ, ω) plane (Figure 2.7b) appears to concentrate in two kinds of regions: (a) along two horizontal lines of energy concentration, at $\omega_f = \pm 0.3$; these lines are the traces in the numerical simulation of the pointwise spatial forcing — almost a Dirac — which oscillates at frequency ω_f,

which is Fourier transformed. (b) Along the dispersion relation curve ; in absence of non-linearity, no energy redistribution can occur away from the immediate input due to the forcing. Both kinds of energy concentration curves correspond to the response of the linear system to the forcing, with one component at its forcing frequency ω_f and one at the natural frequency of the system, which is here the frequency of the waves ω_r. The maximum of $E(\theta, \omega)$ is therefore observed at the crossing points of the forcing and the dispersion relation curves, that is at $\theta \simeq 72.5$. In physical space, this peak energy results in the observation of waves propagating at $\theta \simeq 72.5$, which is indeed what we measure on Figure 2.7.

2.6.2.3 Comparison between analytical and numerical results

This numerically observed solution of the response of the linearized system of equations to harmonic forcing is computed analytically in section 2.6.2.1 from the inviscid Boussinesq-Navier-Stokes equations with a zero initial condition. The analytical solution for the buoyancy field and poloidal velocity field is written in equations (2.55) and (2.56). From this solution, two regions of concentration of energy can indeed be found. One along the line defined by $\omega = \pm\omega_f$ which is the frequency of the forcing and one along the curve $\omega = \pm\omega_r$ which is the frequency of the waves along the dispersion relation. The analytical solution diverges for $\omega_f = \pm\omega_r$ because it is an inviscid solution, but it shows that the maximum of energy is at the intersection of these frequencies. For numerical simulations as the flow has a little bit of viscosity, the energy peaks but does not diverge for $\omega_f = \pm\omega_r$.

Note that several vertical lines at constant angle θ are visible in Figure 2.7b in a log-scale. Each point sharing the same angle θ corresponds to an independent set of Fourier transforms in time of all of the vertical velocity field sharing the same angle θ.

2.6.3 Hann windowing technique, when is it used?

A windowing technique can be particularly useful to filter the data in order to make them periodic. This can be particularly interesting for our cases where Fourier transform of non periodic data is done. We explain here in which cases the Hann windowing technique (sometimes referenced as Hanning windowing technique) is used on a signal. The windowing technique used here on a period T is the Hann window:

$$H(t) = \frac{1}{2} - \frac{1}{2}\cos(2\pi t/T). \tag{2.58}$$

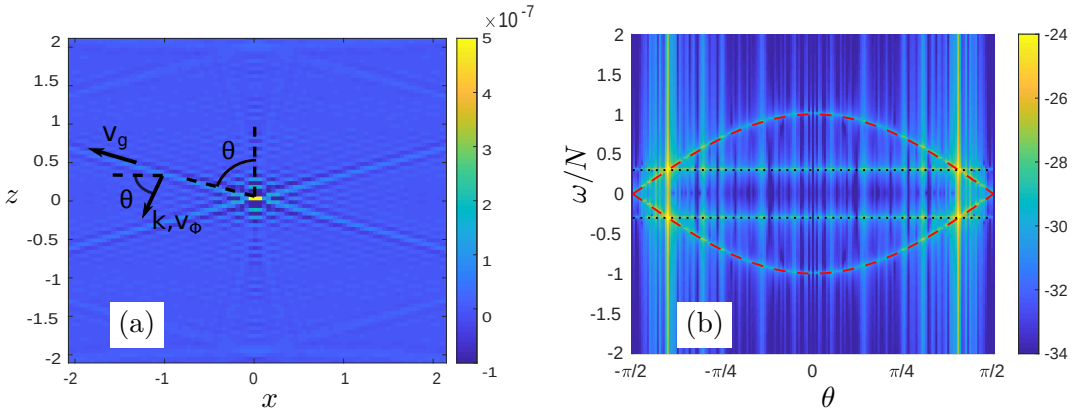

FIGURE 2.7: (a) Distribution of vertical velocity component u_z showing the Saint Andrew's cross pattern of propagation of waves in the (x, z) plane in physical domain (zoomed in, the complete resolution domain is $[-\pi, \pi]^3$) for a simulation with a resolution $n_g = 128$ grid points in each direction, and stratification frequency $N = 1$. The group velocity $\mathbf{v}_g$, phase velocity $\mathbf{v}_\Phi$ and wavevector $\mathbf{k}$ are also represented. (b) The corresponding concentration of energy density $E(\theta, \omega)$ in the (θ, ω) Fourier domain (in log scale). Red dashed line: dispersion relation curve $\omega_r(\theta)$ for internal gravity waves defined by equation (2.33). Black dotted line: forcing frequency ω_f.

We almost never have a perfect periodic signal in turbulence. Therefore, it might be useful to use a windowing technique to help reduce the spectral leakage (the spreading of energy in ω). In figures 2.8 a and b, we can see the effect of the Hann window on the result. The dispersion relation obtained is much sharper in figure 2.8a where a Hann window is used than in figure 2.8b where no windowing technique is used. There is still a little spreading in figure 2.8a, particularly at the intersection between the forcing and the dispersion relation. This is due to the viscous effect and the discretization error.

For a non periodic signal, the drawback of the use of a windowing technique is that the signal it is applied on is modified. Its amplitude and energy are modified depending on the windowing technique used. For example, if a Hann window is used, it is necessary to compensate the signal by a factor of 1.63 in order to keep the same energy or by a factor of 2 in order to keep the same maximum amplitude as shown in [125]. From this, a trade off needs to be made. Should I keep the same energy in my system or keep the same amplitude? This choice could influence our results. Therefore, for the rest of the thesis, the Hann window is used in this thesis for only qualitative results or when no statistics are calculated after. If statistics are computed from the signal, no Hann window is used.

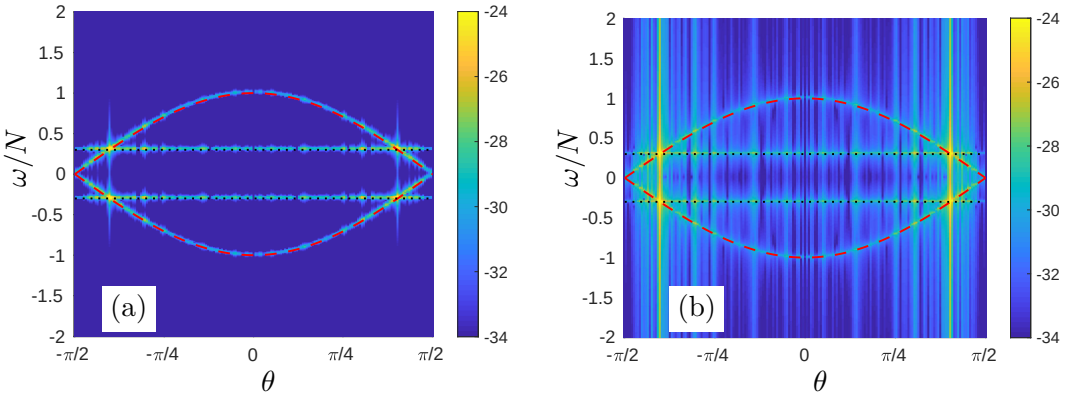

FIGURE 2.8: Energy density $E(\theta, \omega)$ in the (θ, ω) Fourier domain where: (a) a Hann window is applied to the time signal; (b) no windowing technique is applied to the time signal. Red dashed line: dispersion relation curve $\omega_r(\theta)$ for internal gravity waves defined by equation (2.33). Black dotted line: forcing frequency ω_f.

2.7 Non-linear effect on the dispersion relation of waves

In this section, we consider all the possible effects that could modify the dispersion relation of waves in stratified or rotating flows: kinematic effect due to the presence of a large-scale flow, or the dynamical effect due to non-linear interactions.

When looking at the modification of wave frequency, a few phenomena can be considered. The first one is similar to the Doppler effect, and the second one is called sweeping effect. This difference is schematically represented in figure 2.9 where in the case of the Doppler effect, the car is moving compared to the observer and no wind is occurring. In the case of the sweeping effect, it is the wind which is blowing and the car is static compared to the observer. In both cases the frequency of the sound wave emitted by the car and heard by the observer is modified. As shown in section 2.7.1 and 2.7.2, the two cases are not equivalent in the case of IGW in stratified flows or of IW in rotating flows. A third possible phenomenon studied is the effect of a gradient of advective velocity (as if the wind speed was different against height in figure 2.9).

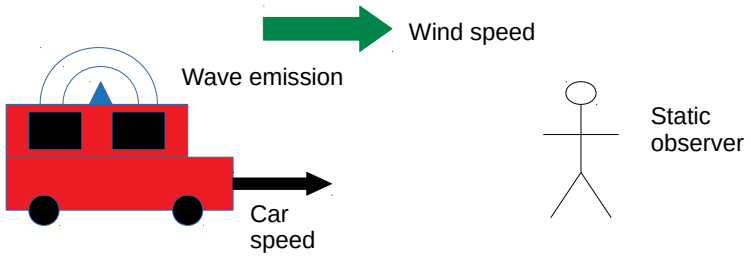

FIGURE 2.9: Doppler effect (car moving and no wind) and sweeping effect (car static and wind blowing)

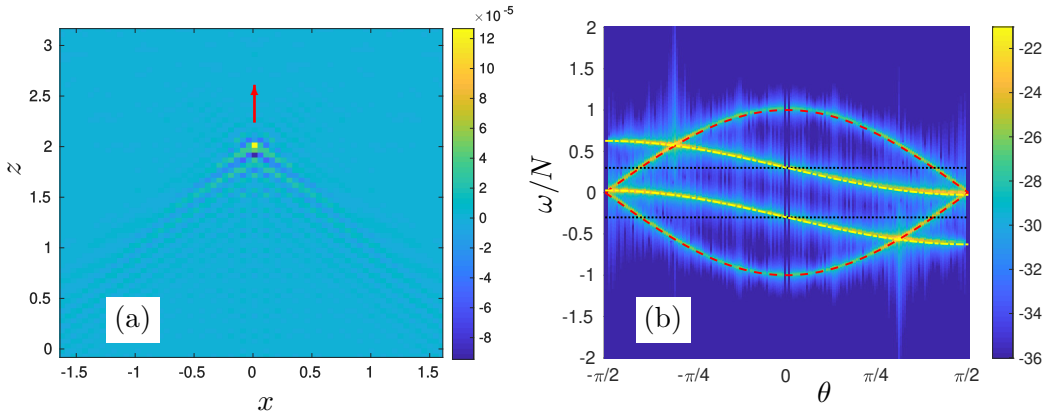

FIGURE 2.10: Doppler effect of a uniform motion of the source generating the internal gravity waves. (a) Vertical velocity u_z in the (x, z) plane in physical space where the red arrow illustrates the vertical velocity of point forcing with $c_z = 6.28 \times 10^{-3}$ (zoomed in). (b) The corresponding concentration of energy density $E(\theta, \omega, 56 < k < 60)$ in the (θ, ω) Fourier domain (in log scale). Red dashed line: dispersion relation curve $\omega_r(\theta)$ for internal gravity waves. Black dotted line: original forcing frequency ω_f. Yellow dash-dotted line: modified frequency of the forcing with k=60 given in (2.60).

Unless stated otherwise, the numerical simulations done in this entire section use the same numerical parameters as the one written in section 2.6.2.2.

2.7.1 Doppler Effect

We investigate a configuration where the wave production mechanism moves at a constant velocity, and in which the modification of the dispersion relation could be different. This new configuration is simulated using a forcing F_b modified so that it is spatially phase-shifted, which, in practice, is done in Fourier space. In physical space, the forcing is thus advected at constant vertical velocity c_z. The new forcing is therefore:

$$F_b = \delta_{\mathbf{x}-\mathbf{c}_z t} \sin(\omega_f t) \tag{2.59}$$

with $\omega_f = 0.3$. The value of $c_z = 6.28 \times 10^{-3}$ is chosen to be large enough (but not too large) to observe a difference in the concentration of energy density (see figure 2.10b).

In Figure 2.10a in the physical vertical plane, the local forcing can be seen to move in the positive z direction in physical space for the same physical and numerical parameter as in paragraph 2.6.2.2.

In the Fourier domain, the dispersion curve is not modified, but only the forcing frequency ω_f is modified by addition of the correction $-\mathbf{c} \cdot \mathbf{k} = -c_z k \sin\theta$. It is modified similarly to the sweeping effect as the new forcing frequency (dash-dotted yellow curve

in Figure 2.10b) is equal to

$$\omega_f' = \omega_f - c_z k \sin\theta. \tag{2.60}$$

Therefore, the Doppler effect does not modify the frequency of internal gravity waves and the original dispersion relation is preserved. This is shown in Figure 2.10b, where the dispersion relation (2.33) is not modified (red dashed curve), whereas the forcing frequency is modified according to equation (2.60) for a wavenumber amplitude between $56 < k < k_{max} = 60$. At the crossing between the two curves indicating the modified frequency of forcing and the dispersion relation, the concentration of energy density $E(\theta, \omega)$ is maximal: at $(\theta, \omega) = (-1.5, 0.1)$ and $(-0.9, 0.6)$, and at the points $(0.9, -0.6)$ and $(1.5, -0.1)$.

2.7.2 Sweeping effect for stratified or rotating fluids

We now consider how the characteristics of the waves can be modified through the advection of a flow. This phenomenon is called sweeping effect and is mostly due to the advection of waves by a large scale flow. It is different from the Doppler effect where the source of the waves moves, but not the background flow.

The effect of the sweeping by an advecting flow on the dispersion relation can be computed by finding the Green's function (*i.e.* the response of a linear system to a Dirac forcing in space and time). First, we compare the dispersion relation obtained numerically and analytically in the case of homogeneous and constant advecting flow for stratified flows. Then, we analyse the effect of non-homogeneous advection on the dispersion relation for rotating or stratified flow.

2.7.2.1 Analytical solution of the sweeping effect for a stratified flow

The influence of the sweeping effect on the waves is easily computed in the case of a homogeneous and constant advecting flow $\mathbf{c}$. In the case of a Dirac forcing in space and time on the buoyancy field, the Navier-Stokes equations in the Boussinesq approximation are:

$$\begin{aligned} \partial_t \mathbf{u} + \mathbf{c}\cdot\boldsymbol{\nabla}\mathbf{u} + \boldsymbol{\nabla} p - \nu\boldsymbol{\nabla}^2\mathbf{u} &= \mathbf{n}b \\ \boldsymbol{\nabla}\cdot\mathbf{u} &= 0 \\ \partial_t b + \mathbf{c}\cdot\boldsymbol{\nabla} b - \chi\boldsymbol{\nabla}^2 b &= -N^2\mathbf{n}\cdot\mathbf{u} + \delta(\mathbf{x})\delta(t) \end{aligned} \tag{2.61}$$

where the forcing $F_b = \delta(\mathbf{x})\delta(t)$ is a dirac forcing in space and time. To solve the linear homogeneous system in equation (2.61) is equivalent to find the Green's function of this system.

As $\mathbf{c} = \boldsymbol{cste}$ then $\boldsymbol{\nabla} \cdot (\mathbf{c} \cdot \boldsymbol{\nabla}\mathbf{u}) = 0$ and $\boldsymbol{\nabla} \cdot \mathbf{c} = 0$. Writing equation (2.61) in matrix form, we get:

$$(\partial_t + \mathrm{i}\mathbf{c}\cdot\mathbf{k}) \begin{pmatrix} \hat{u}^t \\ \hat{u}^p \\ \hat{b} \end{pmatrix} + \begin{pmatrix} \nu k^2 & 0 & 0 \\ 0 & \nu k^2 & -\cos\theta \\ 0 & N^2\cos\theta & \nu k^2 \end{pmatrix} \begin{pmatrix} \hat{u}^t \\ \hat{u}^p \\ \hat{b} \end{pmatrix} = \begin{pmatrix} 0 \\ 0 \\ \delta_t \end{pmatrix}. \tag{2.62}$$

The toroidal component $\hat{u}^t$ has an obvious solution and is not looked at later. We also write $\omega_r = N\cos\theta$. Diagonalising the matrix in equation (2.62):

$$(\partial_t + \mathrm{i}\mathbf{c}\cdot\mathbf{k}) \begin{pmatrix} \hat{u}^p \\ \hat{b} \end{pmatrix} + \mathbf{P} \begin{pmatrix} \nu k^2 - \mathrm{i}\omega_r & 0 \\ 0 & \nu k^2 + \mathrm{i}\omega_r \end{pmatrix} \mathbf{P}^{-1} \begin{pmatrix} \hat{u}^p \\ \hat{b} \end{pmatrix} = \begin{pmatrix} 0 \\ \delta_t \end{pmatrix} \tag{2.63}$$

$$\text{where } \mathbf{P} = \begin{pmatrix} -\mathrm{i}/N & \mathrm{i}/N \\ 1 & 1 \end{pmatrix} \text{ and } \mathbf{P}^{-1} = \begin{pmatrix} \mathrm{i}N/2 & 1/2 \\ -\mathrm{i}N/2 & 1/2 \end{pmatrix}.$$

This equation is then rewritten as:

$$\begin{gathered} (\partial_t + \mathrm{i}\mathbf{c}\cdot\mathbf{k}) \begin{pmatrix} \hat{u}^p_G \\ \hat{b}_G \end{pmatrix} + \begin{pmatrix} \nu k^2 - \mathrm{i}\omega_r & 0 \\ 0 & \nu k^2 + \mathrm{i}\omega_r \end{pmatrix} \begin{pmatrix} \hat{u}^p_G \\ \hat{b}_G \end{pmatrix} = \begin{pmatrix} \delta_t/2 \\ \delta_t/2 \end{pmatrix} \\ \text{where } \begin{pmatrix} \hat{u}^p_G \\ \hat{b}_G \end{pmatrix} = \mathbf{P}^{-1} \begin{pmatrix} \hat{u}^p \\ \hat{b} \end{pmatrix}. \end{gathered} \tag{2.64}$$

Applying the Fourier transform in time to (2.64):

$$\begin{pmatrix} \tilde{u}^p_G \\ \tilde{b}_G \end{pmatrix} = \begin{pmatrix} \frac{1}{2}\frac{1}{\nu k^2 + \mathrm{i}(\omega + \mathbf{c}\cdot\mathbf{k} - \omega_r)} \\ \frac{1}{2}\frac{1}{\nu k^2 + \mathrm{i}(\omega + \mathbf{c}\cdot\mathbf{k} + \omega_r)} \end{pmatrix}. \tag{2.65}$$

The solution for the poloidal and buoyancy component is:

$$\begin{pmatrix} \tilde{u}^p \\ \tilde{b} \end{pmatrix} = \mathbf{P} \begin{pmatrix} \tilde{u}^p_G \\ \tilde{b}_G \end{pmatrix} = \begin{pmatrix} \frac{\mathrm{i}}{2N}\left\{\left[\nu k^2 + \mathrm{i}(\omega + \mathbf{c}\cdot\mathbf{k} + \omega_r)\right]^{-1} - \left[\nu k^2 + \mathrm{i}(\omega + \mathbf{c}\cdot\mathbf{k} - \omega_r\right]^{-1}\right\} \\ \frac{1}{2}\left\{\left[\nu k^2 + \mathrm{i}(\omega + \mathbf{c}\cdot\mathbf{k} + \omega_r)\right]^{-1} + \left[\nu k^2 + \mathrm{i}(\omega + \mathbf{c}\cdot\mathbf{k} - \omega_r\right]^{-1}\right\} \end{pmatrix}. \tag{2.66}$$

From equation (2.66), one can see that the buoyancy energy $\tilde{b}^2$ increases when $\omega \to \pm\omega_r - \mathbf{c}\cdot\mathbf{k}$. This scenario corresponds to the wave domain and the dispersion relation

is modified due to the term $\mathbf{c}\cdot\mathbf{k}$. Hence a uniform advecting flow modify the dispersion relation of waves due to the sweeping effect. The new dispersion relation for internal gravity waves with a constant and homogeneous advecting flow $\mathbf{c}$ is:

$$\omega_c^{\pm} = \pm N\cos\theta - \mathbf{c}\cdot\mathbf{k} \tag{2.67}$$

2.7.2.2 Analytical solution of sweeping effect for a rotating flow

The above analyses done for the stratified case can also be done for the rotating case. The influence of the sweeping effect on the inertial waves is easily computed in the case of a homogeneous and constant advecting flow $\mathbf{c}$. In the case of a Dirac forcing in space and time on the toroidal velocity, the Navier-Stokes equations are:

$$\partial_t\mathbf{u} + \mathbf{c}\cdot\boldsymbol{\nabla}\mathbf{u} + \boldsymbol{\nabla}p - \nu\boldsymbol{\nabla}^2\mathbf{u} = -2\Omega\mathbf{n}\times\mathbf{u} + \mathbf{F}^t \tag{2.68}$$

$$\boldsymbol{\nabla}\cdot\mathbf{u} = 0 \tag{2.69}$$

where $\mathbf{F}^t$ is the projection of a toroidal dirac in the cartesian space. It is derived in the Fourier space as $\hat{\mathbf{F}}^t = (\frac{k_y}{k_h}\delta_t, -\frac{k_x}{k_h}\delta_t, 0)$.

As we get $\mathbf{c} = \boldsymbol{cste}$ then $\boldsymbol{\nabla}\cdot(\mathbf{c}\cdot\boldsymbol{\nabla}\mathbf{u}) = 0$ and $\boldsymbol{\nabla}\cdot\mathbf{c} = 0$. Equation (2.68) can be written in the toroidal-poloidal space:

$$(\partial_t + \mathrm{i}\mathbf{c}\cdot\mathbf{k})\begin{pmatrix}\hat{u}^t\\ \hat{u}^p\end{pmatrix} + \begin{pmatrix}\nu k^2 & -2\Omega\sin\theta\\ 2\Omega\sin\theta & \nu k^2\end{pmatrix}\begin{pmatrix}\hat{u}^t\\ \hat{u}^p\end{pmatrix} = \begin{pmatrix}\delta_t\\ 0\end{pmatrix}. \tag{2.70}$$

We write $\omega_r = 2\Omega\sin\theta$. The matrix involving rotation and viscosity in (2.70) is diagonalized as:

$$(\partial_t + \mathrm{i}\mathbf{c}\cdot\mathbf{k})\begin{pmatrix}\hat{u}^t\\ \hat{u}^p\end{pmatrix} + \mathbf{P}\begin{pmatrix}\nu k^2 - \mathrm{i}\omega_r & 0\\ 0 & \nu k^2 + \mathrm{i}\omega_r\end{pmatrix}\mathbf{P}^{-1}\begin{pmatrix}\hat{u}^t\\ \hat{u}^p\end{pmatrix} = \begin{pmatrix}\delta_t\\ 0\end{pmatrix} \tag{2.71}$$

$$\text{where } \mathbf{P} = \begin{pmatrix}-\mathrm{i} & \mathrm{i}\\ 1 & 1\end{pmatrix} \text{ and } \mathbf{P}^{-1} = \begin{pmatrix}\mathrm{i}/2 & 1/2\\ -\mathrm{i}/2 & 1/2\end{pmatrix}.$$

The equation (2.71) becomes:

$$(\partial_t + \mathrm{i}\mathbf{c}\cdot\mathbf{k})\begin{pmatrix}\hat{u}^t_G\\ \hat{u}^p_G\end{pmatrix} + \begin{pmatrix}\nu k^2 - \mathrm{i}\omega_r & 0\\ 0 & \nu k^2 + \mathrm{i}\omega_r\end{pmatrix}\begin{pmatrix}\hat{u}^t_G\\ \hat{u}^p_G\end{pmatrix} = \begin{pmatrix}\mathrm{i}\delta_t/2\\ -\mathrm{i}\delta_t/2\end{pmatrix}$$
$$\text{where } \begin{pmatrix}\hat{u}^t_G\\ \hat{u}^p_G\end{pmatrix} = \mathbf{P}^{-1}\begin{pmatrix}\hat{u}^t\\ \hat{u}^p\end{pmatrix}. \tag{2.72}$$

Applying the Fourier transform to (2.72) a solution is found:

$$\begin{pmatrix}\tilde{u}^t_G\\ \tilde{u}^p_G\end{pmatrix} = \begin{pmatrix}\frac{\mathrm{i}}{2}\frac{1}{\nu k^2+\mathrm{i}(\omega+\mathbf{c}\cdot\mathbf{k}-\omega_r)}\\ -\frac{\mathrm{i}}{2}\frac{1}{\nu k^2+\mathrm{i}(\omega+\mathbf{c}\cdot\mathbf{k}+\omega_r)}\end{pmatrix}. \tag{2.73}$$

The solution for the toroidal and poloidal component is:

$$\begin{pmatrix}\tilde{u}^t\\ \tilde{u}^p\end{pmatrix} = \mathbf{P}\begin{pmatrix}\tilde{u}^t_G\\ \tilde{u}^p_G\end{pmatrix} = \begin{pmatrix}\frac{1}{2}\left\{\left[\nu k^2 + \mathrm{i}(\omega + \mathbf{c}\cdot\mathbf{k} - \omega_r)\right]^{-1} + \left[\nu k^2 + \mathrm{i}(\omega + \mathbf{c}\cdot\mathbf{k} + \omega_r\right]^{-1}\right\}\\ \frac{\mathrm{i}}{2}\left\{\left[\nu k^2 + \mathrm{i}(\omega + \mathbf{c}\cdot\mathbf{k} - \omega_r)\right]^{-1} - \left[\nu k^2 + \mathrm{i}(\omega + \mathbf{c}\cdot\mathbf{k} + \omega_r\right]^{-1}\right\}\end{pmatrix}. \tag{2.74}$$

Similarly to the stratified case, when $\omega \to \pm 2\Omega\sin\theta - \mathbf{c}\cdot\mathbf{k}$ then the toroidal energy $\tilde{u}^{t^2}$ and poloidal energy $\tilde{u}^{p^2}$ increase. The evolution of the peak of energy varies depending on the viscosity ν. Therefore, when a peak of energy is observed in the frequency ω and spatial domain $\mathbf{k}$, it corresponds to the motion associated with waves. The new dispersion relation for inertial waves with a constant and homogeneous advecting flow $\mathbf{c}$ is:

$$\omega_c^{\pm} = \pm 2\Omega\sin\theta - \mathbf{c}\cdot\mathbf{k}. \tag{2.75}$$

2.7.2.3 Sweeping by a homogeneous flow in a stratified flow

We here study numerically how a constant and uniform advecting flow modifies the frequency of the internal gravity waves. We compare our numerical result to the analytical solution of equation (2.67) with a sweepping effect by a homogeneous and constant advecting flow. It should modify the waves frequency by a factor $\mathbf{c}\cdot\mathbf{k}$.

A numerical simulation is done using a forcing F_b defined in practice in Fourier space. For the rest of the study of the sweeping effect, the forcing F_b is:

$$F_b = \sin(\omega_f t) \tag{2.76}$$

with $\omega_f = 0.3$.

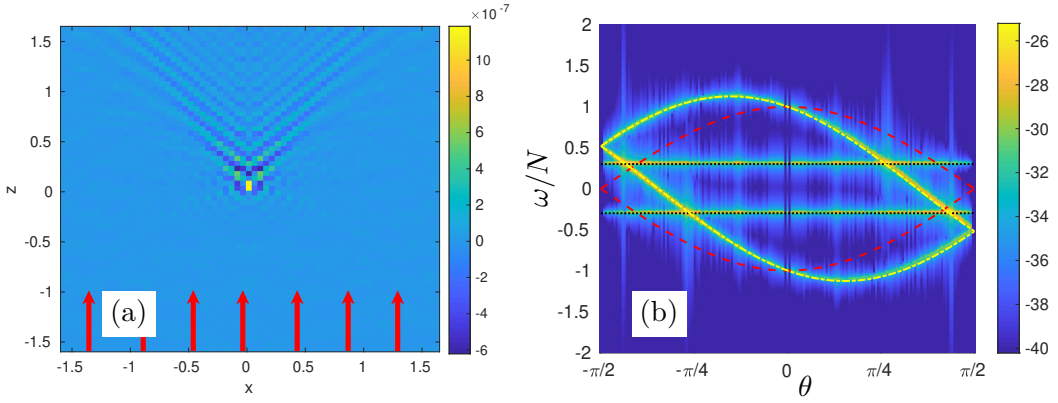

FIGURE 2.11: Sweeping effect of a homogeneous vertical mean velocity field on the propagation of an internal gravity wave. (a) Vertical velocity u_z in the (x, z) plane in physical space where the red arrow illustrate vertical velocity with $c_z = 10^{-2}$ (zoomed in). (b) The corresponding concentration of energy density $E(\theta, \omega, 56 < k \leq 60)$ in the (θ, ω) Fourier domain (in log scale). Red dashed line: original dispersion relation curve $\omega_r(\theta)$ for internal gravity waves defined by equation (2.33). Black dotted line: forcing frequency ω_f. Yellow dashed-dotted line: deviation of the dispersion relation for $k = 60$ defined by equation (2.77).

We consider a vertical advecting velocity field $\mathbf{c} = (0, 0, c_z)$, *i.e.* along the natural axis of symmetry of the system, borne by the gravity vector. The Saint Andrew's cross pattern obtained without mean flow as in paragraph 2.6.2.2 is therefore convected towards positive z direction. As a result the dispersion relation is modified by the term $\mathbf{c} \cdot \mathbf{k} = c_z k_z = c_z k \sin\theta$:

$$\omega' = \omega_r - c_z k \sin\theta \tag{2.77}$$

The result is shown on the two panels of Figure 2.11 for $c_z = 10^{-2}$, with the same physical and numerical parameters as in paragraph 2.6.2.2. The left plot of Figure 2.11 shows that the wave-packet is translated, thus producing a 'wake-like' pattern, much as that of a uniformly propelled boat for surface waves. The right panel of Figure 2.11 shows the distribution of energy density $E(\theta, \omega)$. This figure shows that the dispersion relation is modified according to equation (2.77), and that maximum modification is observed when considering the largest wavenumber range $56 < k \leq k_{max} = 60$. This domain of wavenumber is chosen in order to observe the maximum effect of the sweeping effect. Moreover, the energy density $E(\theta, \omega, 56 < k \leq 60)$ gets very large at the intersection between the forcing and the modified dispersion relation with an asymmetrical angle value of $\theta \simeq \pm 0.8$rad and $\theta \simeq \pm 1.3$rad. Note that the Figure 2.11b is in agreement with Figure 2.4 in quadrant Q_1, $\mathbf{c}$ is in the opposite direction compared to the vertical component of phase velocity $\mathbf{v}_\phi$, and the frequency ω decreases compared to the dispersion relation. In quadrant Q_2, a similar kinematic reasoning leads to an increase of the angular frequency ω. This reasoning could be extended to quadrants Q_3 and Q_4.

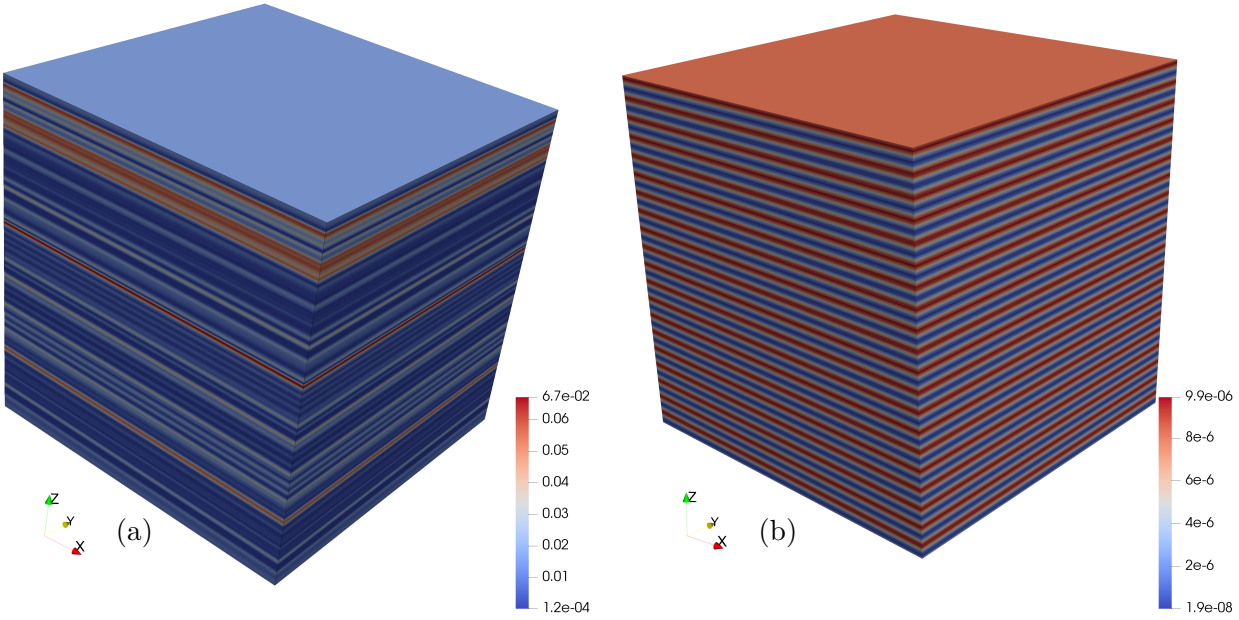

FIGURE 2.12: Total kinetic energy in physical space of a VSHF extracted from (a) a 512^3 points turbulent simulation with $Re_b = 0.1$ and $Fr = 0.0014$ (see section 4.2.4 for more details); (b) our modelled VSHF with $k_z = 10$.

2.7.2.4 Sweeping by an inhomogeneous flow for stratified fluids

In the previous cases, an idealized flow is used to convect IGW. However, actual flows are in general not homogeneous in space. Here, the propagation of waves convected by a large-scale non uniform flow is considered. In a stratified flow, a large-scale shear flow can often dominate the overall structure of the flow, and evolves slowly in time. It is called the Vertically Sheared Horizontal Flow (VSHF). This shear flow is characterized by vertical variation only, without vertical velocity (see figure 2.12a for example). This strong vertical shearing depends only on a vertical wave vector (*i.e.* $k_h = 0$), so that the velocity $u_{shear}(k_h = 0, k_z)$ is parallel to the horizontal plane and the dispersion relation gives a frequency $\omega = 0$ [129]. Its overall structure can be modelled by taking a velocity field $\mathbf{u}(k_h = 0, k_z)$ as done in figure 2.12b. VSHF mode is not considered as a wave and the perturbation density distribution b in this case is uniformly zero. Therefore, these large-scale non uniform flows are often the dominant sources of sweeping of internal gravity waves. This mode has generally been observed in numerical simulations, either in forced turbulence [64, 126, 129] or in decaying turbulence [57], as well as in statistical approaches such as EDQNM models [55] or the statistical state dynamics [46]. Moreover, VSHF appear in strongly stratified turbulence (low Froude number and high buoyancy Reynolds number) and not in weak stratification (high Froude number) [71]. In the context of geophysical fluid dynamics, the VSHF is an ageostrophic horizontal wind and can help to understand the emergence and maintenance of some turbulent jets, such

as banded winds of Jupiter or equatorial deep jets of ocean by an interaction between wave and mean flow [5]. Nevertheless, the formation of VSHF is not really understood in many ways. Several theories try to explain the mechanisms of VSHF's formation, such as resonant interactions among gravity wave [126, 129], rapid distortion theory [50] and recently by a linearized version of statistical state dynamics [46]. It appears that the VSHF is fed by an interaction with small scales of turbulence, so that a little bit of turbulence is required.

An idealized model of a VSHF is created ($u_{shear}(k_h = 0, k_z)$). It has only one vertical wavenumber forced (k_z with $k_h = 0$) and its amplitude is set as a constant. In figure 2.13, we can observe the effect of this model of VSHF ($u_{shear}(k_h = 0, k_z)$ with varying vertical wavenumber k_z (1st column) on the dispersion relation of IGW (2nd column) and on the propagation of the Saint Andrew's cross (3rd column). In the first column of figure 2.13, only the velocity field in the x direction $u_x(x, z)$ in the physical space is shown. In the Fourier domain it is defined as $\hat{u}_x(k_h = 0, k_z)$. The vertical wavenumber is changed from $k_z = 1$ to $k_z = 50$ with an increment of 10 for each different case ($kz = 10$, $k_z = 20$, ...). The horizontal *rms* velocity $c_{h,rms}(k_h = 0)$ for each VSHF is set constant and is equal to $c_{h,rms}(k_h = 0) = 0.008$. The numerical simulations are done with the same physical and numerical parameters as in paragraph 2.6.2.2.

Hence, it is possible to observe the effect of the scale of the VSHF on the dispersion relation. At large scale ($k_z = 1$), the VSHF flow does not fluctuate much and modify the dispersion relation as if the VSHF was homogeneous. The new dispersion relation follows the relation $\omega = \omega_r + \mathbf{u}(k_h = 0) \cdot \mathbf{k}$. When the scale of the VSHF decreases, the dispersion relation has less components at high frequency, but more components at angles $|\theta|$ higher. As the scale of the VSHF diminishes more and more this effect increases. For the smallest scale of the VSHF ($k_z = 50$), the dispersion relation is modified differently than for a large scale VSHF. No energy exists at a frequency higher than the Brunt-Väisälä frequency N. Furthermore, the energy is localized at all angles θ with a frequency smaller than the Brunt-Väisälä frequency. This shows that a small scale VSHF has a very different effect on sweeping than a large scale VSHF. Overall, the Saint Andrew's cross pattern changed a little for a VSHF at high scale (we see some ripples for $x > 0$ which are not here for $x < 0$) but is does not seem to be very modified for small scale VSHF.

To better understand the sweeping effect of a VSHF with high vertical wavenumber, figure 2.14 shows the concentration of energy for points oscillating at a pulsation $\omega_f = 0.3$ for only wavenumbers close to an angle $\theta = \pm\pi/4$. For figure 2.14a, no special effect is

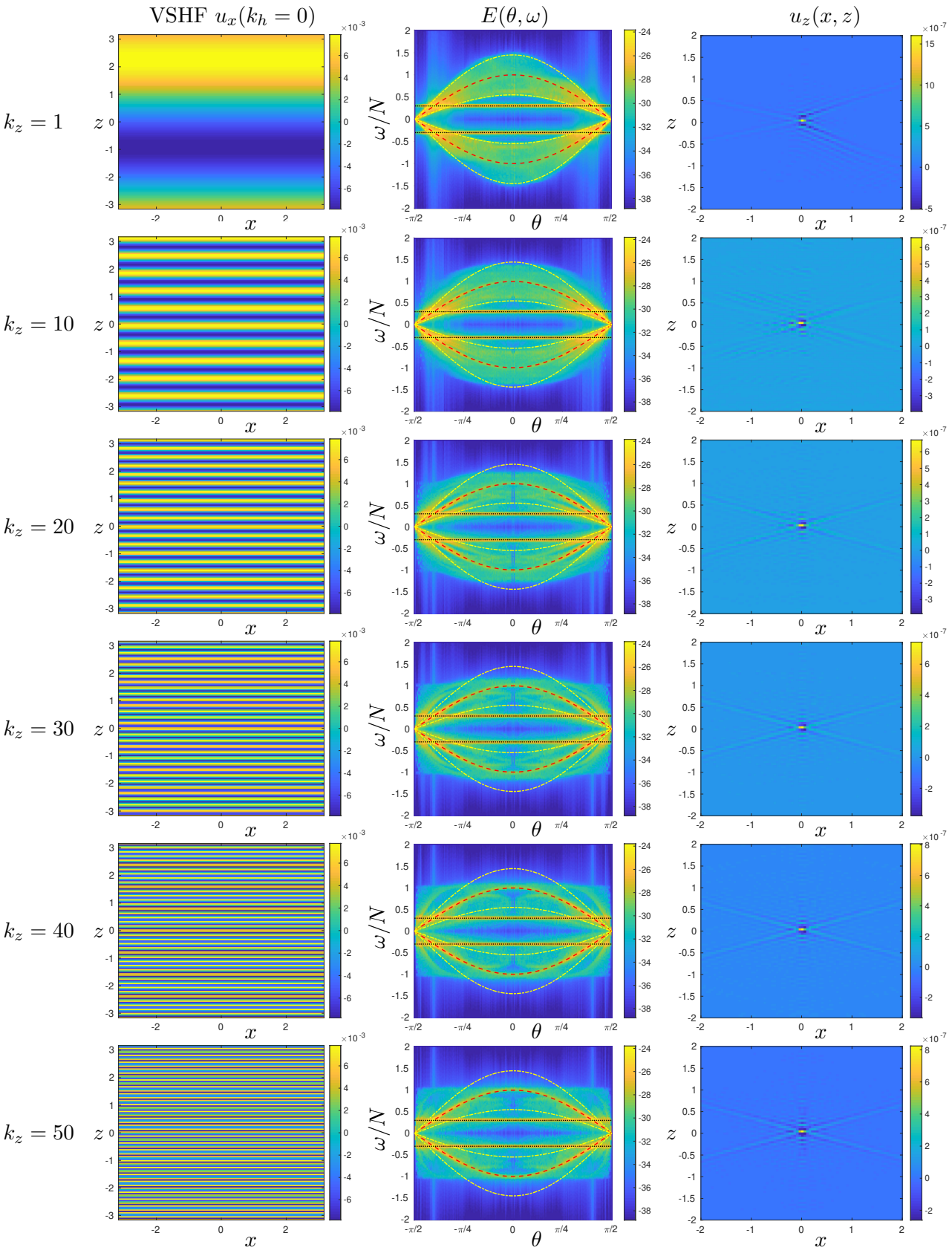

FIGURE 2.13: Sweeping effect of a VSHF flow with varying vertical wavenumber k_z on the Saint Andrew's cross pattern of propagation of IGW. 1st column: VSHF used to convect the Saint Andrew's cross. 2nd column: Density of kinetic energy in the (θ, ω) plane. Red dashed line: dispersion relation curve $\omega_r(\theta)$ for IW. Black dotted line: original forcing frequency ω_f. 3rd column: Saint Andrew's cross convected.

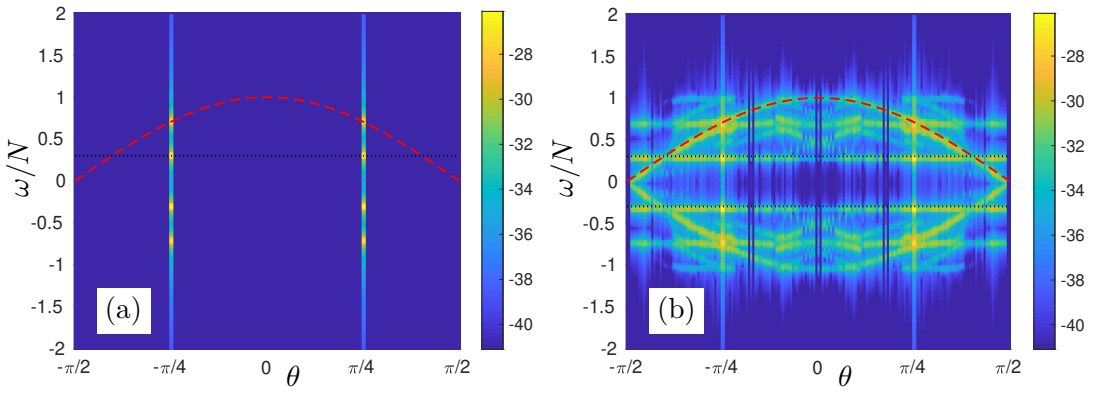

FIGURE 2.14: Concentration of energy density $E(\theta, \omega)$ in the (θ, ω) Fourier domain (in log plot).The only wavenumbers forced have an angle $\theta = 45$. Red dashed line: dispersion relation curve $\omega_r(\theta)$ for IGW. Black dotted line: original forcing frequency ω_f (plotted for all angles θ). (a) No special effect added (as sweeping or gradient). (b) Sweeping with a VSHF $k_z = 50$.

added, but for figure 2.14b, the flow is advected through the sweeping by a VSHF with $k_z = 50$ (similarly to the last line on figure 2.13). In Figure 2.14a, the components of the flow that contains energy has always $\theta = \pm\pi/4$ and most of the energy is either at the forcing point $\omega_f = 0.3$ or at the frequency of the dispersion relation $N \cos \frac{\pi}{4}$. This result is very similar to the figure 2.8a, but with only one angle forced in the flow. On the contrary, this is not the case when the sweeping effect occurs as all the dispersion relation is visible (in figure 2.14b) for any angle θ. This shows that the sweeping effect from a small scale VSHF can modify the original angle of propagation of the waves.
The process of creation of other frequencies and angles could be understood in a few steps:

- The forcing creates energy at the points ω_f and at the points $N \cos \frac{\pi}{4}$ for an angle $\theta = \pi/4$.
- The sweeping by the VSHF changes the angle of the energy. Lines appear at frequencies ω_f and $N \cos \frac{\pi}{4}$ for all angles θ.
- As energy is present for all angles θ, energy appears along the dispersion relation as in step 1 or equations (2.55) and (2.56). The full dispersion relation ω_r is recovered.

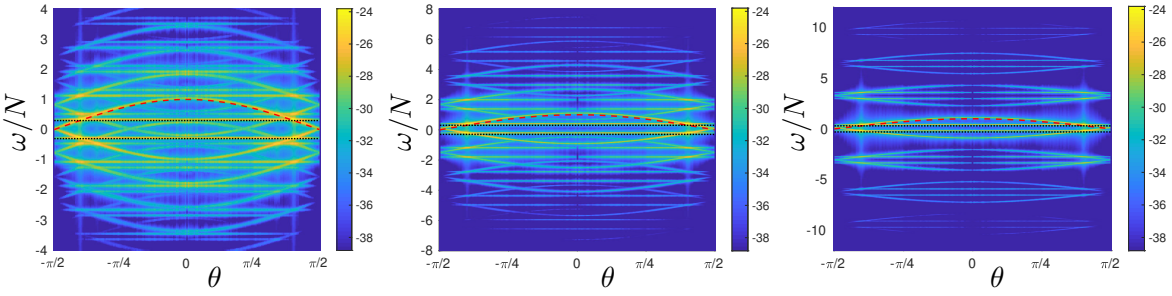

FIGURE 2.15: Sweeping effect of the VSHF with a vertical wavenumber $k_z = 1$ and a varying pulsation ω_F on the dispersion relation created from an oscillating Dirac. (a) $\omega_F = \pi/4$ (b) $\omega_F = \pi/2$ (c) $\omega_F = \pi$.

2.7.2.5 Effect of an advecting flow with a non zero frequency on a stratified flow

In turbulent flow, the VSHF or GM can slowly vary in time. It is necessary to understand how their frequency can modify the sweeping effect. To do so, we make the amplitude of the VSHF vary as a sinusoid with a pulsation ω_F and we use it to advect the Saint Andrew's cross. This means that the VSHF fluctuates at a non zero frequency. As a result the *rms* velocity is modified compared to the previous tests and in order to keep it constant, we multiply it by a factor $\pi/2$. This new oscillating VSHF $\hat{\mathbf{u}}_{shear,\omega_F}$ can be written as:

$$\hat{\mathbf{u}}_{shear,\omega_F} = \frac{\pi}{2}\sin(\omega_F t)\hat{\mathbf{u}}_{shear}. \tag{2.78}$$

Figure 2.15 shows the effect on the dispersion relation of the VSHF oscillating at a pulsation ω_F. We observe that the dispersion relation is repeated in pulsation for every ω_F. The new pulsation created is $\omega_2 = \omega_r + \omega_F$. Then this new pulsation interacts again with the fluctuating VSHF to create another dispersion relation of frequency $\omega_3 = \omega_2 + \omega_F$. This process is repeated many times, but the amplitudes of those new dispersion relations decrease as $|\omega|$ increases. This repetition of the dispersion relation pattern is very similar to the non-linear interaction between components of wavevector $\mathbf{k}, \mathbf{p}, \mathbf{q}$ where $\omega(\mathbf{k}) = \omega(\mathbf{p}) + \omega(\mathbf{q})$ and $\mathbf{k} = \mathbf{p} + \mathbf{q}$ [133]. Suprisingly, there is no modification of the dispersion relation by the sweeping effect. This shows that only close to zero frequency advecting flow can modify the frequency of waves with the sweeping effect.

2.7.2.6 Sweeping by an inhomogeneous flow for rotating fluid

In rotating flows, a large scale flow can often dominate the overall structure of the flow and evolve slowly in time [75]. It is called the geostrophic mode (GM) and is

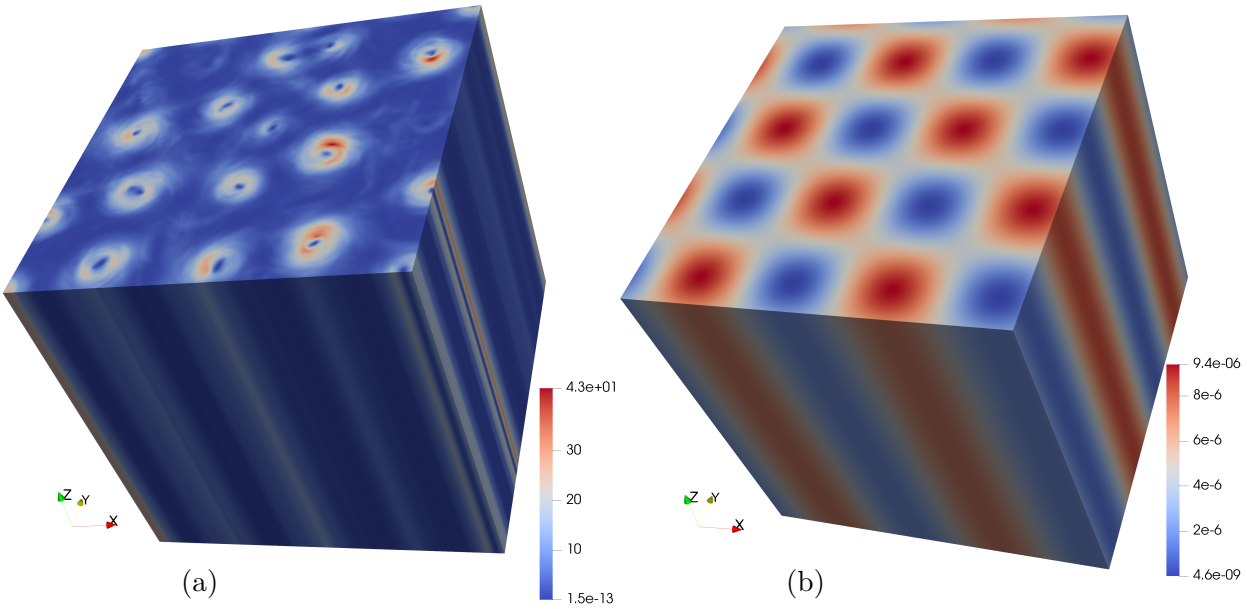

FIGURE 2.16: Total kinetic energy in physical space of a GM extracted from (a) a 512^3 points turbulent simulation with $2\Omega = 80$ (see section 5.2 for more details); (b) our modelled GM with $k_h = 1$

.

characterized by a horizontal variation only (*i.e.* $k_z = 0$) with a purely horizontal velocity $u_{GM}(k_h, k_z = 0)$ (see figure 2.16 for example). This GM is also not considered as waves despite having an angle $\theta = 0$ and a frequency $\omega \sim 0$. As this GM is large scale and often dominates the flow [75], it can be considered as the main source of sweeping of inertial waves [27]. It is not well understood how this GM arises, but several theories exist from near-resonant triadic interaction [78, 127] to quartetic instability [22] or resonant quartet of IW [128] (see section 5.1 for more details on the GM).

We modelled an ideal GM ($u_{GM} = u(k_z = 0, k_h)$) similarly to the VSHF (see section 2.7.2.4) by enforcing only one wavenumber k_h with $k_z = 0$. Our model assumes here that the GM is purely horizontal and has no vertical component. The amplitude of the GM for the different value of k_h is also set as a constant. Then, we did the same analysis for the GM as for the VSHF to explore the effect of the scale of the GM on the sweeping effect. This is done on the rotating case, with the same parameters as in the stratified case and by choosing $2\Omega = 1$. The only difference between the rotating case and stratified case is that the forcing is now done on the vertical velocity component instead of the buoyancy component. The forcing on the vertical velocity component is written $F_{u_z} = \sin(\omega_f t)$. However, it appears that our flow diverged when the scale was getting lower. Why is that so?

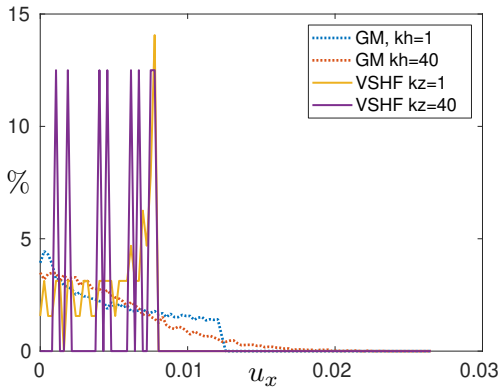

FIGURE 2.17: Probability density function of the amplitude of the velocity in the x direction u_x of the GM and of the VSHF depending on the horizontal (k_h) and vertical (k_z) wavenumber.

In figure 2.17, we observe the *pdf* of the velocity u_x in x direction for a large scale and small scale VSHF and GM having the same horizontal *rms* velocity of 0.008 (here the *rms* velocity in x direction is 0.005) and obtained from a numerical simulation with 128^3 points. The domain is equally divided between 100 intervals from $u_x = 0$ to $u_x = 0.0265$. Therefore, all values within an interval of 0.00265 are considered the same. We observe that the distribution of velocity of the VSHF mode is constant depending on its scale and does not exceed 0.008. On the contrary, the distribution of the velocity of the GM varies a lot and exceeds quite clearly the maximum value of the VSHF. This is expected as the VSHF is similar to a sinusoidal fluctuation while a GM is composed of vortex with a large velocity at its center. At large scale, ($k_h = 1$) the maximum value of the GM is only 0.013 but at smaller scale ($k_h = 40$) the maximum value of the GM mode is 0.0265 but for only for one point. Therefore, we had a problem for our algorithm to reach a convergence with an advecting GM, when dealing with points at very high velocity and small scale.

In figure 2.18, we observe the effect of a model of the GM ($u_{GM} = u(k_z = 0, k_h)$) of varying horizontal wavenumber k_h (1st column) on the dispersion relation (2nd column) and on the propagation of the Saint Andrew's cross (3rd column). The GM keeps the same *rms* velocity in all cases. In the first column of figure 2.18, only the velocity field in the x direction $u_x(x, y)$ in the physical space is shown. In the Fourier domain it is defined as $\hat{u}_x(k_z = 0, k_h)$. We observe that the Saint Andrew's cross is modified a lot by the GM mode contrarily to the VSHF which does significantly modify the propagation of the Saint Andrew's cross.

At large scale ($k_h = 1$) the GM has an effect on the dispersion relation which is very well estimated by the sweeping effect due to the *rms* velocity $c_{h,rms}(k_z = 0)$. When the scale of the GM is smaller ($k_z = 10$), it seems that some energy begins to appear at frequency ω lower than the smallest frequency normally allowed by the sweeping from

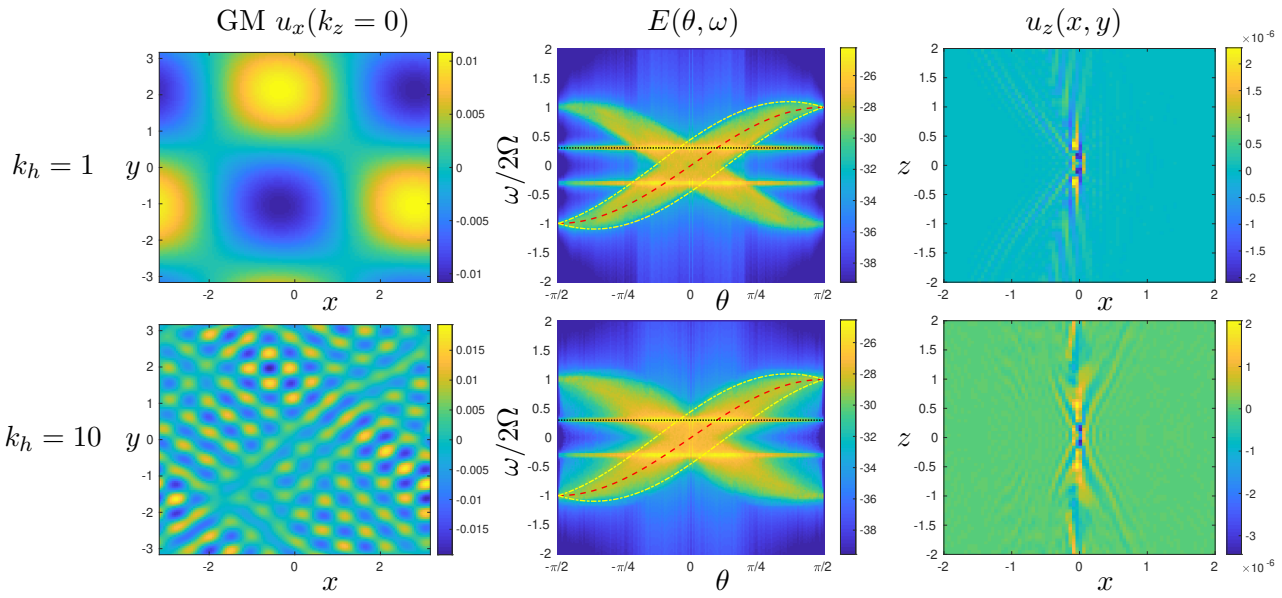

FIGURE 2.18: Sweeping effect of the GM with a horizontal wavenumber $k_h = 1$ or $k_h = 10$ on the Saint Andrew's cross pattern of propagation of IGW. 1st column: GM ($u_x(k_z = 0)$) used to convect the Saint Andrew's cross. 2nd column: Density of kinetic energy in the (θ, ω) plane. Red dashed line: dispersion relation curve $\omega_r(\theta)$ for IW. Black dotted line: original forcing frequency ω_f. 3rd column: Saint Andrew's cross convected.

the *rms* velocity of the GM mode (for $|\theta| > \pi/4$ there is energy between $0.3 < |\omega| < 2\Omega$). Unfortunately, for a smaller ($k_h \geq 20$) GM with the same *rms* velocity the algorithm diverged. As shown in figure 2.17, the GM at small scale reach a higher maximum velocity for a constant *rms* velocity. Hence, it is possible that the maximum velocity limit where the simulation converges is overcome for a small scale GM which leads to the divergence of the simulation. Generally, we observe this divergence very locally in space. This could be the imprint of a critical point, where two physical process balance one another [104]. In our case, this could happen when the sweeping is exactly opposite to the group velocity of waves. As the wave stagnate in this point, the energy could diverge near this point and make the numerical simulation diverge as well.

2.7.3 Effect of a linear gradient of velocity

We observed that the VSHF and GM can modify the frequency of the waves through the sweeping effect with the non-linear term $\mathbf{c} \cdot \nabla \mathbf{u}$. Does the effect of the GM and the VSHF can also influence the dispersion relation through its gradient $(\mathbf{u} \cdot \nabla \mathbf{c})$? We now study analytically and numerically how the GM can modify the dispersion relation in rotating flow and how the VSHF can do the same for stratified flow. The numerical parameters will be the same as in the sweeping cases.

2.7.3.1 Stratified flow

Analytical study

We start by looking at how a gradient of a VSHF can affect the dispersion relation of IGW. To do so, we use a modified version of the Navier-Stokes equations:

$$\begin{aligned} \partial_t \mathbf{u} + \mathbf{u} \cdot \boldsymbol{\nabla} \mathbf{c} + \boldsymbol{\nabla} p - \mathbf{n} b = 0 \\ \boldsymbol{\nabla} \cdot \mathbf{u} = 0 \\ \partial_t b + N^2 \mathbf{n} \cdot \mathbf{u} = 0. \end{aligned} \tag{2.79}$$

We can approximate any gradient by a linear gradient of velocity $\mathbf{c}$ in the three directions of its three components:

$$\mathbf{c} = \begin{pmatrix} A_1 x + B_1 y + C_1 z \\ A_2 x + B_2 y + C_2 z \\ A_3 x + B_3 y + C_3 z \end{pmatrix}. \tag{2.80}$$

If we consider $\mathbf{c}$ to be mainly dependent on the shear flow then $A_1 = A_2 = A_3 = B_1 = B_2 = B_3 = C_3 = 0$. The advection term $\mathbf{u} \cdot \boldsymbol{\nabla} \mathbf{c}$ in the above equation (2.79) becomes:

$$\mathbf{u} \cdot \boldsymbol{\nabla} \mathbf{c} = \begin{pmatrix} C_1 u_z \\ C_2 u_z \\ 0 \end{pmatrix}. \tag{2.81}$$

Taking the Fourier transform in space and time of equation (2.79) and writing it in matrix form:

$$\mathbf{A} \cdot \bar{\mathbf{X}} = \begin{pmatrix} \mathrm{i}\omega & 0 & C_1 & \mathrm{i}k_x & 0 \\ 0 & \mathrm{i}\omega & C_2 & \mathrm{i}k_y & 0 \\ 0 & 0 & \mathrm{i}\omega & \mathrm{i}k_z & -1 \\ \mathrm{i}k_x & \mathrm{i}k_y & \mathrm{i}k_z & 0 & 0 \\ 0 & 0 & N^2 & 0 & \mathrm{i}\omega \end{pmatrix} \begin{pmatrix} \tilde{u}_x \\ \tilde{u}_y \\ \tilde{u}_z \\ \tilde{p} \\ \tilde{b} \end{pmatrix} = 0. \tag{2.82}$$

By calculating the determinant of $\mathbf{A}$, we found two non trivial solutions for $\det A = 0$ if and only if:

$$\omega = \pm \sqrt{-\frac{k_z^2}{4k^4}(C_1 k_x + C_2 k_y)^2 + N^2 \cos^2\theta} - \frac{\mathrm{i}k_z(C_1 k_x + C_2 k_y)}{2k^2}. \tag{2.83}$$

The imaginary term in equation (2.83) can decrease (similarly to the viscosity) or increase the amplitude of the waves. The term under the square root can be real or imaginary depending on its sign.

By assuming $C_1 = C_2$, which is roughly the case for shear flow, we can simplify the square root term of equation (2.83). Then we can compute a turning point when the gradient dominates the dispersion relation, *i.e.* when $k_z^2 C_1^2 (k_x + k_y)^2 = 4N^2 k_h^2 k^2$. This happens when $C_1 = \frac{2Nkk_h}{k_z(k_x+k_y)} \sim 2N$.

- If $C_1 \gg 2N$, the gradient dominates the stratification. The unique non trivial solution for equation (2.83) is $\omega = 2\mathrm{i}\frac{k_z C_1 (k_x+k_y)}{2k^2}$. In this case the solution is purely an amplification or a diffusing term.
- If $C_1 \ll 2N$, the stratification dominates the gradient. We find again the typical dispersion relation with a viscous effect $\omega \simeq \pm N \cos\theta$.

C_1 can be estimated by the average derivative of a velocity $\mathbf{c}(z)$. Here, $C_1 \simeq \partial_z c(z) \sim \frac{c}{\Delta_z^{\mathrm{VSHF}}}$ or in the Fourier domain $C_1 \sim c k_z^{\mathrm{VSHF}}$ where c is the *rms* velocity of the VSHF, k_z^{VSHF} is the average vertical wavenumber of the VSHF and Δ_z^{VSHF} is a typical scale of the VSHF. As the VSHF flow is large scale we mostly have $k_z \sim 1$ so $C_1 \sim c$. Therefore, we can say that if the stratification is high and the *rms* velocity of the VSHF flow is low (*i.e.* $c \ll 2N$) or if the gradient Richardson number $R_i = \frac{N^2}{(\partial_z c)^2}$ is high, then the gradient of VSHF has little effect on the waves.

Numerical simulation

Some numerical simulations are done to observe the effect of the gradient of the VSHF on the dispersion relation. The same VSHF as in section 2.7.2.4 are used. In figure 2.19, the first column is the vertical wavenumber of the VSHF changed from $k_z = 1$ to $k_z = 50$ with an increment of 10 (*i.e.* $k_z = 10$, $k_z = 20$, ...). The second column is the effect of the VSHF on the dispersion relation of IGW obtained from a pulsating Dirac. The third column is the Saint Andrew's cross obtained after the advection by the VSHF.

At large scale ($k_z = 1$) the gradient of the VSHF has no effect on the dispersion relation and no effect on the Saint Andrew's cross pattern. As the vertical wavenumber of the VSHF increases $k_z \geq 10$ the dispersion relation is modified, but no effect is visible on the Saint Andrew's cross. The highest modification is obtained for the largest vertical wavenumber of the VSHF $k_z = 50$. In all cases, the Saint Andrew's cross pattern is not

modified despite the modification in the dispersion relation.

The gradient of the VSHF does not seem to amplify the frequency of the IGW, as no component higher than N exists in the (ω, θ) plane. Instead, it seems that the angle of propagation of the IGW is slightly modified as a higher concentration of energy exists at $|\omega| > |\omega_r|$ for a constant θ. This could result from the modification of the angle of propagation of the waves. Waves propagating vertically (with $\theta \simeq 0$) are subject to large fluctuations of the gradient and their angle of propagation might change while still keeping their frequency. Those waves which normally propagate with an angle $\theta = 0$ end up propagating at an angle $\theta > 0$ or $\theta < 0$ but at the same frequency they initially had, thus a high concentration of energy in the (ω, θ) place for a frequency $\omega > \omega_r$. There is also some energy at $|\omega| < |\omega_r|$ for a constant θ.

To better understand the effect of the gradient of the VSHF with high vertical wavenumber ($k_z = 50$), figure 2.20 shows the concentration of energy for a forcing oscillating at a pulsation $\omega_f = 0.3$ for only wavevector $\mathbf{k}$ with an angle $\theta = \pm\pi/4$. In the previous section, figure 2.14a shows the same case, but with no special effect added (no sweeping or gradient of VSHF) and can be useful to compare against the effect of the gradient of the VSHF. Figure 2.20 shows that the gradient of the VSHF can modify the angle of propagation of the flow. We observe that energy exists for all angles at $\omega = \omega_f = 0.3$, at $\omega = N \cos \frac{\pi}{4}$ and at $\omega = \omega_r$. The result is very similar to the sweeping case. First, the points $\omega = N \cos \frac{\pi}{4}$ and $\omega = \omega_f = 0.3$ propagating at the angle $\theta = \pi/4$ are modified by the gradient of the VSHF and propagate at a new angle with the same pulsation. This creates new energy along the dispersion relation for the new angle θ and this loop is repeated again. Furthermore, the energy seems to be deviated towards larger angles of propagation θ, where the group velocity of IGW is horizontal (see figure 2.7a to visualize the group velocity).

In Figure 2.21, the amplitude of the VSHF is modified (1st column) to observe the effect of its gradient on the dispersion relation (2nd column) and on the Saint Andrew's cross pattern (3rd column). It can be compared with figure 2.19 where the amplitude of the VSHF is fixed constant. Due to convergence problems, the VSHF amplitude for $k_z = 1$ could not be further increased than a maximum velocity of around 0.03 as otherwise the numerical simulation would diverge (for a maximum velocity of 0.15 that is the case). This could be understood by using the analytical study done previously: when C_1 starts to be big enough against N the pulsation can become purely imaginary and lead to an unstable point (in particular for points with large k_z and small k_h).

However, it is still possible to slightly increase the amplitude of the VSHF. We observe that for a VSHF with a vertical wavenumber $k_z = 1$ in the first line of figure 2.21, despite

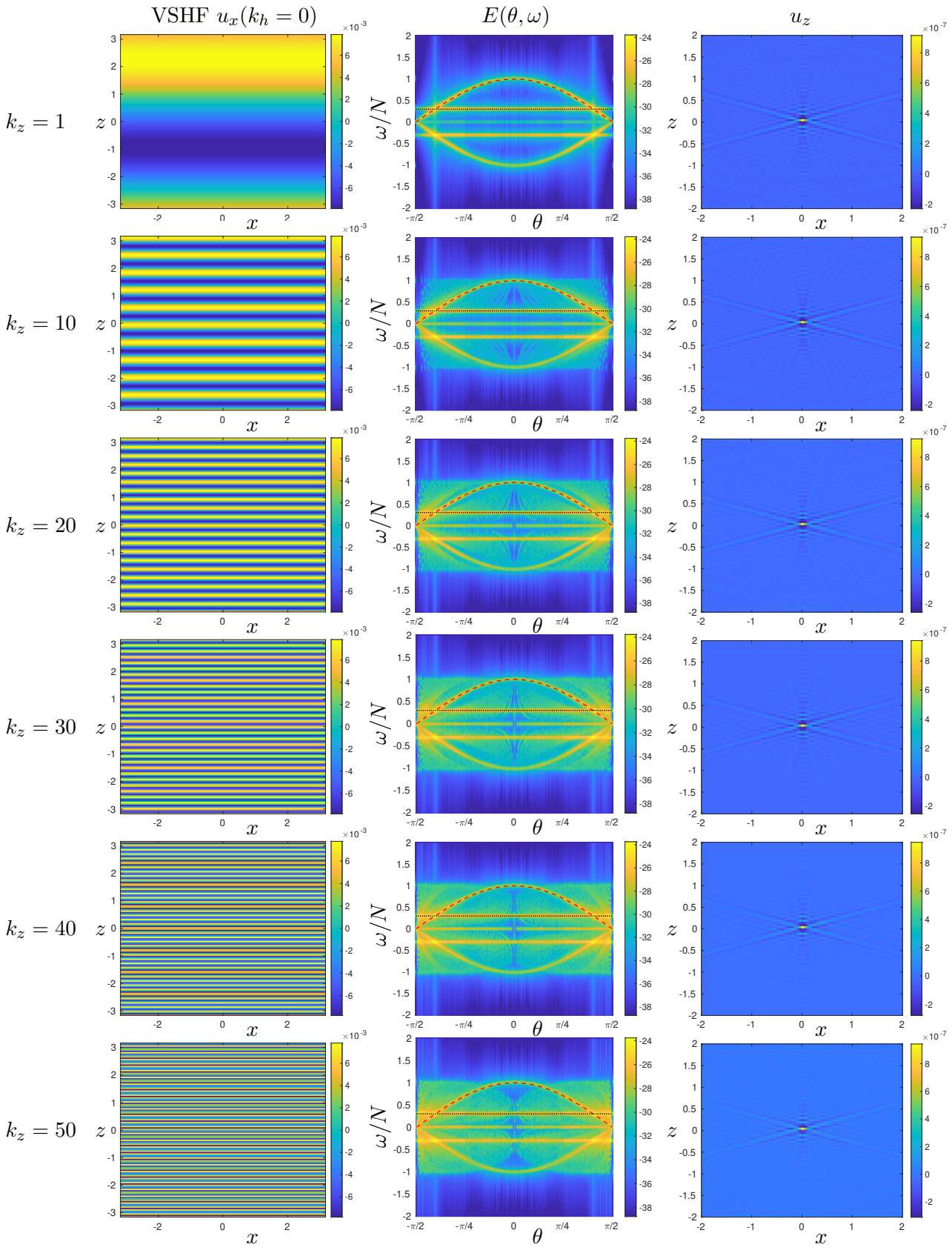

FIGURE 2.19: Effect of the gradient of a VSHF flow with varying vertical wavenumber k_z on the Saint Andrew's cross pattern of propagation of IGW. 1st column: VSHF used to convect the Saint Andrew's cross. 2nd column: Density of kinetic energy in the (θ, ω) plane. Red dashed line: dispersion relation curve $\omega_r(\theta)$ for IW. Black dotted line: original forcing frequency ω_f. 3rd column: Saint Andrew's cross convected.

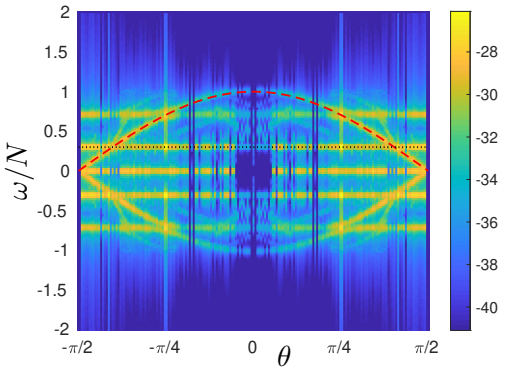

FIGURE 2.20: Effect of the gradient of the VSHF (with $k_z = 50$) on the energy density $E(\theta, \omega)$ in the (θ, ω) Fourier domain (in log scale) of IGW. The only wavenumbers forced have an angle $\theta = \pm\pi/4$ and a forcing frequency $\omega_f = 0.3$. Red dashed line: dispersion relation curve $\omega_r(\theta)$ for IGW. Black dotted line: original forcing frequency ω_f for all angles θ.

increasing the amplitude of the VSHF, there is no effect on the dispersion relation and on the Saint Andrew's cross pattern. On the contrary, the effect of the amplitude of the VSHF does modify a lot the dispersion relation for a small scale $VSHF$ with $k_z = 50$. In the second line of figure 2.21, the dispersion relation is modified, but less than in the last line of figure 2.19. When the VSHF amplitude increases for a constant $k_z = 50$ as in the third line of figure 2.21, the dispersion relation is more spreaded against the angle θ. It even modify the Saint Andrew's cross pattern. This shows that when the amplitude of the VSHF is bigger, the θ spreading on the dispersion relation is bigger as well.

To conclude, the gradient of the VSHF has an effect on IGW, but only for a gradient created from a small scale VSHF with large amplitude. However, this is not the case in stratified flows as the VSHF is large scale. Therefore, we can assume that the gradient of the VSHF does not arouse an important effect on the dispersion relation.

2.7.3.2 Rotating flow

Similarly to the stratified case, we look at how the gradient of the GM can modify the dispersion relation for IW. To do so, we start from a modified version of the Navier-Stokes equations:

$$\begin{aligned} \partial_t \mathbf{u} + \mathbf{u} \cdot \boldsymbol{\nabla} \mathbf{c} + \boldsymbol{\nabla} p &= -2\boldsymbol{\Omega} \times \mathbf{u} \\ \boldsymbol{\nabla} \cdot \mathbf{u} &= 0. \end{aligned} \tag{2.84}$$

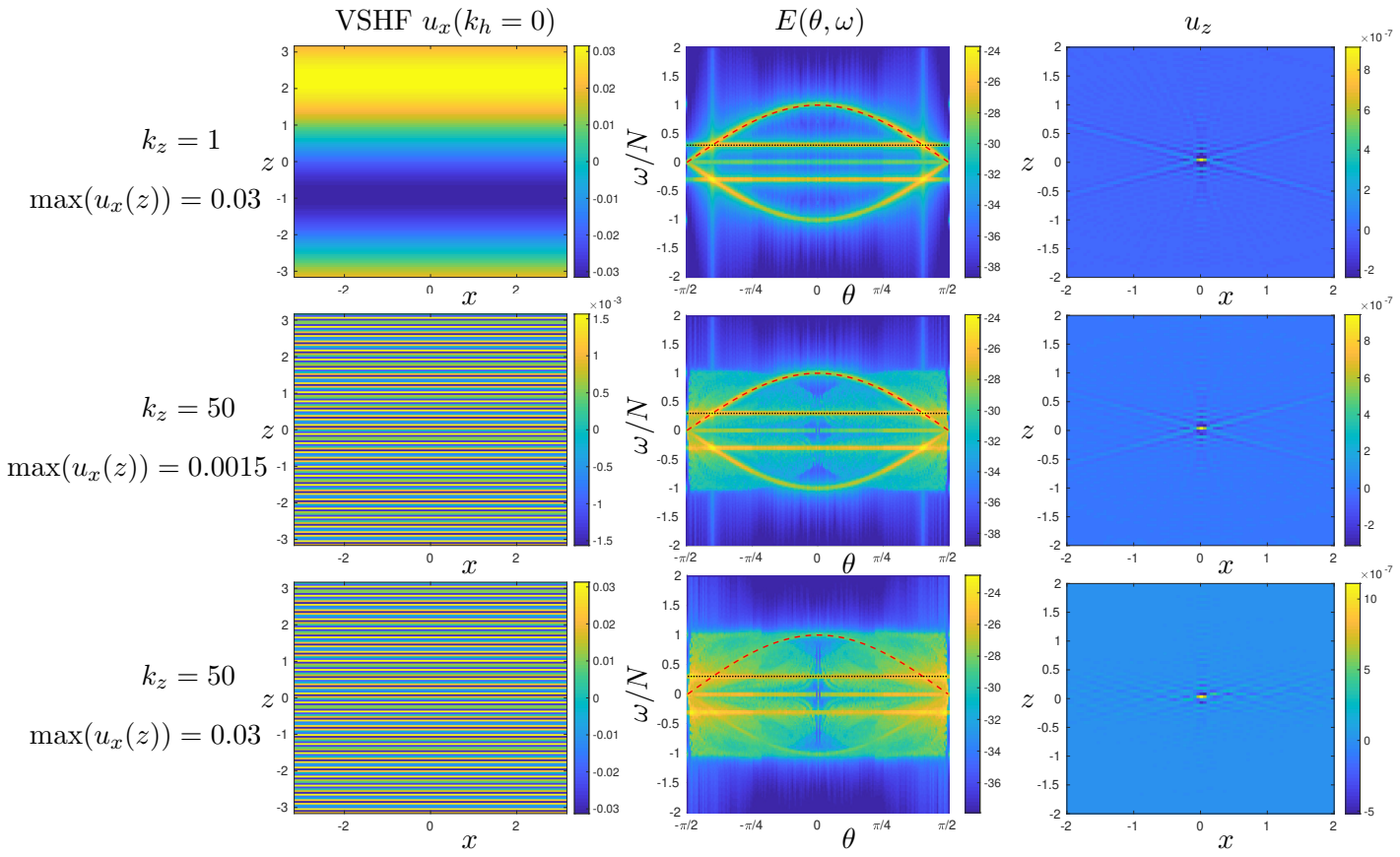

FIGURE 2.21: Effect of the amplitude of the gradient of a VSHF flow with a vertical wavenumber $k_z = 1$ or $k_z = 50$ on the Saint Andrew's cross pattern of propagation of IGW. 1st column: VSHF ($u_x(k_h = 0)$) used to convect the Saint Andrew's cross. 2nd column: Density of kinetic energy in the (θ, ω) plane. Red dashed line: dispersion relation curve $\omega_r(\theta)$ for IGW. Black dotted line: original forcing frequency ω_f. 3rd column: Saint Andrew's cross convected.

We can approximate any gradient by a linear gradient of velocity $\mathbf{c}$ in the three directions of its three components:

$$\mathbf{c} = \begin{pmatrix} A_1 x + B_1 y + C_1 z \\ A_2 x + B_2 y + C_2 z \\ A_3 x + B_3 y + C_3 z \end{pmatrix}. \tag{2.85}$$

If we consider $\mathbf{c}$ to be mainly dependent on the GM then $A_3 = B_3 = C_1 = C_2 = C_3 = 0$. The non-linear term $\mathbf{u} \cdot \boldsymbol{\nabla} \mathbf{c}$ in the Navier-Stokes equations becomes:

$$\mathbf{u} \cdot \boldsymbol{\nabla} \mathbf{c} = \begin{pmatrix} A_1 u_x + B_1 u_y \\ A_2 u_x + B_2 u_y \\ 0 \end{pmatrix}. \tag{2.86}$$

Taking the Fourier transform in space and time of equation (2.84) and writing it in matrix form:

$$\mathbf{A}\cdot\bar{\mathbf{X}} = \begin{pmatrix} \mathrm{i}\omega + A_1 & B_1 - 2\Omega & 0 & \mathrm{i}k_x \\ A_2 + 2\Omega & \mathrm{i}\omega + B_2 & 0 & \mathrm{i}k_y \\ 0 & 0 & \mathrm{i}\omega & \mathrm{i}k_z \\ \mathrm{i}k_x & \mathrm{i}k_y & \mathrm{i}k_z & 0 \end{pmatrix} \begin{pmatrix} \tilde{u}_x \\ \tilde{u}_y \\ \tilde{u}_z \\ \tilde{p} \end{pmatrix} = 0 \tag{2.87}$$

If we suppose that $\boldsymbol{\nabla}\cdot\mathbf{c} = 0$ then $A_1 = -B_2$. By inverting x and y axis and keeping $\boldsymbol{\nabla}\cdot\mathbf{c} = 0$ then we also obtain $A_2 = -B_1$.

The matrix (2.87) has a non trivial solution for $\det A = 0$ if and only if (in the case the terms in the square roots are positive):

$$\omega = \frac{\mathrm{i}A_1(k_y^2 - k_x^2)}{2k^2} \pm \sqrt{-A_1^2(\sin^2\theta + \frac{(k_y^2 - k_x^2)^2}{4k^4}) + \sin^2\theta(B_1 - 2\Omega)^2}. \tag{2.88}$$

Similarly to the stratified case, the gradient A_1 inserts an imaginary part to the dispersion relation. It means that it can amplify or reduce the amplitude of the waves. The square root terms of the equation (2.88), which can be imaginary if the term under the square root is negative, is quite complicated. When $k_y \gg k_x$ or $k_x \gg k_y$ the gradient A_1 would dominate the overall dispersion strongly. As, in average, we expect to have $A_1 \sim B_1$, in the case where $A_1 \gg 2\Omega$ then the dispersion relation would be purely imaginary.
On the contrary, the gradient B_1 does not involve an imaginary term. Its effect solely depends on its value and not on the wavenumber k. The effect of B_1 can be understood as an amplification or reduction of the rotation rate that the waves feel. It can be worth considering only if $B_1 \gtrsim 2\Omega$ as otherwise it is negligible in equation (2.88) against the rotation rate 2Ω.

It is also possible to approximate the value A_1 and B_1 because $A_1 \sim \partial_x c_x \sim \partial_y c_y$ and $B_1 \sim \partial_y c_x \sim \partial_x c_y$. Overall, the GM is equal in all directions (as it rotates), so in average $c_x \sim c_y$. Therefore, with $c = \sqrt{c_x^2 + c_y^2}$ the *rms* velocity of the GM, we get $A_1 \sim ck_x/\sqrt{(2)} \sim ck_y/\sqrt{2}$ and $B_1 \sim ck_y/\sqrt{2} \sim ck_x/\sqrt{2}$. Finally, we can estimate the average value of the gradient $A_1 \sim B_1 \sim ck_h/\sqrt{2}$.

Overall, the effect of the gradient of the GM in rotating flows is larger and more complicated than the VSHF in stratified flows. While both have an amplification or a reduction effect of the amplitude of the waves similar to a viscous term, it can also alter the dispersion relation.

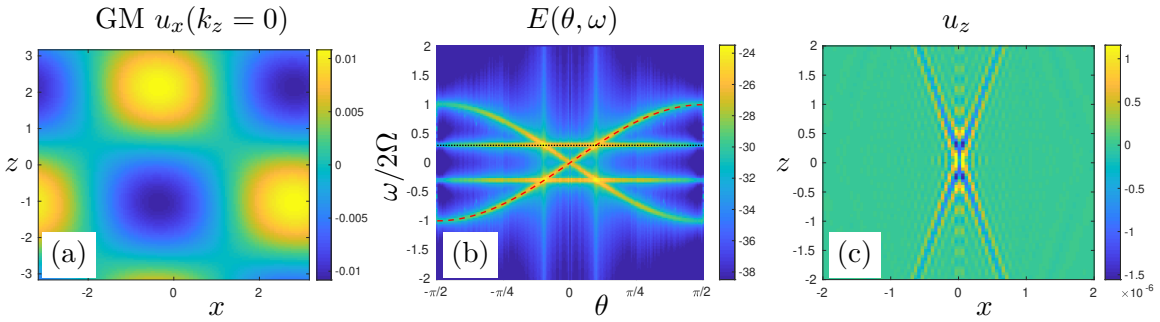

FIGURE 2.22: Effect of the gradient of a GM with a horizontal wavenumber $k_h = 1$ on the Saint Andrew's cross pattern of propagation of IGW. (a) GM ($u_x(k_z = 0)$) used to convect the Saint Andrew's cross. (b) Density of kinetic energy in the (θ, ω) plane. Red dashed line: dispersion relation curve $\omega_r(\theta)$ for IW. Black dotted line: original forcing frequency ω_f. (c) Saint Andrew's cross convected.

Numerical study

As the sweeping effect of the GM, it is not possible to test the effect of a scale smaller than $k_h = 10$ as the algorithm diverges. Only the result with $k_h = 1$ can be presented as others diverge. A possible reason is that, for large horizontal wavenumber, the difference between k_x and k_y increases, and as shown in equation (2.88), this can lead to an unstable flow. Furthermore, the maximum velocity increases for the same *rms* velocity when the GM is at smaller scale. This is even enhanced as for small scales the gradient of velocity is further increased. For all these reasons, it is understandable that the gradient of the GM has a divergence effect on the simulation. Reducing the *rms* velocity field of the GM is not really a solution, as it is quite obvious that a too small velocity gradient will have no effect on the dispersion relation of waves.

In figure 2.22, the effect of the geostrophic mode (figure 2.22a) can be seen on the density of kinetic energy (figure 2.22b) and on the propagation of the Saint Andrew's cross (figure 2.22c). We observe that the gradient of the GM at large scale has no effect on the dispersion relation and on the Saint Andrew's cross propagation.

Chapter 3

Separation of waves and eddies

This chapter describes a new technique to extract the 3D wave field and 3D eddy field from a 3D velocity field and density field. It contains three parts. The first part 3.1 is the description of the separation algorithm of waves and eddies depending on the advective flow. Two techniques are exposed. The second part 3.2 is the application of the separation technique on a Saint Andrew's cross with a homogeneous convective flow. Finally, the third part 3.3 is the limitation and potential improvement of this new separation technique.

3.1 The general method for the 4D analysis

The separation technique of waves and eddies is done by using the Fourier transform in space and time. Its objective is to use the dispersion relation of waves to extract them from the rest of the turbulence called "eddies".

3.1.1 General technique

The algorithm of separation of waves and eddies can be decomposed in a few steps:

1. Direct Numerical Simulation (DNS) provides time-dependent velocity–buoyancy spectral coefficients in 3D Fourier space in terms of the wavevector $\mathbf{k}$. In the following, we denote by $\hat{f}$ either the velocity or buoyancy coefficient, as $\hat{f}(\mathbf{k}, t)$.
2. The 1D time-Fourier transform is done as $FFT(\hat{f}(\mathbf{k}, t)) = \tilde{f}(\mathbf{k}, \omega)$.
3. For each point (k_x, k_y, k_z, ω) in the 4D space, a filter $\zeta(\mathbf{k}, \omega)$ is created where $\zeta(\mathbf{k}, \omega) = 1$ for the points belonging to the "wave" field (denoted $\tilde{f}^w(\mathbf{k}, \omega)$) and

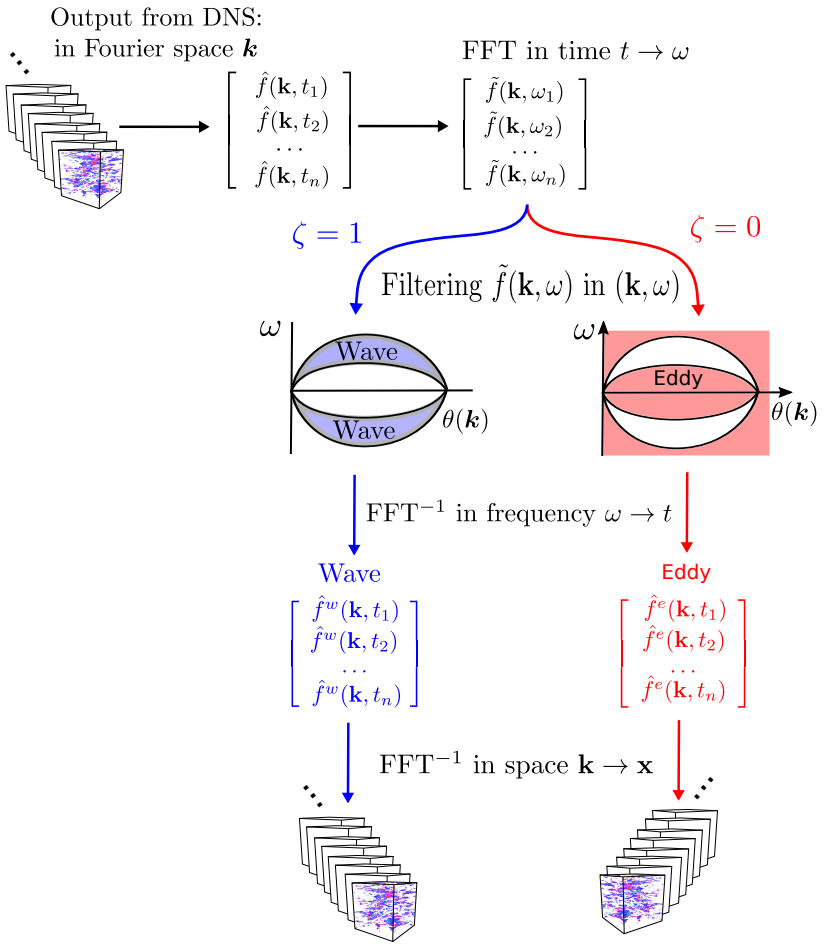

FIGURE 3.1: Description of the different steps for separation of waves and eddies using a 4D Fourier transform.

$\zeta = 0$ for the points belonging to the "eddy" field (denoted $\tilde{f}^e(\mathbf{k},\omega)$). The filter $\zeta(\mathbf{k},\omega)$ can be determined with two different techniques (see sections 3.1.4 and 3.1.5). It is applied on $\tilde{\mathbf{f}}$:

$$\begin{aligned} \tilde{\mathbf{f}}^w(\mathbf{k},\omega) &= \zeta(\mathbf{k},\omega)\tilde{\mathbf{f}}(\mathbf{k},\omega) \\ \tilde{\mathbf{f}}^e(\mathbf{k},\omega) &= (1-\zeta(\mathbf{k},\omega))\tilde{\mathbf{f}}(\mathbf{k},\omega). \end{aligned} \tag{3.1}$$

In the stratified case, the VSHF mode ($k_h = 0$) is removed from the wave and eddy components. It corresponds to the point ($\theta = \pm\pi/2$) in the (θ,ω) plane. In the rotating case, the GM ($k_z = 0$) is removed from the wave and eddy components as well. It corresponds to the point ($\theta = 0$) in the (θ,ω) plane.

4. The 1D inverse Fourier transforms is computed $FFT^{-1}(\tilde{f}^w(\mathbf{k},\omega)) = \hat{f}^w(\mathbf{k},t)$ and $FFT^{-1}(\tilde{f}^e(\mathbf{k},\omega)) = \hat{f}^e(\mathbf{k},t)$ to return to the physical time for the wave and eddy coefficients.

5. The 3D inverse Fourier transform is done in physical space, which permits the recovery of the wave and eddy field in physical space and their visualization. From a velocity or buoyancy component $f(x,t)$, the eddy part and wave part are separated such that $f(\mathbf{x},t) = f^e(\mathbf{x},t) + f^w(\mathbf{x},t)$.

3.1.2 Separation for the stratified case

In this section, we explain how the separation into wave and eddy component is done in the stratified case.

For stratified flows, it is possible to take advantage of the Craya-Herring frame [119] to improve our decomposition. We expect the poloidal and buoyancy terms to be the only components which recover the dispersion relation [92]. On the contrary the toroidal term is considered to be purely composed of eddies and does not recover the dispersion relation. Indeed, in equation (2.62), the IGW are only in the poloidal and buoyancy term and the toroidal term is dropped. This is the basis of the Riley's decomposition [119]. It considers the waves as being composed of the full buoyancy and poloidal component and the eddies to be only composed of the toroidal term. Hence, Riley's decomposition is valid for high stratification and low Reynolds number where eddies are horizontal and 2D. As a result, no vertical eddy can exist (as it is a poloidal term), and this is not physically true especially at high Reynolds number and high stratification.
By merging the spatial decomposition and our space-time separation it is possible to enhance the precision of the decomposition. Hence, step 3 of the algorithm of section 3.1.1 becomes:

$$\begin{aligned} \tilde{\mathbf{u}}^w(\mathbf{k},\omega) &= \zeta(\mathbf{k},\omega)\tilde{u}^p(\mathbf{k},\omega)\mathbf{e}^p \\ \tilde{\mathbf{u}}^e(\mathbf{k},\omega) &= \tilde{u}^t(\mathbf{k},\omega)\mathbf{e}^t + (1-\zeta(\mathbf{k},\omega))\,\tilde{u}^p(\mathbf{k},\omega)\mathbf{e}^p \\ \tilde{b}^w(\mathbf{k},\omega) = \zeta(\mathbf{k},\omega)\tilde{b}(\mathbf{k},\omega), &\qquad \tilde{b}^e(\mathbf{k},\omega) = (1-\zeta(\mathbf{k},\omega))\,\tilde{b}(\mathbf{k},\omega) \end{aligned} \tag{3.2}$$

where the variable f in section 3.1.1 is replaced here by u^p or b.

While the buoyancy term is separated as explained in equation (3.1), the wave velocity is now composed purely of poloidal terms and the eddy velocity is composed of all the toroidal terms and also some poloidal terms.

We also separate the VSHF from the rest of the flow. In the end, for stratified flow, the velocity component $\mathbf{u}(\mathbf{x},t)$ is separated in a wave, eddy and VSHF part such as:

$$\mathbf{u}(\mathbf{x},t) = \mathbf{u}^e(\mathbf{x},t) + \mathbf{u}^w(\mathbf{x},t) + \mathbf{u}^s(\mathbf{x},t), \tag{3.3}$$

while the component of the buoyancy field is separated only in a wave and eddy part:

$$b(\mathbf{x},t) = b^e(\mathbf{x},t) + b^w(\mathbf{x},t). \tag{3.4}$$

The superscript s stands for the VSHF defined in the Fourier space as $\hat{\mathbf{u}}^s(\mathbf{k},t) = \hat{\mathbf{u}}(k_z, k_h = 0, t)$.

We applied the separation technique to the flow components in the Craya-Herring frame. This has numerous advantages in the stratified case; it only requires two velocities (u^t, u^p) components instead of three in the cartesian frame (u_x, u_y, u_z) and IGW are already spatially separated from toroidal eddies. It would also be possible to apply this algorithm directly to the Cartesian velocity fields but the precision would be lower as part of the toroidal component would be considered as waves.

3.1.3 Separation for the rotating case

In this section, we explain how the separation in wave and eddy components is done in rotating cases. For rotating flow, we also take advantage of the Craya-Herring frame to reduce the number of the velocity components from three to two. Yet, there is no equivalent of Riley's decomposition in rotating turbulence, that is why this decomposition is something entirely new. Indeed, inertial waves are expected to be both on the toroidal and poloidal components contrarily to the stratified case. Hence, step 3 of the algorithm of section 3.1.1 becomes:

$$\begin{aligned} \tilde{\mathbf{u}}^w(\mathbf{k},\omega) &= \zeta(\mathbf{k},\omega)(\tilde{u}^t(\mathbf{k},\omega)\mathbf{e}^t + \tilde{u}^p(\mathbf{k},\omega)\mathbf{e}^p) \\ \tilde{\mathbf{u}}^e(\mathbf{k},\omega) &= (1-\zeta(\mathbf{k},\omega))\,(\tilde{u}^t(\mathbf{k},\omega)\mathbf{e}^t + \tilde{u}^p(\mathbf{k},\omega)\mathbf{e}^p) \end{aligned} \tag{3.5}$$

where the variable f in section 3.1.1 is replaced by u^t or u^p.

We also separate the GM from the rest of the flow. For rotating flow, the velocity component $\mathbf{u}(\mathbf{x},t)$ is separated in a wave, eddy and GM part such as:

$$\mathbf{u}(\mathbf{x},t) = \mathbf{u}^e(\mathbf{x},t) + \mathbf{u}^w(\mathbf{x},t) + \mathbf{u}^g(\mathbf{x},t). \tag{3.6}$$

The superscript g stand for the GM defined in the Fourier space as $\hat{\mathbf{u}}^g(\mathbf{k},t) = \hat{\mathbf{u}}(\mathbf{k_h}, k_z = 0, t)$.
It is also possible to use this algorithm directly on the velocities in the Cartesian frame. While no loss of accuracy would be expected, the process would be more computationally

consuming as the filtering needs to be applied to three components (u_x, u_y, u_z) instead of two (u^t, u^p).

3.1.3.1 Orthogonal decomposition

In this section we explain how the decomposition in a wave and eddy components for the stratified or rotating case can be used to define an orthogonal basis. The decomposition of the flow in waves, eddies and VSHF or GM permits to define an orthogonal basis and an inner product in vector function space, by using the complete set of unit vector functions $e^{\mathrm{i}\mathbf{k}\cdot\mathbf{x}}$ and $e^{\mathrm{i}\omega t}$. Applying the inverse four-dimensional Fourier transform from frequency space $(\mathbf{k}, \omega)$ to physical space $(\mathbf{x}, t)$ yields

$$\mathbf{u}^a(\mathbf{x}, t) = \sum_{\mathbf{k},\omega} \tilde{\mathbf{u}}^a(\mathbf{k}, \omega) e^{-\mathrm{i}\mathbf{k}\cdot\mathbf{x} - \mathrm{i}\omega t} \tag{3.7}$$

$$b^a(\mathbf{x}, t) = \sum_{\mathbf{k},\omega} \tilde{b}^a(\mathbf{k}, \omega) e^{-\mathrm{i}\mathbf{k}\cdot\mathbf{x} - \mathrm{i}\omega t}, \tag{3.8}$$

where a stands for w, e, s or g. Note that the letter w means the wave part, e means the eddy part, s means the VSHF part and g means the GM part of the flow.

For two functions $\hat{f}$ and $\hat{g}$, we thus define an inner product in terms of wavevector $\mathbf{k}$ and time t, as $[\hat{f}(\mathbf{k}, t), \hat{g}(\mathbf{k}', t)] \equiv \frac{1}{T}\int_T \hat{f}(\mathbf{k}, t)\overline{\hat{g}(\mathbf{k}', t)}\delta_{\mathbf{k}-\mathbf{k}'}\mathrm{d}t$ where T is the considered time span and $\bar{}$ is the complex conjugate. Due to the orthogonality of vector space functions and orthogonality of Fourier velocity with wavevector space $\mathbf{k}$ from incompressibility, one shows the orthogonality between wave, eddy, and shear or geostrophic parts:

$$\left.\begin{aligned}[\hat{b}^i(\mathbf{k}, t), \hat{b}^j(\mathbf{k}', t)] \neq 0 \\ [\hat{u}^i_m(\mathbf{k}, t), \hat{u}^j_n(\mathbf{k}', t)] \neq 0\end{aligned}\right\} \text{only if } i = j \text{ and } \mathbf{k} = \mathbf{k}' \tag{3.9}$$

where i, j stand for w, e, s or g, and m, n stand for space directions x, y, or z. Note that we also have $[e^{\mathrm{i}\omega_1 t}, e^{\mathrm{i}\omega_2 t}] = \delta_{\omega_1-\omega_2}$, which mean that only components with the same frequency and wavevector are non-zero in the inner product [ ].
Moreover, the overall energetic content is

$$< \hat{f}, \hat{g} >= \sum_{\mathbf{k}} \mathrm{Re}[\hat{f}(\mathbf{k}, t), \hat{g}(\mathbf{k}, t)] \tag{3.10}$$

and the energetic contents against the sphere of radius K is

$$< \hat{f}, \hat{g} >_K= \sum_{\substack{\mathbf{k} \\ |\mathbf{k}|=K}} \mathrm{Re}[\hat{f}(\mathbf{k}, t), \hat{g}(\mathbf{k}, t)]. \tag{3.11}$$

3.1.4 Explicit definition of ζ

In order to complete the algorithm exposed in section 3.1.1, it is necessary to explain how the filter ζ is computed.

First, it is necessary to find a typical velocity, which advects the flow. Generally, the main advective flow is the shear flow $\mathbf{c} = \mathbf{u}_h(k_h = 0)$ for stratified turbulence and the geostrophic mode $\mathbf{c} = \mathbf{u}_h(k_z = 0)$ for rotating turbulence. Indeed, these types of flow are generally large scale and slowly fluctuate with time. Next, the *rms* velocity of the advecting flow $\mathbf{c} = (c_x, c_y, c_z)$ is computed and noted $\mathbf{c}^{rms} = (c_x^{rms}, c_y^{rms}, c_z^{rms})$. As the advecting velocity is chosen as a constant, the numerical simulation (or at least the convective flow) must have reached a statistical stationary state. Then, the filter $\zeta(\mathbf{k}, \omega)$ can be explicity defined as:

$$\zeta(\mathbf{k},\omega) = \begin{cases} 1 & \text{if } \begin{array}{l} \omega_r - |c_x^{rms}k_x| - |c_y^{rms}k_y| - |c_z^{rms}k_z| \leq \omega \leq \omega_r + |c_x^{rms}k_x| + |c_y^{rms}k_y| \\ \quad + |c_z^{rms}k_z| \end{array} \\ 0 & \text{otherwise.} \end{cases}$$

All components $(\mathbf{k}, \omega)$ close to the dispersion relation with a sweeping effect are considered as waves and eddies otherwise. This filter selects as waves a range of frequencies which follows the dispersion relation ω_r advected by a flow between $[-\mathbf{c}^{rms}, +\mathbf{c}^{rms}]$. This type of filtering also implies that the fluctuations of the advecting velocity are close to its *rms* value.

3.1.5 Adaptive definition of ζ

In the explicit definition of ζ the sweeping effect of the advective velocity is constant in space and time. This is clearly not the case in general numerical simulation and it needs to be further improved. In this section we propose a different algorithm where the advective velocity can fluctuate in space and time $\mathbf{c}(\mathbf{x}, t)$.

3.1.5.1 Green's function

Here we explain how the use of the Green's function can help to define the filter ζ.

In the stratified case, for an inhomogeneous advecting velocity $\mathbf{c}(z, t)$, we generalize a property that appears in the analytical wave solution (2.66): when the frequency $\omega \rightarrow$

$\pm N\cos\theta - \mathbf{c}\cdot\mathbf{k}$, the density energy $|\tilde{b}_G|^2$ peaks, only damped by viscosity. This permits to compute the Green's function relevant for the linearized equations (2.61) where $\mathbf{c}(z,t)$ is the inhomogeneous VSHF, numerically extracted from DNS *i.e.* $\hat{\mathbf{c}}(k_z,t) = \hat{\mathbf{u}}(k_h = 0, k_z, t)$ and F_b is an inhomogeneous distribution of Dirac functions in space and time. The precise definition of F_b is:

$$F_b(\mathbf{x},t) = \begin{cases} \delta(\mathbf{x}(t)) \text{ if } t \leq 100\Delta t \\ 0 \text{ otherwise,} \end{cases} \tag{3.12}$$

where Δt is the time step of the original DNS and $\mathbf{x}(t)$ is randomly defined at each time step Δt. Here the distribution of Dirac is varying in time and space to take into account the non-uniform distribution of the advective flow $\mathbf{c}(z,t)$. The set of equations used in this case are:

$$\begin{gathered} \partial_t \mathbf{u}_G + \mathbf{c}\cdot\boldsymbol{\nabla}\mathbf{u}_G + \boldsymbol{\nabla} p_G - \nu_G\nabla^2\mathbf{u}_G = b_G\mathbf{z} \\ \partial_t b_G + \mathbf{c}\cdot\boldsymbol{\nabla} b_G - \mathcal{X}_G\nabla^2 b_G = -N^2 u_{z,G} + F_b \\ \boldsymbol{\nabla}\cdot\mathbf{u}_G = 0 \end{gathered} \tag{3.13}$$

where the subscript G is used to define a variable linked to the computation of the Green's function. While we do not have an analytical solution for this equation with an advective velocity $\mathbf{c}(\mathbf{x},t)$, we can approximate that the set of solutions is very close to the solutions found in equations (2.66).

A good practice is to check that the toroidal term is null. Due to the advective velocity it is possible to get a non-zero toroidal term which could hinder the accuracy of the technique. If the advective flow chosen is the shear flow, there is no problem as the shear flow is neither considered as a toroidal or a poloidal term. The interaction of the VSHF with a poloidal component does not create a toroidal component. The same is true for the interaction of the VSHF and the toroidal component, it cannot create a poloidal component.

In figure 3.2, the successive Dirac of the forcing F_b are shown at the 100th time step (figure 3.2a) and at the end of our simulation after the convection by a VSHF (figure 3.2b). In figure 3.2a, some Diracs are clearly visible and start to advect into the entire physical domain. Not all Diracs are visible because their location are not in the observed plane. Finally, in figure 3.2b, we can see that the waves created by the Diracs have convected a lot and occupied a large area in the (x,z) plane. This is actually what is wanted, that waves occupy a large area and are convected differently depending on where they are in order to follow the fluctuation of the VSHF for stratified fluid and GM for rotating fluid.

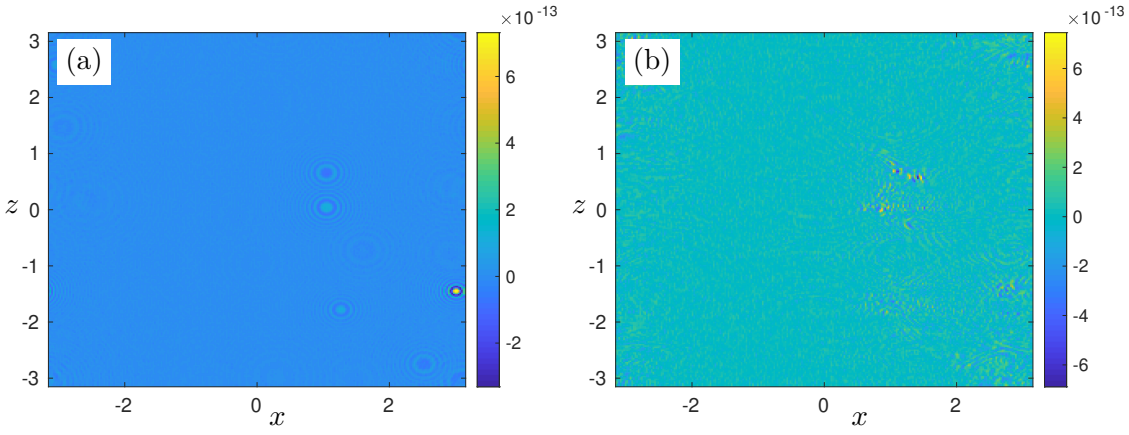

FIGURE 3.2: Visualization of the vertical velocity fields from random Dirac in space at successive 100 time steps. a) after 100 iterations (b) after 5000 iterations when the flows have been convected.

Similarly, in the rotating case, we generalize a property that appears in the analytical wave solution (2.74): when the frequency $\omega \to \pm 2\Omega \sin\theta - \mathbf{c}\cdot\mathbf{k}$, the toroidal energy $|\tilde{u}_G^t|^2$ peaks, only damped by viscosity. This permits the computation of the Green's function relevant for the linearized equations (2.68) where $\mathbf{c}(x,y,t)$ is the inhomogeneous GM, numerically extracted from DNS *i.e.* $\hat{\mathbf{c}}(k_x,k_y,t) = \hat{\mathbf{u}}(k_x,k_y,k_z=0,t)$ and $\mathbf{F}_u^t$ is an inhomogeneous distribution of Dirac functions in space and time on the toroidal part of the flow on the toroidal part of the equation. The precise definition of $\mathbf{F}_u^t$ is:

$$\mathbf{F}_u^t(\mathbf{x},t) = \begin{cases} \boldsymbol{\delta}^{\boldsymbol{t}}(\mathbf{x}(t)) \text{ if } t \leq 100\Delta t \\ \mathbf{0} \text{ otherwise,} \end{cases} \tag{3.14}$$

where Δt is the time step of the original DNS, $\boldsymbol{\delta}^{\boldsymbol{t}}(\mathbf{x}(t))$ is a Dirac in space on the toroidal part of the equation and $\mathbf{x}(t)$ is randomly defined at each time step Δt. Here the distribution of Dirac is varying in time and space to take into account the non uniform distribution of the advective flow $\mathbf{c}(x,y,t)$. The set of equations used in the rotating case are:

$$\begin{gathered} \partial_t \mathbf{u}_G + \mathbf{c}\cdot\boldsymbol{\nabla}\mathbf{u}_G + \boldsymbol{\nabla} p_G - \nu_G \nabla^2 \mathbf{u}_G = -2\Omega \mathbf{n}\times\mathbf{u}_G + F_u^t \\ \boldsymbol{\nabla}\cdot\mathbf{u}_G = 0 \end{gathered} \tag{3.15}$$

Hence, for stratified or rotating flows, when the energy peaks, we assume the $(\omega,\mathbf{k})$ point belongs to the waves. If the energy is low, we assume that the $(\omega,\mathbf{k})$ point belongs to the eddies.

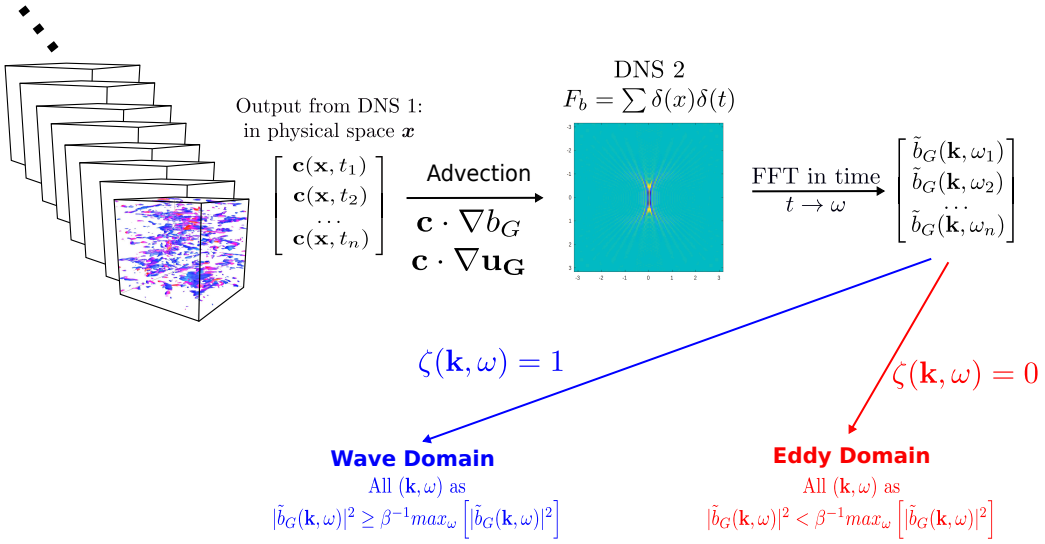

FIGURE 3.3: Description of the different steps for the adaptive definition of ζ of separation of waves and eddies (in the stratified case).

3.1.5.2 Numerical implementation

We explain how the adaptive definition of ζ is done numerically. Here are the steps of the adaptive definition of ζ:

1. From the first non-linear Direct Numerical Simulation (DNS 1) the advecting velocities $\mathbf{c}(\mathbf{x},t)$ in the Cartesian coordinates are recovered against time.

2. A second linear Direct Numerical Simulation (DNS 2) is done. It computes the Green's function by solving equations (3.13) in the stratified case and equations (3.15) in the rotating case with a very low viscosity. For each iteration among the first 100, one Dirac forcing randomly localized in space is done without advecting velocity. Then the advective velocity $\mathbf{c}(\mathbf{x},\mathbf{t})$ is extracted from the DNS 1 and is used to convect the flow after the first 100 iterations for the same duration of simulation as DNS 1.

3. In the stratified case, the 1D Fourier transform in time is done on the buoyancy field $\hat{b}_G$ in DNS 2 using a Hann window: $FFT_{Hann}(\hat{b}_G(\mathbf{k},t))=\tilde{b}_G(\mathbf{k},\omega)$. In the rotating case, the 1D Fourier transform is done on the toroidal velocity $\hat{u}_G^t$ in DNS 2 using a Hann window: $FFT_{Hann}(\hat{u}_G^t(\mathbf{k},t))=\tilde{u}_G^t(\mathbf{k},\omega)$. For both cases, it is done by ignoring the first 100 iterations in step 3.

4. The filter ζ is created and defined as:

   - for stratified flows

$$\text{if } |\tilde{b}_G(\mathbf{k},\omega)|^2\geq\beta^{-1}\max_\omega\left[|\tilde{b}_G(\mathbf{k},\omega)|^2\right] \text{ then } \zeta(\mathbf{k},\omega)=1 \text{ else } \zeta(\mathbf{k},\omega)=0 \quad (3.16)$$

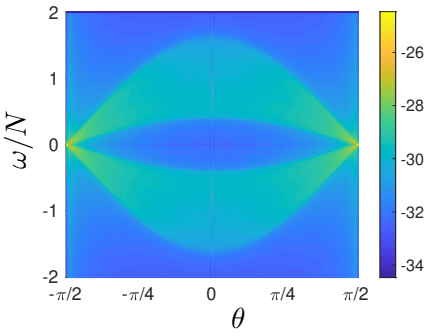

FIGURE 3.4: Density of potential energy energy in the (θ,ω) Fourier domain (in log scale) of a Dirac forcing ($F_b = \delta_{\mathbf{x}}\delta_t$) convected by a constant and homogeneous velocity $\mathbf{c} = (-0.1, 0, 0)$.

- for rotating flows

$$\text{if } |\tilde{u}_G^t(\mathbf{k},\omega)|^2 \geq \beta^{-1}\text{max}_\omega \left[|\tilde{u}_G^t(\mathbf{k},\omega)|^2\right] \text{ then } \zeta(\mathbf{k},\omega) = 1 \text{ else } \zeta(\mathbf{k},\omega) = 0 \quad (3.17)$$

where β is a variable which can be adjusted to select the wave frequencies.

The subscript G stand for the flow components of the second direct numerical simulation where the Green's function solution is computed.

For the stratified case, choosing the advective velocity $\mathbf{c} = \mathbf{u}_h(k_h = 0)$ ensures that the toroidal term in step 2 is zero (at the machine precision). Indeed, in equation (2.62), the toroidal term is ignored and does not possess energy if it is not forced. For rotating flows, the algorithm is similar, except that the filter ζ and the Dirac forcing is based on the toroidal velocity instead of the buoyancy field b_G. In both cases, the filter could also be based on the poloidal velocity. The viscosity in DNS 2 is chosen very low as high viscosity might dampen the peak of energy (see equations (2.74) and (2.66)) and reduce the amplitude difference between eddies area and waves area. A Hann window technique is used because it increases the accuracy of the filter ζ by creating a sharper peak of energy. However, no windowing technique is used when dealing with the data of DNS 1 because it modifies the signal and therefore its statistics. A necessary condition for the success of the separation algorithm is that most of the energy in step 3 is in the wave domain.

The choice of the value β is rather difficult. For example, in the case of a stratified flow with a constant advection $\mathbf{c} = (-0.1, 0, 0)$, $N = 1$ and a Dirac forcing $F_b = \delta_{\mathbf{x}}\delta_t$, we simulate the Green function by solving equations (3.13). The density of potential energy is plotted in figure 3.4. It shows how the dispersion relation is modified. For a specific wavevector $\mathbf{k}_0 = (40, 30, 20)$, we plot the potential energy of $b(\mathbf{k}_0, \omega)$ depending

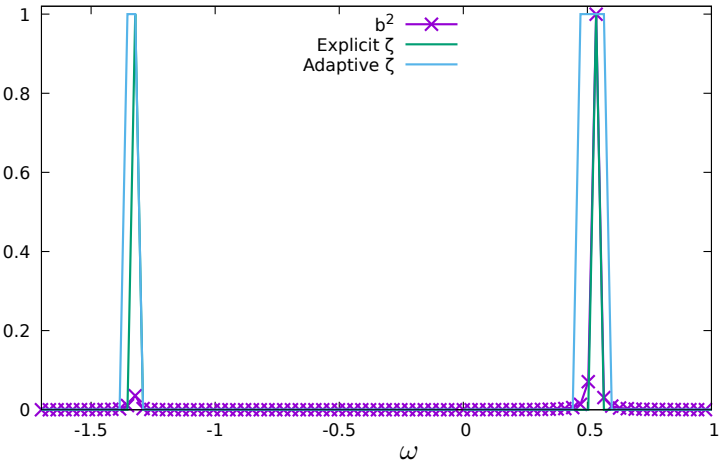

FIGURE 3.5: Comparison between the explicit and implicit definition of ζ at the wavevector $\mathbf{k}_0 = (40, 30, 20)$ against ω. The density of potential energy b^2 is also added.

on ω. To fix β, we compare the explicit definition of ζ (defined in section 3.1.4) with the adaptive definition of ζ (defined in section 3.1.5). With a value of $\beta = 1/100$ we capture all peaks of energy in the signal, for positive and negative frequencies. The explicit method captures only the two peaks of energy, whereas the adaptive method capture the two peaks of energy as well but also the spread of the peak of energy.

Generally, choosing $\beta = 100$ ensures that most (around 90%) of the wave energy is effectively selected as waves. β is the cutoff parameter for identifying the spectral peaks. Two reasons render imprecise the capture of peaks in the simulation of Green's functions. First, even if very low (*e.g.* $\nu_G = \mathcal{X}_G = 10^{-8}$), viscosity tends to smear the peaks around the resonance frequencies $\omega_c^{\pm}(\mathbf{k}) = \pm N \cos\theta - \mathbf{c} \cdot \mathbf{k}$ as shown in the analytical solutions (2.66) and (2.74) with a homogeneous velocity $\mathbf{c}$. Spectral discretization also adds to this smearing: for each wavevector $\mathbf{k}$, 100% of energy is localized in a single frequency $\omega_c^{\pm}(\mathbf{k})$ when analytically computed, whereas it is distributed over a bandwidth of frequencies in simulations. The second reason is due to time discretization: the frequency $\omega_c^{\pm}$ is not exactly measured, but is approximated by the two closest discrete frequencies. These two mechanisms lead to a search for the set of points closest to the peak. When trying to capture the peak in a configuration similar to the analytical solution (2.66), we observe that the peaks span several orders of magnitude in amplitude over a bandwidth of frequencies. In simulations, even if 100% of the energy is distributed over all frequencies, in practice the energy is still located in a small frequency range.

Another possible way to choose β is to increase its value until most of the energy is considered as waves (around 90 %), which also gives a $\beta = 100$. Choosing a higher β is in general not relevant because not much energy will be associated to waves in step 3. However, choosing a lower β might be relevant in highly turbulent cases. Indeed, in the

case where waves and eddies share the same frequency, a lower β might help to avoid select eddies as waves. It would only select space-frequency domain where waves are highly concentrated and trade off the space frequency domain where waves are sparse to be considered as eddy.

This new algorithm is longer and more computationally expensive because it requires a second DNS and a temporal treatment. Furthermore, it also requires more data storage as large batches of 3D fields are required ($\sim$ 1000 3D fields for each component). However, it should be more precise than the explicit algorithm because the physical scale and the variability in time of the advecting flow is taken into account. Furthermore, it still works with non stationary flow (even if the advecting flow varies).

3.2 Practical application on a Saint Andrew's cross

In this section the explicit definition of ζ is applied to separate the wave and the eddy components of the flow. The numerical parameters are the same as in chapter 2.6.2.2. The case of study is a Saint Andrew's cross convected in the x direction. The result is very similar to the Saint Andrew's cross convected in the vertical direction in section 2.7.2. The chosen convective velocity is $\mathbf{c} = (10^{-2}, 0, 0)$. As the convective velocity is in only one direction, one could decide to refine the explicit definition of ζ in section 3.1.4 to take only one direction into account. However, for simplicity, the filtering technique is kept as if the convective flow were in both positive and negative x direction.

According to step 3 of the method, we computed the vertical velocity $u_z(\mathbf{k}, \omega)$ in four-dimensional space $(\mathbf{k}, \omega)$. Since the 4D filtering is defined for every $(\mathbf{k}, \omega)$, the velocity is either a wave part $u_z = u_z^w$ or an eddy part $u_z = u_z^e$, depending on the value of $(\mathbf{k}, \omega)$. Then, the three vertical densities of the energy are defined (denoted with $\star$ to distinguish them with other definitions used before) and associated to u_z, u_z^w and u_z^e:

$$E_z^\star(\theta, \omega) = \sum_{\theta(\mathbf{k}) \in I_\theta, 0 \leq |\mathbf{k}| \leq k_{max}} \frac{1}{2} |\tilde{u}_z(\mathbf{k}, \omega)|^2 \tag{3.18}$$

$$E_z^{\star,e,w}(\theta, \omega) = \sum_{\theta(\mathbf{k}) \in I_\theta, 0 \leq |\mathbf{k}| \leq k_{max}} \frac{1}{2} |\tilde{u}_z^{e,w}(\mathbf{k}, \omega)|^2 \tag{3.19}$$

with this definition, $E_z^\star(\theta, \omega) = E_z^{\star,e}(\theta, \omega) + E_z^{\star,w}(\theta, \omega)$. The energy computation done in equation (3.18) is more precise than the energy computation done in equation (2.50). In Figure 3.6, one can see $E_z^\star$ for the full vertical velocity field (Figure 3.6a), the wave part $E_z^{\star,w}$ (Figure 3.6b) and the eddy part $E_z^{\star,e}$ (Figure 3.6c). In Figure 3.6c, we see

that there is no energy along the dispersion relation (indicated with a red dashed line). This is the imprint of the discretization error of the filtering technique. Furthermore, the density of vertical energy is quite low in Figure 3.6c when, at the same location in (θ, ω) plane in Figure 3.6b, the density of vertical energy is high. Indeed, most of the energy in this area comes from the waves that were modified in angular frequency by the sweeping effect (for large wavenumber k_x, *i.e* small scale). It is the manifestation of the density of energy sharing the same coordinate in the (θ,ω) plane, but for a different wavevector $\mathbf{k}$ and consequently a different sweeping effect.

Compared to the total energy on Figure 2.7 using the calculation for the density of energy shown in section 2.6.1, our 4D analysis appears more precise — *i.e.* without vertical line — whereas no treatment such as Hann windowing is applied to the data. The main reason for this is due to the difference in the two algorithms for obtaining the energy density. The calculations in equations (3.18) and (3.19) first compute the energy density before it gathers the flow component in a $\theta \in I_\theta$ domain. It is only after applying the Fourier transform that the energy density is computed. In order to understand the link between the two methods, by analogy with the total energy defined previously in (2.50), we define the vertical energy by:

$$E_z(\theta,\omega) = \frac{1}{2} TF \left[\left| \sum_{\theta(\mathbf{k})\in I_\theta, 0\leq|\mathbf{k}|\leq k_{max}} \hat{u}_z(\mathbf{k},t) \right|^2 \right]. \tag{3.20}$$

This technique, detailed in section 2.6.1 is less computationally expensive than the detailed calculation of energy shown in equations (3.18) and (3.19). It starts by gathering the flow component in the $\theta \in I_\theta$ domain before computing the energy density. The Fourier transform in time is done at the end, after the computation of the energy. As shown in Maffioli et al. [92], the difference between the two formulations (3.18) and (3.20) of vertical density of energy is:

$$E_z(\theta,\omega) = E_z^\star(\theta,\omega) + \mathrm{Re}\left\{ \sum_{\substack{\theta(\mathbf{k})\in I_\theta \\ \theta(\mathbf{k}')\in I_\theta \\ \mathbf{k}'\neq\mathbf{k}}} \tilde{u}_z(\mathbf{k},\omega)\tilde{u}_z(\mathbf{k}',\omega) \right\} \tag{3.21}$$

with $\mathbf{k}'$ a wave vector different from $\mathbf{k}$ sharing the same domain I_θ. The second term in the right-hand-side corresponds to the error done by the calculation of $E_z(\theta,\omega)$ (which is approximative) against the calculation of $E_z^\star(\theta,\omega)$ (which is exact). The error corresponds to the crossing energy sharing the same domain I_θ. This difference can be summed up in one sentence: the energy of the sum of the flow component in a domain I_θ is different than the sum of the energy of the flow component in the same domain

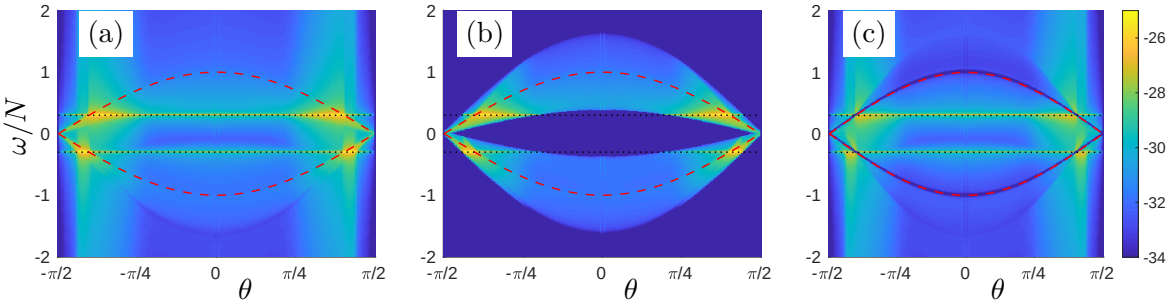

FIGURE 3.6: Sweeping effect of a homogeneous horizontal mean velocity field on the Saint Andrew's cross pattern of propagation of internal gravity wave after filtering the wave and eddy component. Concentration of vertical energy density in the (θ, ω) Fourier domain (in log scale). Red dashed line: original dispersion relation curve $\omega_r(\theta)$ for internal gravity waves defined by equation (2.33). Black dotted line: forcing frequency ω_f. (a) Full field $E_z^\star(\theta, \omega)$ (b) Wave part $E_z^{\star,w}(\theta, \omega)$ (c) Eddy part $E_z^{\star,e}(\theta, \omega)$.

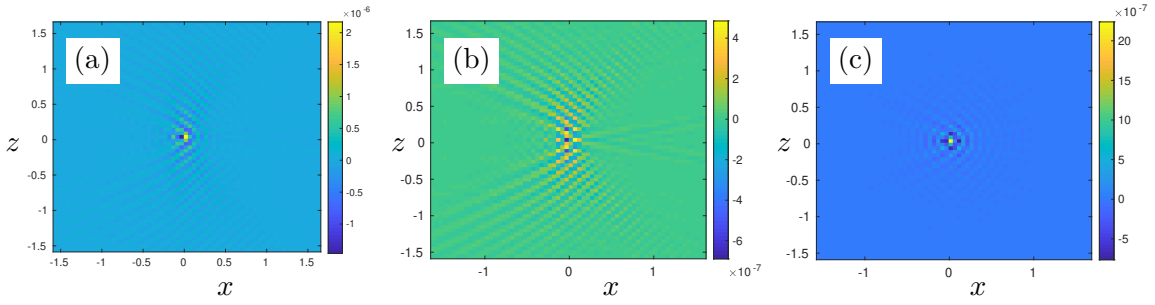

FIGURE 3.7: Sweeping effect of a homogeneous horizontal mean velocity field on the Saint Andrew's cross pattern of propagation of internal gravity wave after filtering the wave and eddy component. Vertical velocity u_z in the (x, z) plane in physical space (a) Full field u_z (b) Wave part u_z^w (c) Eddy part u_z^e.

I_θ. The final result ends up being slightly different for laminar cases. For a turbulent case, we assume that the correlation term $< \hat{\mathbf{u}}(\mathbf{k}, t)\hat{\mathbf{u}}(\mathbf{k}', t) >$ is almost zero on average. An example of the difference between these two techniques can be seen in Maffioli et al. [92].

After the analysis in the domain $(\mathbf{k}, \omega)$, we come back to physical space $(\mathbf{x}, t)$, where the vertical velocity $u_z(\mathbf{x}, t)$ is decomposed into wave and eddy parts $u_z(\mathbf{x}, t) = u_z^e(\mathbf{x}, t) + u_z^w(\mathbf{x}, t)$. Figure 3.7 shows $u_z(\mathbf{x}, t)$, $u_z^w(\mathbf{x}, t)$ and $u_z^e(\mathbf{x}, t)$. In the eddy component (Figure 3.7c), only the Dirac in space is visible whereas for the wave component (Figure 3.7b) only the wave propagation is visible. By doing the sum of the Figures 3.7b and c, the same kind of flow is obtained as in Figure 3.7a. Therefore, we can safely assume that for the case of simple, laminar, convective flow, this filtering technique works rather well.

3.3 Potential improvement and limitation

The ratio $\beta = 100$ could be reduced. Indeed, from the numerical simulation done, choosing this ratio ensures that all the wave energy is assigned to the wave part of the decomposition. However, it also means that eddies might be considered as waves. A better balance between these two possibilities can be found especially in the case of highly turbulent flow where the wave and eddy domain are close to one another. The ratio β could be modified depending on the relative importance of waves and eddies in the flow.

The adaptive algorithm could be further improved. For example, the filter ζ is created as a filter *all or nothing*. Each point $(\mathbf{k}, \omega)$ is supposed to be composed of only waves or only eddies. This is probably not the case and a better filter could be computed. For example, this new filter could be modified depending on the relative importance of energy at $(\mathbf{k}, \omega)$ against the maximum of energy at a wave vector $\mathbf{k}$ for all frequencies ω. In this case, for stratified flows, when the energy at the point $(\mathbf{k}, \omega)$ is $|\tilde{b}_G(\mathbf{k}, \omega)|^2 = \frac{1}{\gamma}\max_\omega \left[|\tilde{b}_G(\mathbf{k}, \omega)|^2\right]$ then we would allocate $\gamma\%$ of this $(\mathbf{k}, \omega)$ point to the eddy part and the rest to the wave part.
Another possibility would be to combine an *all or nothing* filter with a proportional filter. For example, when the energy at the point $(\mathbf{k}, \omega)$ is higher than $\frac{1}{10}\max_\omega \left[|\tilde{b}_G(\mathbf{k}, \omega)|^2\right]$ then this point is allocated entirely to waves (*i.e.* $\zeta = 1$). When the energy at point $(\mathbf{k}, \omega)$ is in a range such that $10 \leq \gamma \leq 100$ with $|\tilde{b}_G(\mathbf{k}, \omega)|^2 = \frac{1}{\gamma}\max_\omega \left[|\tilde{b}_G(\mathbf{k}, \omega)|^2\right]$ then we would allocate $\frac{100}{90}(\gamma - 10)\%$ to eddies and the rest to waves (*i.e.* $\zeta = \frac{\gamma - 10}{90}$). However, using a separation technique which shares some $(\mathbf{k}, \omega)$ points in a wave and eddy part would cancel the interesting property of the orthogonal decomposition of the wave and eddy part obtained in a *all or nothing* filter (see section 3.1.3.1).

This algorithm is also dependent on the choice of the convective velocity. The slow modes (the GM or the VSHF) are expected to be the main responsible of the sweeping effect as it is large scale and slowly varying in time. However, other large scale flow might actively participate in the advection of the waves. For example, in isotropic turbulence, the sweeping effect is caused by the random large scale eddies which contain most of the energy in the flow. They advect the small scale eddies randomly [61, 144]. Hence, small scale waves or eddies in our stratified or rotating flow separation algorithm can be subject to sweeping due to the large scale eddies as well. However, in order to take into account this, a better understanding of the role of the sweeping by large scale eddies in this separation technique would be necessary.

Maybe, selecting all the flow as the advecting flow and using an enhanced algorithm of the adaptive definition of ζ might improve the separation of waves and eddies. Indeed, from a general point of view, all the flow convects the rest of the flow. However, if all the flow is considered as advecting flow and the algorithm used currently is not modified, the sweeping effect would be too large and all the flow would be considered as waves. However, if the filtering is enhanced, by changing from a filter *all or nothing* to a more refined filter, the result might be more precise.

The waves and the eddies are separated in the $(\mathbf{k}, \omega)$ domain. Nevertheless, we observed that large scale flow can extend the area $(\mathbf{k}, \omega)$ where waves are located through the sweeping effect (see section 2.7.2). Therefore, as the sweeping effect gets larger, the domain $(\mathbf{k}, \omega)$ associated with the motion of waves gets bigger. In the case of a very large sweeping effect, this algorithm would nearly consider as waves all the frequencies. To quantify this limit we use the non-dimensionnalized number $N/(ck_\eta)$ where c is the *rms* velocity of the sweeping velocity and k_η is the Kolmogorov wavenumber. When $N/(ck_\eta) \ll 1$, the sweeping effect has a large effect on the smallest scales compared to the frequency of the waves and the separation technique might not be very effective. Otherwise, when $N/(ck_\eta) \gg 1$, the sweeping effect has little effect on the smallest scales compared to the frequency of the waves and the separation technique is likely to be very effective.

Finally, this algorithm involves a lot of steps and is quite complicated. If one is not careful enough, it is very likely that errors are done in the process resulting in some loss of computation time. Furthermore, the algorithm involves the storage of a lot of 3D fields, it requires a lot of memory to be run and it requires a huge amount of data storage.

Chapter 4

Stratified turbulence

4.1 Introduction

In stably stratified turbulence, Internal Gravity Waves (IGW) and eddies are closely entangled and interact with each other at different scales, as observed in the ocean [see *e.g.* 33]. Many studies focus on different kinds of interactions, separately. First, the wave-vortex interaction concerns the propagation of IGW through large quasi-geostrophic eddy flow [105] during which energy is transfered from eddy to waves. The eddies thus appear to deviate rays of IGW [102]. Second, the wave-wave interaction was examined starting from the isolated triadic point of view [112], then considering a stochastic field composed of many resonant triadic interactions [106] and finally extended to the wave turbulence formalism [87]. The creation of IGW in a surrounding quiescent region due to a localized stratified turbulent cloud has been studied by Maffioli et al. [90]. Lelong and Riley [79] studied the weakly non-linear interactions in a highly stratified system between a vortical mode (i.e. a horizontal rotating eddy) and an IGW. They show that the vortical mode acts as a catalyst and facilitates the energy transfer between waves.

Nevertheless, in stably stratified turbulence, mixing by waves and eddies occurs over a wide range of scales, rendering difficult their separation and the precise identification of mutual interactions. According to Brethouwer et al. [19], several regimes of stratified turbulence are found depending on the Froude number $Fr = \varepsilon_u / N u_h^2$ and the buoyancy Reynolds number $Re_b = \varepsilon_u / \nu N^2$ where ε_u is the kinetic energy dissipation, u_h is the rms horizontal velocity, N the Brunt-Väisälä frequency and ν the viscosity (see section 4.2.3). Those two numbers are linked by the horizontal Reynolds number $Re_h = u_h^4/(\varepsilon_u \nu)$ with the equation $Re_b = Fr^2 Re_h$ and $Re_h = \dfrac{u_h^4}{(\varepsilon_u \nu)}$. For a strong stratification, at $Fr \ll 1$ and $Re_b \ll 1$, the regime is a viscosity-affected stratified flow (VASF) and the flow is

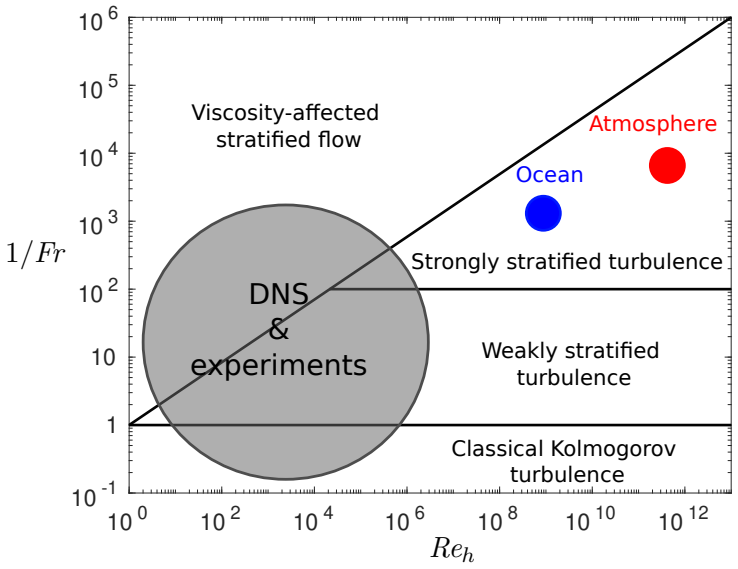

FIGURE 4.1: Schematic of the different regimes found in stably stratified flows (inspired from Brethouwer et al. [19]). Typical regimes found in DNS and experiments are added. Regimes for ocean ($N \sim 10^{-3} rad/s$) and atmosphere ($N \sim 10^{-2} rad/s$) are plotted for indication and can vary considerably.

dominated by large smooth and stable horizontal layers and few turbulent-like structures, such as vortex tubes, are observed. The different regimes are visible on figure 4.1.

This flow appears to be characteristic of a large-scale vortical mode [145]. At $Fr \ll 1$ and $Re_b \gg 1$, the regime is strongly stratified turbulence (SST) where large vertically sheared horizontal flow (VSHF) and three-dimensional (3D) overturning structures are observed. In order to separate a turbulent field into eddy and wave parts, Riley et al. [119] first proposed a 3D spatial decomposition. This decomposition was extensively used for stably stratified flow with or without rotation in many theoretical and numerical studies that explored different properties of IGW, eddies, VSHF and their interactions in terms of energy, transfer and scale dependence (see *e.g.* [55], [9], [129], [69], [62]).

According to Godeferd and Cambon [55], the non linear transfer concentrate the energy along the VSHF, *i.e.* $k_h = 0$. An illustration of this mechanism can be seen on figure 4.2.

This approach appears to be relevant at small Froude number $Fr \ll 1$ and low buoyancy Reynolds number $Re_b \ll 1$ where the eddies are mostly horizontal and the vertical motion and density field are associated to IGW [79]. Nevertheless, when Re_b increases, as in the SST regime, parts of the vertical velocity and density fields are linked to vertical mixing and therefore not to waves. Moreover, IGW are characterized by their dispersion relation $\omega_r(\mathbf{k}) = N \cos\theta(\mathbf{k})$ where $\theta(\mathbf{k})$ is the angle of the wave-vector $\mathbf{k}$ with the horizontal plane. Clearly, Riley's decomposition is a spatial decomposition and does not reflect the temporal properties of the waves, since it includes all frequencies of the

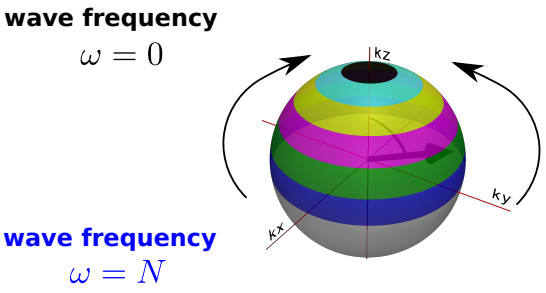

FIGURE 4.2: Visualization of the non linear transfer, which concentrate energy around the VSHF (at $k_h = 0$).

flow motion, even outside the dispersion relation. Therefore, the dispersion relation of IGW cannot be characterized with this decomposition.

Alternative approaches have been developed, for example by selecting only a few Fourier modes [85], and detecting in their temporal signal the presence of frequency peaks linked to their wave vector by the dispersion relation, which is a signature of IGW. Recent detailed analyses have been proposed to study waves in turbulence: in stratified turbulence, a global signature of IGW was observed in experiments of Savaro et al. [121] and in numerical simulations by Di Leoni and Mininni [40] and Maffioli et al. [92] clearly characterized the presence of IGW by using a temporal analysis of reduced energy from Riley's decomposition.

However, there is a heavy computational cost to a complete wave/eddy separation, so that simplifying assumptions are used in the above-mentioned methods: horizontal isotropy, and the fact that transport of IGW occurs in a homogeneous distribution of VSHF. The latter assumption discards possible variations in time and space of the transporting motion that in principle modifies significantly the waves dispersion relation. We extend Riley's decomposition by taking into account the 3D spatial and temporal properties of fields. This method permits the extraction of the 3D fields of IGW and eddies separately, accounting for the overturning of density and vertical velocity.

In this chapter, the adaptive algorithm is applied on a stratified flow using also the Craya-Herring frame. The first section explains:

- the forcing (section 4.2.1),
- the added viscosity (section 4.2.2) used that damps considerably the VSHF in order to achieve statistical stationarity of the flow,
- all the parameters of the DNS (section 4.2.3) that explore various stratified turbulent regimes,

- the influence of the VSHF on the dispersion relation with the sweeping and gradient effect (section 4.2.5).

In the second section (4.3), we present the partition of energy between waves and eddies. It explores the energy ratio as well as the energy spectrum of the wave and eddy part. The third section (4.4) presents an energy budget for waves and eddies, with mutual interaction and different fluxes. The fourth and fifth sections (4.5,4.6) present the dissipation linked to waves and eddies as well as the mixing. The sixth section (4.7) makes a detailed analysis on the different transfer occuring in the flow and the inverse or direct cascade of energy it participated in. The last section (4.8) shows some visualization of the decomposition of the total field in a wave and eddy part.

4.2 Parameters

4.2.1 Forcing technique

Classical forcing techniques such as the forcing on a sphere (a wavenumber shell) in the Fourier domain [45, 93] might give energy to the VSHF modes, which already tends to gather most of the energy of the flow. Indeed, the VSHF with $(k_h = 0, k_z)$ is located on a sphere with a radius k_z. To avoid such a phenomenon, a forcing technique developed by Andrea Maffioli is used [89, 92]. This forcing can be used to avoid the wavenumbers related to the slow modes. The forcing is applied on the suface of a cylinder and takes as argument 4 variables (see figure 4.3):

- the horizontal wavenumber forced $k_{h,f}$
- the minimum vertical wavenumber forced $k_{v,fmin}$
- the maximum wavenumber forced $k_{v,fmax}$
- the energy input by the forcing P.

This cylindrical forcing inserts a constant input of energy P in the system for all wave vectors $\mathbf{k} = (k_x, k_y, k_z)$ in the cylindrical shell $k_h = k_{h,f}$ (at a $\Delta k/2$ precision) and $k_{v,fmin} - \Delta k \leq |k_z| \leq k_{v,fmax} + \Delta k$. It can be seen in Figure 4.3 where two cylinders corresponding to the area forced by the cylindrical forcing are represented.

The input energy is equally divided on average between the toroidal $a_F \hat{f}_1$ and the poloidal $a_F \hat{f}_2$ components of the flow. The forcing is placed at a random position

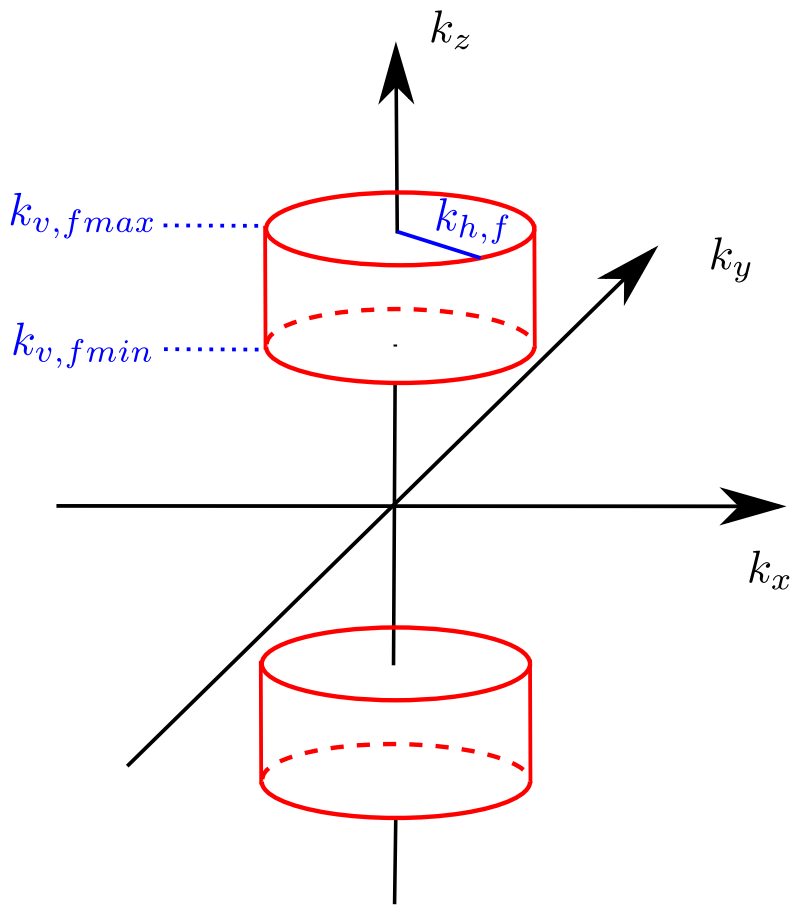

FIGURE 4.3: Visualization of the cylindrical forcing as done in Maffioli et al. [92]

such that $\hat{f}_1 = e^{i\theta_1}\cos\phi$ and $\hat{f}_2 = e^{i\theta_2}\sin\phi$ where θ_1, θ_2 and ϕ are uniformly distributed random numbers between 0 and 2π meaning that the forcing is not correlated in time. The variable a_F is the intensity of the forcing, it is computed later and depends on the power input P chosen. The forcing can be projected on the Cartesian coordinates $\hat{\mathbf{f}} = (\hat{f}_x, \hat{f}_y, \hat{f}_z)$:

$$\begin{aligned} \hat{f}_x &= \frac{1}{k_h}(k_y\hat{f}_1 + k_x k_z \hat{f}_2/k) \\ \hat{f}_y &= \frac{1}{k_h}(-k_x\hat{f}_1 + k_y k_z \hat{f}_2/k) \\ \hat{f}_z &= \frac{-k_h}{k}\hat{f}_2. \end{aligned} \tag{4.1}$$

Between two time steps the forcing is constant so that we can write

$$\frac{\partial\hat{\mathbf{u}}}{\partial_t} = a_F\hat{\mathbf{f}} \Rightarrow \frac{\hat{\mathbf{u}}(t+\Delta t) - \hat{\mathbf{u}}(t)}{\Delta t} \simeq a_F\hat{\mathbf{f}}. \tag{4.2}$$

The forcing power into a wave vector $\mathbf{k}$ is:

$$\frac{\partial\hat{\mathbf{u}}^2/2}{\partial_t} = 0.5\frac{\partial\hat{\mathbf{u}}}{\partial_t}\overline{\hat{\mathbf{u}}} + 0.5\overline{\frac{\partial\hat{\mathbf{u}}}{\partial_t}}\hat{\mathbf{u}} = 0.5a_F\hat{\mathbf{f}}\overline{\hat{\mathbf{u}}} + 0.5\overline{a_F\hat{\mathbf{f}}}\hat{\mathbf{u}}. \tag{4.3}$$

It can be approximated using equation (4.2) as

$$\begin{aligned}\frac{\partial \hat{\mathbf{u}}^2/2}{\partial_t} &\simeq a_F\hat{\mathbf{f}}\cdot\frac{\overline{\hat{\mathbf{u}}(t+\Delta t)+\hat{\mathbf{u}}(t)}}{2}+\overline{a_F\hat{\mathbf{f}}}\cdot\frac{\hat{\mathbf{u}}(t+\Delta t)+\hat{\mathbf{u}}(t)}{2}\\ &= a_F\,\mathrm{Re}(\mathbf{f}\cdot\overline{\hat{\mathbf{u}}(t+\Delta t)})+a_F\,\mathrm{Re}(\mathbf{f}\cdot\overline{\hat{\mathbf{u}}(t)})\\ &= 2a_F\,\mathrm{Re}(\mathbf{f}\cdot\overline{\hat{\mathbf{u}}(t)})+a_F^2\Delta t\,\mathrm{Re}(\hat{\mathbf{f}}\cdot\bar{\hat{\mathbf{f}}}).\end{aligned} \tag{4.4}$$

The energy of this forcing is computed as the sum of the physical forcing ($a_F P_{uf}$) and an artificial forcing ($a_F^2 P_{ff}$) created by the discrete time step where $a_F\hat{\mathbf{f}}$ is constant.

$$\begin{aligned}a_F P_{uf} &= 2a_F\sum_{\mathbf{k}}\mathrm{Re}(\bar{\hat{f}}_x\hat{u}_x+\bar{\hat{f}}_y\hat{u}_y+\bar{\hat{f}}_z\hat{u}_z)\\ a_F^2 P_{ff} &= a_F^2\Delta t\sum_{\mathbf{k}}\mathrm{Re}(\bar{\hat{f}}_x\hat{f}_x+\bar{\hat{f}}_y f_y+\bar{\hat{f}}_z\hat{f}_z).\end{aligned} \tag{4.5}$$

The total input of energy P is supposed to be equal to the energy input by the forcing. Therefore the equality $P = a_F P_{uf} + a_F^2 P_{ff}$ must be imposed with P a constant. This equation has two solutions:

$$\begin{aligned}a_F^+ &= \frac{-P_{uf}+\sqrt{P_{uf}^2+4P_{ff}P}}{2P_{ff}}\\ a_F^- &= \frac{-P_{uf}-\sqrt{P_{uf}^2+4P_{ff}P}}{2P_{ff}}.\end{aligned} \tag{4.6}$$

We decide to keep the minimum amplitude of forcing, so we choose $a_F = \min(a_F^+, a_F^-)$ (this technique is named *constant power minimal forcing*). a_F is updated at each time step in order to keep P constant. Finally the forcing $\hat{\mathbf{F}}_u = a_F(\hat{f}_1\mathbf{e}^t + \hat{f}_2\mathbf{e}^p)$ can be computed in the toroidal-poloidal coordinates.

This forcing has two main advantages. When the flow reaches a statistically stationary state, the input of energy equals the dissipation of energy so $P = \varepsilon_u + \varepsilon_b$. Moreover, as this forcing chooses some wavevectors to be forced, it is possible to avoid sensitive areas, such as close to the shear mode ($k_h = 0$) for stratified flows and the geostrophic mode ($k_z = 0$) for rotating flows. Indeed, these modes tend to dominate the overall structure of the stratified or rotating flows even if there are not directly forced. By using a forcing that input energy far from these modes we slightly reduce its importance.

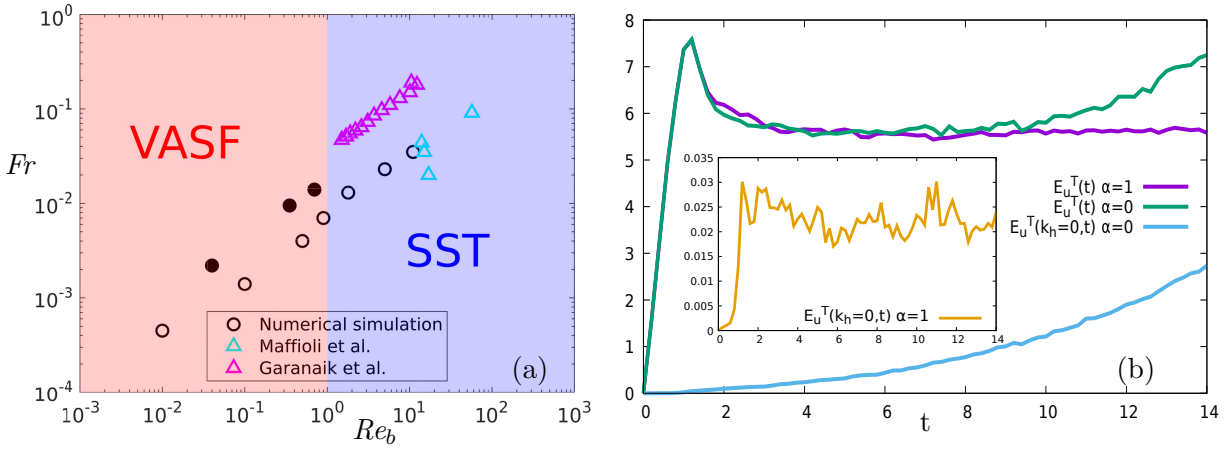

FIGURE 4.4: (a) Our parameters of the numerical simulations (open circle for 512^3 points and filled circle for 256^3 points). For reference, the DNS of Maffioli et al. [91] (from 96^3 points to more than 1024^3 points) and Garanaik and Venayagamoorthy [52] (512^3 points) are shown. (b) Total kinetic energy $E_u^T(t)$ and VSHF energy $E_u(k_h = 0, t)$ for $\alpha = 1$ and $\alpha = 0$ for $Re_b = 5$ and $Fr = 0.023$.

4.2.2 Controling VSHF growth with added viscosity

However, even with this new forcing it is difficult to reach a stationary steady state because the slow modes still slowly grows in time. In order to further reduce the importance of the slow modes, a new viscous term F_α is added in the Navier-Stokes equation as done in rotating turbulence in Le Reun et al. [75].

For stratified flow, this added viscosity is inserted in the kinetic part of the Navier-Stokes equations and equals:

$$\hat{\mathbf{F}}_\alpha(\mathbf{k}, t) = \begin{cases} -\alpha \hat{\mathbf{u}}(\mathbf{k}, t) & \text{if } k_h = 0 \\ 0 & \text{otherwise.} \end{cases} \tag{4.7}$$

where the value of α modifies the relative importance of the VSHF against the overall structure of the flow. Therefore, the value of α is chosen in function of the wanted importance of the VSHF.

4.2.3 Parameter space

Equations (2.9) are solved using a standard pseudo-spectral algorithm in a 2π-periodic three-dimensional spatial domain. A phase shifting method is used to treat aliasing in the non-linear term (see Lam et al. [72] for details). The Prandtl number is $Pr = \nu/\mathcal{X} = 1$. Ten numerical simulations were run with the parameters shown in table 4.1 at resolutions 256^3 and 512^3. The exploration of the parameters is mainly based on 512^3 points, the

lower resolution of 256^3 points is used to confirm and explore trends. We plotted in Figure 4.4 the exploration points in the parameter space (Fr, Re_b), along with data from Maffioli et al. [91] and Garanaik and Venayagamoorthy [52]. In stratified turbulence, results are typically shown against:

$$Fr = \frac{\varepsilon_u}{N u_h^2}, \quad Re_b = \frac{\varepsilon_u}{\nu N^2} \tag{4.8}$$

where ε_u is the kinetic energy dissipation, u_h is the rms horizontal velocity. Fr is the Froude number and is considered as the ratio of flow inertia over the stratification. The buoyancy Reynolds number Re_b can also be written as $Re_b = (\frac{k_\eta}{k_O})^{4/3}$. It can be understood as the ratio of the Kolmogorov wavenumber $k_\eta = (\frac{\varepsilon_u}{\nu^3})^{1/4}$, the biggest wavenumber of the turbulent flow, over the Ozmidov wavenumber $k_O = \sqrt{\frac{N^3}{\varepsilon_u}}$ [114], the wavenumber at which stratification becomes less important. Re_b measures the extent between the large scales dominated by stratification and IGW (up to Ozmidov scale k_O) and small scales dominated by isotropic dissipation (the Kolmogorov scale). N is the Brunt-Väisälä frequency and ν is the viscosity. According to Brethouwer et al. [19], we explore different regimes:

- a viscosity-affected stratified flow (VASF) regime which contains weak IGW interactions where wave anisotropy extends to small scales ($Fr \ll 1$ and $Re_b \ll 1$),
- a strongly stratified turbulence (SST) regime where the scale of wave anisotropy is distinct from small dissipative scales ($Fr \ll 1$ and $Re_b \gg 1$).

The exploration of these two regimes also induces a modification of the Taylor-length-based Reynolds number $Re_\lambda = u_{rms}\lambda/\nu$ with λ the Taylor scale and u_{rms} the *rms* velocity. The regimes studied in our numerical simulations and in other numerical simulations are shown in figure 4.4a. The figure shows that the two resolutions 256^3 and 512^3 explore different regions of parameter space (Fr, Re_b) and we expect this to change the characteristics of the transition regime between the VASF and SST regime. Additional few points in parameter space at 256^3 resolution permit the exploration of a slight variation of Re_b and Fr. The two parameters Fr and Re_b are of course dependent on one another since

$$Re_b = Fr^2 Re_h \quad \text{with} \quad Re_h = \frac{u_h^4}{(\varepsilon_u \nu)}. \tag{4.9}$$

The horizontal Reynolds number $Re_h = u_h^4/(\varepsilon_u \nu)$ defined by Maffioli et al. [91] accounts for the horizontal turbulence intensity. The 256^3 simulations have almost one order of magnitude lower Re_h than 512^3 simulations (see table 4.1) for similar (Re_b, Fr). By adjusting the resolution, one can therefore study the variation of the dynamical system

512^3 points with $\nu = 1/700$

N	Fr	Re_b	Re_h	Re_λ	D_E	$S_E(\%)$	$\omega_{\max}$	$\omega_{\min}$	$u_{rms}k_{max}$	$k_{max}\eta$	Δt $(\times 10^{-4})$
20	0.035	11	9000	146	760	0.3	1570	3	800	1.12	2
30	0.023	5	9500	148	1080	0.4	1570	3	810	1.12	2
50	0.013	1.8	10700	180	980	0.4	1570	3	890	1.12	2
70	0.007	0.9	18000	225	820	0.3	1570	3	990	1.12	2
100	0.004	0.5	31000	290	730	0.3	1570	3	1110	1.12	2
200	0.0014	0.1	51000	430	22	0.08	3140	6	1300	1.13	1
600	0.00045	0.01	49000	510	11	0.005	3140	6	1370	1.19	1

256^3 points with $\nu = 1/250$

N	Fr	Re_b	Re_h	Re_λ	D_E	$S_E(\%)$	$\omega_{\max}$	$\omega_{\min}$	$u_{rms}k_{max}$	$k_{max}\eta$	Δt $(\times 10^{-4})$
50	0.014	0.7	3600	94	2500	1	1570	3	423	1.18	4
70	0.0095	0.35	3900	109	420	0.16	1570	3	450	1.19	5
200	0.0022	0.04	8300	175	74	0.03	1570	3	557	1.21	4

TABLE 4.1: List of parameters in the ten DNS runs. $Re_h = u_h^4/(\varepsilon_u \nu)$ is the horizontal Reynolds number, S_E is the ratio of energy of shear flow over the total kinetic energy, D_E is the ratio of density of shear energy per point against the total kinetic energy per point, $\omega_{\max} = \pi/\Delta t'$ is the maximum pulsation solved and $\omega_{\min} = 2\pi/T$ is the minimum pulsation solved.

either by setting Fr and weakly increasing Re_b (from low to high resolution), or by setting Re_b and weakly increasing Fr (from high to low resolution) in the parameter map. While a wide range of Fr and Re_b number are analysed in this campaign of numerical simulation, the values analysed here are far from the values typically found in ocean and atmosphere (see figure 4.1). In some numerical simulation a Froude number close to the ocean and atmosphere is reached ($Fr \sim 10^{-3}, 10^{-4}$), but this is done at the cost of the buoyancy Reynolds number which is very low for this particular Froude number ($Re_b \sim 10^{-2}$). However, no numerical simulation in our campaign reaches the typical value of Re_b found in ocean and atmosphere. Our analysed flows are significantly less turbulent than flow found in ocean and atmosphere. Hence, no clear and direct conclusion can be drawn for ocean and atmosphere phenomena as their regime are not attained here, but some trends can still be determined.

4.2.4 Numerical parameters

The time step Δt varies with the stratification N to agree with the CFL condition. For the spatial resolution of 512^3 points, the maximum wavenumber is $k_{\max} = 241$ such that

$k_{\max}\eta \sim 1.1$, η being the Kolmogorov scale (see table 4.1). This moderate number of points is necessary because our wave/eddy decomposition requires many 3D fields in time. Turbulence reaches a statistically stationary state due to the added body force F_u in equation (2.17), as in Maffioli et al. [92] who injected a constant power

$$P = \int \mathbf{F_u} \cdot \mathbf{u} \, \mathrm{d}v = 10. \tag{4.10}$$

$\mathbf{F_u}$ is spectrally localized on a cylindrical spectral surface of horizontal wave number $k_h = 4$ and vertical wave number $1 \leq k_z \leq 3$, away from the VSHF at $\hat{\mathbf{u}}(k_h = 0, k_z)$. It forces the poloidal and toroidal parts of the velocity equally. Thus, this choice allows on average the wave and vortex components of the flow (in the sense of Riley's decomposition) to be excited in equal proportions. The forced wavenumbers are at an angle θ_f between the wavevector $\mathbf{k}$ and the horizontal plane, in the range $0.72 \leq \theta_f \leq 1.31$, meaning that high frequencies close to N are forced and a wave turbulence cascade may develop with lower frequency. To delay the emergence of VSHF at large scale, we add a friction term $\hat{\mathbf{F}}_u - \alpha\hat{\mathbf{u}}(\mathbf{k}_h = 0, k_z)$ (with $\alpha = 1$) as proposed by Le Reun et al. [75] to stabilise the geostrophic mode in rotating turbulence. The latter authors also note that this term mimics the effect of a horizontal wall. It also helps the numerical simulation to reach a stationary state as shown in figure 4.4b. This figure shows the total kinetic energy $E_u^T(t)$ and the kinetic energy of VSHF $E_u^T(k_h = 0, t)$ for $\alpha = 1$ and $\alpha = 0$. Both energies diverge when $\alpha = 0$ but stay bounded when $\alpha = 1$. This statistical stationarity allows the computation of time Fourier transforms with fewer truncation-related spurious effects. Furthermore, the divergence of the kinetic energy $E_u^T(t)$ for $\alpha = 0$ is about the same as that of VSHF energy $E_u^T(k_h = 0, t)$, meaning that roughly the same amount of energy is advected by the VSHF. The main difference between the two cases with and without friction is that the flow is significantly advected by VSHF in the first case ($\alpha = 0$) whereas this advection is much less in the case with friction ($\alpha = 1$).

Our simulations contrast with those of Maffioli et al. [92] in that we apply a friction term to quench VSHF to less than a few percent of the total kinetic energy, though still active enough to contribute to the flow structuration. We show in table 4.1 that the percentage of shear energy over the total kinetic energy ($S_E = E_u^T(k_h = 0, t)/E_u^T(t)$) is very low. However, we still consider the VSHF to be the main advecting flow.

We consider that all wavevectors k_x, k_y, k_z (512^3 points) are 'active' — *i.e.* they are prone to contributing significantly — in the total kinetic energy, whereas in the kinetic energy of the VSHF, we only consider as active wavevectors with $k_h = 0$, at whatever k_z (512 points). Then, from these total kinetic energy E_u^T and kinetic energy of VSHF $E_u^T(k_h = 0)$, it is possible to define the following average energy densities: $e_K = E_u^T/512^3$ and $e_{\text{shear}} = E_u^T(k_h = 0)/512$. These average densities take explicitly into account the

number of active wavenumbers they involve. Finally, we can define the average density ratio per wavevector by $D_E = e_{\text{shear}}/e_K$. The value D_E is given in table 4.1 and shows the relative importance of the VSHF compared to the number of points in the DNS involved. $D_E \sim 1000$ shows that the VSHF importance per point is strong for weaker stratification, but decreases while still intense for higher stratification.

In a second kind of DNS we run in order to build the ζ function, in preparation for the DNS with 512^3 points, the Green's function is simulated during $T = 10000\Delta t$ by using equation (2.17) with the forcing term $F_b = \sum_{\mathbf{x},t} \delta(\mathbf{x})\delta(t)$ where each Dirac function is set at a random position and enforced at each time step Δt during the first $100\Delta t$. The initial condition of this calculation is zero. The velocity $\mathbf{c}$ comes from the VSHF $\hat{\mathbf{u}}(k_h = 0, kz)$ extracted every $\Delta t' = 10\Delta t$ from the DNS, after it has reached statistical stationarity. To ensure that IGW are not dissipated, we use very small viscosity $\nu_G = \mathcal{X}_G = 10^{-8}$ and we check that only the poloidal part $\hat{u}^p$ and the density $\hat{b}$ are active with respect to the toroidal part $\hat{u}^t$ that is close to machine-precision zero. We apply the FFT in time on 1000 fields of $\hat{b}_G$ extracted every $\Delta t'$. For DNS with 256^3 points the time step Δt can be taken larger and result in a DNS with less iterations ($T = 4000$ or $5000\Delta t$) but with statistics written on the same time step $\Delta t' = 0.002$ as in numerical simulations with 512^3 points. The time step is chosen very small in order to capture the sweeping effect from the full *rms* velocity u_{rms} on the highest frequency of eddies $u_{rms}k_{\max}$ [30, 139], as validated in homogeneous and isotropic DNS simulation by Di Leoni et al. [41]. The highest frequency of eddies $u_{\text{rms}}k_{\max}$ must be compared to maximum frequency $\omega_{\max}$ and minimum frequency ω_{min} resolved by the numerical algorithm. The fields are not extracted at every Δt both to reduce the memory cost and because in the DNS this time step comes mainly from the CFL constraint.

The value $\beta = 100$ is based on the simulation of the Green's function under conditions similar to the analytical solution (2.66) for buoyancy $\tilde{b}_{G,a}$ which is a benchmark for our method. Indeed, two reasons render imprecise the capture of peaks in the simulation of Green's functions. First, even if very low (*e.g.* $\nu_G = \mathcal{X}_G = 10^{-8}$), viscosity tends to smear the peaks around the resonance frequencies $\omega_c^{\pm}$. Spectral discretization also adds to this smearing: for each wavevector $\mathbf{k}$, 100% of energy is localized in a single frequency $\omega_c^{\pm}(\mathbf{k})$ when analytically computed, whereas it is distributed over a bandwidth of frequencies in simulations. The second reason is due to time discretization: the frequency $\omega_c^{\pm}$ is not exactly measured, but is approximated by the two closest discrete frequencies. These two mechanisms lead to a search for the set of points closest to the peak. When trying to capture the peak in a configuration similar to the analytical solution (2.5), we observe that the peaks span several orders of magnitude in amplitude over a bandwidth of frequencies. In simulations, even if 100% of the energy is distributed over all frequencies, in practice a large percentage is still located in a small frequency

range. In numerical simulations in the exact configuration of the analytical solution $\tilde{b}_{G,a}$, we adjusted β to 100 because we observe that 95% of the total potential energy is selected as waves around a small bandwidth of frequencies. This 95% value is retained for all the simulations of the Green's function from equation (2.61). Choosing lower β means that less potential energy from equation (2.61) would be considered as waves, meaning that some eddies would be assigned as waves. Conversely, choosing a higher β would not change much in the wave energy in equation (2.61) and might increase the number of eddies associated to IGW. In configurations other than the analytical solution, simulations of Green's functions also show that more or less 95% of the total potential energy is preserved as waves.

4.2.5 VSHF influence on the dispersion relation

What is the effect that influence the most the dispersion relation? It is the sweeping effect or the effect of the gradient? In this section we answer these questions by studying the VSHF influence on the dispersion relation through the sweeping effect and the effect of the gradient. While in sections 2.7.3.1 and 2.7.2.4, these studies are done on an idealized VSHF, this time the analyses are done on a VSHF extracted from one of the turbulent flow we are studying (from the DNS with 256^3 points and $N = 50$ in table 4.1).

In figure 4.5, we can observe the effect of a full VSHF on the dispersion relation. The forcing used here is a multitude of Diracs in space at successive time steps exactly as explained in the second step of the separation technique (in section 3.1.5.2). The sweeping effect of the full VSHF is shown in figure 4.5a and the gradient effect of the full VSHF is shown in figure 4.5b.

Example of energy spectrum of the VSHF can be found in figure 4.11. It shows that the VSHF is mostly large scale. The sweeping effect of the VSHF on the dispersion relation, visible in figure 4.5a is very large and is well estimated by the *rms* velocity of the full VSHF flow in yellow. On the contrary the gradient effect is visible in figure 4.5b and does not modify the dispersion relation (in red).

From these observations, we can safely assume that the dispersion relation of IGW is mostly modified by the sweeping effect. It can be well estimated by computing the *rms* velocity of the VSHF flow.

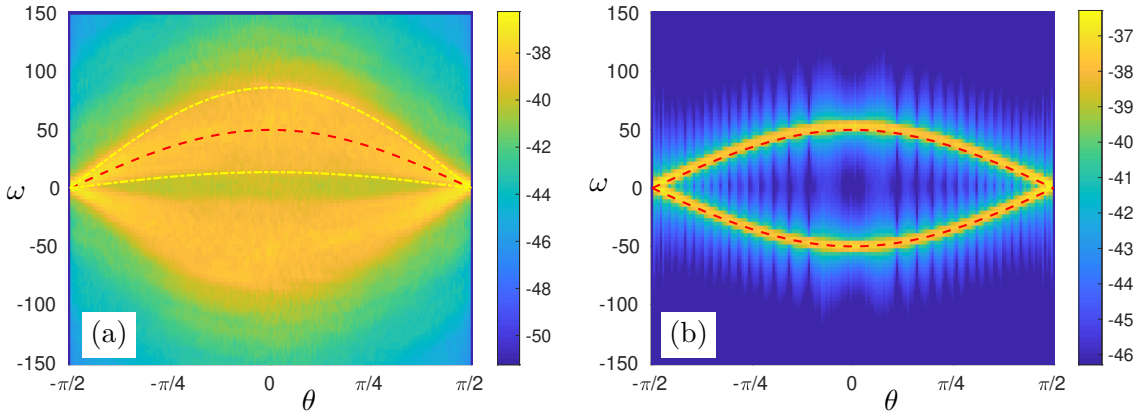

FIGURE 4.5: Effect of the the VSHF on the dispersion relation. (a) Sweeping effect of the VSHF on the dispersion relation (b) Gradient effect of the VSHF on the dispersion relation. Yellow lines is the dispersion relation modified by the sweeping effect calculated by the *rms* velocity. Red lines are the initial dispersion relation.

4.3 Partition of energy between IGW and eddy

4.3.1 Energy ratio

In this subsection, we consider the separation of energy between IGW and eddies in terms of percentage. This distribution is analysed against the typical non-dimensional numbers of stratified turbulence, the Froude number Fr and the buoyancy Reynolds number Re_b.

4.3.1.1 Total

The total mechanical energy $E^T = E_u^T + E_b^T$ is the sum of kinetic energy E_u^T and potential energy E_b^T. Based on our orthogonal decomposition, we split these energies into their wave and eddy parts as $E^T = E^w + E^e$ and $E^l = E_u^l + E_b^l$, with $E_u^l = 0.5 < \hat{\mathbf{u}}^l, \hat{\mathbf{u}}^l >$ and $E_b^l = 0.5N^{-2} < \hat{b}^l, \hat{b}^l >$ where l stands for w (wave), e (eddy) or T (total) and $<,>$ is defined in section 3.1.1. The eddy part of the poloidal kinetic energy is defined as $E^{p,e} = 0.5 < \hat{\mathbf{u}}^{p,e}, \hat{\mathbf{u}}^{p,e} >$.

Figures 4.6a and 4.6b show for both resolutions, the energy distribution between waves and eddies, E^e and E^w compared to total energy E^T. Since two parameters Fr and Re_b appear to be strongly correlated (recall that $Re_b = Re_h Fr^2$), we plot the distribution against Fr and Re_b separately. Moreover, we can observe the evolution of these energies either at constant Re_b and weakly increasing Fr (from high to low resolution on figure 4.6a), or at constant Fr and weakly decreasing Re_b (from high to low resolution on figure 4.6b). As expected, on figure 4.6 we observe that the eddy part of any form of energy

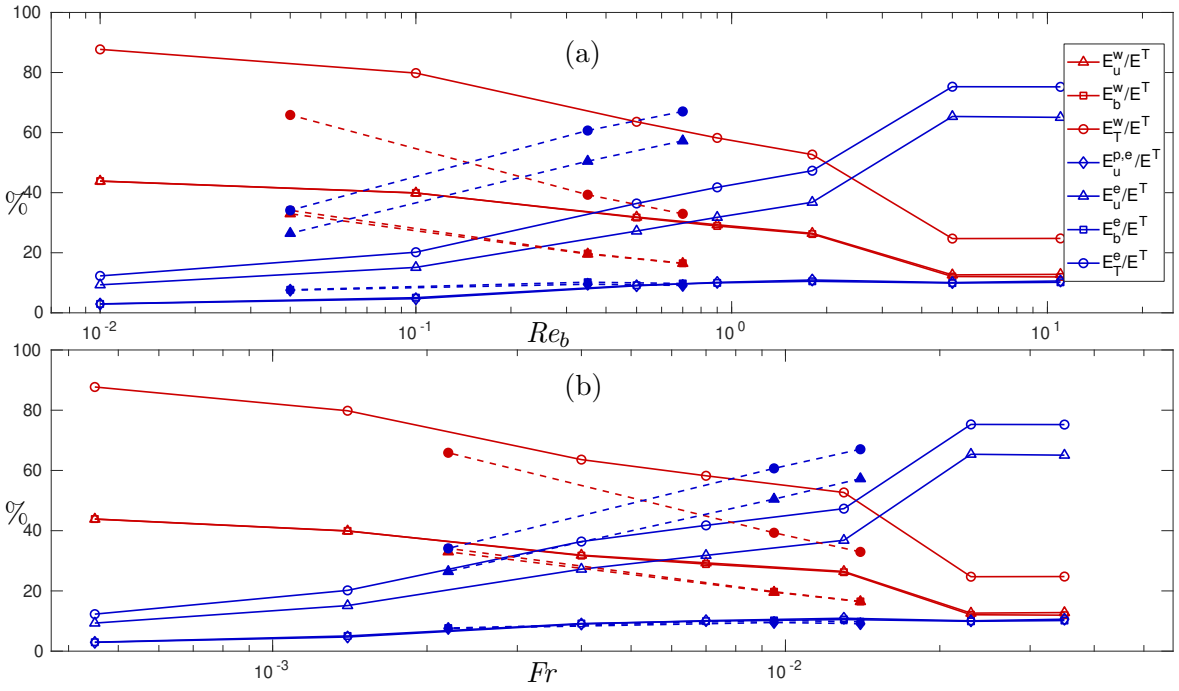

FIGURE 4.6: Evolution of the percentage of energy in waves and eddies ($E_i^e/E^T, E_i^w/E^T$) for kinetic, potential and total energy ($i = b, u, T$ respectively) against (a) Re_b; (b) Fr. Numerical simulations with 512^3 points are shown with open symbols and solid lines, and numerical simulations with 256^3 points are shown with filled symbols and dotted lines.

E^e increases and the wave part E^w decreases, both when Re_b increases (figure 4.6a) and when Fr increases (figure 4.6b).

Staquet and Godeferd [132] found a similar distribution of kinetic energy (60% to eddies and 40% to waves) at $Fr \simeq 0.006$ for decaying turbulence. Moreover, at fixed Re_b (figure 4.6a), when Fr increases, there is more energy in the eddy part than in the wave part, as expected by the meaning of Fr (inertial effects are more important than gravity effects). By increasing Fr, the evolution of E^w, E^e as a function of Re_b seems to be shifted to smaller values of Re_b as well as towards the equilibrium point where $E^w = E^e$. Nevertheless, at fixed Fr (figure 4.6b), when Re_b decreases, there is more energy in the eddy part than in the wave part, which is not obvious. Once again, this evolution seems to be shifted towards a smaller value of Fr.

To analyse this result, we must analyse the composition of each type of energy. Figures 4.6a and 4.6b show the ratio of potential and kinetic energy distribution of waves (E_b^w, E_u^w) and eddies (E_b^e, E_u^e) compared to total energy E^T. First, we observe that the potential energy E_b^w and kinetic energy E_u^w contain the same percentage of total energy of waves, *i.e.* $E_b^w \sim E_u^w$ for any Re_b or any Fr, as generally expected for gravity waves. Secondly, we observe that the potential energy of eddies is less than the kinetic energy of eddies *i.e.* $E_u^e > E_b^e$ for any Fr or Re_b. Nevertheless, at fixed Fr, for instance at

$Fr \sim 0.014$, when Re_b decreases, there is more kinetic energy in eddy for lower Re_b *i.e.* $E_u^e(Fr = 0.014, Re_b = 0.7) > E_u^e(Fr = 0.013, Re_b = 1.8)$.

This non obvious result can be analysed by decomposing the kinetic energy of eddies into poloidal and toroidal parts. By following the decomposition (3.2), the eddy part can be decomposed into a poloidal and a toroidal component: $E_u^e = E_u^{p,e} + E_u^{t,e}$ where $E_u^{p,e} = 0.5 < \hat{\mathbf{u}}^{p,e} \cdot \mathbf{e^p}, \hat{\mathbf{u}}^{p,e} \cdot \mathbf{e^p} >$ and $E_u^{t,e} = 0.5 < \hat{\mathbf{u}}^{t,e} \cdot \mathbf{e^t}, \hat{\mathbf{u}}^{t,e} \cdot \mathbf{e^t} >$. On figures 4.6a and 4.6b we only show $E_u^{p,e}$, from which the value of $E_u^{t,e} = E_u^e - E_u^{p,e}$ can be deduced. We observe the same percentage of total energy in the poloidal and buoyancy eddy energy, *i.e.* $E_b^e \sim E_u^{p,e}$ independently of Fr or Re_b. This percentage increases slowly with Re_b or with Fr. Note that the total potential energy $E_b^T = E_b^w + E_b^e$ is linked to the available potential energy (see section 14.1 in Davidson [35]). The available potential energy is a mechanical form of gravitational potential energy that stores the energy of an unstable density pattern, *i.e.* the light- and heavy-density fluid parcels are not in equilibrium. While a part of this unstable configuration is related to the IGW (E_b^w) as the waves induce spatial variations of density fluctuation, the other part (E_b^e) contains, among other things, the density overturns (light density over heavy density). It seems that the equality $E_b^e \sim E_u^{p,e}$ reflects the effect of eddies in the vertical plane, which is directly related to the poloidal part of the velocity field. Since $E_b^e \sim E_u^{p,e}$ is more or less constant with Re_b at fixed Fr, this means that only the toroidal part $E_u^{t,e}$ increases when Re_b decreases. The increase of $E_u^{t,e}$ leads to an increase of the total kinetic energy of the eddy part E_u^e. We remind that the toroidal part ($k_h \neq 0$) does not include the VSHF ($k_h = 0$). Generally, large scales contain more kinetic energy than small scales dominated by the dissipation, so that the large scale vortical modes are well represented by the toroidal part of the energy. We therefore argue that the *relative* increase — with respect to total energy — of the part of kinetic energy in the vortical modes can be associated with an increase in large, smooth and stable horizontal layers as the flow is more and more in the VASF regime by decreasing Re_b, as in the nomenclature by Brethouwer et al. [19]. This observation could explain the shift of the distribution of energy E^w, E^e towards smaller Fr as Re_b decreases.

Note that at $Re_b \geq 5$ and $Fr \geq 0.02$, it seems that $E_u^{p,e} \simeq E_b^e \simeq E_b^w \simeq E_u^w$.

In the original decomposition by Riley et al. [119], at large Re_b all the potential energy of eddies E_b^e and the poloidal part of the kinetic energy of eddies $E_u^{p,e}$ are wrongly assigned to the wave part (*i.e.* $\sim 10\%$ for each part), thus inducing a departure of 40% in comparison to our results: $+20\%$ of energy in IGW and -20% of energy in eddies.

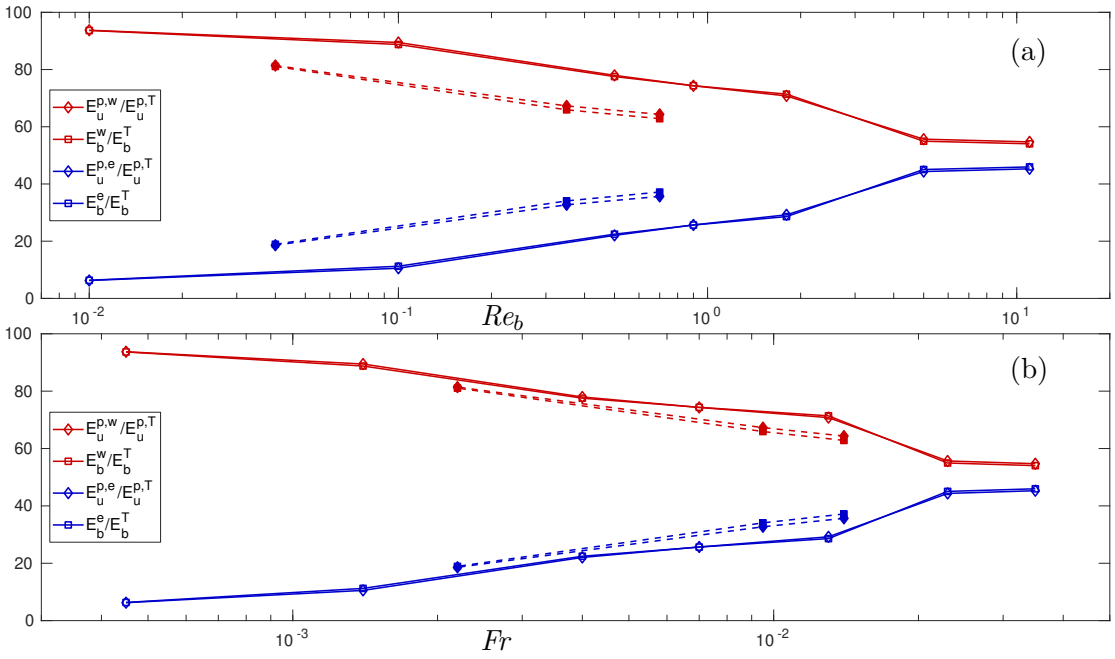

FIGURE 4.7: Evolution of the percentage of energy for poloidal ($E_u^{p,i}/E_u^{p,T}$ and potential (E_b^i/E_b^T energy in waves and eddies ($i = w, e$ respectively) against (a) Re_b; (b) Fr. Numerical simulations with 512^3 points are shown with open symbols and solid lines, and numerical simulations with 256^3 points are shown with filled symbols and dotted lines.

4.3.1.2 Poloidal and potential

In the previous section where the eddy energy is examined as the sum of a part of the poloidal term and all the toroidal term, the effect of our separation technique is slightly hidden by the toroidal part. Therefore, in this section we directly study at the separation of just the poloidal energy and just the potential energy in a wave and eddy part.

Figure 4.7 shows the ratio of poloidal energy of waves ($i = w$) and eddies ($i = e$) over the total poloidal energy $E_u^{p,i}/E_u^{p,T} =< \hat{\mathbf{u}}^{p,i} \cdot \mathbf{e_P}, \hat{\mathbf{u}}^{p,i} \cdot \mathbf{e_P} > / < \hat{\mathbf{u}}^{p,T} \cdot \mathbf{e_P}, \hat{\mathbf{u}}^{p,T} \cdot \mathbf{e_P} >$ as well as the ratio of potential energy of waves ($i = w$) and eddies ($i = e$) over the total potential energy $E_b^i/E_b^T =< \hat{b}^i, \hat{b}^i > / < \hat{b}^T, \hat{b}^T >$ against the buoyancy Reynolds number (figure 4.7a) and against the Froude number (figure 4.7b).

First, we observe that the distribution in potential and poloidal energy of waves and eddies is exactly the same. At the same Re_b, we observe that for a higher Froude number, the ratio of wave energy decreases and the ratio of eddy energy increases. For a constant Fr, surprisingly the ratio of waves slightly increases with Re_b and the ratio of eddies decreases slightly as well (by a few percent). We could say that the distribution of energy in the poloidal and potential energy between waves and eddies is strongly dependent on the Fr number. This underline the observation done in figure 4.6, and

	Wave		Eddy	
Term	velocity	buoyancy	velocity	buoyancy
Riley's decomposition	u^p	b	u^t	$\times$
4D decomposition	$u^{p,w}$	b^w	$u^t + u^{p,e}$	b^e

TABLE 4.2: Difference in velocity and buoyancy components for the Riley's decomposition [119] and our 4D decomposition

shows that the increase in eddy energy when Re_b decreases is due to the increase of toroidal energy in the flow, and not an increase of poloidal eddy energy.

4.3.2 Energy spectra against k

In the next section, we analyse the energy spectrum. While the result in the DNS with 256^3 points are available, we prefer to only consider the simulation with 512^3 points because the scaling of the energy spectrum is clearer with more points.

4.3.2.1 Riley's decomposition vs 4D decomposition

First, we remind the reader that the Riley's decomposition sets the wave part as the full poloidal terms and the eddy part as the full toroidal term. On the contrary, our decomposition (see section 3.1.2) sets the wave part as only a part of the poloidal term (around the dispersion relation) and the eddy part as the sum of the full toroidal term and a poloidal part (away from the dispersion relation). In Riley's decomposition the kinetic wave energy is E_u^p and the kinetic eddy energy is E_u^t whereas in our decomposition the kinetic wave energy is $E_u^{p,w}$ and the kinetic eddy energy is $E_u^t + E_u^{p,e}$. These differences are sum up in table 4.2.

We can observe the added value of our decomposition against the Riley's decomposition in figure 4.8. We observed that the Riley's decomposition is very similar to our decomposition at low wavenumber k which is expected because the sweeping effect is weak at low wavenumber as it is proportional to the wavenumber k. At large wavenumber k we observe that the kinetic energy for eddies in figure 4.8a is slightly underestimated with the Riley's decomposition. For the kinetic energy of waves in figure 4.8b the kinetic energy of waves is clearly different in the Riley's decomposition than in our decomposition. This can be understood as our eddy part is the sum of the full toroidal part and slight portion of the poloidal part of the flow. As a result adding a part of the poloidal component does not change a lot the overall energy as it is hidden

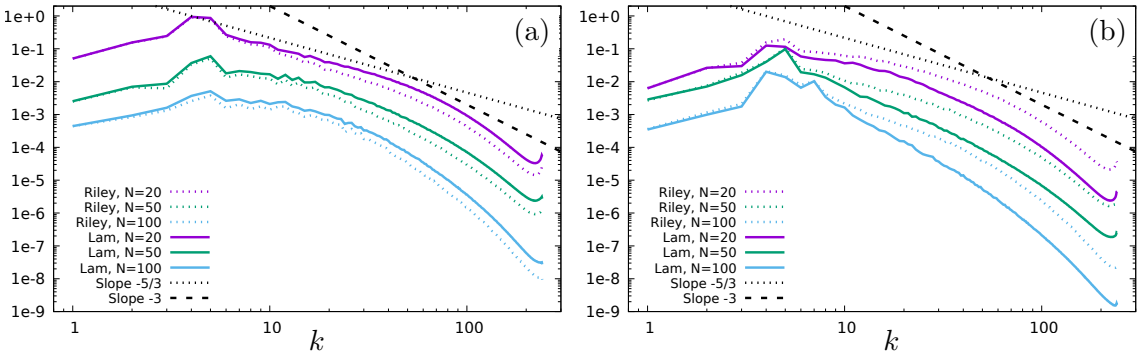

FIGURE 4.8: Kinetic energy spectra difference between the Riley's decomposition and our decomposition (named Lam in the legend) for (a) toroidal and eddy. (b) poloidal and wave. Numerical simulations with the different Brunt-Väisälä frequency are shifted by a power of 10 for clarity.

by the toroidal energy. On the contrary the wave kinetic energy is solely composed of poloidal energy and when this poloidal energy is separated in two parts (*i.e.* an eddy and wave part), it is more visible that the waves lose energy.

Therefore the study of the typical scaling in the energy spectra for IGW and eddies is different depending on the separation technique used. We expect different results of energy spectra if only the Riley's decomposition is used as in Kimura and Herring [69] or if our decomposition is used. Our separation technique takes into account both the spatial and spatial/temporal properties of waves. We expect it to be more precise than Riley's decomposition as Riley's decomposition solely takes into account the spatial properties of waves. Compared to Riley's decomposition, our decomposition increases the scaling of the eddy energy spectrum as it adds energy to it when k increases. On the contrary, the scaling of the wave energy spectrum decreases as we remove some energy in it when k increases.

4.3.2.2 IGW and eddy energy spectra

The energy spectra for the wave part and eddy part of our decomposition is visible in figure 4.9 against the wavenumber k.

The eddy part of the energy spectrum seems to follow a $k^{-5/3}$ scaling for both the kinetic energy and potential energy and for all numerical simulations (see figures 4.9a and 4.9c). If one is only interested in the poloidal component of the kinetic energy spectra, one can look directly at the potential energy spectra. Indeed the potential and poloidal terms are linked, and we expect the eddy part of these two to be very similar.

The wave part of the energy spectrum is exactly the same for the kinetic energy spectra (figure 4.9b) as for the potential energy spectra. This is expected because the poloidal component strongly interacts with the potential component. It seems that the wave part of the flow follows a k^{-3} scaling for $N > 50$. For highly turbulent flow ($N \leq 30$), the scaling is much lower, possibly even lower than the $-5/3$ Kolmogorov-like slope.

In all plots of figure 4.9, we observe a decline in energy at large wavenumber when the stratification increases. This comes from the smallest scale k_η which decreases slightly when our stratification increases.

The result that we obtained are very similar to the atmospheric measurements done in Nastrom and Gage [109]. In this article they observed the kinetic energy spectrum near the tropopause and found an energy spectrum close to k^{-3} at large scale and an energy spectrum close to $k^{-5/3}$ at small scale. This is exactly what we could obtain. At large scale, IGW energy spectrum dominates and are close to a k^{-3} scaling and at small scale eddies dominate with a scaling close to $k^{-5/3}$. In numerical simulations done in Kimura and Herring [69], they found that, at large stratification, the total kinetic energy spectrum was close to a k^{-3} scaling and, at small stratification, the total kinetic energy spectrum is close to $k^{-5/3}$. This is again an outcome that shares similarities with our results. At large stratification, we encounter mostly IGW with a scaling close to k^{-3} whereas at small stratification we face both IGW and eddies with a scaling close to $k^{-5/3}$.

4.3.3 Energy spectra against k_z

The stratification creates an asymmetry in the flow. Vertical components are strongly influenced by the variation of the stratification whereas the horizontal components are not subject to the stratification. This means that the energy spectra against a 3D direction (*i.e.* the wavenumber k) is probably not the best parameter to observe energy spectra. Instead, we can use the vertical k_z and horizontal k_h wavenumber which takes into account the variability of the flow in the vertical and horizontal directions.

In Figure 4.10 are plotted the kinetic and potential energy spectra of eddies and waves against the vertical wavenumber k_z. In Figure 4.10a and c, it is difficult to find a typical scaling for the eddy energy. On the contrary, the scaling for the wave part in figures 4.10b and d tends to be close to k^{-3} at large stratification $N \geq 50$ or when $Re_b < 2$. This can be nuanced for large stratification at $N = 200$ and $N = 600$ because the dissipative scale is at a smaller wavenumber and the inertial scale where the scaling is visible is very

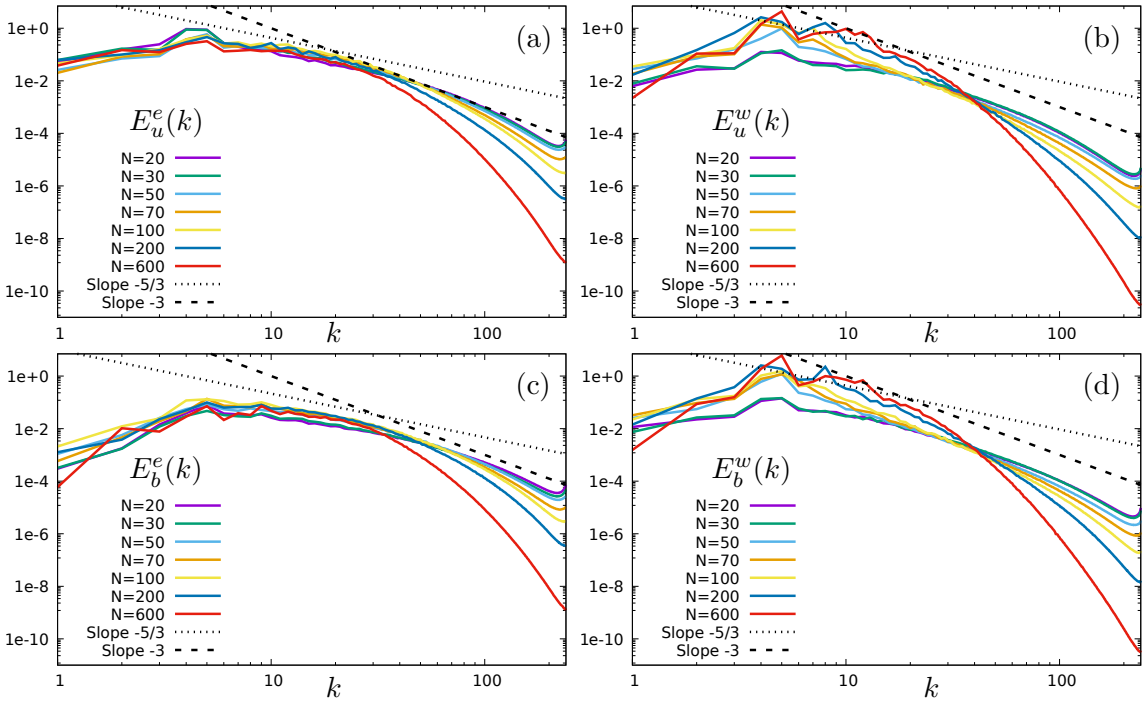

FIGURE 4.9: Kinetic (first row) and potential (second row) energy spectra for for numerical simulations with 512^3 points shown in table 4.1 against wavenumber k for (a,c) eddies. (b,d) waves. Typical slopes are placed for reference.

small. For small stratification ($N \leq 30$), we do not observe any typical scaling. The wave energy at low stratification seems very close to the eddy energy.

This result can be compared with other works where Brethouwer et al. [19] found a potential energy spectrum with a k_z^{-3} scaling for $Re_b > 1$ and no inertial scaling for $Re_b < 1$. Similarly, Maffioli [89] found a k_z^{-3} scaling in stratified turbulence for a large scale horizontal flow (by selecting only flow components with a wavenumber lower than a certain value). This is an ingenious way to select mostly waves as the figure 4.9 shows that IGW dominate at small scales. However, this separation of scale is not done in our paper. On the contrary, Kimura and Herring [69] found two different scalings in their poloidal energy spectrum: a k_z^{-2} scaling for flows at small stratification and a k_z^{-3} scaling for flows with a large stratification. From the new perspective of our decomposition we can say that when a scaling close to k_z^{-3} is observed, it means that IGW are dominating the flow for small Re_b. On the contrary, when a different scaling is observed, it means that the eddy energy spectrum modifies the overall energy spectrum (or the poloidal energy spectrum for Kimura and Herring [69]).

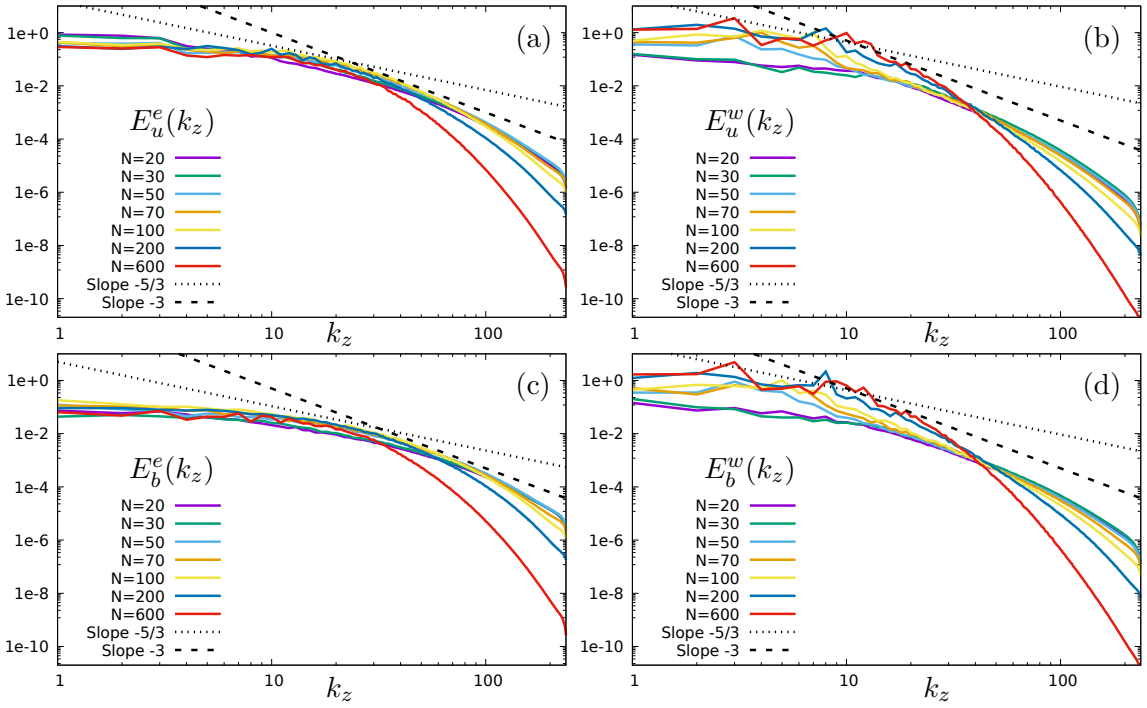

FIGURE 4.10: Kinetic (first row) and potential (second row) energy spectra for numerical simulations with 512^3 points shown in table 4.1 against the vertical wavenumber k_z for (a,c) eddies. (b,d) waves. Typical slopes are placed for reference.

4.3.3.1 Energy spectra of the VSHF

Figure 4.11 shows the energy spectrum of the VSHF from different numerical simulation with varying Brunt-Väisälä frequencies. We observe that at large scale ($k < 10$), the energy is high and constant. For smaller scale ($k > 10$) the energy of the VSHF decreases rapidly, following a scaling close to k^{-7}. We do not know why this scaling arises. Due to the very steep energy spectrum of the VSHF, a different fit could have been made in the form of a stretched exponential as shown in Verma et al. [143] (but not done here). As a viscous effect is added to the VSHF, a different added viscosity value of α could change the energy spectrum of the VSHF. Yet, this shows that the VSHF is large scale and is composed of a multitude of wavenumber k_z. Note that the energy spectrum of the VSHF is exactly the same against the wavenumber k and k_z as the horizontal wavenumber is null $k_h = 0$.

4.3.4 Energy spectra against k_h

Figure 4.12 shows the kinetic and potential energy spectra of eddies and waves against the horizontal wavenumber k_h.

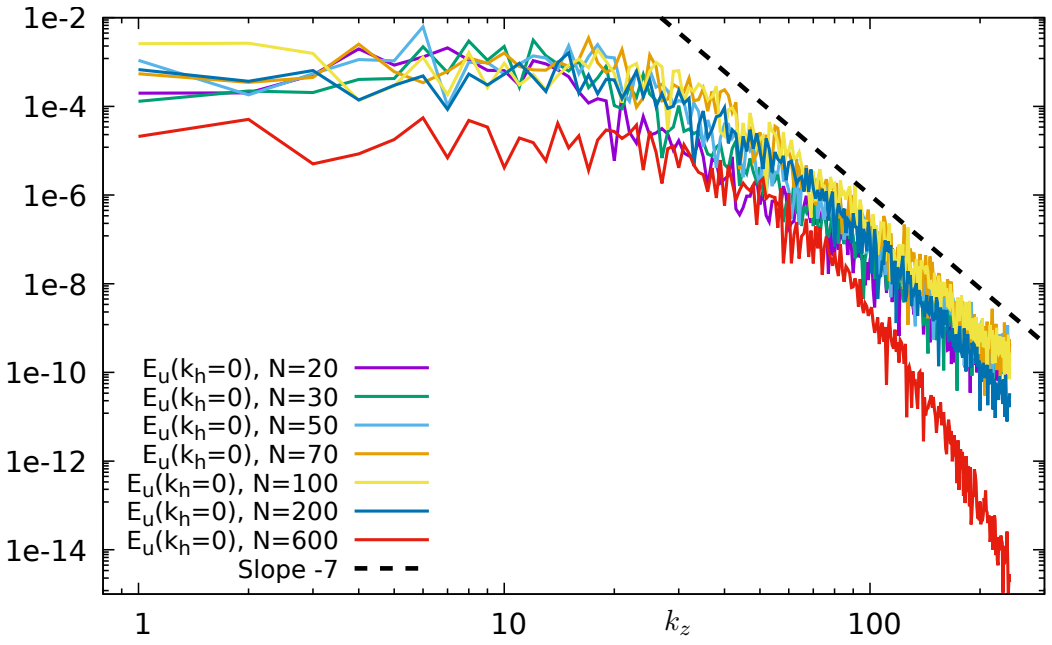

FIGURE 4.11: Energy spectrum of the VSHF for numerical simulations with 512^3 points shown in table 4.1 against the vertical wavenumber k_z.

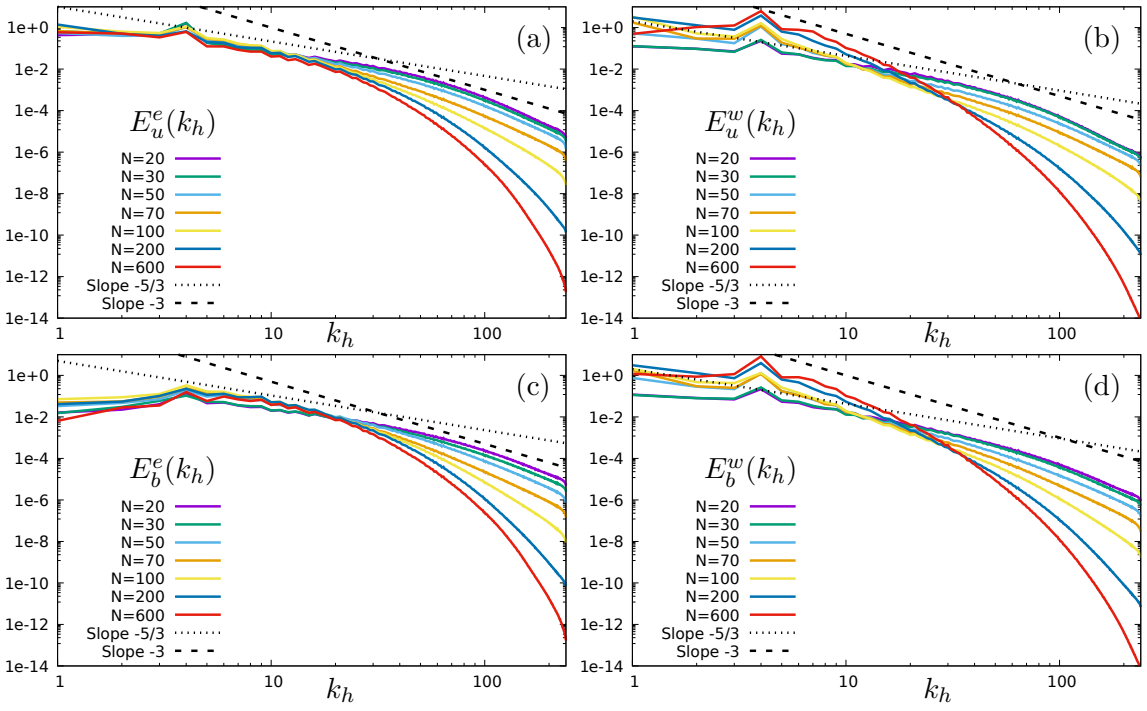

FIGURE 4.12: Kinetic (first row) and potential (second row) energy spectra for numerical simulations with 512^3 points shown in table 4.1 against the horizontal wavenumber k_h for (a,c) eddies. (b,d) waves. Typical slopes are placed for reference.

This time, the eddy energy is very well adapted to a scaling close to $k_h^{-5/3}$ for all stratification strengths. For the wave energy at large stratification ($N \geq 50$), the waves follow a k_h^{-3} scaling, whereas at smaller stratification ($N \leq 30$), the wave energy seems to follow a scaling similar to the eddy energy, a $k_h^{-5/3}$ scaling.

This result can be compared with the numerical simulation done in Lindborg [84]. In this article, Lindborg found a potential and kinetic energy spectrum of scaling $k_h^{-5/3}$ especially for low Froude number ($Fr \sim 10^{-3}$) with a box larger in the horizontal direction than in the vertical direction. Similarly, Brethouwer et al. [19] found a kinetic and potential energy spectrum to be close to $k_h^{-5/3}$ when the Froude number ($Fr \sim 0.001$) and buoyancy Reynolds number ($Re_b \sim 10$) is higher. When Fr and Re_b decrease, they found a steeper slope for the kinetic and potential energy spectrum. Furthermore, they analysed the energy spectrum with a constant $Re_b = 9$ and by varying the Froude and Reynolds number and found that the kinetic and potential energy spectrum scaling was constant at $k_h^{-5/3}$. Comparing these results with our data, we could say that the observation done by Brethouwer et al. [19] and Lindborg [84] were done in cases with a lot of eddies ($Re_b \gg 1$) and where IGW have a horizontal energy spectrum close to $k_h^{-5/3}$.

The Riley's decomposition was done in [69]. They show that the toroidal energy spectrum against the horizontal wavenumber have two scalings: a k_h^{-3} scaling at small horizontal wavenumber and a $k_h^{-5/3}$ scaling at higher horizontal wavenumber. It is possible that, if our decomposition were used in their DNS, the added poloidal term to the toroidal part would modify the scaling of the eddy energy spectrum to be only close to a $k_h^{-5/3}$. For the poloidal energy spectrum against the horizontal wavenumber in Kimura and Herring [69], they found that the energy spectrum was close to a k_h^{-2} scaling for high stratification and close to a $k_h^{-5/3}$ for high stratification. Again, if our decomposition were used in their DNS, the slope of the wave part would be increased as we take more and more poloidal terms as k_h increases to transfer to the eddy part. It is possible that if they had used our decomposition, they could find a slightly higher slope for high stratification DNS obtaining similar results than us.

In conclusion the eddy energy spectrum can be approximated by a slope of $-5/3$ for the wavenumber k and horizontal wavenumber k_h. The wave energy spectrum can be approximated to a -3 slope for all types of wavenumber (k, k_h and k_z) at large stratification $N \geq 50$. For lower stratification $N \leq 30$ the result seems closer to a $-5/3$ slope. This sudden change in the wave energy slope might come from two factors. The physic of the waves might be altered by eddies at low stratification or enough eddies

remain in the wave part of the flow to influence the result of the wave energy spectra at low stratification.

While our analysis focuses only on the energy spectrum against the spatial wavenumber spectrum, other works consider the energy spectrum against the angular frequency ω. For instance, this was done in an empirical model by Garrett and Munk [53, 54] for internal gravity waves. Numerous works tried to further improve this model, as done in Levine [81], Lvov and Tabak [86]. An example of an energy spectrum against the angular frequency can be found in Polzin and Lvov [118].

4.4 Balance of energy and flux

In homogeneous and isotropic turbulence the Lin equation is useful to assess the evolution of energy through time t and wavenumber k. It is written as:

$$\partial_t E(k,t) = T(k,t) - 2\nu k^2 E(k,t) \tag{4.11}$$

where $T(k,t)$ correspond to the spectral transfer term [120] and $E(k,t)$ is the kinetic energy. The Lin equation is also the equivalent of the Kármán Horwarth equation [37] in the Fourier space. In this section we will use our new decomposition to derive an equation similar to the above Lin equation for waves and eddies.

4.4.1 Derivation of the Lin type equation

The evolution of total energy in stratified turbulence is driven by the flux of energy in equation $dE^T/dt = P - \varepsilon_T$ where the total dissipation $\varepsilon_T = \varepsilon_u + \varepsilon_b$ with $\varepsilon_u = \nu < k^2\hat{\mathbf{u}}, \hat{\mathbf{u}} >$ and $\varepsilon_b = \mathcal{X}N^{-2} < k^2\hat{b}, \hat{b} >$. During the statistically stationary regime, the total energy stored is constant, so that $dE^T/dt = 0$ and, for all stratification intensities, the output flux balances the input flux as $P \simeq \varepsilon_T$. The wave and eddy decomposition now permits adressing the question how do wave- and eddy-related fluxes evolve with stratification?

We compute the Lin type equation — *i.e.* the balance equation in spectral space — for the waves and the eddies in a stratified flow as done in Verma [142]. To do so, we start by taking the Fourier transform in space of the stratified part of equations (2.17):

$$\begin{aligned} \partial_t \hat{\mathbf{u}}(\mathbf{k},t) &= -\widehat{\boldsymbol{\omega} \times \mathbf{u}}(\mathbf{k},t) - \mathrm{i}\mathbf{k}p(\mathbf{k},t) - \nu k^2 \hat{\mathbf{u}}(\mathbf{k},t) + \hat{b}(\mathbf{k},t)\mathbf{z} + \hat{\mathbf{F}}_{\mathbf{u}}(\mathbf{k},t) \\ \partial_t \hat{b}(\mathbf{k},t) &= -\widehat{\mathbf{u} \cdot \boldsymbol{\nabla} b}(\mathbf{k},t) - \chi k^2 \hat{b}(\mathbf{k},t) - N^2 \hat{u}_z(\mathbf{k},t) \end{aligned} \tag{4.12}$$

where $\widehat{\boldsymbol{\omega} \times \mathbf{u}}(\mathbf{k},t)$ and $\widehat{\mathbf{u} \cdot \boldsymbol{\nabla} b}(\mathbf{k},t)$ are the 3D Fourier transform in space of $\boldsymbol{\omega} \times \mathbf{u}(\mathbf{x},t)$ and $\mathbf{u} \cdot \boldsymbol{\nabla} b(\mathbf{x},t)$.

Multiplying equations (4.12) by $\dfrac{\overline{\hat{\mathbf{u}}^l(\mathbf{k},t)}}{2}$ for the kinetic part and by $\dfrac{\overline{\hat{b}^l(\mathbf{k},t)}}{2N^2}$ for the potential part and adding the resultant equation with its complex conjuguate, we obtain:

$$\begin{aligned}
\partial_t \operatorname{Re}\left\{\frac{\hat{\mathbf{u}} \cdot \overline{\hat{\mathbf{u}}^l}}{2}\right\}(\mathbf{k},t) = &-\operatorname{Re}\left\{\widehat{\boldsymbol{\omega} \times \mathbf{u}} \cdot \overline{\hat{\mathbf{u}}^l}\right\}(\mathbf{k},t) - \nu k^2 \operatorname{Re}\left\{\tfrac{\hat{\mathbf{u}} \cdot \overline{\hat{\mathbf{u}}^l}}{2}\right\}(\mathbf{k},t) + \operatorname{Re}\left\{\overline{\hat{u}_z^l}\hat{b}\right\}(\mathbf{k},t) \\
&+ \operatorname{Re}\left\{\hat{\mathbf{F}}_{\mathbf{u}} \cdot \overline{\hat{\mathbf{u}}^l}\right\}(\mathbf{k},t) \\
\partial_t \operatorname{Re}\left\{\frac{1}{2N^2}\hat{b}\overline{\hat{b}^l}\right\}(\mathbf{k},t) = &-\tfrac{1}{N^2}\operatorname{Re}\left\{\widehat{\mathbf{u} \cdot \boldsymbol{\nabla} b} \cdot \overline{\hat{b}^l}\right\}(\mathbf{k},t) - \chi k^2 \operatorname{Re}\left\{\tfrac{1}{N^2}\hat{b}\overline{\hat{b}^l}\right\}(\mathbf{k},t) \\
&- \operatorname{Re}\left\{\hat{u}_z\overline{\hat{b}^l}\right\}(\mathbf{k},t)
\end{aligned} \tag{4.13}$$

where l stands for w for the wave part or e for the eddy part.

As the wave and eddies components are disjoint in the spatial and time Fourier domain, the average on the large period T_0 is $[\hat{\mathbf{u}}^l, \hat{\mathbf{u}}] = [\hat{\mathbf{u}}^l, \hat{\mathbf{u}}^w + \hat{\mathbf{u}}^e + \hat{\mathbf{u}}^s] = [\hat{\mathbf{u}}^l, \hat{\mathbf{u}}^l]$ where $[,]$ is defined in equation (3.9). Yet, as $\hat{u}^s \ll \hat{u}^w$ and $\hat{u}^s \ll \hat{u}^e$, the VSHF velocity field $\hat{u}^s$ is not taken into account. This is also the case for the buoyancy field $[\hat{b}^l, \hat{b}] = [\hat{b}^l, \hat{b}^l]$ and the interaction between the velocity field and the buoyancy field $[\hat{u}_z, \hat{b}^l] = [\hat{u}_z^l, \hat{b}^l]$ (or $[\hat{b}, \hat{u}_z^l] = [\hat{b}^l, \hat{u}_z^l]$.

Thus, taking the average over the period T_0 of equations (4.13), summing all wavevectors $\mathbf{k}$ on a sphere of radius $K = |\mathbf{k}|$, decomposing the non-linear term in their wave or eddy part and as the wave and eddy part of the flow are close to stationarity (*i.e.* $d/dt \sim 0$), we get:

$$\begin{aligned}
0 &= t^l_{u,ww}(K) + t^l_{u,we}(K) + t^l_{u,ew}(K) + t^l_{u,ee}(K) - 2\nu K^2 e^l_u(K) + t^l_{u\to b,l}(K) + P^l(K) \\
0 &= t^l_{b,ww}(K) + t^l_{b,we}(K) + t^l_{b,ew}(K) + t^l_{b,ee}(K) - 2\chi K^2 e^l_u(K) - t^l_{u\to b,l}(K).
\end{aligned} \tag{4.14}$$

To define all the terms in equation (4.14), we use the operator $<>_K$ defined at the end of section 3.1.3.1. The kinetic energy is $e^l_u(K) =< \hat{\mathbf{u}}, \hat{\mathbf{u}}^l >_K$, the potential energy is $e^l_b(K) =< \hat{b}, \hat{b}^l >_K$, the kinetic transfers are $t^l_{u,ij}(K) = - < \widehat{\boldsymbol{\omega}^i \times \mathbf{u}^j}, \hat{\mathbf{u}}^l >_K$, the potential transfers are $t^l_{b,ij}(k) = -N^{-2} < \widehat{\mathbf{u}^i \cdot \boldsymbol{\nabla} b^j}, \hat{b}^l >_K$, the buoyancy flux are $t^l_{u\to b,l}(K) =< \hat{b}, \hat{u}^l_z >_K =< \hat{u}_z, \hat{b}^l >_K$, and the forcing is $p^l(K) =< \mathbf{F}_{\mathbf{u}}, \hat{\mathbf{u}}^l >_K$. The non-linear terms produce four different possibilities for every l part as the terms $\boldsymbol{\omega} \times \mathbf{u} = \sum_{i,j=w,e} \boldsymbol{\omega}^i \times \mathbf{u}^j$ and $\mathbf{u} \cdot \boldsymbol{\nabla} b = \sum_{i,j=w,e} \mathbf{u}^i \cdot \boldsymbol{\nabla} b^j$ have their two components decomposed in a wave or eddy part.

It can be shown as in Verma [142] that the potential transfer is also $t^l_{b,ij}(K) = \frac{1}{T}\int_T \mathrm{Im}\left\{ \sum_{\substack{\mathbf{k}\\|\mathbf{k}|=K}} \sum_{\mathbf{p}+\mathbf{q}=\mathbf{k}} (\mathbf{k}\cdot\mathbf{u}^i(\mathbf{q}))(b^j(\mathbf{p})\overline{b^l(\mathbf{k})}) \right\}$. For a triadic interaction of only waves elements $(i,j,l) = (w,w,w)$ the frequencies of the waves elements are $(\omega_c(\mathbf{q}), \omega_c(\mathbf{p}), \omega_c(\mathbf{k}))$ where ω_c is the dispersion relation modified by the sweeping effect and defined in equation (2.67). Hence, the particular transfer $t^w_{b,ww}(K)$ corresponds to the triad interaction where for any wavevector $\mathbf{p}$, $\mathbf{q}$ and $\mathbf{k}$ we obtain a spatial resonance $\mathbf{p}+\mathbf{q}=\mathbf{k}$ and a temporal resonance $\omega_c(\mathbf{p}) + \omega_c(\mathbf{q}) = \omega_c(\mathbf{k})$ [133] because $< e^{\mathrm{i}\omega_c(\mathbf{q})} e^{\mathrm{i}\omega_c(\mathbf{p})}, e^{\mathrm{i}\omega_c(\mathbf{k})} >= 1$ if $\omega_c(\mathbf{p}) + \omega_c(\mathbf{q}) = \omega_c(\mathbf{k})$. Hence, the transfers $t^w_{u,ww}$ and $t^w_{b,ww}$ are wave turbulence transfers.

When considering other types of transfer such as the interaction with only eddies, the spatial resonance ($\mathbf{p}+\mathbf{q}=\mathbf{k}$) is still verified, but the temporal resonance is modified to take into account all possible frequencies ($\omega(\mathbf{p}) + \omega(\mathbf{q}) = \omega(\mathbf{k})$). Here, ω is a different frequency than the dispersion relation of the waves. The same observations can be made for other types of potential transfer $t^l_{b,ij}$ and the kinetic transfer $t^l_{u,ij}(K)$.

4.4.2 Balance of energy

Summing over all wavenumbers K in equations (4.14), we obtain the equation of balance of global energy:

$$\begin{aligned} 0 &= T^l_{u,ww} + T^l_{u,we} + T^l_{u,ew} + T^l_{u,ee} - \varepsilon^l_u + T^l_{u\to b,l} + P^l \\ 0 &= T^l_{b,ww} + T^l_{b,we} + T^l_{b,ew} + T^l_{b,ee} - \varepsilon^l_b - T^l_{u\to b,l} \end{aligned} \tag{4.15}$$

where the kinetic dissipation is $\varepsilon^l_u = \nu < k^2\hat{\mathbf{u}}^l, \hat{\mathbf{u}}^l >$ and the potential dissipation is $\varepsilon^l_b = \mathcal{X}N^{-2} < k^2\hat{b}^l, \hat{b}^l >$. The kinetic transfer is $T^l_{u,ij} = - < \widehat{\boldsymbol{\omega}^i \times \mathbf{u}^j}, \hat{\mathbf{u}}^l >$ and the potential transfer is $T^l_{b,ij} = -N^{-2} < \widehat{\mathbf{u}^i \cdot \nabla b^j}, \hat{b}^l >$. The transfer from the kinetic to potential part is $T^l_{u\to b,l} =< u^l_z, b^l >$. The total injected power is $P = P^w + P^e = 10$ and for the l part it is $P^l =< \hat{\mathbf{F}}_\mathbf{u}, \hat{\mathbf{u}}^l >$.

Summing the two equations in (4.15), we compute the overall balance equation for waves and eddies:

$$\begin{aligned} 0 &= T^w_{ee} + T^w_{we} - \varepsilon^w_T + P^w \\ 0 &= T^e_{ww} + T^e_{ew} - \varepsilon^e_T + P^e \end{aligned} \tag{4.16}$$

where $\varepsilon^l_T = \varepsilon^l_u + \varepsilon^l_b$ is the total dissipation rate for each part $l = w, e$ and the exchange term is $T^l_{ij} = T^l_{u,ij} + T^l_{b,ij} = - < \widehat{\boldsymbol{\omega}^i \times \mathbf{u}^j}, \hat{\mathbf{u}}^l > -N^{-2} < \widehat{\mathbf{u}^i \cdot \nabla b^j}, \hat{b}^l >$. The transfers $T^l_{il} = 0$ disappeared because these transfers are only between the same l components.

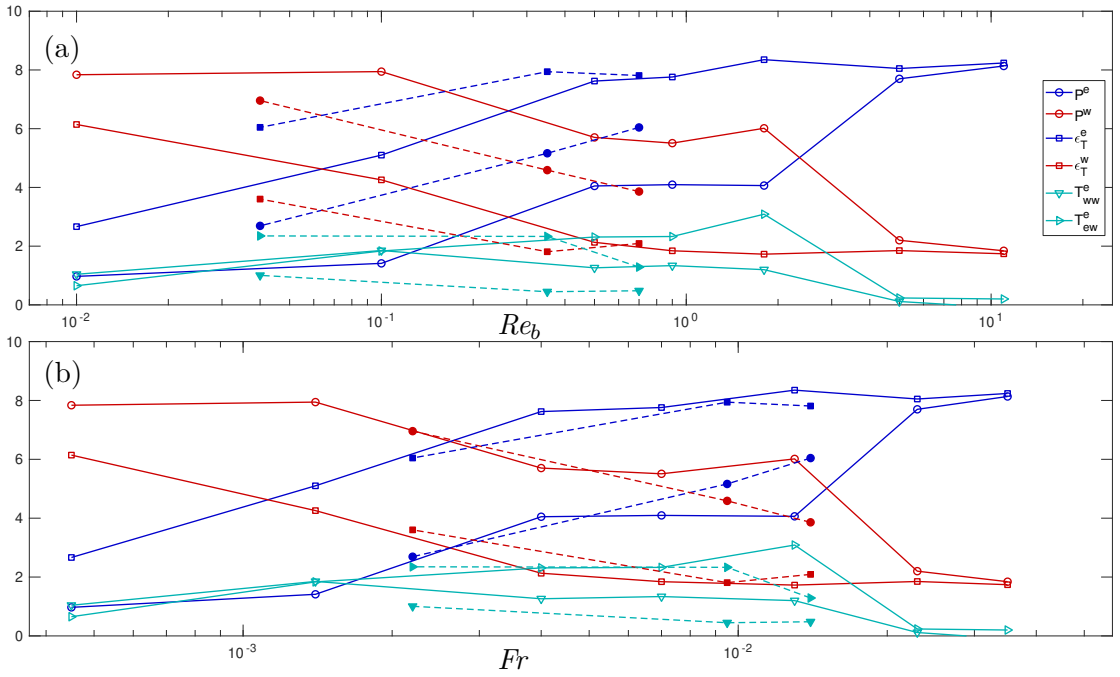

FIGURE 4.13: Evolution with (a) Re_b, and (b) Fr, of the contributions of forcing P^l, dissipation ε^l and transfer T^e_{iw} from waves to eddies. The transfer from eddies to waves is easily computed as the inverse of the transfer from waves to eddies $T^w_{ie} = -T^e_{iw}$. Numerical simulations with 512^3 points correspond to open symbols and solid lines, numerical simulations with 256^3 points to filled symbols and dotted lines.

They are akin to more classical transfer and are shown later in section 4.7. It pumps and gives the same amount of energy to the l component, so it is a kind of cascade of energy.

In equations (4.16), one neglects the interactions T^l_{sj} of waves and eddies with VSHF because in our simulations, these terms are small compared to others (for $N = 100$, $T^l_{sj} \sim \mathcal{O}(10^{-7}T^l_{ij})$). As discussed by Verma [142], triadic transfers are such that $T^l_{ij} = -T^j_{il}$ so that $T^w_{we} = -T^e_{ww}$ and $T^e_{ew} = -T^w_{ee}$. The detailed proof for this equality is done in appendix B. T^l_{ij} is an energy exchange term between l and j parts, due to the interaction between the part j 'convected' by part i that exchanges energy with part l.

Thus, $T^j_{ij} = 0$ so that such terms are not net exchange terms, but are dynamically similar to convection terms, since they convey the modification of part j by part i that acts onto part j [142]. For instance, $T^e_{ee} = 0$ and $T^w_{ww} = 0$ are respectively similar to a classical non-linear transfer between eddies and to a non-linear transfer between waves. In the statistically stationary regime, $dE^{w,e}/dt = 0$ and the equilibrium of the fluxes is reached since all terms compensate one another.

Figures 4.13a and 4.13b show, for both resolutions, the evolution with Re_b and with Fr of the amount of the different terms in equation (4.16). Again, we can estimate the

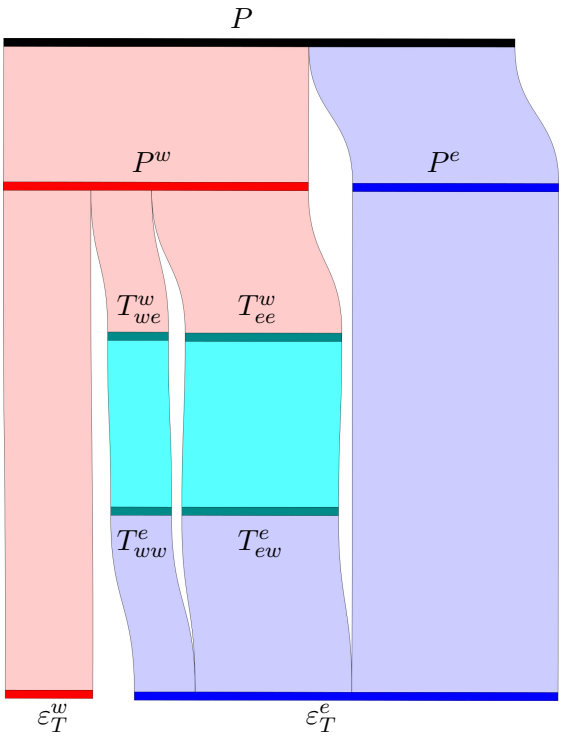

FIGURE 4.14: Sankey's diagram of energy flux at $Re_b = 1.8$ and $Fr = 0.013$ (see text).

evolution of these values either at fixed Re_b and weakly increasing Fr (from high to low resolution) or at fixed Fr and weakly decreasing Re_b (from high to low resolution). In order to facilitate physical interpretation, we show a corresponding flux diagram (a.k.a. Sankey's diagram) in figure 4.14 for $Re_b = 1.8$ and $Fr = 0.013$ to visualize quantitatively the energy flux from the injection P to the two dissipations ε^w_T and ε^e_T, either directly, or indirectly by wave/eddy exchange terms T^l_{ij}. Each band represents a component of the balance of energy, with a width proportional to the energy flux it involves. Red, blue and cyan respectively indicate the wave, eddy and exchange parts.

Figures 4.13a and 4.13b show that at $Re_b > Re_b^T \simeq 2$ and $Fr > Fr^T \simeq 0.02$, the input power for waves and eddies is in balance exclusively with the dissipation, *i.e.* $P^e \simeq \varepsilon^e_T$ and $P^w \simeq \varepsilon^w_T$ and there is no exchange between waves and eddies. This does not mean that there is no transfer between waves and eddies, it only means that, overall, no net transfer occurs, but a scale-by-scale transfer (a 'cascade') is still possible between them. Moreover, injected energy is mainly pumped by eddies since $P^e > P^w$. This changes completely when Re_b decreases or Fr decreases as $Re_b < Re_b^T$ or $Fr < Fr^T$. Indeed, in the most stratified case $Fr = 0.00045$ at very low $Re_b = 0.01$, the input power and dissipation are more important for the wave part than for the eddy part ($P^w > P^e$ and $\varepsilon^w_T > \varepsilon^e_T$) and the exchange terms T^w_{we} and T^w_{ee} remove energy from waves ($P^w > \varepsilon^w_T$) and redistribute it to eddies ($P^e < \varepsilon^e_T$). As Re_b increases and Fr increases close to the

transition $Re_b \sim Re_b^T$ and $Fr = Fr^T$, the dissipation associated with eddies gets larger ($\varepsilon_T^e > \varepsilon_T^w$) as expected but, surprisingly, the input power for waves remains large and there is a significant transfer from the wave part to the eddy part which amounts to a total up to 50% of the eddy dissipation. During this transition, the exchange between wave and eddy is dominant. Similarly, in Godeferd and Cambon [55], a lot of the energy appears to be pumped from the waves by the exchange term T_{we}^w. In this transition zone, at fixed Re_b, when Fr increases, as expected, the eddy part takes more importance and the evolution seems to be shifted to a lower Re_b^T.

Nevertheless, by comparing the numerical simulations with 512^3 points and 256^3 points, it appears that the transfer mostly depends on the Froude number, although its amplitude varies slightly between the two resolutions. Moreover, the way the forcing and the dissipation are distributed between waves and eddies seems relatively invariant against the Froude number.

These observations result in a global analysis of transfers between waves and eddies: the global exchange is zero for the exchange terms, *i.e.* $T_{ee}^e = T_{ww}^w = T_{ew}^w = T_{we}^e = 0$, but these terms are associated to 'cascades' and therefore influence indirectly the transfers between wave and eddies. For example, the global term $T_{ew}^w = 0$, meaning there is no global exchange, but there is still a scale-by-scale transfer between waves aided by an eddy that acts as a mediator [142].

4.4.3 Detailed analysis of the transfers between different parts

The analysis was done before without differentiating the potential and kinetic transfer as done in equation (4.16). Here we study the exchange of energy by separating the kinetic and potential transfer as done in equation (4.15). Figure 4.15 shows the potential $T_{b,ij}^l$ and kinetic $T_{u,ij}^l$ transfer from eddies to waves and inversely ($j \neq l$). As the transfer is simply a term of exchange of energy, its sum is zero and we have $T_{b,ij}^l = -T_{b,il}^j$ for the potential transfer and $T_{u,ij}^l = -T_{u,il}^j$ for the kinetic transfer.

We observe that the potential transfer in figures 4.15 b and d dominate the kinetic transfer in figures 4.15 a and c. In the potential transfer most of the energy is pumped from waves and give to eddies. On the contrary, in the kinetic transfer no clear trend can be observed and the transfers are very small except at large Re_b where the energy is pumped from eddies to be given to the waves. At constant Fr the amplitude of the potential transfer increases a lot as Re_b increases. The transfer seen from waves to eddies in the figure 4.13, where the kinetic and potential part are merged, is mostly due

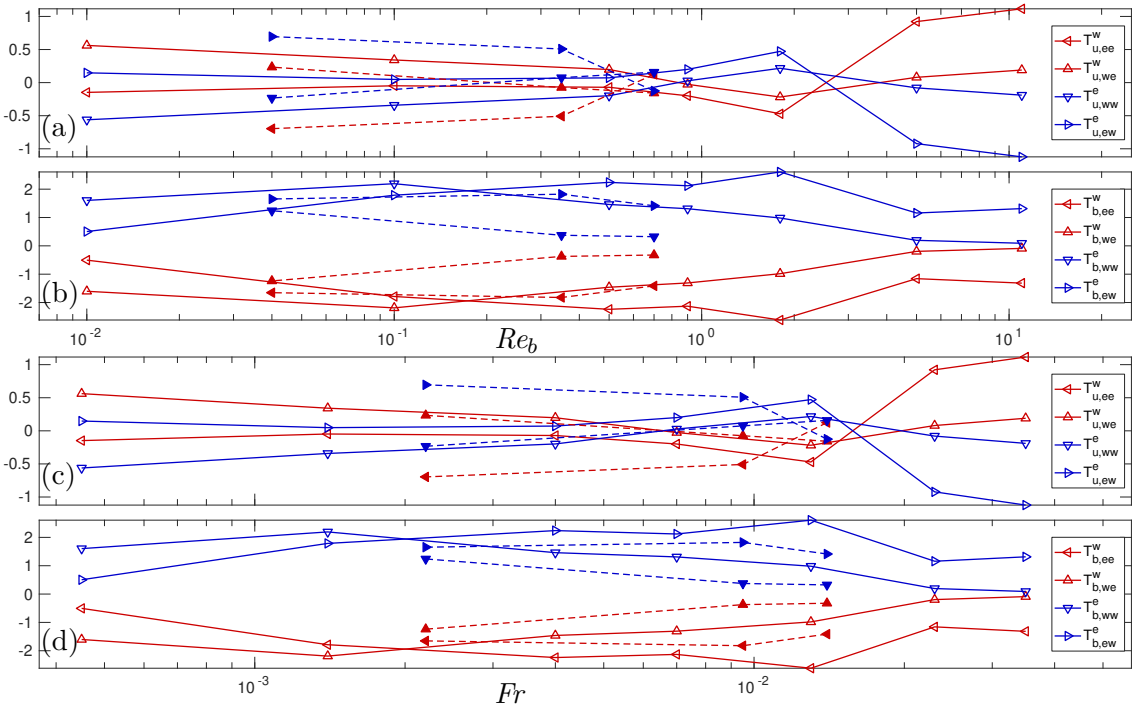

FIGURE 4.15: Evolution of the potential transfer of energy (b, d) $T^{+,l}_{b,ij}$ and of the kinetic transfer of energy (a, c) $T^{+,l}_{u,ij}$(with $i = w$ or $i = e$) from waves to eddies ($j = w$ and $l = e$) or from eddies to waves ($j = e$ and $l = w$) against (a, b) Re_b; (c, d) Fr. Numerical simulations with 512^3 points are shown with open symbols and solid lines, and numerical simulations with 256^3 points are shown with filled symbols and dotted lines.

to the potential transfer as the amplitude of the potential transfer is greater than the amplitude of the kinetic transfer.

4.5 Mixing

The above wave/eddy flow decomposition also permits to understand the contribution of IGW and eddies to mixing. The total mixing coefficient is defined by $\Gamma = \varepsilon_b/\varepsilon_u$ [117]. For oceanographic application, the eddy diffusity of density κ_ρ can be used for parameterizing the stratification mixing with equation $\kappa_\rho = \mathcal{X} Pr \Gamma Re_b$ [29]. In this formulation, it is possible that a highly efficient mixing at low Re_b lead to a smaller eddy diffusity of density than flows with a higher Re_b. Γ is also useful for calculating the vertical diffusivity of density used in the model proposed by Osborn [113]. Whereas Γ was approximated to a constant $\Gamma \simeq 0.2$ in the ocean where $Re_b \sim 100-1000$ [96], recent DNS in decaying stratified turbulence at resolution 512^3 [52] and forced stratified DNS at larger resolution [91], suggest a dependence of Γ with Fr and Re_b. On figure 4.16b, we reported these authors' values for Γ in a Froude range similar to ours, *i.e.* $Fr \ll 1$ and

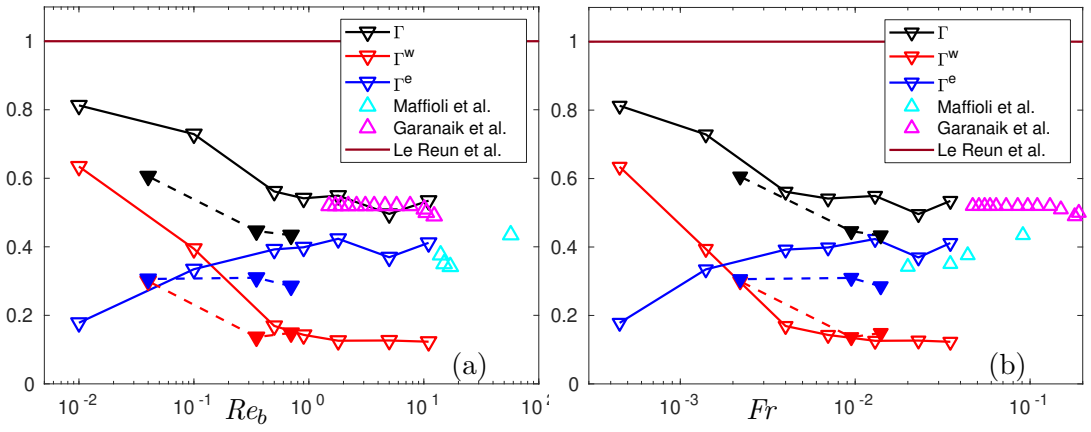

FIGURE 4.16: Mixing coefficients Γ, Γ^w, Γ^e compared with data from literature against (a) Re_b, and (b) Fr. Numerical simulations with 512^3 points are shown by open symbols and solid lines, and numerical simulations with 256^3 points with filled symbols and dotted lines.

associated with $Re_b \simeq 10-20$ (forced case) and $Re_b \simeq 1-10$ (decaying case). Moreover, in a wave regime of superposed low-amplitude IGW with weak nonlinear interactions, Le Reun et al. [76] find that $\Gamma = 1/Pr = 1$.

Our simulations explore the transition between these two regimes. In order to understand separately the effect of waves and eddies on mixing, we therefore separate the total mixing coefficient $\Gamma = \varepsilon_b/\varepsilon_u = \Gamma^w + \Gamma^e$ into mixing due to waves $\Gamma^w = \varepsilon_b^w/(\varepsilon_u^e + \varepsilon_u^w)$ and mixing due to eddies $\Gamma^e = \varepsilon_b^e/(\varepsilon_u^e + \varepsilon_u^w)$ by using $\varepsilon_u = \varepsilon_u^e + \varepsilon_u^w$ and $\varepsilon_b = \varepsilon_b^e + \varepsilon_b^w$. On figures 4.16a and 4.16b, the coefficients Γ, Γ^w, Γ^e are plotted versus Re_b and Fr respectively, and compared to the above-mentioned data. Our coefficient values seem to coincide better with a variation in Fr rather than with a variation in Re_b (as in the flux analysis discussed previously in section 4.4). For $Re_b \geq 1$ and $Fr \geq 10^{-2}$, we find a value $\Gamma \simeq 0.5$ similar to that in Garanaik and Venayagamoorthy [52] at similar resolution and slightly lower Froude number. Moreover, we observe that the wave mixing and eddy mixing reach a plateau, as expected, but the eddies mix more than waves since $\Gamma^e \simeq 0.4 \geq \Gamma^w \simeq 0.1$. Note that our decomposition considers as eddies, among others, the breaking of internal waves or overturning with vertical velocity. This could nuance the belief that overturning is the main source of mixing [60]. The global mixing coefficient found by Maffioli et al. [91] is close to our mixing coefficient by eddies Γ^e. As their DNS are done at a higher $Re_b \simeq 10-20$, it is possible that their flows contain mostly eddies, resulting in a mixing coefficient dependent only on mixing by eddies. When $Re_b \to 0$, the total mixing increases and tends to $\Gamma \simeq 1$ as expected by Le Reun et al. [76]. In this case, Γ^w increases a lot, whereas Γ^e decreases. Indeed, we expect at very low buoyancy Reynolds number that the waves dominate the flow and become the main factor of mixing. At fixed Fr, when Re_b decreases, the same physics is shifted

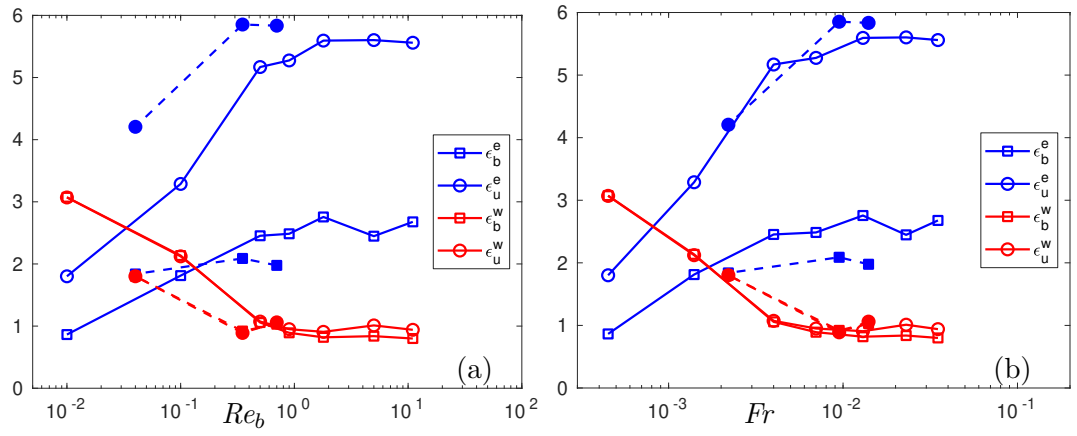

FIGURE 4.17: Kinetic and buoyancy dissipation for waves and eddies against (a) Re_b, and (b) Fr. Numerical simulations with 512^3 points are shown by open symbols and solid lines, and numerical simulations with 256^3 points with filled symbols and dotted lines.

to low Re_b but in a non-obvious way the plateau value seems to be constant for wave mixing $\Gamma^w \simeq 0.1$, while mixing by eddy seems to be weaker $\Gamma^e \simeq 0.3$. However, the mixing coefficient Γ can depend on the forcing used as explained in Howland et al. [65]. This implies that the eddy mixing coefficient and the wave mixing coefficient depend on the forcing used as well. In Howland et al. [65], when waves are forced, stronger values of Γ are obtained than when eddies are forced. We could expect similar behaviour in our results as our forcing forces mostly waves at $Re_b < 2$ and $Fr < 10^{-2}$ and mostly eddies otherwise. It would be interesting to modify the forcing to control the distribution between waves and eddies in each of our numerical simulations. This would allow us to assess its effect on our computation of the mixing coefficient of waves Γ^w and eddies Γ^e.

4.6 Dissipation

In order to better understand the physical phenomena underlying mixing and its modelling, an in-depth analysis of the different dissipation terms is necessary. Note that while kinetic and buoyancy energies are more related to large scales, the different dissipations are related to small scales. On Figures 4.16c and 4.16d, we plotted the different contributions to dissipation as functions of Re_b and Fr. Note that during statistically stationary regime, the constant forcing $P = 10$ and dissipation are in balance so that $P \simeq \varepsilon_u^e + \varepsilon_u^w + \varepsilon_b^e + \varepsilon_b^w$. First, as expected for IGW, the kinetic and potential dissipations of the waves are equal, *i.e.* $\varepsilon_b^w \sim \varepsilon_u^w$. Moreover, this confirms the idea proposed by Le Reun et al. [76] that $\Gamma = 1$ is always true for the IGW even if they are mixed with eddies. Secondly, the kinetic dissipation of eddies is greater than the potential dissipation of eddies *i.e.* $\varepsilon_u^e > \varepsilon_b^e$. Thirdly, all these values tend towards a plateau when Fr is

large and $Re_b \simeq 1$, with $\varepsilon_b^w \sim \varepsilon_u^w \sim \varepsilon_u^e/6$. In this regime, as all the statistics $\varepsilon_b^{w,e}$ and $\varepsilon_u^{w,e}$ involved reach a plateau, so does the mixing coefficient. Apparently, our coefficient values seem to coincide better with a variation in Fr rather than a variation in Re_b which shifts the evolution to a lower Re_b. At fixed Fr and decreasing Re_b, all dissipation terms remain unchanged except ε_b^e, which implies that the mixing Γ^e due to eddies decreases.

4.7 Scale by scale analysis of transfer

Whereas in the section 4.4, we were interested in the global exchange of energy from waves to eddies, in this section we will focus on the transfer between waves and eddies in the flow as well as the transfer between scales. Some focus will be done on the strength of the forward or backward cascade in the flow.

It was believed that in stratified flows, an inverse cascade due to a 2D phenomenon [49, 83] was occurring. Then, in numerical simulations done in Herring and Métais [64], only a weak inverse cascade was obtained. Furthermore, the transfer between waves (poloidal mode) and vortical mode (toroidal mode) was also calculated in Herring and Métais [64] using Riley's decomposition. In numerical simulations of stratified flows with variable rotation rate, Métais et al. [97] found that no inverse cascade was occurring when $2\Omega \ll N$ but an inverse cascade occurred when $2\Omega \sim N$. Moreover, a forward cascade of IGW was hypothesized in Gage [49], and the famous poem of Richardson was adapted to IGW to become: "*big waves have little waves that feed on deformation, and little waves have lesser waves to turbulent dissipation (in the eddy sense)*". In his paper, Dewan [39] exposed the idea of a forward cascade of IGW similarly to the classical cascade of eddies in isotropic turbulence. Then, in more recent numerical simulation done in Lindborg [84] and Lindborg and Brethouwer [85], a forward cascade is observed in stratified flows for both the potential and kinetic energy flux. Hence, numerous works tried to tackle the presence of inverse or direct cascade.

From the separation of waves and eddies it is possible to understand how the transfer between them occurs and which interaction is responsible for a forward or a backward cascade. In our case, there is a very large number of different possible transfers. For the potential and kinetic transfers, four interactions ($w + w$, $w + e$, $e + w$ and $e + e$) can occur which can lead to a transfer of energy between the wave or eddy. This means that in total, the kinetic and potential transfer possess each eight possible transfers. If the transfer between the kinetic to potential energy is also taken into account as well, it adds four other transfers. In total there are 20 different transfers that could occur in our numerical simulation, and yet, here we neglected the transfer by the VSHF. If the

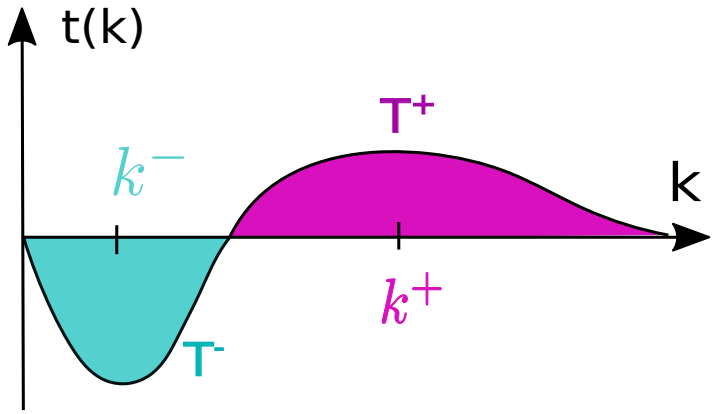

FIGURE 4.18: An idealized transfer reduced in four variables T^+, T^-, k^+, k^-

VSHF was taken into account, this could lead to an impressive 27 different transfers for the kinetic and for the potential transfers and still four possible transfers for the kinetic to potential transfer. In total, this would lead to an astonishing number of 58 possible transfers (27 kinetic transfers +27 potential transfers +4 kinetic to potential transfers). Furthermore, analysing each of those transfers against the wavenumber (as it is usually done [4]) is quite complex as there are lot of fluctuations. We characterize all the terms of the cascade of energy (see equations (4.15)) by analyzing for each terms four different values:

- $T^{+,l}_{a,ij} = \sum_{k,\, t^l_{a,ij}(k)>0} t^l_{a,ij}(k)$, the total value of transfer given to l by the interaction between i and j,
- $T^{-,l}_{a,ij} = \sum_{k,\, t^l_{a,ij}(k)<0} t^l_{a,ij}(k)$, the total value of transfer pumped from l by the interaction between i and j,
- $k^{+,l}_{a,ij} = \sum_{k,\, t^l_{a,ij}(k)>0} \frac{k t^l_{a,ij}(k)}{T^{+,l}_{a,ij}}$, the weighted average scale of transfer given to l by the interaction between i and j,
- $k^{-,l}_{a,ij} = \sum_{k,\, t^l_{a,ij}(k)<0} \frac{k t^l_{a,ij}(k)}{T^{-,l}_{a,ij}}$, the weighted average scale of transfer pumped from l by the interaction between i and j,

where a stand for u for the kinetic transfer, b for the potential transfer and $u \to b$ for the buoyancy flux (note that for the buoyancy flux, there is no variable j).

Through these four variables illustrated in figure 4.18, the transfer $t^l_{a,ij}(k)$ can be summmarized. It is possible to determine the strength of the transfer as well as the

scale it is operating. The transfer related to the cascade of energy is characterized by $T^{+,l}_{a,ij} = -T^{-,l}_{a,ij}$, as opposed to the transfer of exchange of energy $T^{l}_{a,ij} = T^{+,l}_{a,ij} + T^{-,l}_{a,ij} \neq 0$ shown in section 4.4.3. In order to facilitate the understanding of the scale of transfer we use the ratio of weighted average scale $k^{+/-,l}_{a,ij} = \dfrac{k^{+,l}_{a,ij}}{k^{-,l}_{a,ij}}$ for the potential and kinetic transfers. When this ratio is lower than one ($k^{+/-,l}_{a,ij} < 1$), this means that an inverse cascade is occurring, the energy is pumped at small scales and given back at larger scale. When this ratio is greater than one ($k^{+/-,l}_{a,ij} > 1$), this means that a direct cascade is occurring, the energy is pumped at large scales and given back at smaller scales.

4.7.1 Transfer between waves and eddies themselves

4.7.1.1 Transfer amplitude

In figure 4.19, I only show the positive potential and kinetic transfer between eddies $T^{e}_{a,ie}$ and waves $T^{w}_{a,iw}$ themselves (with $i = e$ or $i = w$). As these transfers do not give or take energy to another part of the flow, the net transfer is zero, meaning that the negative transfer is exactly the opposite of the positive transfer ($T^{+,l}_{a,ij} = -T^{-,l}_{a,ij}$). There is a cascade of energy.

In figure 4.19, we observe that at low Re_b and Fr (in a wave turbulence regime), the wave cascade dominates as the wave turbulence transfer (*i.e.* $T^{+,w}_{a,ww}$) dominates. At high Re_b and Fr, it is the eddy cascade that becomes dominant (the transfer $T^{+,e}_{a,ee}$). This supports the fact that our decomposition is relevant and allows us to extract the relevant dynamics of the flow as we investigate a regime dominated by wave turbulence and also a more turbulent regime. Furthermore, the transfer related to waves $T^{+,w}_{a,ww}$ is stronger for the potential transfer than the kinetic transfer (*i.e.* $T^{+,w}_{b,ww} > T^{+,w}_{u,ww}$) while the transfer related to eddies $T^{+,e}_{a,ee}$ is stronger for the kinetic transfer than for the potential transfer (*i.e.* $T^{+,e}_{u,ee} > T^{+,e}_{b,ee}$). Hence, waves are more active in the potential part of the flow while eddies are more active in the kinetic part of the flow. It shows that the importance of transfer is probably dependent on the quantity of that type of energy in the flow. In the kinetic part of the flow, there is a large quantity of eddies (all the toroidal part and a bit of the poloidal part) while in the potential part of the flow, there is a large quantity of waves.

To be more precise, on figures 4.19 a and c, we observe that the transfers involving interactions between waves and eddies (*i.e.* $T^{+,e}_{b,we}$ and $T^{+,w}_{b,ew}$) are more or less constant for all Re_b and Fr. Yet, the strength of these two transfers differ and we always

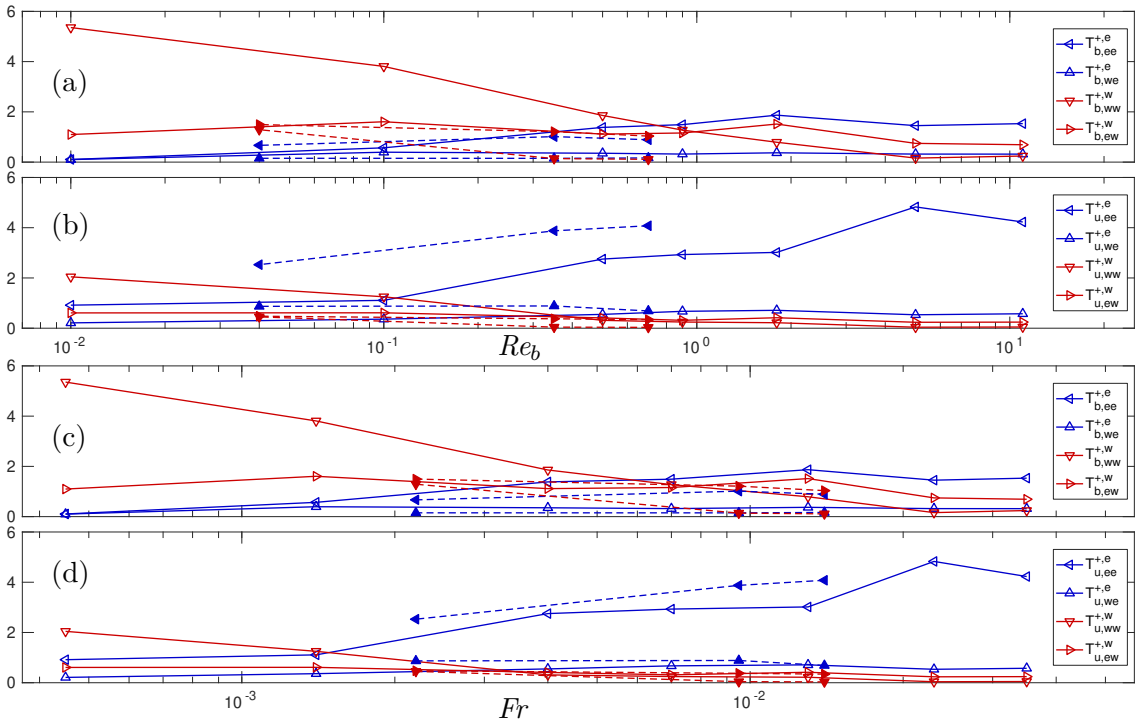

FIGURE 4.19: Evolution of the positive potential transfer (a,c) $T^{+,j}_{b,ij}$ and positive kinetic transfer $T^{+,j}_{u,ij}$ (with $i = w$ or $i = e$) between waves ($j = w$) or eddies ($j = e$) against (a, b) Re_b; (c, d) Fr. Numerical simulations with 512^3 points are shown with open symbols and solid lines, and numerical simulations with 256^3 points are shown with filled symbols and dotted lines.

experience $T^{+,w}_{b,ew} > T^{+,e}_{b,we}$. For the transfer involving only the waves $T^{w}_{b,ww}$, we observe that its value increases significantly when Re_b increases and Fr decreases. The transfer of waves dominates when waves dominates the flow as seen in the ratio of energy in section 4.3.1 (at small Fr and to a lesser extent at large Re_b). On the contrary, for the transfer involving only the eddies, we observe that the value of the transfer does not change much with Fr but seems to increase when Re_b increases. As Re_b increases, more overturning occurs and this could lead to an increase of eddy transfer as density overturning is an eddy phenomenon involving the potential energy (high density over low density). The maximum value of transfer is largely dominated by the transfer between waves only, especially at small Fr.

More specifically, on figures 4.19 b and d, the transfers involving waves ($T^{+,w}_{u,ew}$ and $T^{+,w}_{u,ww}$) are rather weak. Yet, we can see that $T^{+,w}_{u,ww}$ increases slightly when Re_b increases or when Fr decreases. In comparison, the transfer involving only eddies $T^{+,e}_{u,ee}$ is stronger, especially at high Re_b and high Fr. $T^{+,e}_{u,ee}$ increases significantly when Fr increases at constant Re_b and increases slightly when Re_b decreases at constant Fr. It follows the

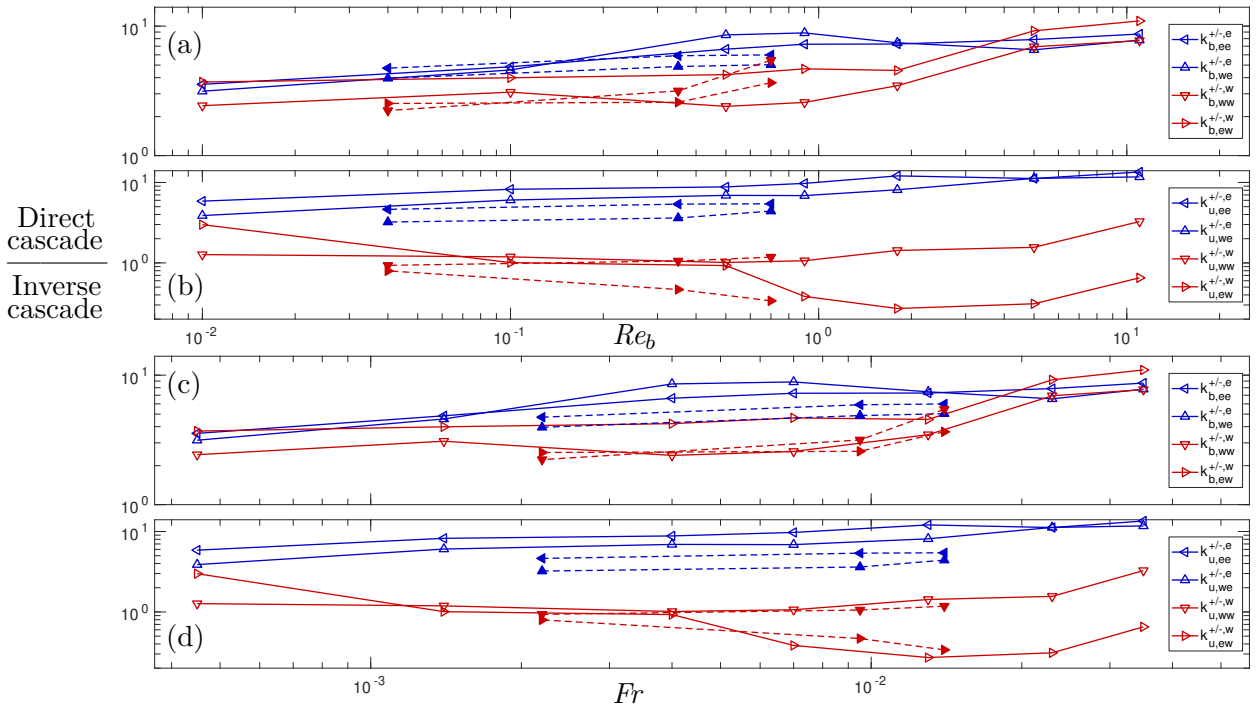

FIGURE 4.20: Evolution of the ratio of scales of potential transfer (a, c) $k_{b,ij}^{+/-,j}$ and of kinetic transfer (b, d) $k_{u,ij}^{+/-,j}$ (with $i = w$ or $i = e$) between waves ($j = w$) or eddies ($j = e$) against (a, b) Re_b; (c, d) Fr. Numerical simulations with 512^3 points are shown with open symbols and solid lines, and numerical simulations with 256^3 points are shown with filled symbols and dotted lines.

evolution of the energy ratio of eddies shown in figure 4.6 against Fr and Re_b. No clear trend can be observed for the transfer $T_{u,we}^{+,e}$.

4.7.1.2 Ratio of scales

First, we consider the ratio of scales of potential transfer $k_{b,ij}^{+/-,j}$ and of kinetic transfer $k_{u,ij}^{+/-,j}$ between waves ($j = w$) or eddies ($j = e$) themselves as shown in figure 4.20. We do not analyse the average ratio of negative transfer $k_{a,ij}^{-,j}$ and at the average ratio of negative transfer $k_{a,ij}^{+,j}$ because the interpretation of these two variables differentiated becomes difficult. Furthermore, the average scale of negative transfers $k_{a,ij}^{-,j}$ are roughly constant around the value of the forcing scale. On the contrary, it is generally the average scale of positive transfers $k_{a,ij}^{+,j}$ which fluctuate.

From a general perspective, we observe that the cascade is direct for all transfers for eddies $k_{a,ij}^{+/-,e} > 1$ and for the potential transfer for waves $k_{b,ij}^{+/-,w} > 1$. This direct cascade is also stronger as Re_b increases and Fr decreases. No cascade for $k_{u,ww}^{+/-,w} \sim 1$ can be observed and a slight inverse cascade exists for $k_{u,ew}^{+/-,w} < 1$ at high Fr.

To be more precise on $k_{b,ij}^{+/-,j}$, we observe that there is always a direct cascade (*i.e.* $k_{b,ij}^{+/-,j} > 1$) and that the direct cascade is slightly stronger for eddies than for waves $k_{b,ie}^{+/-,e} \gtrsim k_{b,iw}^{+/-,w}$. Not much trend can be guessed on the figure 4.20a against the buoyancy Reynolds number as the 256^3 points and 512^3 points results cross each other. However, the results are much clearer on the figure 4.20c against the Froude number. We observe that, for a constant Fr number and increasing slightly Re_b, the ratio of scales $k_{b,we}^{+/-,e}$, $k_{b,ee}^{+/-,e}$ and $k_{b,ew}^{+/-,w}$ increase. All of those ratio of scales have at least an eddy component associated with it. It probably means that it is the eddy component that influences the direct cascade to be stronger when the flow is more turbulent. Indeed on the ratio of scales involving only waves $k_{b,ww}^{+/-,w}$ no particular trend can be observed depending on Fr or Re_b.

More specifically, on $k_{u,ij}^{j}$, the direct cascade is stronger for eddies than for waves $k_{u,ie}^{+/-,e} \gg k_{u,iw}^{+/-,w}$. The direct cascade is also stronger for eddies ($k_{u,ie}^{+/-,e}$) as the stratification decreases, while no clear trends against the stratification can be drawn for the cascade of waves.

Surprisingly, an inverse cascade occurs for small stratification as the ratio of scales $k_{u,ew}^{+/-,w} < 1$. It corresponds to the transfer by the advection of a wave by an eddy that give or pump energy to a wave. For a constant Re_b the ratio of scales $k_{u,we}^{+/-,e}$, $k_{u,ee}^{+/-,e}$ and $k_{u,ew}^{+/-,w}$ increase as the Fr number decreases. For a constant Fr, the ratio of scales $k_{u,we}^{+/-,e}$ and $k_{u,ee}^{+/-,e}$ increase as the Re_b number increases, but no trend can be concluded for $k_{u,ew}^{+/-,w}$ in this case. Indeed, as $Re_b = Re_h^2 Fr$, when Fr is constant and Re_b increases, it means that the horizontal Reynolds number Re_h increases as well. If the Reynolds number increases, we expect smaller scales of the flow to be created, and this small scale flow needs to be fed some energy. As the only source of energy to the smaller scales is the transfer of energy, it is the transfers related to eddies that are mostly reponsible for the creation of smaller scale flow. This shows that, when the flow is more turbulent, the direct cascade is stronger, which is expected as the Kolmogorov scale decreases. However, we show that the direct cascade depends especially on the transfer that involves eddies.

4.7.2 Ratio of scales for the transfers of exchange of energy

Then, we consider the ratio of scales of potential transfer $k_{b,ij}^{+/-,l}$ and of kinetic transfer $k_{u,ij}^{+/-,l}$ from waves to eddies ($j = w$ and $l = e$) and from eddies to waves ($j = e$ and $l = w$) as shown in figure 4.21. The ratio of scales analysed here is linked to the transfer

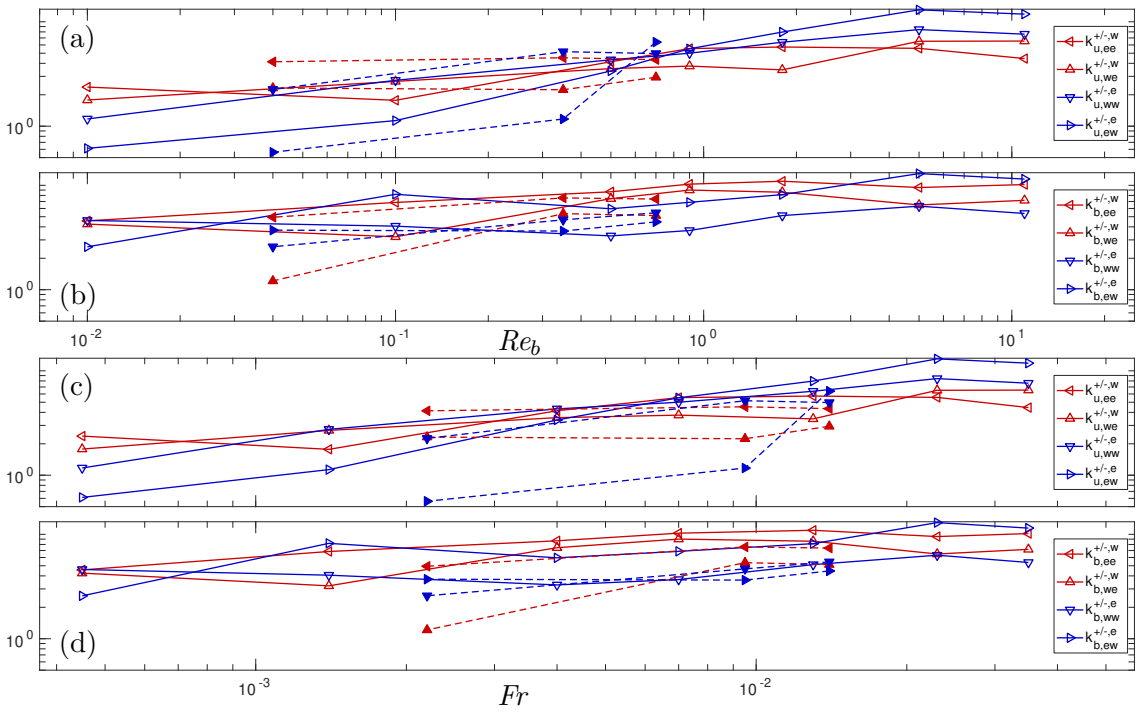

FIGURE 4.21: Evolution of the ratio of scales of potential transfer (a, c) $k^{+/-,l}_{b,ij}$ and of kinetic transfer (b, d) $k^{+/-,l}_{u,ij}$ (with $i = w$ or $i = e$) from waves to eddies ($j = w$ and $l = e$) or from eddies to waves ($j = e$ and $l = w$) against (a, b) Re_b; (c, d) Fr. Numerical simulations with 512^3 points are shown with open symbols and solid lines, and numerical simulations with 256^3 points are shown with filled symbols and dotted lines.

of exchange of energy studied in section 4.4.3.

In general we observe that the cascade is direct and is slightly stronger as the stratification increases. At very large stratification, only the ratio of scales $k^{+/-,e}_{u,ew}$ is lower than one.

To be more precise, for a constant Fr, the ratio of scales $k^{+/-,e}_{u,ew}$, $k^{+/-,e}_{u,ww}$ and $k^{+/-,w}_{u,we}$ increases as Re_b increases. No particular trend can be drawn against Fr or for the ratio of scales $k^{+/-,w}_{u,ee}$. For a constant Fr the ratio of scales $k^{+/-,w}_{b,we}$, $k^{+/-,w}_{b,ee}$ and $k^{+/-,e}_{b,ew}$ increases as Re_b increases. For a constant Re_b the ratio of scales $k^{+/-,w}_{b,we}$ and $k^{+/-,w}_{b,ee}$ increases as well when Fr decreases. No clear trend can be drawn for the ratio of scales $k^{+/-,e}_{b,ww}$.

4.7.3 Buoyancy flux transfer

In the previous sections, we analysed the transfer between only the waves and the eddies in the kinetic or the potential part of the equations. However, it is also possible that a transfer of energy occurs from the kinetic to potential term, this is called the buoyancy

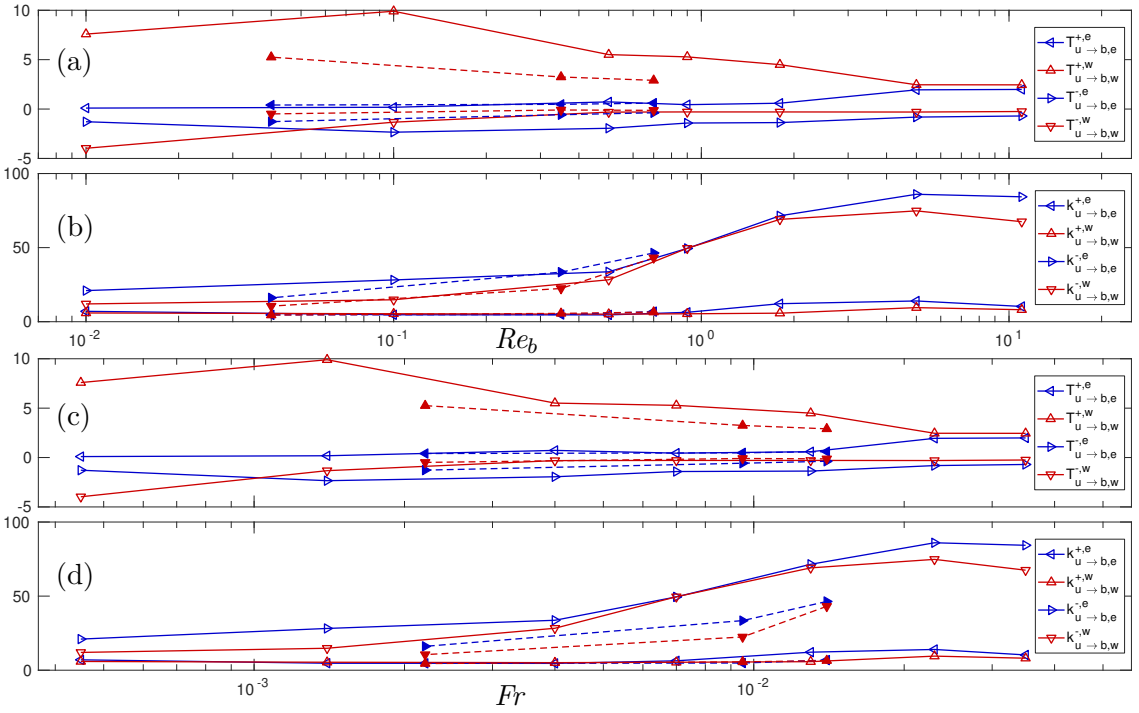

FIGURE 4.22: Evolution of the positive $T^{+,j}_{u\to b,j}$ and negative $T^{+,j}_{u\to b,j}$ buoyancy flux (a, c) and of the average scale of positive $k^{+,j}_{u\to b,j}$ and negative $k^{-,j}_{u\to b,j}$ buoyancy flux (b, d) between waves ($j = w$) or eddies ($j = e$) against (a, b) Re_b; (c, d) Fr. Numerical simulations with 512^3 points are shown with open symbols and solid lines, and numerical simulations with 256^3 points are shown with filled symbols and dotted lines.

flux. Indeed, the forcing is only done on the kinetic part of the equation so we can expect a positive transfer from the kinetic to potential energy.

On a long period T_0, we expect the transfers from the kinetic wave to the buoyancy eddy, and from poloidal eddy to potential wave to be close to zero, because for any $\mathbf{k}$ the frequency of the wave domain terms is different than the frequency of the eddy domain. Hence, we have $t^e_{u\to b,w}(k) \to 0$ when $T_0 \to \infty$. Furthermore, the vertical velocity u_z involve only in the poloidal component (and not in the toroidal component). Hence, there is no transfer from the toroidal eddy to the buoyancy wave as well despite both components sharing some similar frequencies. This means that we also get $t^w_{u\to b,e}(k) \to 0$ when $T_0 \to \infty$.

Figures 4.22 a and c show the positive and negative value of the buoyancy flux. The overall sum is positive as expected as the forcing is only done in the kinetic part of the equations and a transfer naturally occur from the kinetic energy to the potential energy.

We observe that it is mostly waves that transfer energy to the potential part of the flow with $T^{+,w}_{u\to b,w}$. This transfer of energy increases as Fr decreases or Re_b increases. A smaller amount of energy is transferred from the potential to the kinetic energy with the

transfer involving only eddies $T^{-,e}_{u\to b,e}$. IGW do not transfer energy from the potential to kinetic part of the flow, except at very large stratification. The transfer $T^{+,w}_{u\to b,w}$ is stronger when Re_b increase, it means that the flow is more turbulent, it can overcome the stratification and transfer energy to the potential part of the flow. When the flow is more stratified (Fr decreases) but at constant Re_b, there is more wave energy (see section 4.3.1) and, as the waves interact between their potential and poloidal terms, it seems logical that the transfer $T^{+,w}_{u\to b,w}$ increases as well.

Figures 4.22 b and d show the average scale of positive and negative kinetic to potential transfer. We observe that the positive scale is constant for all simulations and is close to the forcing values $k_{forc} \sim 5$. However the negative average scale of kinetic to potential transfer seems to evolve with Re_b. $k^{-,l}_{u\to b,i}$ increases when Re_b increases as well. Its value also increases slightly when eddies are involved rather than when waves are involved (*i.e.* $k^{-,e}_{u\to b,e} > k^{-,w}_{u\to b,w}$). This means that, as Re_b increases, the direct cascade from potential to kinetic energy is stronger.

4.8 Visualization

From the separation of waves and eddies, it is possible to observe the eddy and wave velocity and buoyancy fields in the physical space. It is difficult to draw quantitative result from those fields, but they are useful to understand the different eddies and waves phenomena.

4.8.1 Buoyancy fields

Figure 4.23 shows the total, wave and eddy buoyancy field for different stratification strength of the DNS with 512^3 points. In the total buoyancy field (1st column) of figure 4.23, the flow is more turbulent and there is more overturning (black line crossing) when the stratification decreases. The amplitude of $b(x, y)$ increases because the potential energy increases when N increases. Furthermore, the structures are small scale for $N = 20$, while being large scale for $N = 600$.

In the wave buoyancy field (2nd column) of figure 4.23, the flow is quite similar to the total buoyancy field, but the black lines are smoother especially for the cases with $Re_b > 1$, meaning that little to no overturning happens in the wave part.

In the eddy buoyancy field (3rd column) of figure 4.23, the flow seems always at small scale. While no overturning is visible for large stratification cases, for low stratification cases ($N < 70$), there is a significant part of overturning visible. This is indeed expected

as overturning starts to occur when $Re_b \gtrsim 1$. The amplitude of the eddy buoyancy field is also significantly smaller for large stratification than the waves. On the contrary, for small stratification the amplitudes of the wave and eddy buoyancy fields are similar. This supports the energy distribution shown for these cases in section 4.3.1.

4.8.2 Vertical velocity fields

Figure 4.24 shows the total, wave and eddy vertical velocity field for different stratification strength of the DNS with 512^3 points. In the total vertical velocity field (1st column) of figure 4.24, the flow is more turbulent when the stratification decreases. The difference of the flow scale is clearly visible. At small stratification $N = 20$ the flow is small scale whereas at large stratification ($N = 600$), the flow is very large scale. The amplitude of $u_z(x, y)$ increases slightly with the stratification when N increases. Furthermore the structures are small scale for $N = 20$ while being large scale for $N = 600$.

In the wave vertical velocity field (2nd column of figure 4.24), the general pattern of the flow is similar to the total vertical velocity field. It is especially true for very large stratification ($N = 600$).

In the eddy vertical velocity field (3rd column of figure 4.24), the flow seems always at small scale and very turbulent. The amplitude of the eddy part of the vertical velocity field is nearly constant in all cases except at $N = 600$ where it decreases.

4.9 Conclusion

In this chapter, we used the separation technique presented in chapter 3 using an implicit definition of the dispersion of waves explained in section 3.1.5 in the case of stably stratified flows. We apply this separation technique on a campaign of numerical simulation for varying values of Fr and Re_b number. We observe that the distribution of poloidal and potential energy between waves and eddies depends mostly on Fr number. We also observe that the energy spectrum of eddies follows a $k^{-5/3}$ slope and a $k_h^{-5/3}$ slope as well. As for the energy spectra of waves, it follows a steeper slope than eddies closer to a k^{-3}, k_z^{-3} and k_h^{-3} when $N > 50$ and a slope closer to a $k^{-5/3}$, $k_z^{-5/3}$ and $k_h^{-5/3}$ when $N \leq 50$.

Then, a balance of energy and flux for waves and eddies is computed. We observe that a large transfer occurs from waves to eddies for numerical simulations with $Re_b < 2$ and $Fr < 0.02$. Most of the mixing is due to waves at low Fr number, but

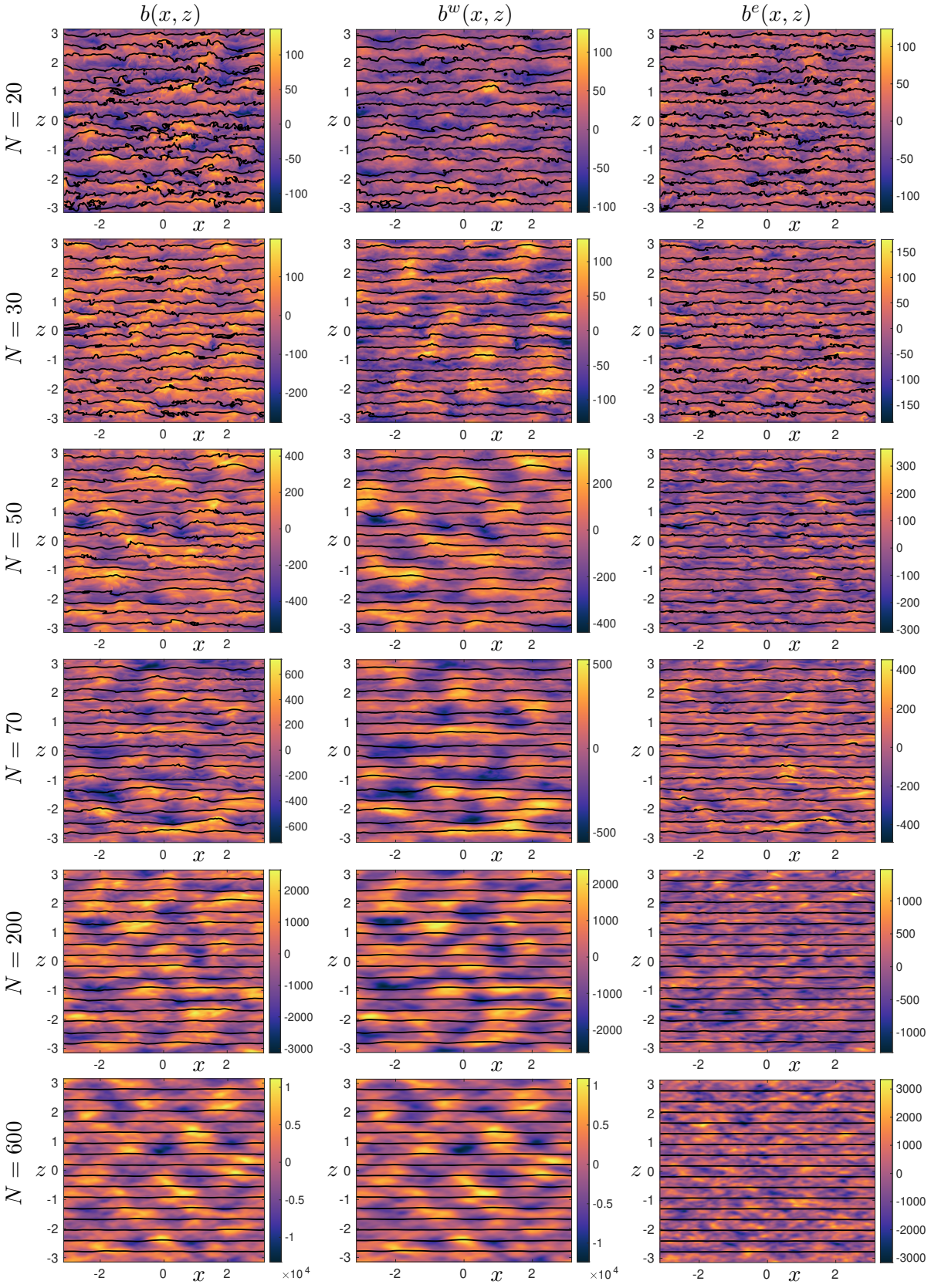

FIGURE 4.23: Total $b(x,z)$, wave $b^w(x,z)$ and eddy $b^e(x,z)$ buoyancy field, with superimposed iso-density lines in black in the (x,z) plane in the middle of the y interval.

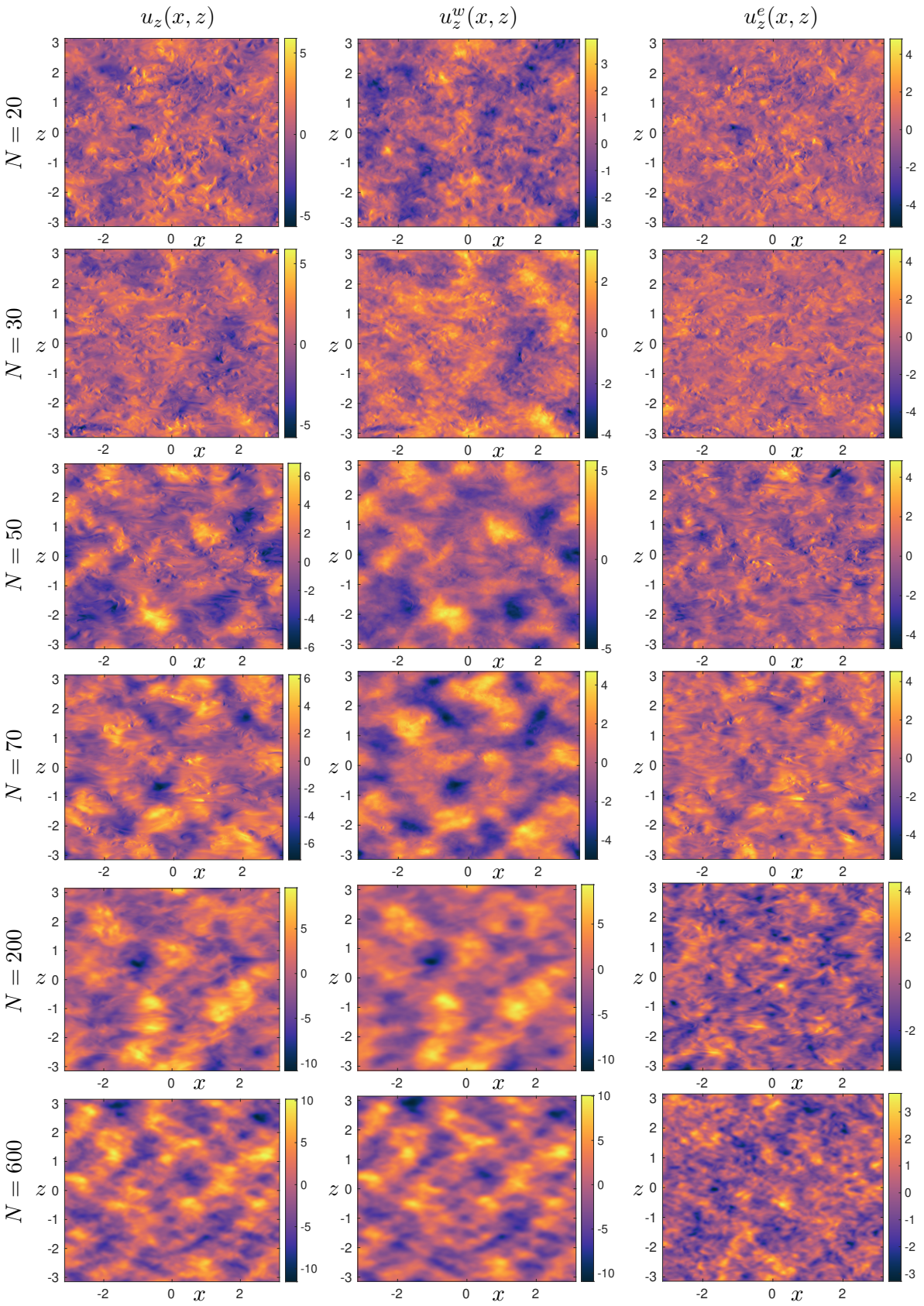

FIGURE 4.24: Total $u_z(x,z)$, wave $u_z^w(x,z)$ and eddy $u_z^e(x,z)$ vertical velocity field in the (x,z) plane in the middle of the y interval.

at large Fr the mixing due to eddies is two to three times higher than the mixing due to waves. Furthermore, the kinetic and buoyancy dissipation of waves seems to be dependent against the Froude number Fr and decrease as Fr increases. Wave and eddy cascade of energy are observed. A wave cascade of energy dominates at low Fr and low Re_b while an eddy cascade of energy dominates at high Fr and high Re_b. Direct cascades of energy are mostly observed except for a few types of interactions.

Finally, 2D buoyancy and vertical velocity fields are visible for the different numerical simulations. Large differences can be observed between the wave and eddy part which support that our separation technique actually works in a turbulent stratified flow.

Chapter 5

Rotating turbulence

5.1 Introduction

In rotating turbulence, inertial waves (IW), eddies and the geostrophic mode (GM) are mixed and interact together. Contrarily to the stratified case, no spatial separation such as the Riley's decomposition [119] exist in the rotating case to separate waves and eddies. In a turbulent case where all structures are stongly interacting, how the interactions between waves, eddies and GM are organised?

The characteristics of IW are detected in turbulent flow both in experiments [27, 147] and numerical simulations [41, 75]. On the other hand, the GM is a powerful, large structure that greatly influences the properties of turbulence [56, 120]. IW can also be impacted by the presence of the GM. Indeed, inertia-gravity waves, which are created when both rotation and stratification occur, are subject to diffusivity by the GM [68, 122]. As shown in figure 5.1, different regimes for rotating flows can be observed [56]. It depends on the Reynolds number ($Re = Ul/\nu$) and Rossby number ($Ro = U/(2\Omega l)$) where U is a velocity scale associated with an integral scale l. At $Ro \ll 1$ and $Re \ll 1$ the flow is dominated by inertial waves. For $Ro \ll 1$ and $Re > 1$ the flow is dominated by inertial waves which interact weakly and constitute the wave turbulence regime. For $Ro < 1$ and $Re \gg 1$ quasi-two dimensional turbulence is observed. However, in our numerical simulations, we controlled the emergence of the GM and the flow is less dominated by the 2D flow at high Reynolds number and low Rossby number.

Moreover, the formation of the GM is not totally understood. It is compatible with the linear theorem of Taylor-Proudman [58] which predict that in rapidly rotating flow, the flow is invariant along the axis of rotation (*i.e.* $k_z = 0$) [13] but this theorem does not determine whether this 2D flow has two or three components. For moderate Rossby

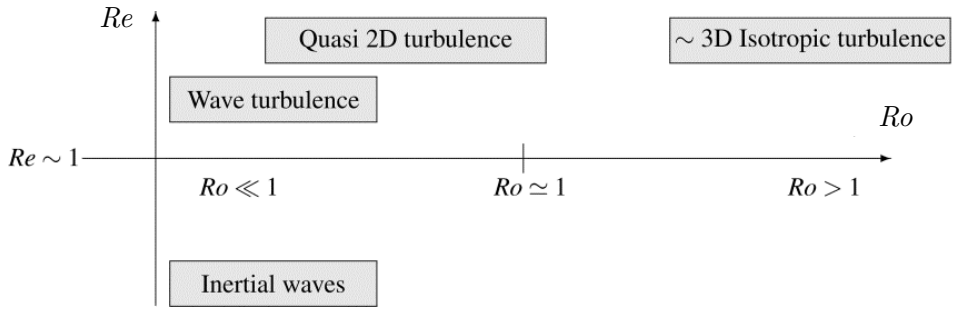

FIGURE 5.1: Schematic of the different regimes found in rotating flows (reproduced from Godeferd and Moisy [56]).

($Ro \sim 1$) in DNS and in asymptotic theories [25], the non-linear transfer concentrate the energy along the GM (*i.e* $k_z = 0$). Sharma et al. [124] also found that the transfer of energy was toward $k_z = 0$ in decaying rotating turbulence and in forced rotating turbulence (for larger wavenumber than the forcing wavenumber) for a $Re_I < 0.4$ (see section 5.2 for a definition of Re_I). An illustration of this mechanism can be seen in figure 5.2.

Different mechanisms are proposed to understand the emergence of the GM. For example, in inhomogeneous flows, Davidson et al. [36] proposed that the vertical coherent structures could develop due to linear inertial wave propagation. No non-linear processes are involved here, but a modification of the phase of the various Fourier modes can create columnar eddies. This was demonstrated from an experiment with a cloud of turbulence, where the distance travelled by the leading edge of the columnar structures comply with the group velocity of inertial waves. A similar analysis have been conjectured for homogeneous flow in Staplehurst et al. [131]. Smith and Waleffe [128] say that the exact resonant triad (*i.e.* $\mathbf{k} + \mathbf{p} + \mathbf{q} = 0$ and $\omega(\mathbf{p}) + \omega(\mathbf{q}) + \omega(\mathbf{k}) = 0$, with $\mathbf{k}$, $\mathbf{p}$, $\mathbf{q}$ 3D wave vectors) transfer energy so that it tends to decrease the ratio k_z/k due to the "instability assumption" [146] but never reach exactly the GM (*i.e.* $k_z = 0.$) because the resonant interaction cannot occur. Similarly, the asymptotic theory [10] excludes the possibility of a GM at large-time limit at very low Ro ($Ro \ll 1$). Indeed, from a general perspective, Greenspan [59] demonstrated that exact triadic resonance cannot transfer energy to the GM (*i.e.* $k_z = 0$, $\omega(k) = 0$ with $\omega(\mathbf{q}) = -\omega(\mathbf{p})$ and $p_z = -q_z$ in Waleffe [146]). To reach $k_z = 0$, two other mechanism [111, 128] bypass Greenspan's results and transfer energy to the GM:

- the first mechanism would be a near resonant triad interaction $\mathbf{p} + \mathbf{q} = \mathbf{k}$ with $p_z = -q_z$, $k_z = 0$ and $\omega(\mathbf{p}) + \omega(\mathbf{q}) + \omega(\mathbf{k}) \sim 0$. Similarly, in Le Reun et al. [78], an instability mechanism is shown numerically and analytically to excite the GM by inertial waves. This is driven by near-resonant triadic interaction.

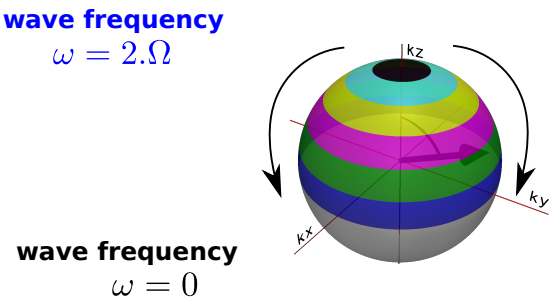

FIGURE 5.2: Visualization of the non linear transfer, which concentrate energy around the GM (at $k_z = 0$).

- The second mechanism explained in Smith and Waleffe [128] would be a quartet mechanism. The resonant quartet occurs when two successive triad interaction occur, it leads to $\mathbf{k}+\mathbf{p}+\mathbf{q}=0$, $\omega(\mathbf{p})+\omega(\mathbf{q})+\omega(\mathbf{k})=0$ and $\mathbf{p}+\mathbf{r}+\mathbf{s}+\mathbf{t}=0$ and $\omega(\mathbf{p})+\omega(\mathbf{r})+\omega(\mathbf{s})+\omega(\mathbf{t})=0$ where $\mathbf{k},\mathbf{p},\mathbf{q},\mathbf{r},\mathbf{s}$ are 3D wavevectors and $\mathbf{t}$ is a 2D wavevector representing the GM (*i.e.* $t_z = 0$). In Newell [111], a quartet mechanism is also introduced so that a resonant quartet of Rossby waves can transfer energy to a zonal flow. In Brunet et al. [22], it is a quartetic secondary instability that is evoked to be responsible of the geostrophic mode. Nevertheless, experiments seem to show that the resonant quartets of IW can trigger an instability at the origin of the GM [22] in the case where the rotating turbulence is dominated by IW in wave turbulence regime (low Rossby number).

The different mechanisms presented concern the emergence of the GM due to wave-wave interaction. Beyond that mechanism of onset, in homogenous turbulence, Bourouiba et al. [18] found that the GM is driven by the interaction of two small-scale horizontal and small-frequency 3D components. One question appears: in the presence of waves and eddies, what interactions transfer energy to the GM? Is it the wave-wave, wave-eddy, eddy-wave or eddy-eddy interactions that manage the GM?

Finally, two types of cascade can appear in rotating turbulence, a direct cascade as in homogenenous and isotropic turbulence and inverse cascade as in 2D turbulence. In a forced rotating experiment by Baroud et al. [8], they observed an inverse cascade as small vortices merged into larger vortices at the start of their experiment. In a decaying rotating experiment, Morize et al. [100] observed a net inverse cascade at large scale. Yet, these inverse cascades are not directly observed and it is not absolutely sure if an inverse cascade was really observed in these two experiments [26]. In more recent experiments, Yarom et al. [148] also observe an inverse cascade in a rotating turbulence experiment for the horizontal part of the flow. Campagne et al. [26] show the presence of direct cascade (for small horizontal scale) and an inverse cascade for large horizontal scale. In numerical simulations of rotating flows, Smith et al. [130] found that inverse

and direct cascade of energy can coexist. Mininni and Pouquet [98] also found an inverse cascade of energy and a direct cascade of energy and of helicity. In these experiments and simulations, the inverse cascade is not associated to a particular structure of the flow. Is it due to the GM? the wave? the eddy?

In Bourouiba and Bartello [17], the flow is separated in three parts, a GM with a vertical velocity ($u_z(k_z = 0)$) field and a horizontal velocity ($u_x(k_z = 0), u_y(k_z = 0)$) field, and a 3D component ($\mathbf{u}(k_z \neq 0)$). They looked at the different transfers occurring between these three parts and found that at their moderate Rossby number $Ro = 0.2$, the transfer involving only the horizontal GM created an inverse cascade. In Buzzicotti et al. [23], DNS are done where the GM is removed from the equations. They observed that the GM played an important role in the inverse cascade of energy, but other 3D phenomenon also bring energy to the larger scale. Then, in Buzzicotti et al. [24], they found that an inverse cascade occurred close to the forcing scale for homochiral interaction that fed the GM. For the direct cascade, they show that it is dominated by interactions that do not involve the GM.

While previous works seem to link the GM (which is close to a 2D flow at small Ro) to an inverse cascade, all these works do not separate the effect of wave and eddies in the inverse or direct cascade of energy. Hence, this question arises: which transfer is responsible of the inverse or direct cascade? Is it the wave-wave, eddy-eddy, GM-wave...?

To answer these questions, the adaptive algorithm is applied on various rotating flows using also the Craya-Herring frame. The first section explains:

- the added viscosity (section 5.2.1) used that damps considerably the GM in order to achieve statistical stationnarity of the flow,
- all the parameters of the DNS (section 5.2) that explore various rotating turbulent regimes,
- the necessity to take into account the vertical velocity in the GM (section 5.2.3),
- the influence of the GM on the dispersion relation with the sweeping and gradient effect (section 5.2.4).

In the second section (5.3), we present the partition of energy between waves and eddies. It explores the energy ratio as well as the energy spectrum of the wave, eddy and GM part. The third section (5.4) presents an energetical budget for waves, eddies and the GM, with mutual interactions and different fluxes. The fourth section (5.5) presents the dissipation linked to waves and eddies. The fifth section (4.7) makes a detailed analysis

on the different transfer occuring in the flow and the inverse or direct cascade of energy it participated in. The last section (4.8) shows some visualization of the decomposition of the total field in a wave and eddy part.

5.2 Parameters

5.2.1 Controling GM growth with added viscosity

For the rotating case the same cylindrical forcing is used as in the stratified case, but with slightly different parameters (see section 4.2.1). The forcing is done here on a cylindrical spectral surface of horizontal wave number $k_h = 1$ and vertical wave number $2 \leq k_z \leq 4$. However, even with this new forcing, it is difficult to reach a stationary steady state because the GM slowly grows in time, as with the VSHF in the stratified case. In order to further reduce the importance of the GM, a new viscous term F_α is added in the Navier-Stokes equation as done by Le Reun et al. [75].

For rotating flow, this added viscosity is:

$$\hat{\mathbf{F}}_\alpha(\mathbf{k}, t) = \begin{cases} -\alpha \hat{\mathbf{u}}(\mathbf{k}, t) & \text{if } k_z = 0 \\ 0 & \text{otherwise.} \end{cases} \tag{5.1}$$

where the value of α modifies the relative importance of the slow modes against the overall structure of the flow. Therefore, the value of α is chosen in function of the wanted importance of the slow modes.

5.2.2 Parameter space

Equations (2.16) are solved using the same code as explained in section 4.2.3. Nine numerical simulations have been run with the parameters shown in table 5.1 at resolutions 256^3 and 512^3. Contrarily to the stratified cases, the exploration of the parameters is mainly based on 256^3 points, the higher resolution of 512^3 points is used to confirm and explore trends. Yet, for particular statistics such as energy spectrum, the results are based on the simulations with 512^3 points.

The results of the numerical simulation are shown against

- the Rossby number $Ro = \dfrac{\varepsilon}{2\Omega U_h^2}$ with $U_h = u_h - u_h(k_z = 0)$ which account for the ratio of the horizontal flow inertia over the effect of the rotation rate and ε is the

kinetic energy dissipation. This Rossby number is akin to the Froude number in stratified flow, but the horizontal velocity of the GM is removed from the definition of the typical horizontal velocity of the Rossby number. In the stratified case, the VSHF was damped a lot, it had negligible energy, and the added viscosity α was set constant for every numerical simulations. It did not infuence the value of the Froude number. In the rotating case, we changed the value of α, so that the GM has varying importance in the flow. Removing the horizontal velocity of the GM in the calculation of the Rossby number removes its dependence on the value of α.

- the inertial Reynolds number $Re_I = \dfrac{\varepsilon}{\nu(2\Omega)^2}$ as in Marino et al. [94] which is akin to the buoyancy Reynolds number in stratified turbulence.

The Zeman-Hopfinger scale $k_\Omega = \sqrt{\dfrac{(2\Omega)^3}{\varepsilon}}$ defined in [101, 149] and the Kolmogorov scale $k_\eta = (\dfrac{\varepsilon}{\nu^3})^{1/4}$ can be used to compute the inertial Reynolds number $Re_I = (\dfrac{k_\eta}{k_\Omega})^{4/3}$. The Zeman-Hopfinger scale is the limit wavenumber above which the rotation is still considered important while the Kolmogorov scale is the smallest scale in the turbulent flow. Hence, the ratio of these two quantities is very useful to measure the importance of the effect of rotation against the dissipation. We study the same range of regime as in the stratified flow, a regime strongly dominated by the rotating term (*i.e.* $Ro \ll 1$) with varying values for Re_I. We adapt the classification proposed in Brethouwer et al. [19] in the case of stratified turbulence to the rotating case. When we focus on the regime where $Ro \ll 1$ and $Re_I \ll 1$, there is a weak wave interaction and the wave dissipates up to the small scales; we will call it the "viscosity-affected rotating flow" (VARF). When we focus on the regime where $Ro \ll 1$ and $Re_I \gg 1$ the wave dissipation occurs at a scale much larger than the dissipative scale; we will call it "strongly rotating turbulence" (SRT).

We plot in Figure 5.3 the exploration points in the parameter space (Ro, Re_I). The exploration of these two regimes also induces a modification of the Taylor-length-based Reynolds number $Re_\lambda = u_{rms}\lambda/\nu$ with λ the Taylor scale and u_{rms} the *rms* velocity. By adjusting the resolution, one can therefore study the variation of the dynamical system either by setting Ro and weakly increasing Re_I (from low to high resolution), or by setting Re_I and weakly increasing Ro (from high to low resolution) in the parameter map. While in the stratified case (in chapter 4), the analysis was based on 512^3 points and secondarily with 256^3 points, here, the analysis is based more on direct numerical simulation with 256^3 points than 512^3 points as we did more simulation with 256^3 points in the rotating case.

The Ekman number $E_k = \frac{Ro}{Re_h}$ can also be used when dealing with rotating flows [99]. Rotating flows are particularly studied in planetary cores, where for example in the

512^3 points, $\nu = 1/700$ and $\alpha = 0.5$

2Ω	Ro	Re_I	Re_h	Ek	Re_λ	k_Ω	P	ε
15	0.06	28	7780	7.7×10^{-6}	255	19	10	9
80	0.007	1	20400	3.4×10^{-7}	720	240	14	7
300	0.0011	0.074	61200	1.8×10^{-8}	1350	1400	20	9.5

256^3 points, $\nu = 1/250$ and $\alpha = 0.5$

2Ω	Ro	Re_I	Re_h	Ek	Re_λ	k_Ω	P	ε
5	0.2	95	1960	1.1×10^{-4}	120	3.6	10	9.5
15	0.07	14	2860	2.5×10^{-5}	150	16	14	13
30	0.03	3.5	3900	7.7×10^{-6}	210	47	14	12.5
80	0.0076	0.4	6930	1.1×10^{-6}	395	230	14	10
300	0.0015	0.04	17800	8.4×10^{-8}	600	1400	20	14

256^3 points, $\nu = 1/2500$ and $\alpha = 0.01$

2Ω	Ro	Re_I	Re_h	Ek	Re_λ	k_Ω	P	ε
5	0.04	1	625	6.4×10^{-5}	400	112	0.01	0.01

TABLE 5.1: List of parameters in the DNS runs. $Re_h = (u_h - u_h(k_z = 0))^4/(\varepsilon\nu)$ is the horizontal Reynolds number.

Earth's core the dimensionless numbers are close to $Re \sim 10^9$ and $E_k = 10^{-15}$ [74]. The micro rossby $Ro_\omega = \frac{\omega}{2\Omega}$ is also used in Mininni and Pouquet [98] as the ratio of the vorticity over the rotation rate.

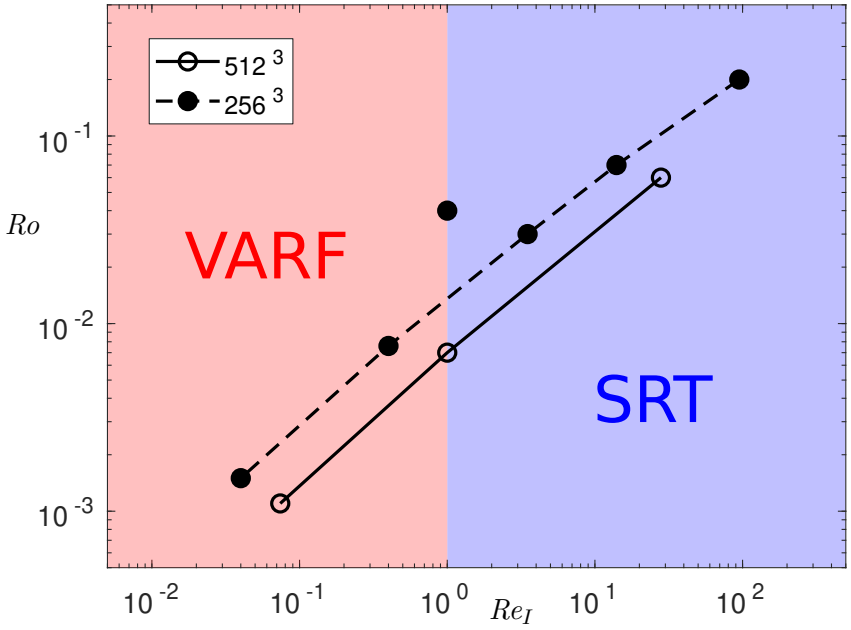

FIGURE 5.3: Parameters of the numerical simulations (open circle for 512^3 points and filled circle for 256^3 points).

5.2.3 Should the GM contain u_z?

The GM agrees with the Taylor Proudman theorem which states that the structure is invariant along the vertical axis (2D flow) in rapidly rotating flow [58]. In the case of unbounded domain, some linear instabilities arise and break the vortex pair to create 3D flow [13]. It is not possible to deduce from the Taylor Proudman theorem whether the flow has two or three components. Here we answer this question for the GM.

In a stratified flow, no vertical flow exists that satisfies the VSHF definition (*i.e.* $u_z(k_h = 0)$). This is due to the incompressibility of the fluid because for a wavevector $\mathbf{k}$ with $k_h = 0$, we verify $\mathbf{k} \cdot \hat{\mathbf{u}} = k_z \hat{u}_z = 0$. In rotating flow, the GM is defined by a flow invariant along the vertical axis (*i.e.* $\mathbf{u}(k_z = 0)$). The incompressibility constraint $\hat{\mathbf{u}} \cdot \mathbf{k} = 0$ does not constrain the flow to be purely horizontal, and three components can exist (u_x, u_y, u_z).

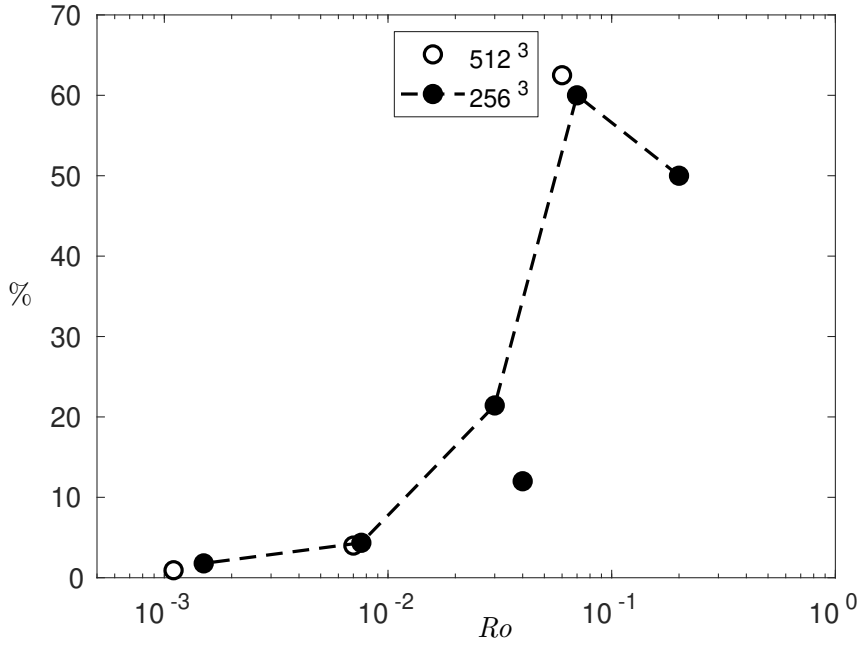

FIGURE 5.4: Percentage of energy of the vertical velocity field $u_z^2(k_z = 0)$ over the total GM energy in 3D $u_x^2(k_z = 0) + u_y^2(k_z = 0) + u_z^2(k_z = 0)$ against the Rossby number Ro.

On the contrary, even if the vertical velocity field $u_z(k_z = 0)$ is damped with the added dissipation shown in section 4.2.2, no external forces prevent a vertical velocity. Hence, it is possible to obtain a velocity field $u_z(k_z = 0)$, that is not insignificant. This is shown in figure 5.4 where the ratio of energy of the vertical velocity field over the total kinetic energy is plotted against the Rossby number and defined as

$$\frac{u_z^2(k_z = 0)}{u_x^2(k_z = 0) + u_y^2(k_z = 0) + u_z^2(k_z = 0)}. \tag{5.2}$$

We observe that at very small Rossby number, the velocity $u_z(k_z) = 0$ is negligible. However, when the Rossby number increases ($Ro > 0.04$), this is no longer the case and the velocity $u_z(k_z = 0)$ can even dominate the structure of the GM. Overall, the importance of the velocity $u_z(k_z = 0)$ evolves with the Rossby number. The lone point in figure 5.4 done with 256^3 points with $\alpha = 0.001$ has less vertical component in the GM. This means that if no added viscosity is enforced (*i.e.* $\alpha = 0$), the GM tends to become more horizontal with little vertical velocity. In this case, we would probably recover a quasi 2D horizontal GM.

Finally, due to the importance of the vertical velocity $u_z(k_z = 0)$, we decide to consider the GM as a 2D flow with three components (2D3C) satisfying the condition on the vertical wavenumber $k_z = 0$.

5.2.4 Effect of the advection and gradient of the GM on the dispersion relation

In figure 5.5, we can observe the vertical energy spectrum in figure 5.5a of the horizontal GM taken from the numerical simulation with $2\Omega = 5$ and $\nu = 1/2500$ (see table 5.1). The sweeping effect on the dispersion relation of the horizontal GM is shown in figures 5.5b and c. It is the numerical simulation equivalent of equations (2.68) and (2.69). More precisely, figure 5.5b shows the sweeping effect of a varying horizontal GM with time ($\hat{\mathbf{u}}_h(k_z = 0, t)$) whereas figure 5.5b shows the sweeping effect of a constant horizontal GM with time ($\hat{\mathbf{u}}_h(k_z = 0)$). The effect of the gradient of the horizontal GM on the dispersion relation is shown in figure 5.5d. It solves the numerical simulation equivalent to equations (2.84).

Again, the GM is large scale here as its energy spectrum decreases close to a -4 slope. We cannot compare the result for the GM with the result for the VSHF as the forcing and added dissipation terms for the rotating case are different from the stratified case. Similarly to the stratified case, the gradient of the full GM has no effect on the dispersion relation. However, the sweeping effect of the GM is very large. The effect of sweeping with the *rms* velocity of the GM (*i.e.* $u_{h,rms}(k_z = 0)$) is shown in yellow and is clearly not strong enough to take into account the advection of IW by the GM.

The variability in time of the GM has a large effect on the sweeping effect as in the figure 5.5c the sweeping effect is closely approximated by the *rms* velocity of the GM (by a factor of around 1.5) because the GM is set constant in time. On the contrary,

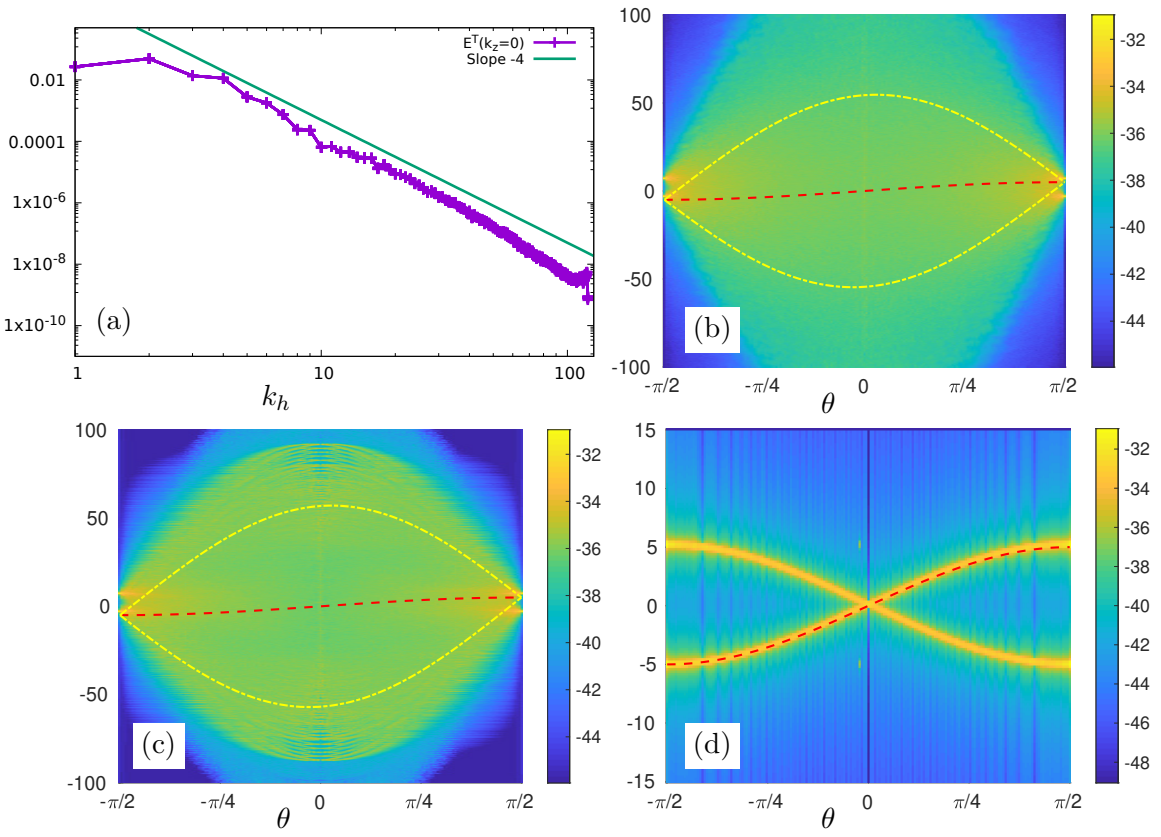

FIGURE 5.5: Effect of the horizontal 2D GM on the dispersion relation. (a) Energy spectrum of the horizontal 2D GM used (b) Sweeping effect of the horizontal GM on the dispersion relation (with time fluctuation) (c) Sweeping effect of the constant value of the horizontal GM on the dispersion relation (no time fluctuation) (d) Gradient effect of the GM on the dispersion relation. Yellow lines are the dispersion relation modified by the sweeping effect calculated by the *rms* velocity. Red lines are the initial dispersion relation.

in figure 5.5b, the GM is allowed to evolve in time and the corresponding effect on the dispersion relation is much larger.

Furthermore, the simulation did not diverge as the simplified cases done with a GM with a constant vertical wavenumber (as in section 2.7.2.6). The reason for this is probably because there is a continuum of wavenumber in the GM. When an unstable point is created with one particular vertical wavenumber, the increasing energy is potentially killed by the convection from another vertical wavenumber.

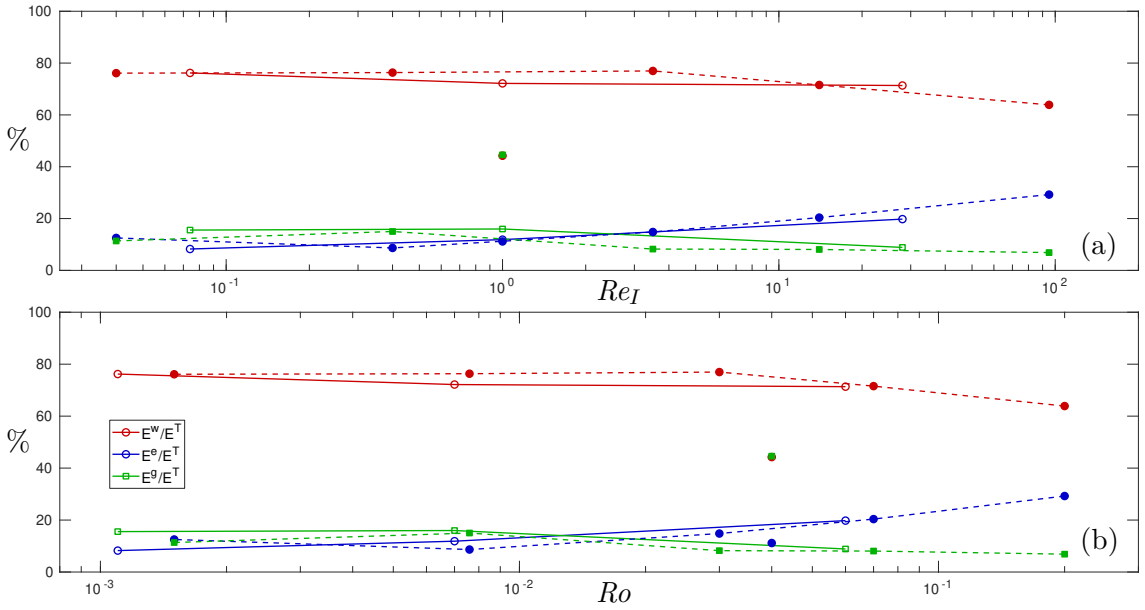

FIGURE 5.6: Evolution of the percentage of energy E^i/E^T for waves ($i = w$), eddies ($i = e$) and geostrophic mode ($i = g$) against (a) Re_I; (b) Ro. Numerical simulations with 512^3 points are shown with open symbols and solid lines, and numerical simulations with 256^3 points are shown with filled symbols and dotted lines.

5.3 Partition of energy

5.3.1 Energy ratio

To get a global understanding of the energy distribution, we first examine the ratio of energy for the wave, eddy and geostrophic modes.

Fgiure 5.6 shows the ratio of the wave energy $E^w = 0.5 < \hat{\mathbf{u}}^w, \hat{\mathbf{u}}^w >$, of the eddy energy $E^e = 0.5 < \hat{\mathbf{u}}^e, \hat{\mathbf{u}}^e >$ and of the GM energy $E^g = 0.5 < \hat{\mathbf{u}}^g, \hat{\mathbf{u}}^g >$ against the total energy $E^T = 0.5 < \hat{\mathbf{u}}, \hat{\mathbf{u}} >$, where $<>$ is defined in equation (3.10) and $\mathbf{u}^w$, $\mathbf{u}^e$ and $\mathbf{u}^g$ are defined in section 3.1.3. Similarly to the stratified case, the result is plotted against the Rossby number Ro and against the inertial Reynolds number Re_I. Simulations with 256^3 points and with 512^3 points are used to compare the influence of the Rossby and inertial Reynolds numbers. At fixed Rossby number, going from the 256^3 points numerical simulations to the 512^3 points simulations increases the Re_I number. At fixed Re_I number, going from the 256^3 points numerical simulations to the 512^3 points simulations decreases the Ro number.

Figure 5.6 shows that, when Ro decreases at fixed Re_I, the GM energy increases slightly and when Ro is fixed and Re_I increases, the GM energy increases slightly as well. The

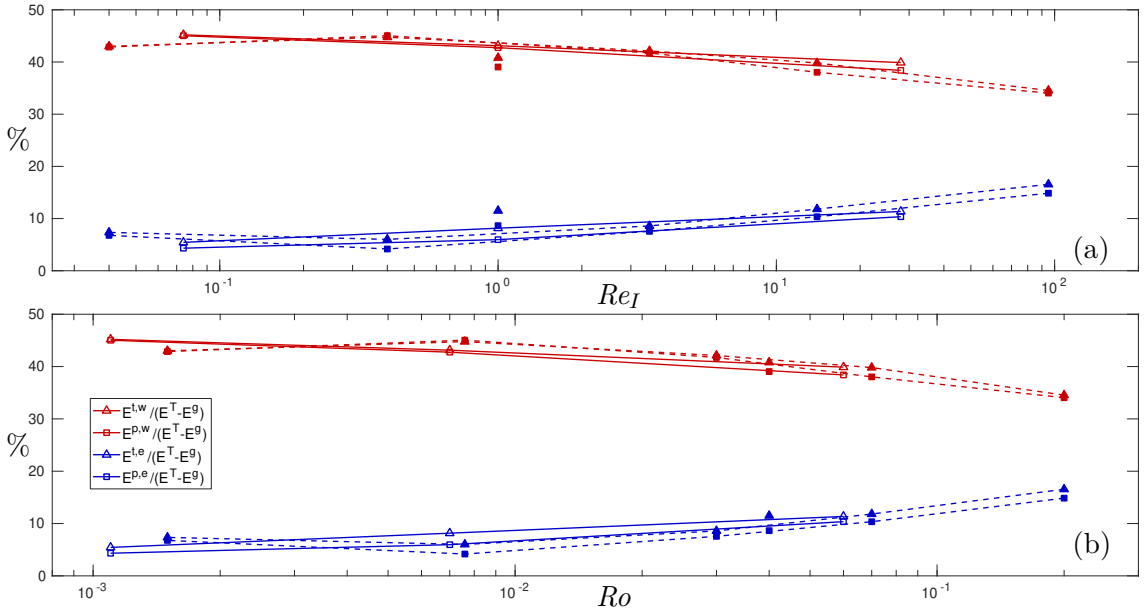

FIGURE 5.7: Evolution of the percentage of poloidal energy ($E^{p,i}/(E^T - E^g)$) and toroidal energy ($E^{t,i}/(E^T - E^g)$) for waves ($i = w$) and eddies ($i = e$) against (a) Re_I; (b) Ro. Numerical simulations with 512^3 points are shown with open symbols and solid lines, and numerical simulations with 256^3 points are shown with filled symbols and dotted lines.

particular numerical simulation with $E^g \simeq 40\%$ of the total energy is higher than the other point because the viscosity added to the GM is smaller in this case ($\alpha = 0.001$) than in the other cases ($\alpha = 0.5$). As for the ratio of wave and eddy energy, it is quite complicated to draw any conclusion as the ratio of these energies is affected by the quantity of energy in the GM.

In figure 5.7, we remove the energy of GM, in order to better analyse the ratio of wave and eddy energy. It shows the toroidal and poloidal wave energies $E^{i,w} = 0.5 < \hat{\mathbf{u}}^{i,w}, \hat{\mathbf{u}}^{i,w} >$ and eddy energies $E^{i,e} = 0.5 < \hat{\mathbf{u}}^{i,e}, \hat{\mathbf{u}}^{i,e} >$ (with $i = t$ or p) against the total energy without the geostrophic mode $E^T - E^g$. First, we observe that the toroidal and potential energy are very close for both the wave and eddy energies. Yet, for both of them the toroidal energy is slightly higher than the poloidal energy. This could be due to the fact that the vertical component $u_z(k_z = 0)$ is removed from the wave and eddy energies and associated with the GM. Furthermore the ratio of wave and eddy energies seems to be dependent on the Rossby number. This is especially clear in the case with 256^3 points with $\alpha = 0.001$. Hence, when the Rossby number increases, the importance of waves decreases and the importance of eddies increases. No conclusion about the dependence with the inertial Reynolds number can be drawn.

5.3.2 Energy spectra

While the ratio of energy of waves and eddies is interesting, more information can be understood from the energy spectra. We observe at the energy spectra against the wavenumber k, horizontal wavenumber k_h and vertical wavenumber k_z for the numerical simulations done with 512^3 points. We do not study the numerical simulations with 256^3 points because their inertial range is smaller and it is hard to draw any conclusion from them.

From the work done in Zeman [149], it is suggested that a k^{-2} scaling could arise in rotating flows. This was also shown in Zhou [151] where an energy scaling of $k^{-5/3}$ was obtained without rotation and an energy scaling k^{-2} with strong rotation. In the intermediate rotation rate, the slope would depend on the ratio of the wavenumber k to the Zeman-Hopfinger wavenumber k_Ω [101, 149]. This slope was also seen in experiments in Baroud et al. [8] where an energy spectrum close to k^{-2} was observed from PIV measurements of a rotating flow with $Ro = 0.06$ and $Re_\lambda = 360$. More recently a k^{-2} scaling was observed in the DNS done in Mininni et al. [99] at small wavenumber and in Müller and Thiele [108] where they found a k_h^{-2} scaling in their DNS.

However, other scaling could be expected. In the theoretical work by Galtier [51], he found that in the limit where $k_h \gg k_z$ with structure elongated along the horizontal plane, the anisotropic spectra obtained are $E(k) \sim k_h^{-5/2} k_z^{-1/2}$. Numerous works tried to recover these anisotropic spectra such as in Sharma et al. [123] where they found similar anisotropic spectra as Galtier [51] but by selecting precise values of vertical wavenumber $1 \leq k_z \leq 6$ and a precise value of horizontal wavenumber $k_h = 35$.

Other works seem to observe a $k^{-5/3}$ energy scaling. For example, Mininni et al. [99] found an energy scaling $k^{-5/3}$ for large wavenumber in their DNS. In an experiment done in Baqui and Davidson [6] at a large Rossby number $Ro \simeq 0.4$ the energy spectrum found was $k_h^{-5/3}$ but also $k_z^{-5/3}$. Baqui et al. [7] also found that for smaller Ro number no slope was observed. In Alexakis and Biferale [3], it is explained that in rotating flow we expect a $k^{-5/3}$ energy spectrum when the wavenumber k is bigger than the Zeman-Hopfinger scale $k > k_\Omega$ and when the wavenumber k is bigger than the forcing scale. When the wavenumber k is between the forcing and Zeman-Hopfinger wavenumber, the energy spectrum slope will depend on the process that drives the cascade of energy. It can be the weak wave turbulence, the helicity transfer, the energy cascade, the enstrophy cascade or a mix of them.

Finally, Vallgren et al. [141] found an energy slope ranging from k^{-3} for $Ro = 0$ to an energy slope $k^{-5/3}$ at large Rossby $Ro = 0.2$. Moreover, Le Reun et al. [77] also found a k^{-3} scaling for low Rossby number in their DNS with a linear forcing.

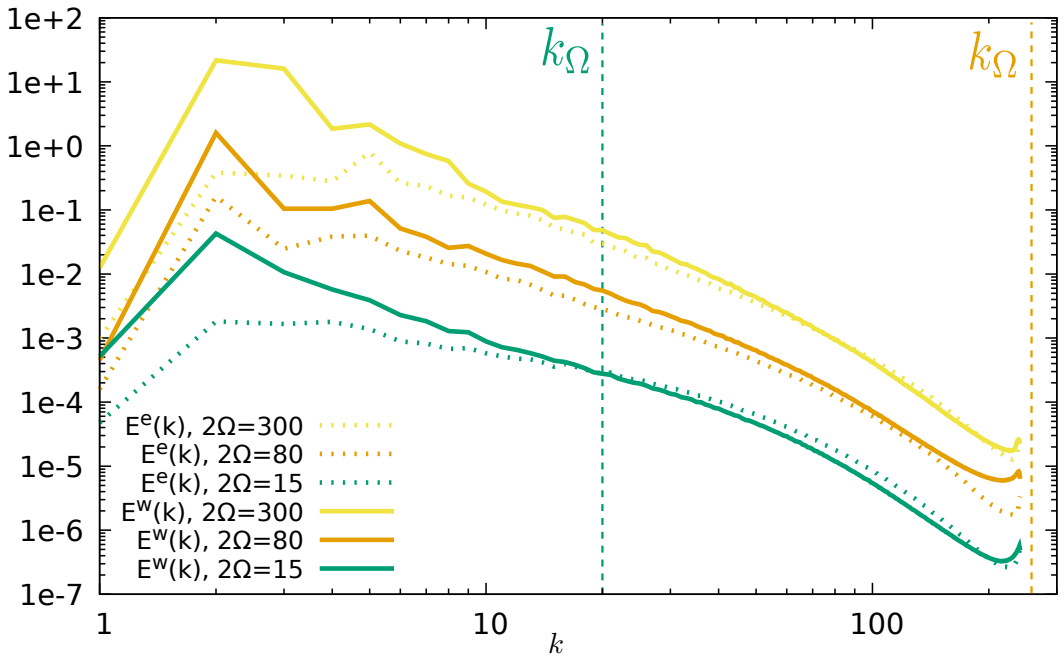

FIGURE 5.8: Comparison between the energy spectra of the eddy part and wave part. The Zeman-Hopfinger scale k_Ω is also represented when possible. Numerical simulations with a different rotation rate 2Ω are shifted by a power of 10 for clarity.

5.3.2.1 Energy spectra vs k

In a first approach, we consider the energy spectra against the wavenumber k. The eddy energy spectrum is $E^e(k) = 0.5 < \hat{\mathbf{u}}^e, \hat{\mathbf{u}}^e >_k$ and wave energy spectrum is $E^w(k) = 0.5 < \hat{\mathbf{u}}^w, \hat{\mathbf{u}}^w >_k$ where $<>_k$ is defined in (3.11). Figure 5.8 shows the difference between the wave and eddy energy for the three cases of study with 512^3 points. At large scale (or small wavenumber k), the wave energy dominates a lot the eddy energy. When the scale decreases (or wavenumber k increases) the difference between the wave and eddy energy decreases. Hence the slope observed for wave energy spectra should be higher than for the eddy energy spectra. In the case $2\Omega = 15$ the eddy energy is higher than the wave energy for a wavenumber $k \leq 20$. For the two other cases, the eddy energy is close (or overcome slightly) the wave energy for a wavenumber $k \simeq 100$. This result can be analysed against the Zeman-Hopfinger wavenumber $k_\Omega = \sqrt{\frac{(2\Omega)^3}{\varepsilon}}$ which is the wavenumber at which we expect eddies to dominate the waves. For $2\Omega = 15$, the Zeman-Hopfinger wavenumber is $k_\Omega = 20$ which is not exactly the result we obtained. For $2\Omega = 80$ the Zeman-Hopfinger wavenumber is $k_\Omega \simeq 240$ and for $2\Omega = 300$ the Zeman-Hopfinger wavenumber is $k_\Omega \simeq 1700$. The result for larger rotation rate is a bit different than the expected result from the Zeman-Hopfinger wavenumber. Yet the overall trend is respected, the limit wavenumber where the eddies are more important than the waves increase with the rotation rate.

We compared the wave and eddy energy spectrum qualitatively, we now focus on the quantification of each energy spectrum. Figure 5.9 shows the energy spectra of waves (figure 5.9a) and eddies (figure 5.9b) against the wavenumber k with some typical slope that can be found in the litterature.

We observe that the wave energy spectra are closer to a -2 slope for the most turbulent cases $2\Omega = 80$ and $2\Omega = 15$. For the rotating case $2\Omega = 300$, the wave energy spectrum seems closer to a -3 slope. The eddy energy spectra seems closer to a $-5/3$ slope in the event $2\Omega = 80$ and $2\Omega = 300$. In the case where $2\Omega = 15$ the energy spectrum is flatter than a $-5/3$ slope.

These results can be observed against the literature. At high rotation rate, Le Reun et al. [77], Vallgren et al. [141] found an energy scaling close to k^{-3}. This is indeed what we found in the wave part of the flow which dominate the flow. No scaling close to $k^{-5/3}$ is observed in this regime as this seems to be related to the eddies and they are hidden by the waves as they dominate the flow. For lower rotation rate, we observe a clear k^{-2} scaling for the waves. This is again a result that has been found in numerous works [8, 99, 149, 151]. In the work of Sharma et al. [123], the scaling obtained is steeper and closer to a $k^{-5/2}$ slope, but it could be due to the fact that the forcing is relatively small scale and the scaling is applied on a scale larger than the forcing. On the contrary, in our numerical simulation the forcing is large scale and the scaling is applied to a smaller scale than the forcing. Hence, different physical phenomena are responsible for an inverse and direct cascade of energy and it could result in a steeper energy spectrum for a backward cascade of energy than for a forward cascade of energy. For the very small slope in the eddy part at $2\Omega = 15$, we can do two hypotheses. It can be related to the physics of the flow, but it can also be a representation of the limit of the algorithm where some parts of the eddy spectrum are assimilated to waves. As the waves dominate the flow this does not necessarily change the energy spectrum of waves, but it could modify substantially the energy spectrum of eddies.

5.3.2.2 Energy spectra vs k_z

As the rotation rate modifies the flow, the flow is anisotropic. It means that the statistics of the flow change with different directions. Hence, similarly to the stratified case, the energy spectra can be studied against the vertical and horizontal wavenumber to take into account the anisotropic properties of the flow. In this subsection, we consider the energy spectrum of waves and eddies against the vertical wavenumber k_z.

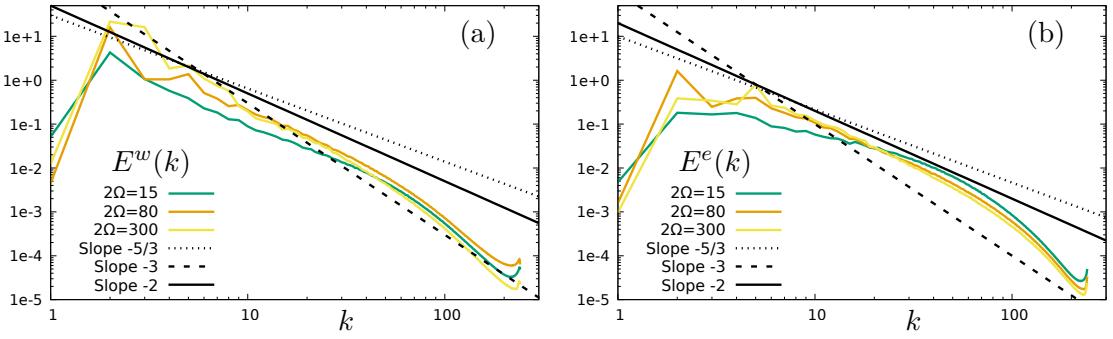

FIGURE 5.9: Wave (a) and eddy (b) energy spectra for numerical simulations with 512^3 points shown in table 5.1 against wavenumber k. Typical slopes are placed for reference.

Figure 5.10 shows the energy spectra of waves (figure 5.10a) and eddies (figure 5.10b) against the vertical wavenumber k_z with some typical slope that can be found in the literature. For the wave energy spectra, it seems that the slope increases as the rotation rate increases as well. For $2\Omega = 15$ the energy wave spectrum is close to a $-5/3$ slope and for $2\Omega = 80$ the energy wave slope is between a -2 and a -3 slope. For large rotation rate $2\Omega = 300$ the wave energy spectrum has a very high slope, higher than a -3 slope. For the eddy energy spectrum, the same overall analyses can be made. When the rotation rate increases, the slope of the eddy energy spectrum increases as well. For $2\Omega = 15$ the eddy energy spectrum slope is lower than the $-5/3$ slope. For $2\Omega = 80$ the eddy energy spectrum slope is slightly lower than the -2 slope. For $2\Omega = 300$ the eddy energy spectrum is lower than the -3 slope.

The higher slope at a higher rotation rate can be explained as, when the rotation rate increases, the energy tends to be more and more two dimensional so that the energy decreases faster against k_z.

These results are quite far from the analytical solution found in Galtier [51] where $E(k) \sim k_h^{-5/2} k_z^{-1/2}$. This could be explained as we do not select a particular k_h and vary the value of k_z as done in Le Reun et al. [77] which recover the Zakharov-Kolmogorov spectrum derived in Galtier [51]. At a large Rossby number $Ro \simeq 0.4$, Baqui and Davidson [6] found an energy spectrum evolving as $k^{-5/3}$ which seems to be very close to our result for $2\Omega = 15$ (and a $Ro = 0.06$).

5.3.2.3 Energy spectra vs k_h

In this subsection, we consider the energy spectra against the horizontal wavenumber k_h.

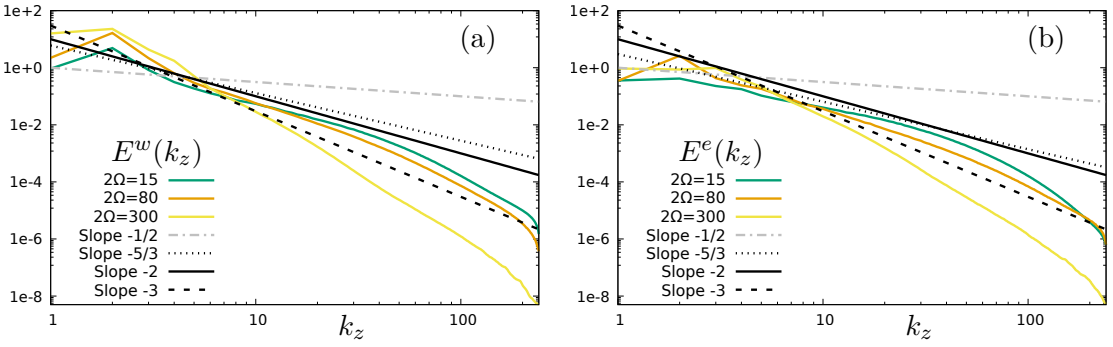

FIGURE 5.10: Wave (a) and eddy (b) energy spectra for numerical simulations with 512^3 points shown in table 5.1 against the vertical wavenumber k_z. Typical slopes are placed for reference.

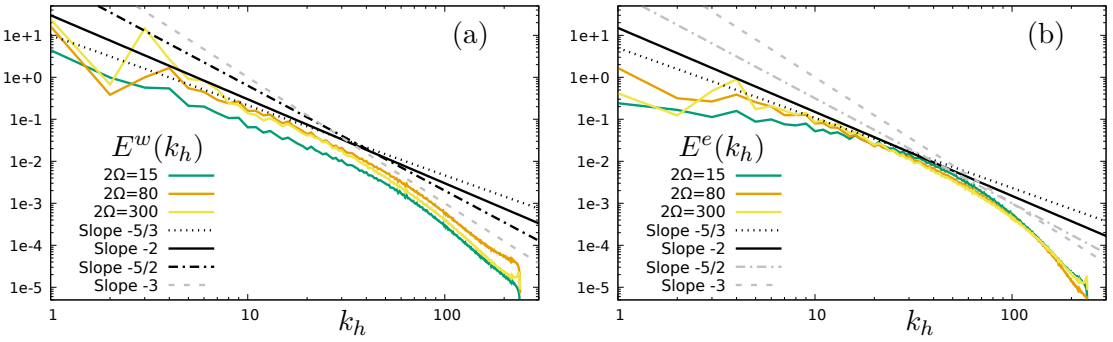

FIGURE 5.11: Wave (a) and eddy (b) energy spectra for numerical simulations with 512^3 points shown in table 5.1 against the horizontal wavenumber k_h. Typical slopes are placed for reference.

Figure 5.11 shows the energy spectra of waves (figure 5.11a) and eddies (figure 5.11b) against the horizontal wavenumber k_h with some typical slope that can be found in the literature. For $2\Omega = 80, 300$, a -2 slope for the wave energy spectra is obtained. In the case $2\Omega = 15$, it seems that we are closer to a $k^{-5/3}$ slope. For the eddy energy spectra, a $-5/3$ slope is obtained for $2\Omega = 80$ and $2\Omega = 300$. For the eddy energy spectrum at $2\Omega = 15$ the slope obtained is lower than a $-5/3$ slope.

These results are again quite far from the analytical study done in [51] where $E(k) \sim k_h^{-5/2} k_z^{-1/2}$. However, for the same reason as in section 5.3.2.2 we select all k_z in our energy spectrum against k_h and that could modify our results. In a different DNS done in Le Reun et al. [77] where such separation is done the analytical solution found by Galtier [51] is obtained. Furthermore, it is not sure that we have $k_h \gg k_z$. Yet, our result still matches other works as for example in Müller and Thiele [108] an energy spectrum close to k^{-2} was found for a $Ro \sim 10^{-2}$. This suggests that the energy spectrum that they measured was probably mostly composed of IW. For a large Rossby number ($Ro \simeq 0.4$), Baqui and Davidson [6] found an energy spectrum to be close to $k_h^{-5/3}$. This could

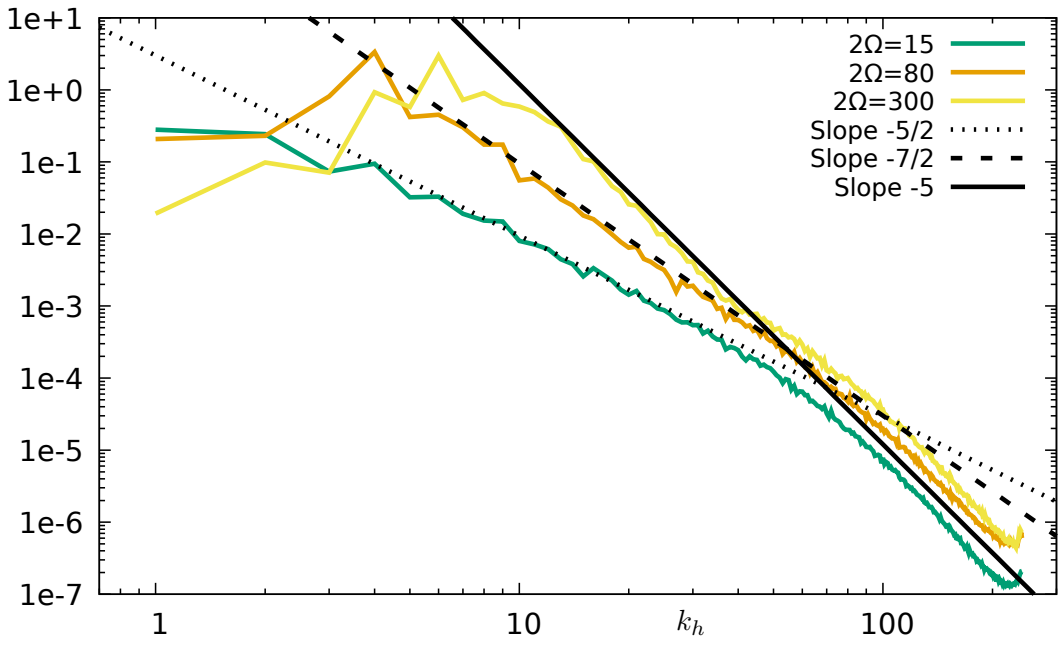

FIGURE 5.12: Energy spectrum of the 3D GM for various numerical simulations against the horizontal wavenumber k_h.

be the imprint of the eddy energy spectrum (as we expect few waves at that Rossby number). Yet, our eddy energy spectrum flatten at $2\Omega = 15$ while we should probably recover the same energy spectrum as in the other two rotation rate. This strange, sudden change supports the hypothesis that our separation technique could set as waves what should normally be an eddy. This could result in a lower than expected scaling for the eddy energy. Similarly to section 5.3.2.1, the scaling of the energy spectrum obtained in Verma et al. [143] against the horizontal wavenumber k_h is steeper than our scaling. Again, this could be due to the fact that in Verma et al. [143], the scaling is done on a larger scale than the forcing, whereas our scaling is done at a scale smaller than the forcing scale. As a result, the scaling could be different because in one case a forward cascade of energy occurs and in the other case an inverse cascade of energy occurs.

Figure 5.12 shows the energy spectrum of the 3D GM (with $u_h(k_z = 0)$ and $u_z(k_z = 0)$) from different numerical simulations with varying rotation rate. We observe that the larger the rotation rate the steeper the slope of the energy spectrum of the GM. Starting from $2\Omega = 15$, the energy of the GM follows a $k^{-5/2}$ slope, whereas at $2\Omega = 300$, the energy follows a k^{-5} slope. Hence the GM is indeed large scale, but that scale seems to get slightly smaller as 2Ω increases (the peak of energy is obtained at a larger wavenumber k). We do not know why these slopes arise. There might be an effect of the added viscosity α. A different added viscosity value of α could change the energy spectrum of the GM. Note that the energy spectrum of the GM is exactly the same against the wavenumber k and k_h as the vertical wavenumber is null $k_z = 0$.

5.4 Balance of energy and flux

5.4.1 Equation of energy

We compute the Lin type equation for the waves, eddies and the GM in a rotating flow as done in Verma [142] for isotropic turbulence or as done in section 4.4 for stratified flows. To do so, we start by taking the Fourier transform in space of equation (2.17):

$$\partial_t \hat{\mathbf{u}}(\mathbf{k},t) = -\widehat{\boldsymbol{\omega}\times\mathbf{u}}(\mathbf{k},t) - \mathrm{i}\mathbf{k}\hat{p}(\mathbf{k},t) - \nu k^2\hat{\mathbf{u}}(\mathbf{k},t) - 2\Omega\times\hat{\mathbf{u}}(\mathbf{k},t) + \hat{\mathbf{F}}_{\mathbf{u}}(\mathbf{k},t) \tag{5.3}$$

where $-\widehat{\boldsymbol{\omega}\times\mathbf{u}}(\mathbf{k},t)$ is the 3D Fourier transform in space of $\boldsymbol{\omega}\times\mathbf{u}(\mathbf{x},t)$.

Multiplying equations (5.3) by $\dfrac{\overline{\hat{\mathbf{u}}^l(\mathbf{k},t)}}{2}$ and adding the resultant equation with its complex conjuguate, we obtain:

$$\partial_t \,\mathrm{Re}\left\{\frac{\hat{\mathbf{u}}\cdot\overline{\hat{\mathbf{u}}^l}}{2}\right\}(\mathbf{k},t) = -\,\mathrm{Re}\left\{\widehat{\boldsymbol{\omega}\times\mathbf{u}}\cdot\overline{\hat{\mathbf{u}}^l}\right\}(\mathbf{k},t) - \nu k^2\,\mathrm{Re}\left\{\frac{\hat{\mathbf{u}}\cdot\overline{\hat{\mathbf{u}}^l}}{2}\right\}(\mathbf{k},t) + \mathrm{Re}\left\{\hat{\mathbf{F}}_{\mathbf{u}}\cdot\overline{\hat{\mathbf{u}}^l}\right\}(\mathbf{k},t) \tag{5.4}$$

where l stands for w=wave, e=eddy or g=GM.

As the wave, eddies and GM components are defined disjoint in spatial and time Fourier domain in our decomposition, the average on the large period T_0 is $[\hat{\mathbf{u}}^l,\hat{\mathbf{u}}] = [\hat{\mathbf{u}}^l,\hat{\mathbf{u}}^w + \hat{\mathbf{u}}^e + \hat{\mathbf{u}}^g] = [\hat{\mathbf{u}}^l,\hat{\mathbf{u}}^l]$ where $[,]$ is defined in equation (3.9). This time the GM has enough energy and is kept into account.

Thus, taking the average over the period T_0 of equation (5.4), summing over all wavevectors $\mathbf{k}$ on a sphere of radius $K = |\mathbf{k}|$ and decomposing the non-linear term in its wave, eddy or GM parts, we obtain:

$$\partial_t e^l(K) = \sum_{i=w,e,g} t^l_{iw}(K) + t^l_{ie}(K) + t^l_{ig}(K) - 2\nu K^2 e^l(K) + p^l(K) \tag{5.5}$$

To define all the terms in equation (4.14), we use the operator $<>_K$ defined at the end of section 3.1.3.1. The kinetic energy is $e^l(K) =< \hat{\mathbf{u}},\hat{\mathbf{u}}^l >_K$, the transfers are $t^l_{ij}(K) = - < \widehat{\boldsymbol{\omega}^i\times\mathbf{u}^j},\hat{\mathbf{u}}^l >_K$ and the forcing is $p^l(K) =< \mathbf{F}_{\mathbf{u}},\hat{\mathbf{u}}^l >_K$. The non-linear term produces nine different possibilities for every l part as the term $\boldsymbol{\omega}\times\mathbf{u} = \sum_{i,j=w,e,g}\boldsymbol{\omega}^i\times\mathbf{u}^j$. As explained in section 4.4, the particular transfer $t^w_{ww}(K)$ corresponds to the triad interaction where for any wavevector $\mathbf{p}$, $\mathbf{q}$ and $\mathbf{k}$ we get a spatial resonance $\mathbf{p}+\mathbf{q}=\mathbf{k}$ and a temporal resonance $\omega_c(\mathbf{p})+\omega_c(\mathbf{q}) = \omega_c(\mathbf{k})$ [133] with $\omega_c(\mathbf{k})$ the dispersion relation of waves modified by the sweeping effect and defined in equation (2.75).

Summing over all wavenumbers K in equation (5.5), we obtain:

$$dE^w/dt = T^w_{ee} + T^w_{we} + T^w_{wg} + T^w_{ge} + T^w_{eg} + \varepsilon^w + P^w \tag{5.6a}$$

$$dE^e/dt = T^e_{ww} + T^e_{ew} + T^e_{wg} + T^e_{gw} + T^e_{eg} + \varepsilon^e + P^e \tag{5.6b}$$

$$dE^g/dt = T^g_{ee} + T^g_{we} + T^g_{ww} + T^g_{ew} + \varepsilon^g \tag{5.6c}$$

where the kinetic dissipation is $\varepsilon^l = \nu < k^2\hat{\mathbf{u}}^l, \hat{\mathbf{u}}^l >$ for $l = w$ or e and $\varepsilon^g = \nu < k^2\hat{\mathbf{u}}^g, \hat{\mathbf{u}}^g > +\alpha < \hat{\mathbf{u}}^g, \hat{\mathbf{u}}^g >$. The kinetic transfer is $T^l_{ij} = - < \widehat{\boldsymbol{\omega}^i \times \mathbf{u}^j}, \hat{\mathbf{u}}^l >$ and the injected power $P = P^w + P^e$ for each part is $P^l =< \hat{\mathbf{F}}_\mathbf{u}, \hat{\mathbf{u}}^l >$. As the small evolution in time of the wave E^w, eddy E^e and geostrophic mode E^g energy is known as well as the transfer T^l_{ij} and dissipation ε^l, it is possible to compute the forcing in the wave P^w and the forcing in the eddy P^e. In the statistically stationary regime, $dE^{w,e,g}/dt \simeq 0$ and the equilibrium of the fluxes is reached since all terms compensate one another.

As all our numerical simulations in the rotating case involve a varying forcing power P (from $P = 0.01$ to $P = 20$), this means that the transfer and the different components depend on that variable. Hence, contrary to the stratified case (where P is constant), all transfer components are expressed as a percentage of the total forcing value P.

5.4.2 Sankey diagram

In order to better understand the transfer between the waves, eddies and the GM, we draw the Sankey diagram which represents the full balance of energy (written in equation (5.6)). This representation offers a more visual and less complex analysis of the physical phenomena than a representation of the different parameters of the equations (5.6) against Ro or Re_I.

In the Sankey diagram, for the rotating case, the transfers take the energy from forcing P in part P^w and P^e then they bring the energy to the dissipation composed of three parts ε^w, ε^e and ε^g. While in the stratified case the transfers are only in one direction (from waves to eddies), in the rotating case the energy can be transferred many times from one part of the flow to another part of the flow without being dissipated. This means that, an input/output balance of energy is needed for each part, for eddies (noted B^e), for waves (noted B^w) and for the geostrophic mode (noted B^g). This problem can be understood with an example: since no forcing goes to the GM, there is no origin for the transfer from the GM to eddies or to waves. Hence, there is no source of flux for this transfer, and no graphical link in the Sankey diagram. Hence, it is necessary

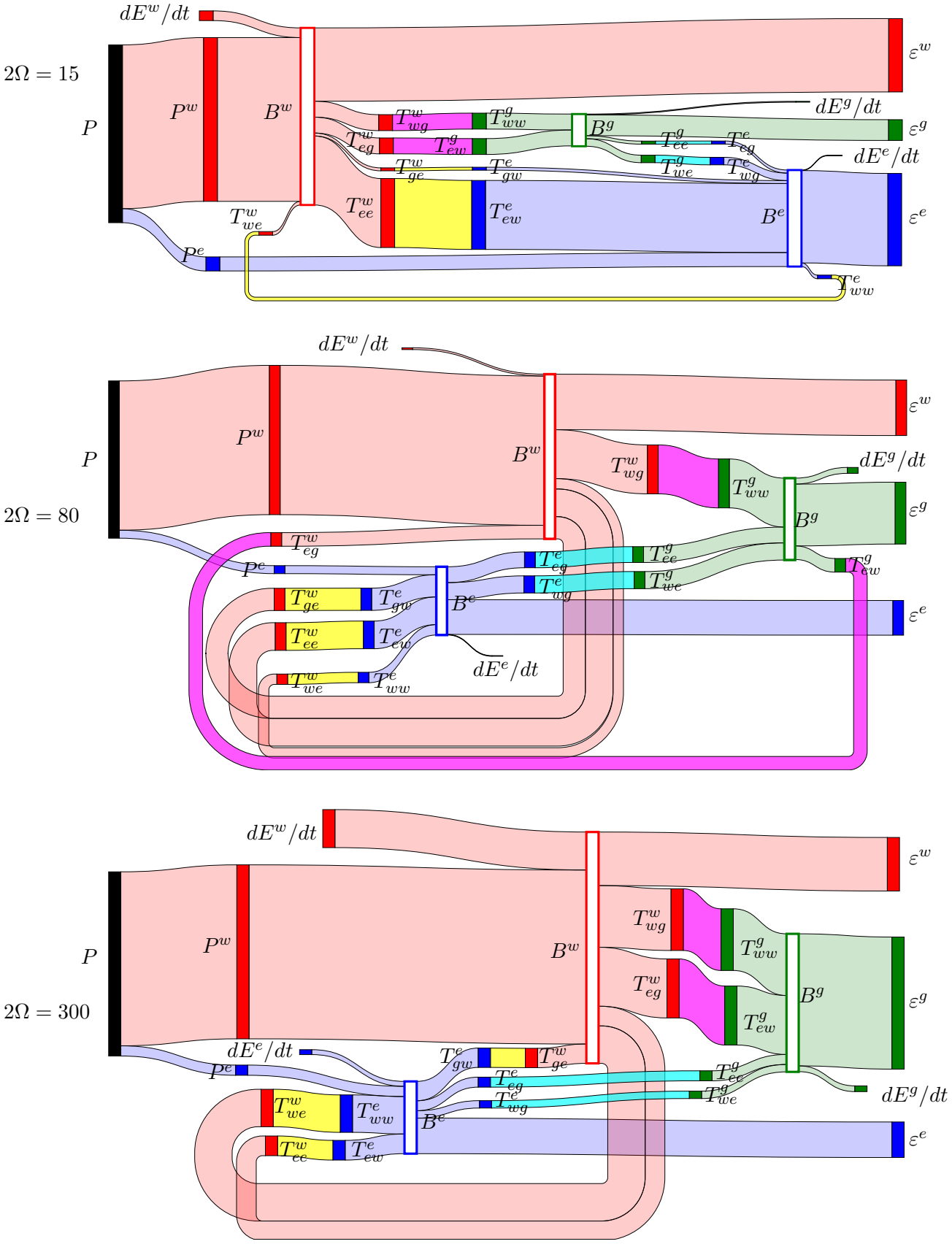

FIGURE 5.13: Sankey diagram representing the different terms of the full Lin equation written in equation (5.6) for the numerical simulation with 512^3 points. The boxes B^l(with $l = w, e, g$) represent the input/output balance of energy for any part l.

to introduce the input/output balance of energy for the GM. All transfers, must take energy to a part B^j to give that energy to a different part B^l. The forcing P^l feeds directly the input/output balance of energy B^l and all the dissipation ε^l dissipates the energy from the input/output balance of energy B^l. We also draw the importance of the variation in time of each energy $\partial_t E^l$ which can give (if negative) or take (if positive) energy to its input/output balance of energy B^l.

A few general and qualitative observations can be made from these Sankey diagrams:

- First, we observe from figure 5.13 that most of the forcing enforces waves as $P^w \gg P^e$ for any Ro and Re_I (see section 5.4.3 and figure 5.14 for a detailed and quantitative analysis).
- Secondly, a lot of energy is transferred from the wave part to the eddy part due to many interactions. The transfer T^e_{ew} is always strong for all cases, but other transfers such as T^e_{gw} and T^e_{ww} appear in some cases. For a detailed and quantitative analysis, you can read section 5.4.3 and section 5.4.4.
- Thirdly, a lot of energy is transferred from the wave part to the GM. It can be due to wave-wave interaction T^g_{ww} in accordance with mechanism find by Brunet et al. [22] or Le Reun et al. [78] in wave turbulence regime. In our simulations, it seems to be still valid in a turbulent regime at higher Re_I. Nonetheless, eddy-wave interaction T^g_{ew} can still play an important role in the transfer of energy from waves to eddies (see section 5.4.5 for a detailed and quantitative analysis).
- Fourthly, at low Ro and Re_I, a small part of energy come from the eddy part to the GM due to the wave-eddy (T^g_{we}) and eddy-eddy (T^g_{ee}) interaction. However, at high Ro and Re_I a small part of energy is taken from the GM to the eddy part through the same mechanism (see section 5.4.5).

5.4.3 Global flux of energy

According to the Sankey diagram (5.13), we describe globally and quantitatively the different fluxes occuring in rotating turbulence. In order to do this, we introduce the global transfer between each part. We introduce :

- the total transfer from eddies to waves: $T^w_{*e} = T^w_{we} + T^w_{ee} + T^w_{ge}$
- the total transfer from waves to eddies: $T^e_{*w} = T^e_{ww} + T^e_{ew} + T^e_{gw}$
- the total transfer from eddies to the GM: $T^g_{*e} = T^g_{we} + T^g_{ee}$

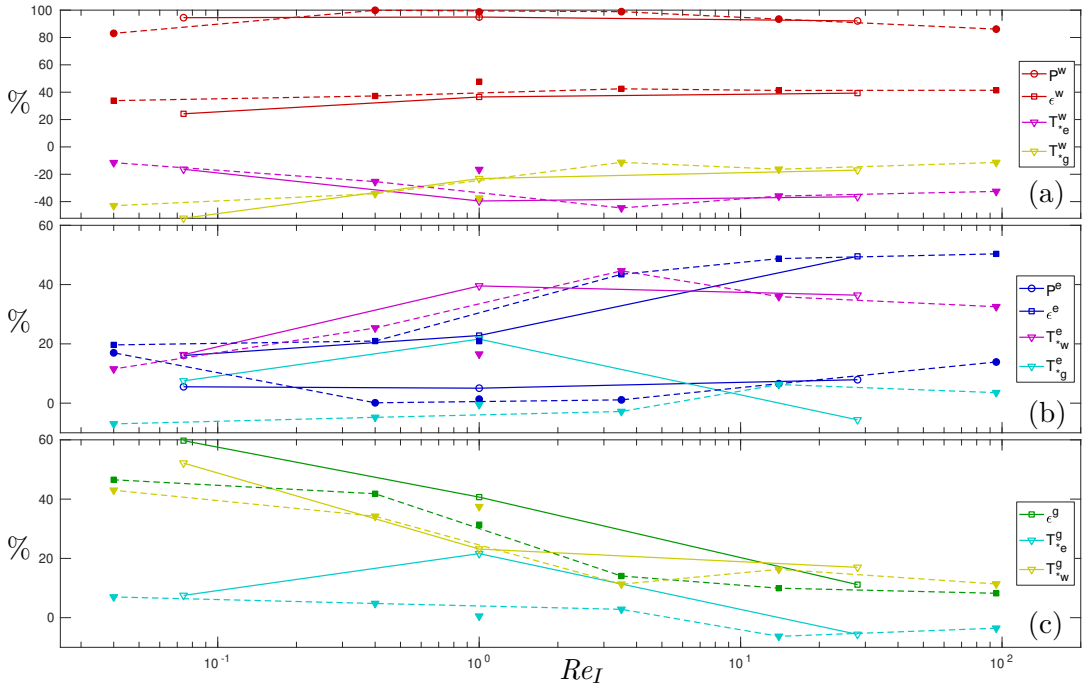

FIGURE 5.14: Evolution with Re_I of the percentage of the contributions of forcing P^l, dissipation ε^l and transfer T^l_{*j} from j to l for (a) $l = w$, (b) $l = e$, (c) $l = g$. Numerical simulations with 512^3 points correspond to open symbols and solid lines, numerical simulations with 256^3 points to filled symbols and dotted lines.

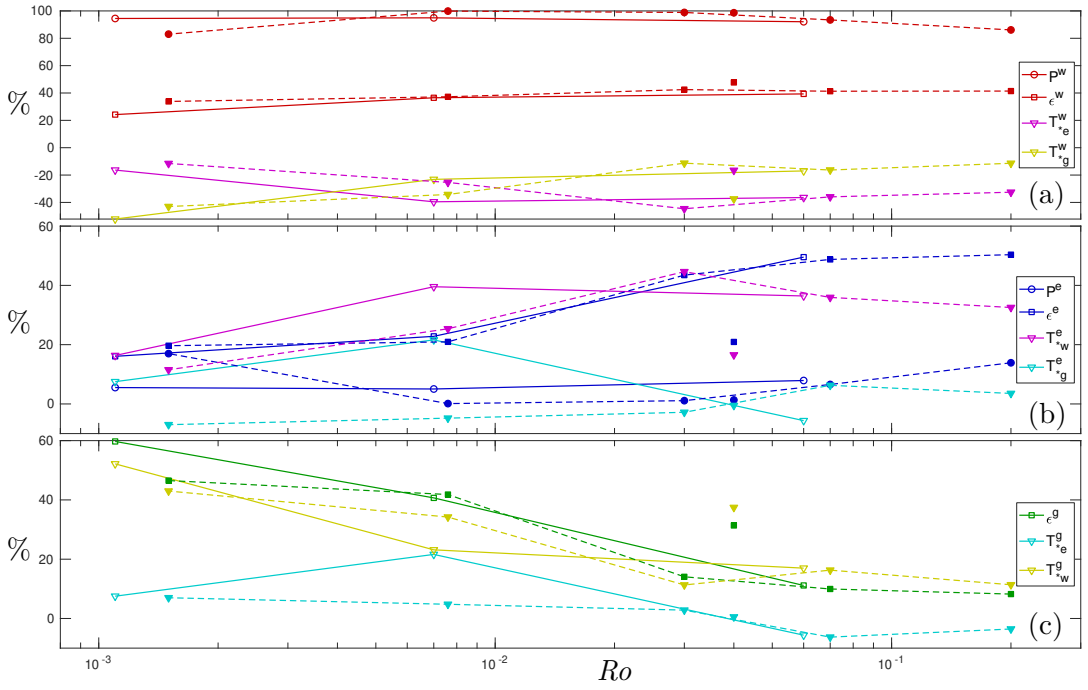

FIGURE 5.15: Evolution with Ro of the percentage of the contributions of forcing P^l, dissipation ε^l and transfer T^l_{*j} from j to l for (a) $l = w$, (b) $l = e$, (c) $l = g$. Numerical simulations with 512^3 points correspond to open symbols and solid lines, numerical simulations with 256^3 points to filled symbols and dotted lines.

- the total transfer from waves to the GM: $T^g_{*w} = T^g_{ww} + T^g_{ew}$

Figure 5.14a shows the component of the simple and condensed Lin equation for the wave part (a), for the eddy part (b), and for the GM (c) of the equation (5.6) against the inertial Reynolds number Re_I. The same figure is done against the Rossby number in the figure 5.15.

As the forcing amplitude P differs between all cases, all results are shown in terms of percentage against the total amplitude of forcing P. We observe that P^w always contains more than 85% whereas P^e contains less than 15% of the total forcing. Therefore, most of the forcing P goes to the waves especially at medium Re_I.

Since the waves receive most of the energy of the forcing, then it explains why the transfer T^e_{*w} in figure 5.14 is huge and pumps up to 40% of the total energy from the waves to give it to eddies through the transfer T^e_{*w} visible in figure 5.14b. This transfer increases with Ro and Re_I.

There is no forcing on the GM, so we observe that the sum of transfer in the GM is roughly equal to the dissipation of the GM (as the flow is stationary). We observe that in all cases of figure 5.14c, most of the GM energy comes from waves. Eddies do not give much energy and can even take energy from the GM at small rotation rate. Transfer from eddies to GM (T^g_{*e}) and waves to GM (T^g_{*w}) tend to decrease as Ro and Re_I increase. It becomes negative for the transfer from eddies to GM (T^g_{*e}) at the highest Ro and Re_I. This means that the energy of the GM is transferred to the eddy part and the GM energy decreases as seen in figure 5.6.

5.4.4 Detailed analysis of the transfers from waves to eddies

In the previous analysis of transfer we focused only on the general transfer between the same quantities (between waves themselves, or eddies themselves or GM themselves). We did not separate the effect of the different interactions. Here, we consider how the transfer of energy occurs from the waves to the eddies by analysing the different components T^e_{iw} of the transfer T^e_{*w}. Note that, as $T^e_{iw} = -T^w_{ie}$ (see appendix B for a detailed proof), we do not consider the transfer between eddies to waves.

Figure 5.16 shows the transfers from waves to eddies T^e_{iw}. First, we can say that in nearly all cases and all transfers there is a global transfer from waves to eddies. It seems that the transfer T^e_{ww} tends to decrease when the rotation rate decreases, this is especially true for the simulations with 512^3 points, yet for the numerical simulations with 256^3 points the conclusion is harder. When the Rossby number increases, we expect less

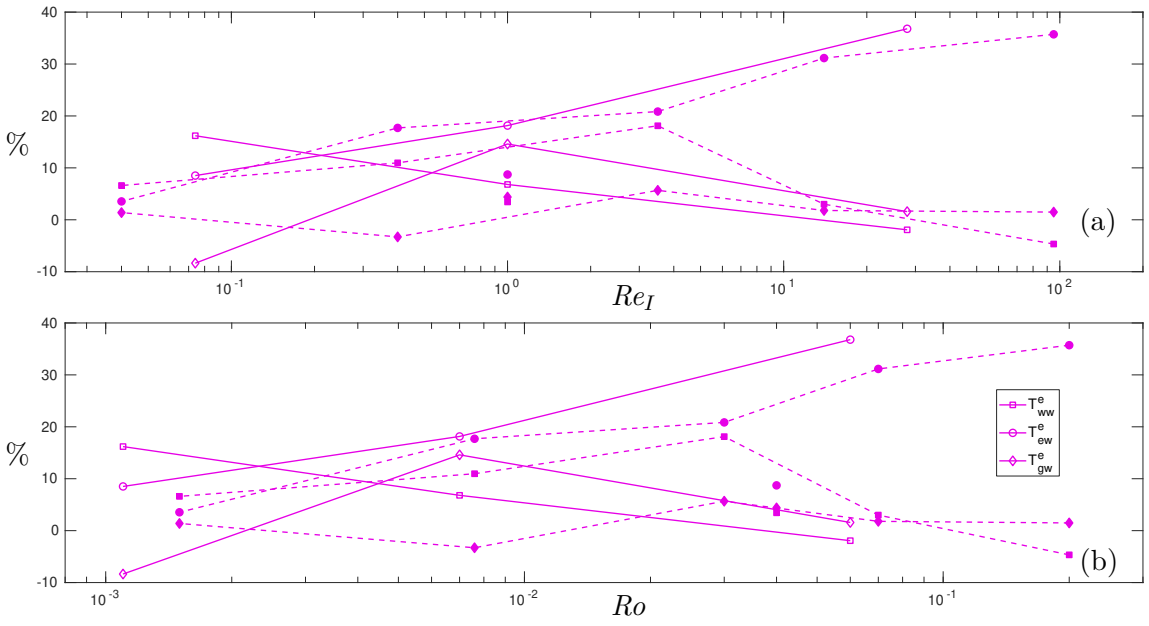

FIGURE 5.16: Evolution of the total transfer from waves to eddies T^e_{iw} (with $i = w$ or e or g) against (a) Re_I; (b) Ro. Numerical simulations with 512^3 points are shown with open symbols and solid lines, and numerical simulations with 256^3 points are shown with filled symbols and dotted lines.

waves in the flow (see section 5.3.1), so it seems logic that the transfer T^e_{ww} decreases as it involves the interactions between two waves. The result of the transfer T^e_{ew} is a bit clearer. It seems to increase mainly with Re_I, when the flow is more turbulent. When the flow becomes more turbulent and since we force mainly the wave part, this interaction lead to a transfer from the waves to the eddies. Not much can be said on the transfer T^e_{gw} as many fluctuations occur.

5.4.5 Detailed analysis of the transfers from waves or eddies to the GM

We consider how the transfer of energy occurs from the waves or eddies to the GM by analysing the different components T^g_{ij} of the transfer T^g_{*j} (with $j = w, e$). Note that, as $T^g_{ij} = -T^j_{ig}$, we do not consider how the energy is pumped from the GM.

Figure 5.17 shows the transfers T^g_{ij} that take energy from waves or eddies to give energy to the GM. We observe that, in general the wave-wave interaction (T^g_{ww}) is higher than the other transfer. However, for a few cases of large or small Ro and Re_I, we observe that the eddy-wave interaction (T^g_{ew}) is equivalent to the wave-wave interaction ($T^g_{ew} \sim T^g_{ww}$). Nevertheless, around $Ro \sim 0.01$ and $Re_I \sim 1$, the transfer $T^g_{ew} < 0$, meaning that energy is pumped from the GM to be given to the waves.

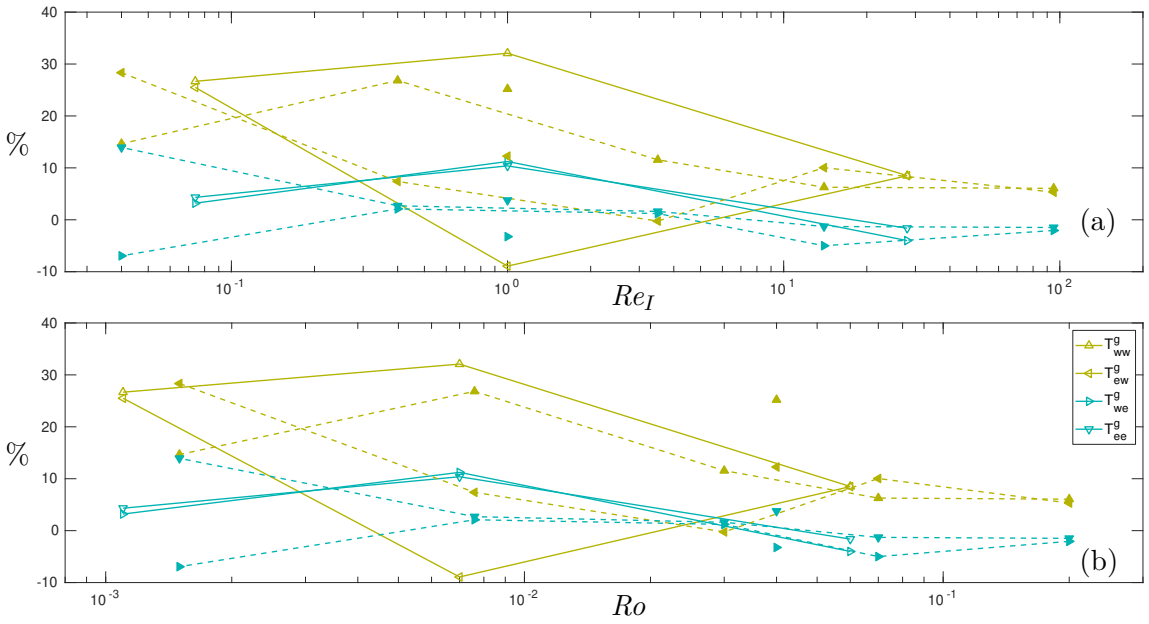

FIGURE 5.17: Evolution of the total transfer from waves or eddies to the GM $T^g_{ij} = T^{+,g}_{ij} + T^{-,g}_{ij}$ (with $i, j = w$ or e) against (a) Re_I; (b) Ro. Numerical simulations with 512^3 points are shown with open symbols and solid lines, and numerical simulations with 256^3 points are shown with filled symbols and dotted lines.

The eddy-eddy interaction T^g_{ee} transfer always slightly more to the GM than the wave-eddy interaction T^g_{we}. It is also less prone to pump energy of the GM at large Ro and Re_I.

We conclude that in rotating turbulence, the GM is mostly fed by the waves. The first type of transfer found which feeds the GM is the wave-wave interaction (T^g_{ww}). This result opposes the impossibility of exact triadic resonant interaction that feed the GM explained in Greenspan [59]. Yet, it is in accordance with other mechanisms described in Brunet et al. [22], Le Reun et al. [78] for example. The second type of transfer found which feeds the GM is new, it is the eddy-wave interaction T^g_{ew}. Such conclusion shows the diversity of mechanism that can feed the GM.

5.5 Dissipation

After analysing the different properties of the transfer, we can examine the different ratios of the dissipation term by the waves, the eddies and the GM.

In equation (5.6) most of the dissipative terms are already defined. We also define the dissipation rate for the GM due to the added viscous term ν by:

$$\varepsilon^{\nu,g} = \nu < k^2 \hat{\mathbf{u}}^g, \hat{\mathbf{u}}^g > . \tag{5.7}$$

There is still one more dissipation term that occurs. It comes from the added dissipative term α. The dissipation linked to that term is:

$$\varepsilon^{\alpha,g} = \alpha < \hat{\mathbf{u}}^g, \hat{\mathbf{u}}^g > . \tag{5.8}$$

So that the total dissipation term is $\varepsilon^T = \varepsilon^w + \varepsilon^w + \varepsilon^{\nu,g} + \varepsilon^{\alpha,g}$ and the total GM dissipation is $\varepsilon^g = \varepsilon^{\nu,g} + \varepsilon^{\alpha,g}$.

Figure 5.18 shows the percentage of the different dissipative terms against the inertial Reynolds number and the Rossby number. First, we observe that the dissipation of the GM due to the viscosity ν evolves with Re_I. The lower Re_I is, the higher the dissipation on the GM is as well. This is different for the dissipation of the GM due to the viscous term α because it does not seem to be linked to the Ro or Re_I number but simply increases when the rotation rate increases. Overall, the dissipation by the GM increases as the rotation rate increases as well and reach 60% of the total dissipation of the 512^3 points simulations at $Ro = 0.0011$. As for the dissipation by the waves and eddies, they could seem to depend on the Rossby number, but this is actually not the case as their importance is hindered by the modification of the dissipation by the GM.

To better analyse the dissipation of waves and eddies, we prefer to analyse the ratio of the dissipation of waves and eddies against the total dissipation without the dissipation of GM. Furthermore, we define the dissipation by the toroidal and poloidal velocity field by:

$$\begin{aligned} \varepsilon^{t,i} &= \nu < k^2 \hat{\mathbf{u}}^{t,i}, \hat{\mathbf{u}}^{t,i} >, \\ \varepsilon^{p,i} &= \nu < k^2 \hat{\mathbf{u}}^{p,i}, \hat{\mathbf{u}}^{p,i} > \end{aligned} \tag{5.9}$$

where i stands for e or w.

Figure 5.19 shows the percentage of poloidal and toroidal dissipation for waves and eddies against Re_I and Ro. We observe that, when the dissipation is dominated by waves, the poloidal dissipation for waves and eddies is slightly higher than the toroidal dissipation for the same component. When the dissipation is dominated by eddies, it is the toroidal dissipation for waves and eddies that is slightly higher than the poloidal dissipation. This phenomenon could come from the fact that a large part of the toroidal components is removed from the eddy and wave parts to be placed in the GM at small Re_I and Ro. Contrarily, at large Re_I and Ro, we observed that the energy was pumped from the GM

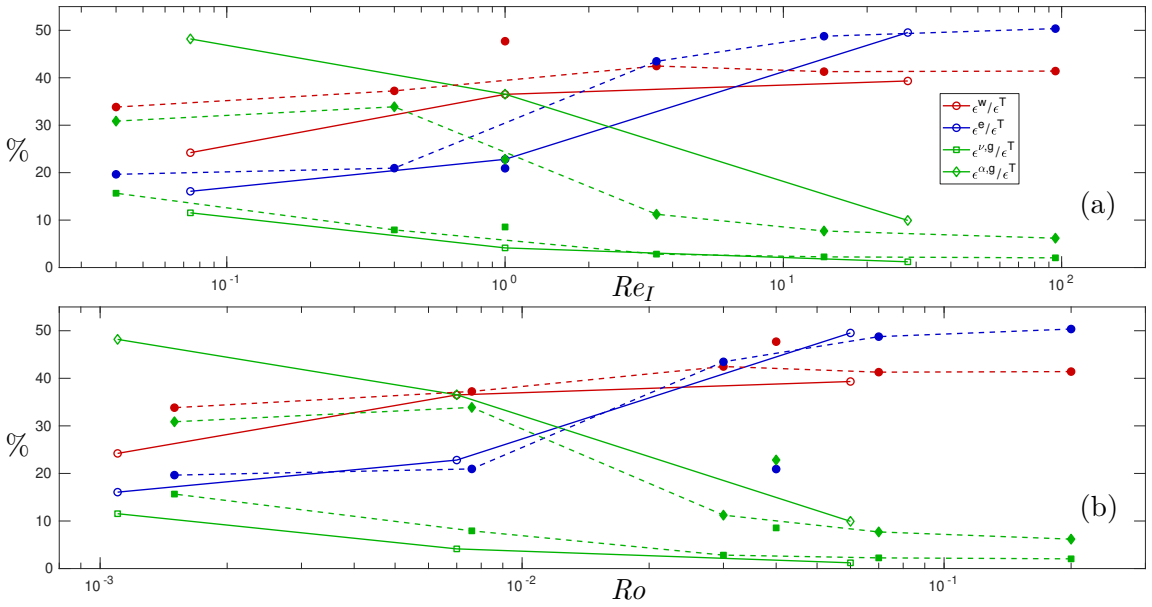

FIGURE 5.18: Evolution of the percentage of dissipation ($\varepsilon^i/\varepsilon^T$ for waves ($i = w$), eddies ($i = e$), geostrophic mode due to the kinematic viscosity ($i = \nu, GM$) and geostrophic mode due to the added viscosity α ($i = \alpha, GM$) against (a) Re_I; (b) Ro. Numerical simulations with 512^3 points are shown with open symbols and solid lines, and numerical simulations with 256^3 points are shown with filled symbols and dotted lines.

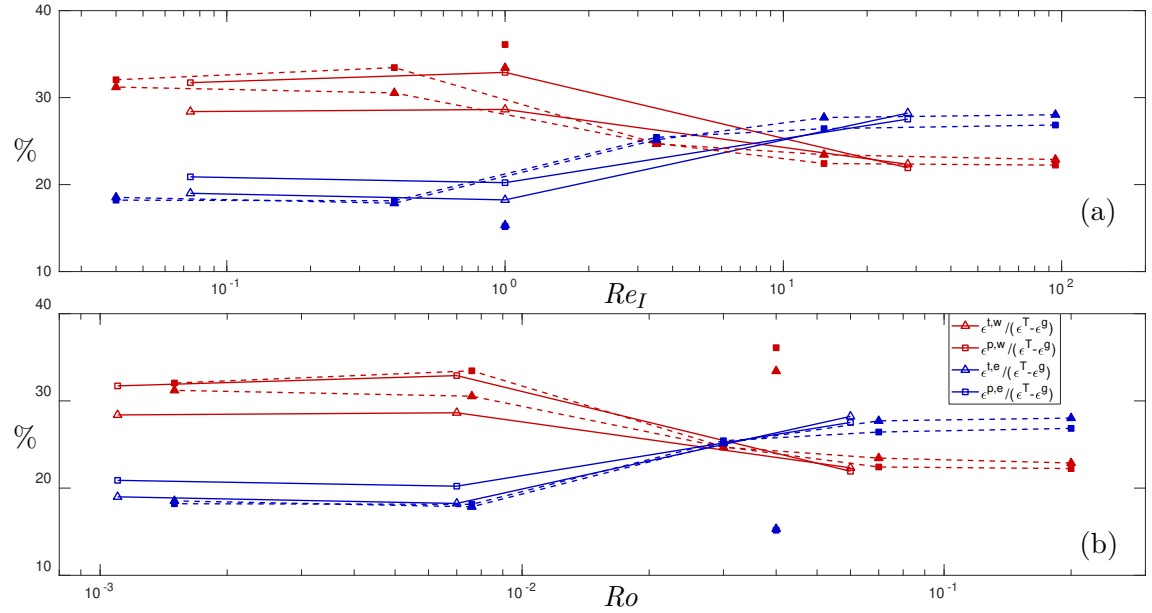

FIGURE 5.19: Evolution of the percentage of toroidal dissipation ($\varepsilon^{t,i}/(\varepsilon^T - \varepsilon^{GM})$ and poloidal dissipation ($\varepsilon^{p,i}/(\varepsilon^T - \varepsilon^{GM})$ for waves ($i = w$) and eddies ($i = e$) against (a) Re_I; (b) Ro. Numerical simulations with 512^3 points are shown with open symbols and solid lines, and numerical simulations with 256^3 points are shown with filled symbols and dotted lines.

to eddies (see section 5.4.5) which could result in more energy in the toroidal part that is dissipated. Moreover, in most previous analyses, we ignored the numerical simulation with 256^3 points and $\alpha = 0.01$ because the numerical parameters were very different from the other numerical simulations. It resulted in a very high quantity of GM in the flow. However, as we focus on the ratio of dissipation without GM, this piece of data is very useful, especially if we assume that the repartition of dissipation between waves and eddies do not significantly depend on the GM. In figure 5.19, it is possible to use this numerical simulation to determine that the ratio of dissipation of waves and eddies depends mostly on the Re_I number. The wave dissipation becomes more important than the eddy dissipation when $Re_I \lesssim 3$. This dependence of the repartition of the wave and eddy dissipation against Re_I can be understood with its definition. As $Re_I = (\frac{k_\eta}{k_\Omega})^{4/3}$, when $k_\Omega \gg k_\eta$ most of the dissipation is done by waves whereas when $k_\Omega \ll k_\eta$ most of the dissipation is done by eddies.

5.6 Scale by scale analysis of transfer

In the analysis of section 5.4, we were interested in the global exchange of energy between waves, eddies and the GM. In this section we focus on the transfer between waves, eddies and the geostrophic mode with themselves in the flow. Some focus will be done on the strength of the forward or backward cascade in the flow.

From the separation of the flow in waves, eddies and GM, it is possible to examine how the transfer between them occurs. In our case, there is a very large number of different possible transfers. Nine interactions ($w+w$, $w+e$, $e+w$, $e+e$, $w+g$, $g+w$, $e+g$, $g+e$ and $g+g$) can occur which can lead to a transfer of energy between the waves or eddies or GM. This means that in total, there are 27 possible transfers.

Yet, all of these transfers are not possible. For example, it is not possible to obtain an eddy or wave component from the interaction of two GM. Indeed, as the GM has $k_z = 0$, it means that the interaction of two GM can only create a new GM: with non-linear interaction of two GM with a wavevector $\mathbf{k} = (k_x, k_y, 0)$ and $\mathbf{p} = (p_x, p_y, 0)$, the resulting wavevector $\mathbf{q}$ must satisfy the equation $\mathbf{k} = \mathbf{p} + \mathbf{q}$. This means that the new wavevector $\mathbf{q} = (k_x - p_x, k_y - p_y, 0)$ is also a GM.
Similarly, it is not possible to obtain a GM through the interaction of a GM with a wave or eddy component. Indeed, a wave or eddy component has a vertical wavenumber $k_z \neq 0$. Hence, for the interaction of a GM with a wavevector $\mathbf{k} = (k_x, k_y, 0)$ with a wave or eddy component with a wavector $\mathbf{p} = (p_x, p_y, p_z \neq 0)$ then the third wave

vector $\mathbf{q}$ of the non-linear interaction must satisfy the equation $\mathbf{k} = \mathbf{p} + \mathbf{q}$. This is the case if and only if $\mathbf{q} = (k_x - p_x, k_y - p_y, -p_z \neq 0)$. This means that no GM can receive energy when it comes from the interaction of a GM and a wave or eddy component. Ultimately, there are only 21 possible transfers in our decomposition. Five transfers take or give energy to the GM and eight transfers that give or take energy to the waves and to the eddies.

Similarly to the stratified case, considering each of these transfers against the wavenumber is very tedious. Instead, we decided to study the same set of variables used in section 4.7 to summarize the transfer $t(k)$, which are redefined here as a reminder:

- $T_{ij}^{+,l} = \sum_{k,\, t_{ij}^l(k)>0} t_{ij}^l(k)$, the total value of transfer given to l by the interaction between i and j,
- $T_{ij}^{-,l} = \sum_{k,\, t_{ij}^l(k)<0} t_{ij}^l(k)$, the total value of transfer pumped from l by the interaction between i and j,
- $k_{ij}^{+,l} = \sum_{k,\, t_{ij}^l(k)>0} \frac{k t_{ij}^l(k)}{T_{ij}^{+,l}}$, the weighted average scale of transfer given to l by the interaction between i and j,
- $k_{ij}^{-,l} = \sum_{k,\, t_{ij}^l(k)<0} \frac{k t_{ij}^l(k)}{T_{ij}^{-,l}}$, the weighted average scale of transfer pumped from l by the interaction between i and j.

Again, in order to facilitate the comprehension of the scale of transfer we use the ratio of weighted average scale $k_{ij}^{+/-,l} = \frac{k_{ij}^{+,l}}{k_{ij}^{-,l}}$ for the potential and kinetic transfers. When this ratio is lower than one ($k_{ij}^{+/-,l} < 1$), this means that an inverse cascade is occurring, the energy is pumped at small scales and given back at larger scale. When this ratio is greater than one ($k_{ij}^{+/-,l} > 1$), this means that a direct cascade is occurring, the energy is pumped at large scales and given back at smaller scales. We also always hold $T_{ij}^{+,j} = -T_{ij}^{-,j}$ and we can recover the transfer from the j part to the l part computed in equation (5.6) as $T_{ij}^l = T_{ij}^{+,l} + T_{ij}^{-,l}$.

Contrary to the stratified case, where the forcing is constant in all cases, in the rotating case the forcing amplitude differs. Hence, the transfer variable $T_{ij}^{+,l}$ are non-dimensionnalised against the forcing P.

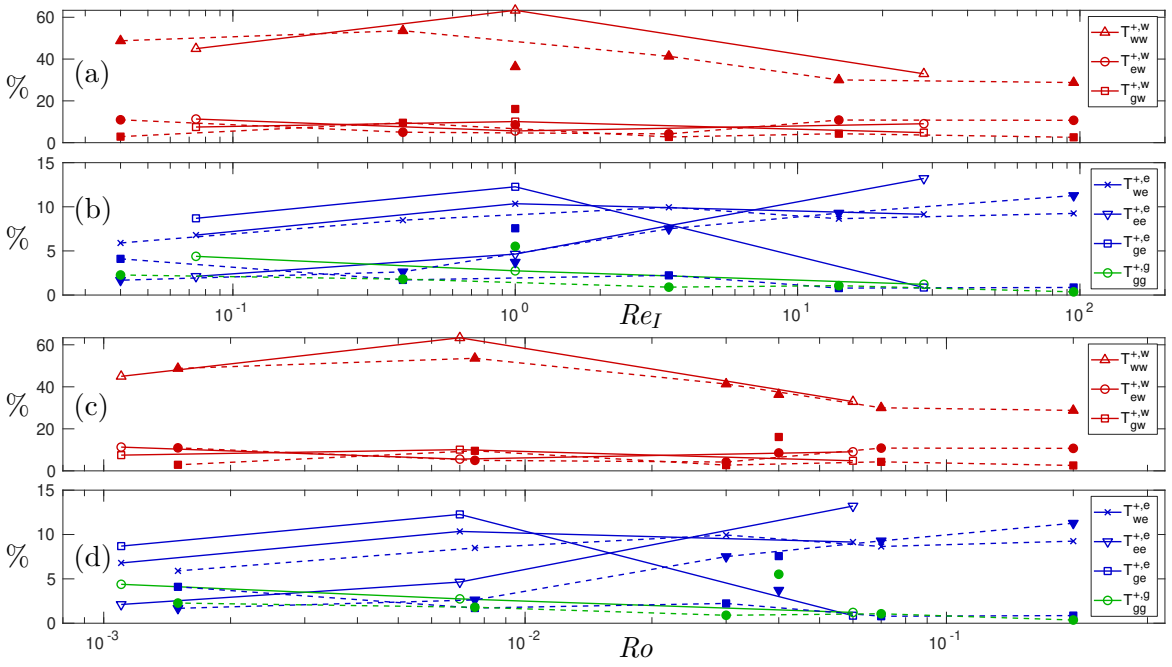

FIGURE 5.20: Evolution of the positive transfer $T^{+,j}_{ij}$ (with $i = w, e$ or g) between (a,c) waves themselves ($j = w$) and (b,d) eddies ($j = e$) or GM ($j = g$) themselves against (a, b) Re_I; (c, d) Ro. Numerical simulations with 512^3 points are shown with open symbols and solid lines, and numerical simulations with 256^3 points are shown with filled symbols and dotted lines.

5.6.1 Local transfers

First, we consider the transfer between waves themselves. This means that a component i which can be an eddy, a wave or a GM advects a wave component to give or take energy to a wave. Figure 5.20 shows the total value of positive transfer from waves to waves $T^{+,w}_{iw}$, eddies to eddies $T^{+,e}_{ie}$ and GM to GM $T^{+,g}_{gg}$ against the inertial Reynolds number Re_I and the Rossby number Ro. We never plot the total value of negative transfer $T^{-,j}_{ij}$ as it is exactly the inverse of the total value of positive transfer $T^{+,j}_{ij} = -T^{-,j}_{ij}$.

We observe that it is the triadic interaction of waves $T^{+,w}_{ww}$ (figure 5.20a and c) which dominates all other transfers. It can even transfer $50-60\%$ of the total energy for large rotation rate. The value of this transfer seems mostly dependent on the Ro number. At fixed Ro, when Re_I increases, we observe that the strength of the triadic interaction $T^{+,w}_{ww}$ is slightly stronger. This means that triadic interactions of IW are stronger when the Rossby number decreases and also stronger when the flow is more turbulent. For the other transfers involving waves $T^{+,w}_{ew}$ and $T^{+,w}_{gw}$, their amplitude fluctuates with Re_I and Ro and no particular trend can be drawn.

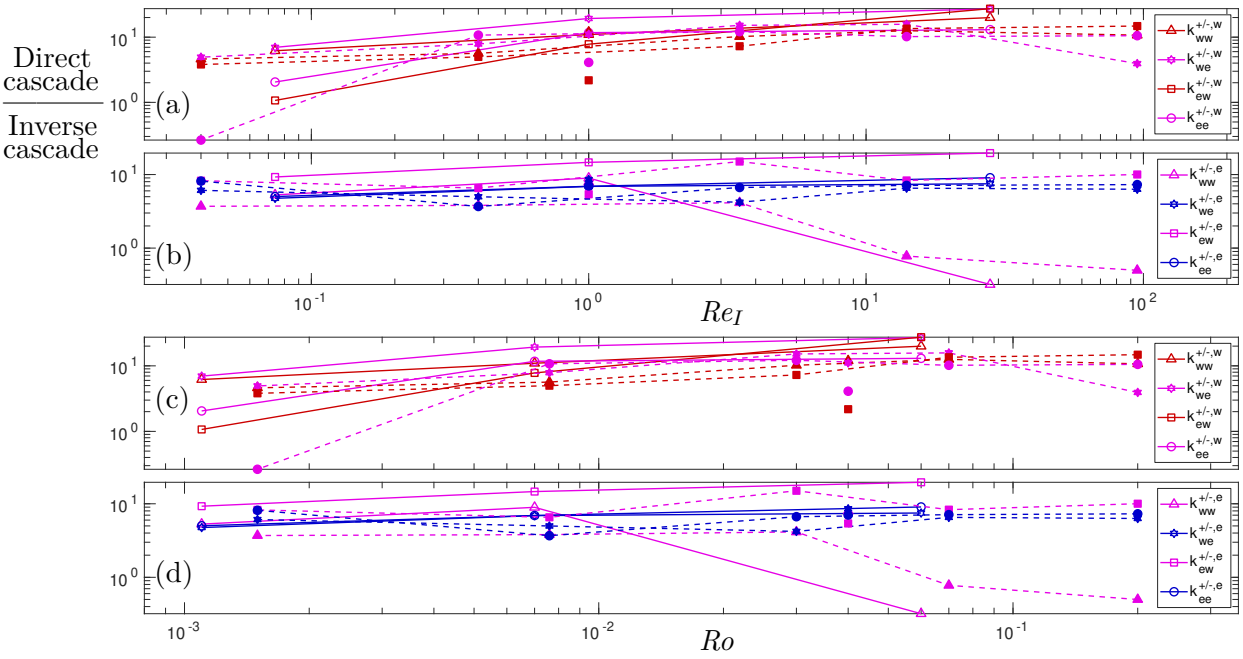

FIGURE 5.21: Evolution of the average ratio of scales of transfer $k_{ij}^{+/-,l}$ (with $i,j =$ w or e) in (a,c) waves ($l = w$) and in (b,d) eddies ($l = e$) against (a,b) Re_I; (c,d) Ro. Numerical simulations with 512^3 points are shown with open symbols and solid lines, and numerical simulations with 256^3 points are shown with filled symbols and dotted lines.

In figures 5.20b and d, we notice that, as Ro decreases at fixed Re_I and as Re_I increases at fixed Ro, the transfer linked to the GM ($T_{gg}^{+,g}$) is stronger. This could be expected as we have shown in section 5.3.1 that the GM becomes more important (for the same added viscosity α) when Ro decreases at constant Re_I and when Re_I increases at constant Ro. It is normal to obtain a stronger transfer if these quantities contain more energy. Similarly the transfer $T_{ge}^{+,e}$ decreases when Ro decreases at constant Re_I and when Re_I increases at constant Ro. This observation can be analysed similarly to the previous case. When Ro decreases at constant Re_I and when Re_I increases at constant Ro, the GM energy decreases and fewer GM advect eddies to exchange energy with another eddy.

The transfer $T_{we}^{+,e}$ seems more dependent on Re_I and increases slightly with it. The transfer $T_{ee}^{+,e}$ increases a lot when Re_I increases. When Re_I increases, the flow is more turbulent and we expect more eddies to interact with one another.

5.6.2 Ratio of scales

5.6.2.1 Only waves and eddies involved

Figure 5.21 shows the ratio of average scale of transfer in waves k_{ij}^{w} (figures 5.21a and c) and in eddies k_{ij}^{e} (figures 5.21b and d) without any GM component involved. First, we can observe that the cascade is mostly forward ($k_{ij}^{+/-,l} > 1$). Overall, when the rotation rate decreases, the strength of the forward cascade increases. Yet, two particular transfers seem to show an inverse cascade. At small rotation rate an inverse cascade is visible for the ratio of scales $k_{ww}^{+/-,e}$ and at large rotation rate an inverse cascade is visible for the ratio of scales $k_{ee}^{+/-,w}$. The reason for this is still unclear. This is supported in a study by Buzzicotti et al. [23] where 3D phenomena different from the GM are involved in an inverse cascade of energy.

Some ratio of scales involving mostly waves (*i.e.* $k_{ww}^{+/-,w}$ and $k_{we}^{+/-,w}$) increase as Ro decreases and as Re_I increases. When Re_I increases at constant Ro and when Ro decreases at constant Re_I, it seems that the ratio of scales $k_{ew}^{+/-,e}$ increases as well, meaning that the forward cascade is stronger. No particular trend is observable for the ratio of scales $k_{ew}^{+/-,w}$, $k_{ee}^{+/-,e}$ and $k_{we}^{+/-,e}$.

5.6.2.2 GM involved in a transfer in waves or eddies

After focusing on the ratio of scales for transfers where only waves or eddies components are involved, we can examine the effect of the GM on the cascade of energy. In this part, we consider the ratio of scales where the GM is involved in the transfer to/from waves or eddies.

Figure 5.22 shows the ratio of scales of transfer in waves $k_{ij}^{+/-,w}$ and in eddies $k_{ij}^{+/-,e}$ with some GM involved ($i = g$ or $j = g$). First, we observe that, contrary to section 5.6.2.1, more transfers reach an inverse cascade $k_{ij}^{+/-,l} < 1$ at a large rotation rate. In figure 5.22a and c, this is the case when the GM advects an eddy or a wave to give or take energy from waves (for the ratio of scales $k_{gj}^{+/-,w}$). In figures 5.22b and d, it is the case only for the ratio of scales $k_{wg}^{+/-,e}$. This result is similar to the observation done in [23], where the GM is observed to play a strong role in the inverse cascade of energy. Yet, our results go further, it details the type of interaction where the GM participates in an inverse cascade with waves and eddies. In general, we remark that the stronger the rotation rate, the lower the ratio of scales. No clear conclusion can be drawn on the dependence of the Rossby or inertial Reynolds number.

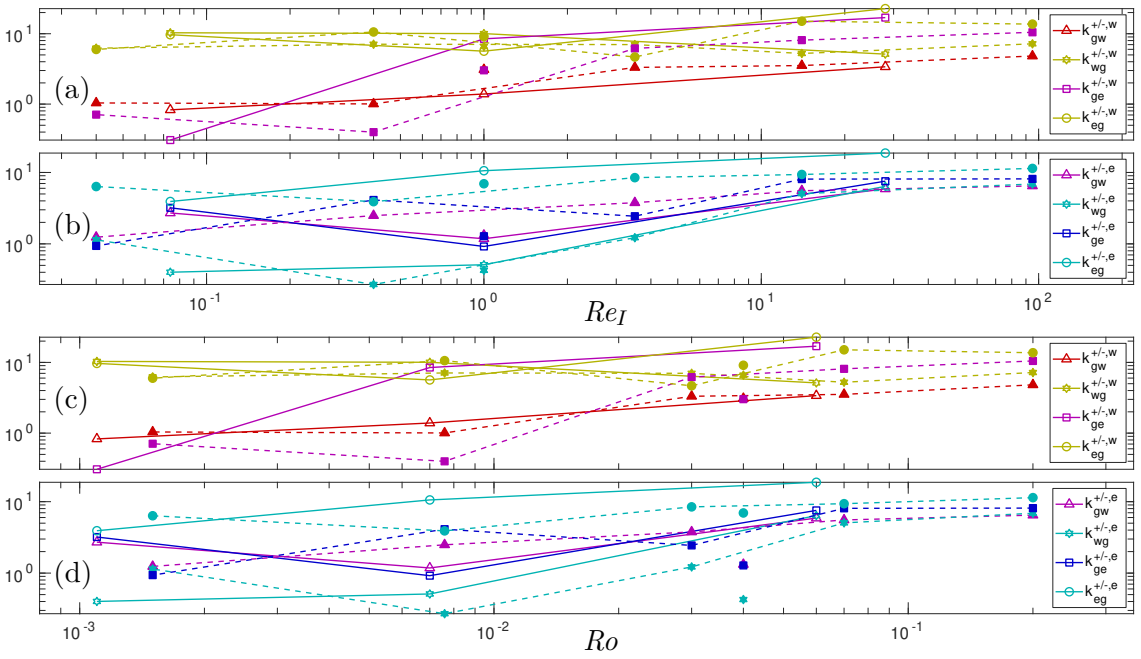

FIGURE 5.22: Evolution of the average ratio of scales of transfer $k_{ij}^{+/-,l}$ (with $i,j = w$ or e or g) in (a,c) waves ($l = w$) and in (b,d) eddies ($l = e$) against (a,b) Re_I; (c,d) Ro. Numerical simulations with 512^3 points are shown with open symbols and solid lines, and numerical simulations with 256^3 points are shown with filled symbols and dotted lines.

5.6.2.3 Ratio of scales for the transfer in the GM

Finally, we consider the ratio of scales $k_{ij}^{+/-,g}$ from the transfer that pumps or gives energy to the GM. Figure 5.23 shows the ratio of average scale in the GM $k_{ij}^{+/-,g}$ with only eddies or waves involved ($i,j = w$ or e). The attentive reader can already spot a discrepancy in figure 5.23, since there are a few points that are lacking (for example $k_{ww}^{+/-,g}$ and $k_{ew}^{+/-,g}$ have many points missing). This is because no negative transfer $T_{iw}^{-,g}$ exist, so there is no average scale of negative transfer $k_{iw}^{-,g}$ and the ratio of average scale is ill-defined. Overall, the average ratios $k_{iw}^{+/-,g}$ are mostly smaller than one which means waves give energy to the GM mostly in a backward cascade. Furthermore, there are many cases where waves give energy to the GM without even pumping energy to the GM. There is also a backward cascade at low rotation rate for the ratio of scales $k_{ee}^{+/-,g}$ but no specific dependence with Re_I and Ro can be observed. The ratio of scales $k_{we}^{+/-,g}$ oscillates, but seems mostly responsible for a forward cascade. As for the ratio of scales of the transfer involving only the GM $k_{gg}^{+/-,g}$, it seems relatively invariant with the Re_I number, increases with it and is subject to a direct cascade. This result seems in opposition with the result found in [17] with a definition the GM different from ours, involving only the horizontal component. Note that, from preliminary result (not presented here) if the definition of the GM was 2D (only the horizontal velocity field)

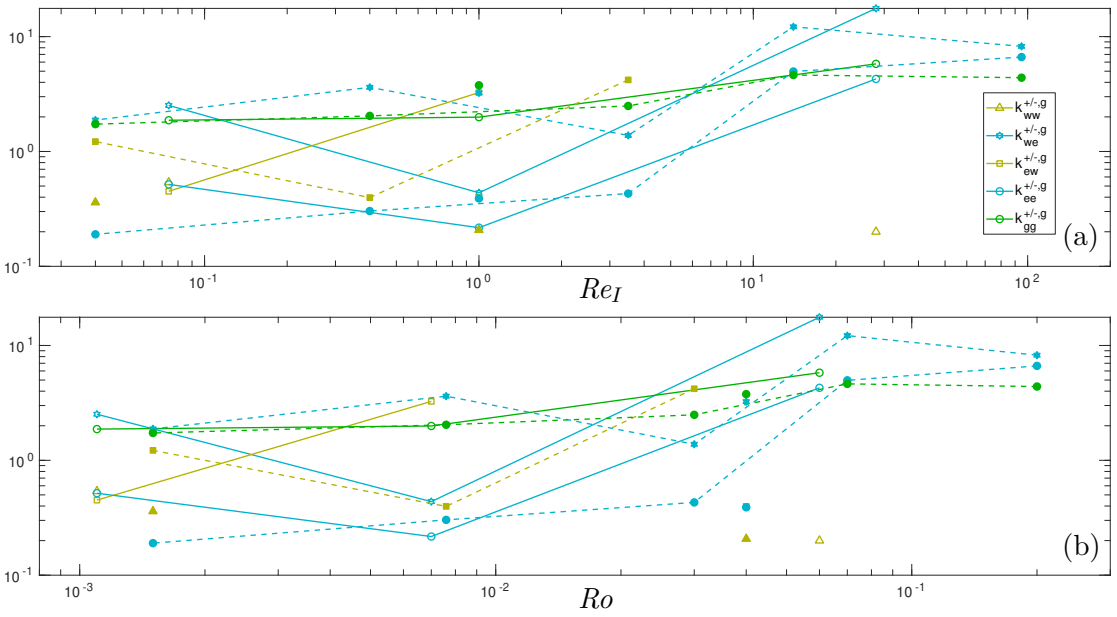

FIGURE 5.23: Evolution of the average ratio of scales of transfer $k_{ij}^{+/-,g}$ (with $i, j = w$ or e) against (a) Re_I; (b) Ro. Numerical simulations with 512^3 points are shown with open symbols and solid lines, and numerical simulations with 256^3 points are shown with filled symbols and dotted lines. Some points are missing because there is no negative average scale of transfer $k_{ij}^{-,g}$, there is no pumping from the GM to j component. No ratio of scales $k_{ij}^{+/-,g}$ can be defined for those points.

we would get a backward cascade for the transfer involving only the GM.

5.6.2.4 Summary on the ratio of scales

Due to the very high number of different transfer and high complexity of the analysis against Ro and Re_I, the conclusions on the different ratios of scale $k_{ij}^{+/-,l}$ can be confusing. If one wants a general conclusion, it is that when no GM is involved in a transfer, most of the interactions results in a forward cascade of energy. On the contrary, when the GM is involved in a transfer, some transfers are prone to inverse cascade of energy. This is the case particularly at low Ro and low Re_I when the GM starts to get more and more two dimensional.

5.7 Visualization

Finally, we focus on the wave, eddy and total velocity fields. This section allows us to understand more qualitatively our decomposition. In order to reach high spatial accuracy in our velocity cuts, we only plot the data from the 512^3 points numerical

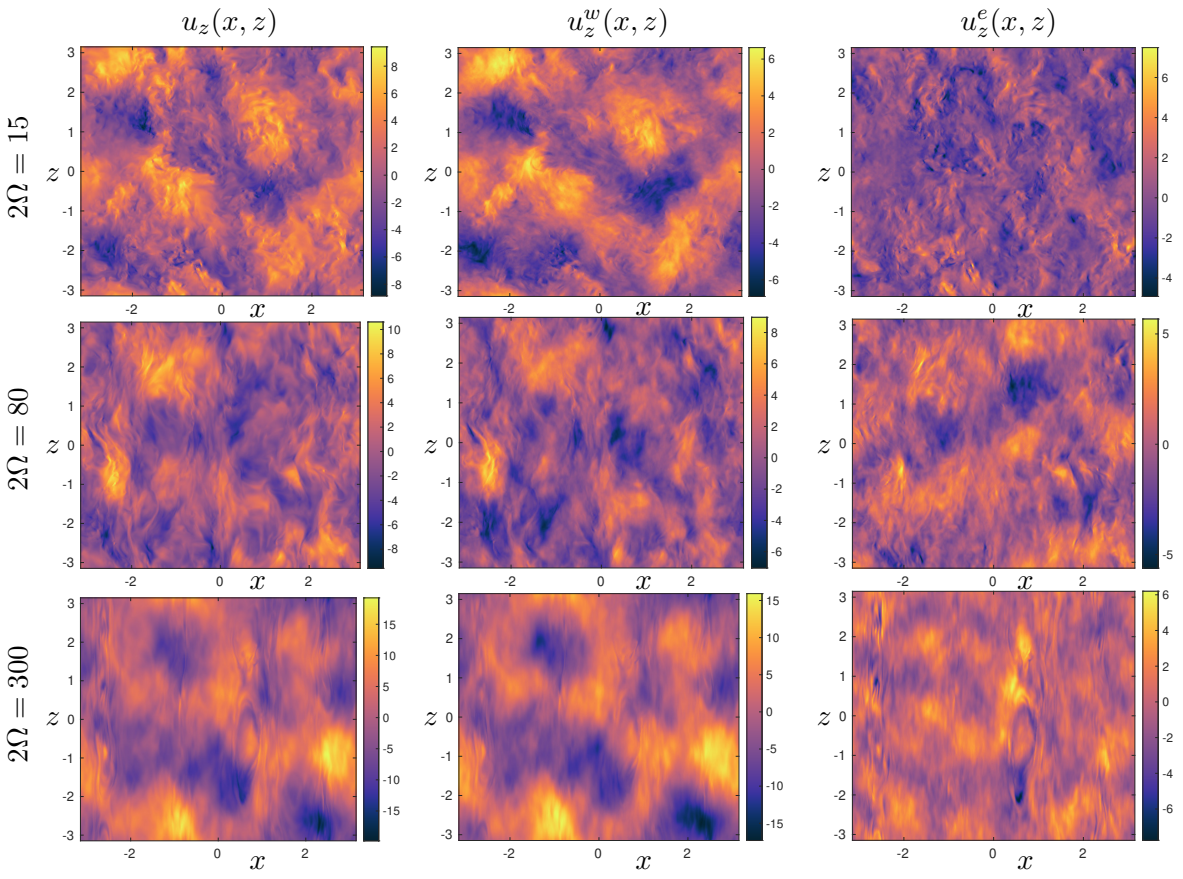

FIGURE 5.24: Total $u_z(x,z)$, wave $u_z^w(x,z)$ and eddy $u_z^e(x,z)$ vertical velocity field in the middle of the y interval.

simulations.

Figure 5.24 shows the vertical velocity field $u_z(x,z)$ for the total part (1st column), the wave part (2nd column) and the eddy part (3rd column). For the different vertical velocity field shown, the rotation rate is changed at each different line, it starts at $2\Omega = 15$ (1st line), then at the rotation rate $2\Omega = 80$ (2nd line) to finish with a rotation rate at $2\Omega = 300$ (3rd line). The vertical velocity fields are computed from the poloidal velocity field in the Fourier domain, which is projected to the Cartesian frame as:

$$\hat{u}_z^i = \frac{-k_h}{k}\hat{u}^{p,i} \tag{5.10}$$

where i stands for w or e.

We observe that most of the large structures are in the wave part of the velocity field. The eddy part of the velocity field is smaller scale. The higher the rotation rate, the higher the total and wave vertical velocity field. On the contrary, the amplitude of the eddy vertical velocity field does not change much when the rotation rate is changed.

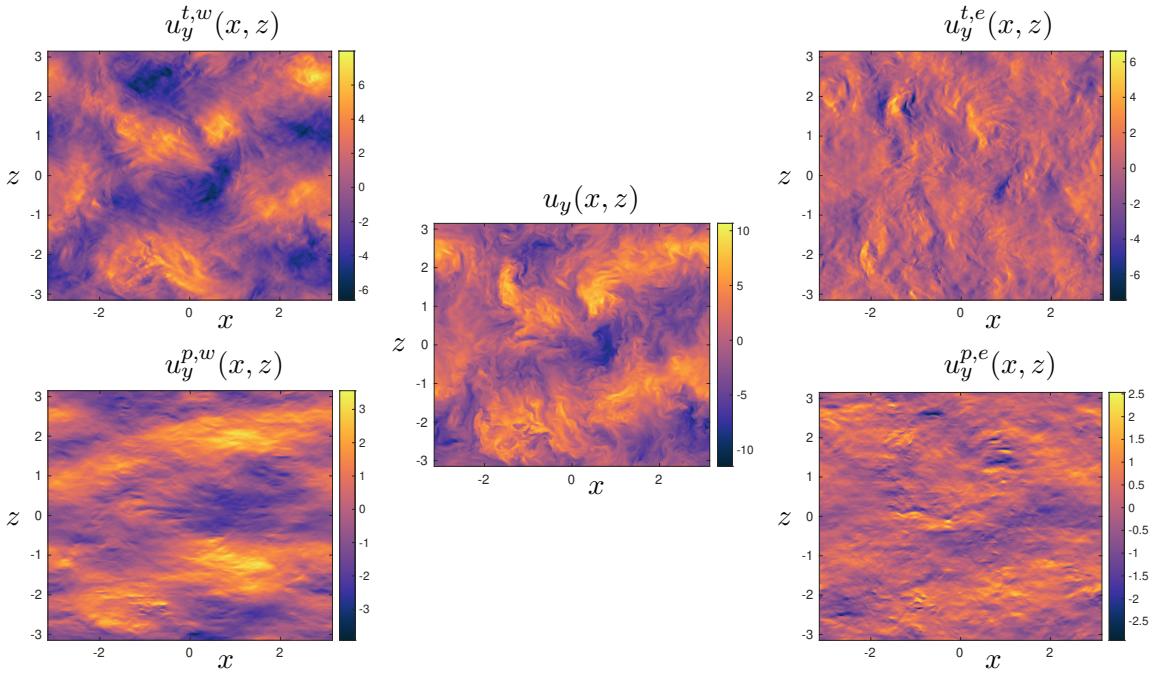

FIGURE 5.25: Total $u_y(x,z)$, toroidal wave $u_y^{t,w}(x,z)$, poloidal wave $u_y^{p,w}(x,z)$, toroidal eddy $u_y^{t,e}(x,z)$ and poloidal eddy $u_y^{p,e}(x,z)$ velocity field in the middle of the y interval for $Ro = 0.06$ and $Re_I = 28$.

Figure 5.25 shows the velocity $u_y(x,z)$ for the wave, eddy and total parts of the flow. As the filtering is done in the Craya-Herring frame, the velocity u_y is separated in a velocity that comes from the toroidal component u_y^t or that comes from the poloidal component u_y^p. Hence two velocities can be computed from the wave and eddy components, a toroidal and a poloidal velocity field. They are defined as:

$$\begin{aligned} \hat{u}_y^{t,i} &= \frac{k_x \hat{u}^{t,i}}{k_h} \\ \hat{u}_y^{p,i} &= \frac{k_y k_z \hat{u}^{p,i}}{k k_h} \end{aligned} \tag{5.11}$$

where i stands for w or e.

We observed that the toroidal velocity field is greater than the poloidal velocity field. This is expected as the toroidal velocity field is divided in two parts (u_x, u_y) but the poloidal velocity field is divided in three parts (u_x, u_y, u_z). Hence the total horizontal velocity field $u_y(x,z)$ is closer to the toroidal wave velocity field $u_y^{t,w}$ than the poloidal wave velocity field $u_y^{p,w}$. Similarly to the observation made in figure 5.24, the eddy velocity field is small scale whereas the wave velocity field is large scale.

5.8 Conclusion

In this chapter, we used the separation technique presented in chapter 3 using an implicit definition of the dispersion of waves explained in section 3.1.5 for the case of rotating flow. We apply this separation technique on a campaign of numerical simulation for varying values of Ro and Re_I number. We observe that the distribution of energy between waves and eddies depends on Ro number and the distribution of wave and eddy dissipation depends on Re_I. We also observe that the energy spectrum of eddies and waves seems to intersect close to the Zeman-Hopfinger scale k_Ω. The eddy energy spectrum follow a scaling close to $k^{-5/3}$ and $k_h^{-5/3}$. As for the wave energy spectrum, it follows a steeper scaling, close to k^{-2} and k_h^{-2}.

Then, a balance of energy and flux for waves, eddies and the geostrophic mode (GM) is computed. We observe a large transfer from waves to eddies for all numerical simulations. In particular the eddy-wave interactions increasingly feed the eddy part as Re_I increases. Furthermore, we witness that mostly waves feed the GM due to wave-wave interactions, but also eddy-wave interactions. For the cascade of energy terms, we observed that wave interactions dominate for all numerical simulations and particularly at low Ro. Eddy interactions increased as Re_I increased as well but its value is still far below wave interactions for all cases. Transfers linked to the GM are more prone to undergo a backward cascade that transfers that do not involve the GM. This is especially true for large rotation rate, when the GM is two dimensional.

Finally, 2D cuts of the wave and eddy vertical velocity are plotted. Large differences can be observed between the wave and eddy part which support that our separation technique actually works in a turbulent rotating flow. This is also done in one case for the velocity u_y which is decomposed into its toroidal/poloidal part as well as its wave and eddy part.

Chapter 6

Conclusion and perspectives

Conclusion

In this thesis, we tried to separate the waves from the rest of the turbulence (called eddies) in stratified or rotating flows. This separation therefore permits the consideration and analysis of flow statistics or visualizations, as in classical turbulence, but with a special focus on wave or eddy dynamics, separately.

Chapter 2 starts by presenting the equations solved in the stratified and rotating cases and how they are computed. The classical dispersion relation of waves is derived in both the stratified or rotating cases. The computation of space-time statistics is defined. It is used to observe numerically the trace of the dispersion relation of waves. Then, we analysed the effect of non-linearity of the flow on the dispersion relation. We analyse the advection (sweeping effect) and gradient effect (refraction) on the waves by varying the frequency (in time) and the scale of the flow. In the end, we observe that it is mostly the advection of waves by a large scale flow (the vertical sheared horizontal flow (VSHF) or the gesotrophic mode (GM)) that modifies the most the dispersion relation of waves.

Chapter 3 shows how the waves and eddies are separated from the turbulent flow in the stratified or rotating case by taking into account the advection by a large scale flow. It requires a 4D Fourier transform of the different quantities (the velocity field and/or the buoyancy field) in time and space. Then, a filter ζ is defined which filters the waves from the rest of the flow in the $(\omega, \mathbf{k})$ domain. The definition of this filter can be done through two different techniques: a technique which directly defines its value in the $(\omega, \mathbf{k})$ domain, or a technique that uses the Green's function to define the $(\omega, \mathbf{k})$

domain of the waves implicitly. Finally, a simple example where a Saint Andrew's cross is convected is used to assess the ability of this separation technique.

Chapter 4 shows the results of the separation of waves and eddies in a stratified turbulent flow. Numerous numerical simulations are done and results are shown against the Froude number Fr or against the buoyancy Reynolds number Re_b. We observe that the energy partition between waves and eddies is mainly dependent on the Froude number. Eddies follow an energy spectrum close to a $-5/3$ scaling against the wavenumbers k and k_h. Waves follow an energy spectrum close to a -3 scaling at large stratification against the wavenumber k, k_h and k_z whereas at lower stratification the powerlaw obtained is smaller. The balance of energy for waves and eddies separately are computed. Different interactions occur (wave-wave, eddy-eddy, wave-eddy and eddy-wave interactions) between the wave and eddy parts of the flow. We observe a large transfer from the waves to the eddies, particularly due to the potential transfer. We also compute the contribution to the mixing coefficient of IGW and eddy. At large Re_b, a plateau is reached on the split mixing contribution and we observe that the eddy mixing is four times that of waves. Most of the dissipation is due to eddies except at very high stratification where dissipation is dominated by waves. Finally, a deeper analysis of the transfers is done on the waves and eddies terms, where the focus is put on the strength of the transfers as well as the scale they are operating. We notice that the potential transfer involving only waves dominates at large stratification and that the kinetic transfer involving only eddies dominates at small stratification. Most transfers involve a forward cascade of energy except the kinetic transfer where an eddy convects a wave to give or take energy to a wave (T^w_{ew}). At small stratification, this transfer is responsible of an inverse cascade. Finally, we plot 2D velocity field which shows the decomposition of the full flow in a wave and eddy part. We remark that waves are larger scale than eddies and that isodensity-lines show that overturning is occurring mainly in the eddy part of our decomposition.

Chapter 5 is similar in construction to chapter four, but it shows the results of the separation of waves and eddies in a rotating turbulent flow. Numerous numerical simulations are done and results are shown against the Rossby number Ro or against the inertial Reynolds number Re_I. Again, we observe that the distribution between wave and eddy energy depends mostly on the Rossby number. For the distribution of the dissipation, it depends mostly on the inertial Reynolds number. The balance of energy for the waves, the eddies and the geostrophic mode separately are computed. We observe a large transfer from the waves to the eddies. A large transfer from waves to the GM also occurs due to wave-wave interaction, but also due to eddy-wave interaction. A refined analysis of the transfers is also done. The transfer involving only the wave-wave interaction on the

wave part T^w_{ww} is much stronger than all other transfers even if its effect decreases as the rotation rate decreases. We mostly see direct cascade when only waves and eddies are involved, except for the wave-wave interaction on the eddy part T^e_{ww} which undergoes an inverse cascade at small rotation. When the GM is involved, there is a mix between inverse and direct cascades. Visualisation of the total, wave and eddy velocity field are done and we discern that in our cases, waves are larger scale than eddies and keep the general pattern of the total flow.

Perspectives

Such a separation technique is new in the field of stratified or rotating turbulence, so that numerous possibilities exist for future work. We listed a few perspectives that seem the most relevant below.

- This separation technique could be used in flows that mix stratification and rotation. In this case, one should first answer this question: what is the main advecting flow? Then, similar results than the one presented in this thesis could be computed, such as energy distribution between waves and eddies, transfers, cascade of energy...
- This separation technique could be adapted to other cases where waves follow a dispersion relation. For example, it could be applied to capillary waves or to magnetohydrodynamics with Alfvén waves.
- There is still room for improving the algorithm of separation of waves and eddies (see section 3.3 for more details). In particular, there might be better advecting flow than the VSHF or the GM depending on the case of study. For example, it could be possible to choose also the large scale eddies or even all the flow. Moreover, in the search for the peaks of the Green function, the choice of β used to define the value of ζ can probably be further optimized. The type of filter which is currently used is an *all or nothing* filter, and this is a good first approximation, but in reality, waves and eddies can share the same wave vector and frequency in the $(\mathbf{k}, \omega)$ domain. To take this into account, a finer filter would be necessary. Besides, the smallest scale of the flow (*i.e.* the Kolmogorov scale k_η) is subject to a strong sweeping effect ($k_\eta c$) against the stratification strength N or the rotation rate 2Ω. Hence, in our numerical simulations, we do not verify $\frac{N}{k_\eta c} \ll 1$ or $\frac{2\Omega}{k_\eta c} \ll 1$ so that the small scales of waves and eddies can more easily share the same points in the $(\mathbf{k}, \omega)$ domain.

- We mostly used the implicit definition of ζ in our campaign of numerical simulation in rotating or stratified flows. This seems the most relevant approach in the rotating case as the explicit estimation of the dispersion relation do not encompass all waves (see figure 5.5). However, in the stratification case, the explicit approach could be used as well (and this would reduce slightly the computation cost compare to the implicit approach) as all waves seem well encompassed with this technique (see figure 4.5).

- A higher Reynolds number Re_b or Re_I for a constant Froude or Rossby number is necessary to get closer to oceanic or atmosphere measurements to confirm and confront our results. In this case, more computing power and also more storage would be necessary to run these new numerical simulations.

- A different forcing could be used. One that gives more energy to eddies, in particular for rotating flow where nearly all the forcing is done in waves. The scale of the forcing could also be changed in order to better observe a backward cascade for example. Indeed, the choice of forcing can have a significant impact on the statistics of the flow such as mixing [65].

- In the stratified case other numerical simulations could be done without dampening as much as we did the VSHF (by choosing $\alpha = 0.5$ as in the rotating case for example). This could allow us to study the implication of the VSHF on the transfers, as done in this thesis in the rotating case with the GM for example.

- Generally, many characterizations in the case of homogeneous and isotropic turbulence could be applied separately on the wave and eddy parts of the flow.

- Other analyses could be done, such as the calculation of the structure function to characterize the fluctuations of the wave and eddy part, the calculation of the bicoherence to observe the transition of instabilities to turbulence or the calculation of ring-to-ring energy transfer as in Sharma et al. [124] but for the eddy and wave parts.

- Our separation technique defines clearly what is considered as waves: the areas in the (θ, ω) space that follows the dispersion relation advected through the sweeping effect. However, it does not define clearly what is considered as eddies. Indeed, our eddy part is defined as everything that is not waves (and not the VSHF in stratified flows or GM in rotating flows). To have a better understanding of what contains the eddy part in our separation technique, one could also try to characterize if our eddy part of the flow is similar to eddies found in homogeneous and isotropic turbulence. One way to do so would be to check if the structure function of order p of the eddy part of our separation technique is similar to the

one found in homogeneous and isotropic turbulence. For example, do we recover some intermittent behaviour as shown in Frisch [48] in our eddy part of the flow?

- Improve statistical model such as EDQNM or RANS in the modelization of wave and eddy energy.

Appendix A

Saint Andrew's cross with viscosity

In this appendix, we calculate the response of the full Navier-Stokes equations in Boussinesq approximation (with viscosity) of an oscillating particle in the flow. This analytical study is linked to section 2.6.2.1 where the same analytical calculation is done in the inviscid case.

The Navier-Stokes equation in Boussinesq approach is projected in the Craya-Herring frame (see equation (2.29)) with a pointwise sinusoidal forcing on the buoyancy term:

$$\partial_t \begin{pmatrix} \hat{v}^p \\ \hat{b} \end{pmatrix} + \begin{pmatrix} \nu k^2 & -\cos\theta \\ N^2 \cos\theta & \nu k^2 \end{pmatrix} \begin{pmatrix} \hat{v}^p \\ \hat{b} \end{pmatrix} = \begin{pmatrix} 0 \\ \sin(\omega_f t) \end{pmatrix} \tag{A.1}$$

The two equations in (A.1) can be solved using the Green's function

$$\partial_t \begin{pmatrix} \hat{v}^p \\ \hat{b} \end{pmatrix} + \mathbf{P} \begin{pmatrix} \nu k^2 - \mathrm{i}\omega_r & 0 \\ 0 & \nu k^2 + \mathrm{i}\omega_r \end{pmatrix} \mathbf{P}^{-1} \begin{pmatrix} \hat{v}^p \\ \hat{b} \end{pmatrix} = \begin{pmatrix} 0 \\ \sin(\omega_f t) \end{pmatrix} \tag{A.2}$$

$$\text{where } \mathbf{P} = \begin{pmatrix} -\mathrm{i}/N & \mathrm{i}/N \\ 1 & 1 \end{pmatrix} \text{ and } \mathbf{P}^{-1} = \begin{pmatrix} \mathrm{i}N/2 & 1/2 \\ -\mathrm{i}N/2 & 1/2 \end{pmatrix}.$$

This equation is then rewritten as:

$$\partial_t \begin{pmatrix} \hat{v}_G^p \\ \hat{b}_G \end{pmatrix} + \begin{pmatrix} \nu k^2 - \mathrm{i}\omega_r & 0 \\ 0 & \nu k^2 + \mathrm{i}\omega_r \end{pmatrix} \begin{pmatrix} \hat{v}_G^p \\ \hat{b}_G \end{pmatrix} = \begin{pmatrix} 1/2 \sin(\omega_f t) \\ 1/2 \sin(\omega_f t) \end{pmatrix} \tag{A.3}$$
$$\text{where } \hat{\mathbf{v}}_G = \mathbf{P}^{-1}\hat{\mathbf{v}}.$$

We first look for a particular solution for $b_G(t)$. Let $\mu = e^{(\mathrm{i}N\sin\theta + \nu k^2)t}$ then

$$\partial_t(\hat{b}_G\mu)(t) = \partial_t\hat{b}_G(t)\mu(t) + \hat{b}_G(t)\partial_t\mu(t) = \mu(t)\frac{1}{2}\sin(\omega_f t). \tag{A.4}$$

Therefore, solving (A.3) is equivalent to solving (A.4). By doing two integrations by parts and by writing $K = \mathrm{i}\omega_r + \nu k^2$, one can obtain:

$$\begin{aligned}\int_0^t \mu(x)\sin(\omega_f x)dx &= (-[\frac{\cos(\omega_f x)}{\omega_f}\mu(x)]_0^t + \int_0^t K\mu(x)\frac{\cos(\omega_f x)}{\omega_f}dx) \\ &= -\frac{\cos(\omega_f t)}{\omega_f}\mu(t) + \frac{1}{\omega_f} + [\frac{\sin(\omega_f x)}{\omega_f^2}K\mu(x)]_0^t - \int_0^t \mu(x)\frac{\sin(\omega_f x)}{\omega_f^2}K^2dx.\end{aligned} \tag{A.5}$$

Putting all terms in (A.5) of the form $\mu(x)\sin(\omega_f x)$ on the left-hand-side and multiplying by ω_f^2:

$$\int_0^t \mu(x)\sin(\omega_f x)(\omega_f^2 + K^2)dx = -\cos(\omega_f t)\omega_f\mu(t) + \omega_f + K\mu(t)\sin(\omega_f t). \tag{A.6}$$

The solution for $\hat{b}_G(t)$ is the sum of the particular solution and homogeneous solution:

$$\hat{b}_G(t) = 0.5\frac{-\cos(\omega_f t)\omega_f + \omega_f e^{-(\mathrm{i}\omega_r + \nu k^2)t} + K\sin(\omega_f t)}{\omega_f^2 + (i\omega_r + \nu k^2)^2} + Be^{-(\mathrm{i}\omega_r + \nu k^2)t}. \tag{A.7}$$

Using the initial condition $\hat{v}_G(t=0) = 0$ and $\hat{b}_G(t=0) = 0$, the second term in equation (A.7) can be dropped:

$$\hat{b}_G(t) = 0.5\frac{-\cos(\omega_f t)\omega_f + \omega_f e^{-Kt} + K\sin(\omega_f t)}{\omega_f^2 + (K)^2}. \tag{A.8}$$

Taking the Fourier transform of (A.8) in time:

$$\begin{aligned}\tilde{b}_G(\omega) =& 0.5\frac{-(\delta(\omega-\omega_f)+\delta(\omega+\omega_f))\frac{\omega_f}{2}+\omega_f[\int_{-\infty}^{+\infty}\delta(\lambda-\omega_r)\frac{-\nu k^2}{\pi((\omega-\lambda)^2+\nu^2k^4)}d\lambda]}{\omega_f^2+K^2}\\ &+0.5\frac{\frac{K}{2\mathrm{i}}(\delta(\omega-\omega_f)+\delta(\omega+\omega_f)}{\omega_f^2+K^2}.\end{aligned} \tag{A.9}$$

Simplifying the convolution term and writing $K' = -\mathrm{i}\omega_r + \nu k^2$ the solution of (A.3) is:

$$\begin{aligned}\tilde{b}_G(\mathbf{k},\omega) =& 0.5\frac{-(\delta(\omega-\omega_f)+\delta(\omega+\omega_f))\frac{\omega_f}{2}+\omega_f\frac{-\nu k^2}{\pi((\omega-\omega_r)^2+\nu^2k^4)}}{\omega_f^2+K^2}\\ &+0.5\frac{\frac{K}{2\mathrm{i}}(\delta(\omega-\omega_f)+\delta(\omega+\omega_f)}{\omega_f^2+K^2}\\ \tilde{v}_G^p(\mathbf{k},\omega) =& 0.5\frac{-(\delta(\omega-\omega_f)+\delta(\omega+\omega_f))\frac{\omega_f}{2}+\omega_f\frac{-\nu k^2}{\pi((\omega+\omega_r)^2+\nu^2k^4)}}{\omega_f^2+K'^2}\\ &+0.5\frac{\frac{K'}{2\mathrm{i}}(\delta(\omega-\omega_f)+\delta(\omega+\omega_f)}{\omega_f^2+K'^2}.\end{aligned} \tag{A.10}$$

The final solution is:

$$\begin{aligned}\tilde{v}^p(\mathbf{k},\omega) &= -\frac{\mathrm{i}}{N}\tilde{v}_G^p(\mathbf{k},\omega)+\frac{\mathrm{i}}{N}\tilde{b}_G(\mathbf{k},\omega)\\ \tilde{b}(\mathbf{k},\omega) &= \tilde{v}_G^p(\mathbf{k},\omega)+\tilde{b}_G(\mathbf{k},\omega).\end{aligned} \tag{A.11}$$

From the equation (A.11), we observe that when $\omega_f \sim \omega_r$, a peak of energy will be observed. The biggest difference with the inviscid case is that the viscosity makes that peak of energy reach a finite value.

Appendix B

Detailed proof of $T^l_{u,ij} = -T^j_{u,il}$

In this appendix, we detailed the analytical proof for $T^l_{u,ij} = -T^j_{u,il}$ with $T^l_{u,ij} = - < \widehat{\boldsymbol{\omega}^i \times \mathbf{u}^j}, \hat{\mathbf{u}}^l >$. Note that in the rotating case $T^l_{u,ij}$ is written as T^l_{ij} (there is no potential transfer).

The Fourier transform of the non-linear term can be rewritten as:

$$\begin{aligned}
\widehat{\boldsymbol{\omega}^i \times \mathbf{u}^j}(\mathbf{k}) &= \sum_{\mathbf{k}=\mathbf{p}+\mathbf{q}} \hat{\boldsymbol{\omega}}^i(\mathbf{p}) \times \hat{\mathbf{u}}^j(\mathbf{q}) \\
&= \sum_{\mathbf{k}-\mathbf{p}-\mathbf{q}=0} \hat{\boldsymbol{\omega}}^i(\mathbf{p}) \times \hat{\mathbf{u}}^j(\mathbf{q}) \\
&= \sum_{\mathbf{k}-\mathbf{p}-\mathbf{q}=0} \overline{\hat{\boldsymbol{\omega}}^i(-\mathbf{p})} \times \overline{\hat{\mathbf{u}}^j(-\mathbf{q})} \\
&= \sum_{\mathbf{k}+\mathbf{P}+\mathbf{Q}=0} \overline{\hat{\boldsymbol{\omega}}^i(\mathbf{P})} \times \overline{\hat{\mathbf{u}}^j(\mathbf{Q})} \text{ with } P = -p \text{ and } Q = -q \\
&= \sum_{\mathbf{k}+\mathbf{p}+\mathbf{q}=0} \overline{\hat{\boldsymbol{\omega}}^i(\mathbf{p})} \times \overline{\hat{\mathbf{u}}^j(\mathbf{q})} \text{ by dropping the upper case,}
\end{aligned} \tag{B.1}$$

where $\overline{\ }$ is the complex conjuguate.

By applying the identity $(\mathbf{A} \times \mathbf{B}) \times \mathbf{C} = (\mathbf{C} \cdot \mathbf{A})\mathbf{B} - (\mathbf{C} \cdot \mathbf{B})\mathbf{A}$ then

$$\begin{aligned}
\hat{\boldsymbol{\omega}^i} \times \hat{\mathbf{u}^j} = (\mathrm{i}\mathbf{p} \times \hat{\mathbf{u}^i}) \times \hat{\mathbf{u}^j} = (\hat{\mathbf{u}^j} \cdot \mathrm{i}\mathbf{p})\hat{\mathbf{u}^i} - (\hat{\mathbf{u}^j} \cdot \hat{\mathbf{u}^i})\mathrm{i}\mathbf{p} \\
\hat{\boldsymbol{\omega}^i} \times \hat{\mathbf{u}^l} = (\hat{\mathbf{u}^l} \cdot \mathrm{i}\mathbf{p})\hat{\mathbf{u}^i} - (\hat{\mathbf{u}^l} \cdot \hat{\mathbf{u}^i})\mathrm{i}\mathbf{p},
\end{aligned} \tag{B.2}$$

which means that

$$\left(\hat{\boldsymbol{\omega}^i} \times \hat{\mathbf{u}^j}\right) \cdot \hat{\mathbf{u}^l} = (\hat{\mathbf{u}^j} \cdot \mathrm{i}\mathbf{p})(\hat{\mathbf{u}^i} \cdot \hat{\mathbf{u}^l}) - (\hat{\mathbf{u}^j} \cdot \hat{\mathbf{u}^i})(\mathrm{i}\mathbf{p} \cdot \hat{\mathbf{u}^l}) = -\left(\hat{\boldsymbol{\omega}^i} \times \hat{\mathbf{u}^l}\right) \cdot \hat{\mathbf{u}^j}. \tag{B.3}$$

With equations (B.3) and (B.1) we obtain:

$$\begin{aligned}
\widehat{\boldsymbol{\omega}^i \times \mathbf{u}^j}(\mathbf{k}) \cdot \overline{\hat{\mathbf{u}}^l(\mathbf{k})} &= \sum_{\mathbf{k}+\mathbf{p}+\mathbf{q}=0} \overline{\hat{\boldsymbol{\omega}}^i(\mathbf{p})} \times \overline{\hat{\mathbf{u}}^j(\mathbf{q})} \cdot \overline{\hat{\mathbf{u}}^l(\mathbf{k})} \\
&= -\sum_{\mathbf{k}+\mathbf{p}+\mathbf{q}=0} \overline{\hat{\boldsymbol{\omega}}^i(\mathbf{p})} \times \overline{\hat{\mathbf{u}}^l(\mathbf{k})} \cdot \overline{\hat{\mathbf{u}}^j(\mathbf{q})} \text{ using (B.3)} \\
&= -\sum_{\mathbf{k}+\mathbf{p}+\mathbf{q}=0} \overline{\hat{\boldsymbol{\omega}}^i(\mathbf{p})} \times \overline{\hat{\mathbf{u}}^l(\mathbf{q})} \cdot \overline{\hat{\mathbf{u}}^j(\mathbf{k})} \\
&= -\widehat{\boldsymbol{\omega}^i \times \mathbf{u}^l}(\mathbf{k}) \cdot \overline{\hat{\mathbf{u}}^j(\mathbf{k})}.
\end{aligned} \tag{B.4}$$

Using the equality shown in equation (B.4) as well as the definition for $<\quad>$ and $[\quad]$ given in section 3.1.3.1, we finally show:

$$\begin{aligned}
T^l_{u,ij} = -<\widehat{\boldsymbol{\omega}^i \times \mathbf{u}^j}, \hat{\mathbf{u}}^l> &= \sum_{\mathbf{k}} \mathrm{Re}[\widehat{\boldsymbol{\omega}^i \times \mathbf{u}^j}(\mathbf{k},t), \hat{\mathbf{u}}^l(\mathbf{k},t)] \\
&= \sum_{\mathbf{k}} \mathrm{Re}\left(\frac{1}{T} \int_T \widehat{\boldsymbol{\omega}^i \times \mathbf{u}^j}(\mathbf{k},t) \cdot \overline{\hat{\mathbf{u}}^l(\mathbf{k},t)} \delta_{\mathbf{k}-\mathbf{k}'} \mathrm{d}t \right) \\
&= \sum_{\mathbf{k}} \mathrm{Re}\left(\frac{1}{T} \int_T -\widehat{\boldsymbol{\omega}^i \times \mathbf{u}^l}(\mathbf{k},t) \cdot \overline{\hat{\mathbf{u}}^j(\mathbf{k},t)} \delta_{\mathbf{k}-\mathbf{k}'} \mathrm{d}t \right) \\
&= <\widehat{\boldsymbol{\omega}^i \times \mathbf{u}^l}, \hat{\mathbf{u}}^j> = -T^j_{u,il}.
\end{aligned} \tag{B.5}$$

Similarly, we can prove that $T^l_{b,ij} = -N^{-2} < \widehat{\mathbf{u}^i \cdot \nabla b^j}, \hat{b}^l >= -T^j_{b,il}$.

Appendix C

Rough estimation of CO_2 emissions related to this thesis

In this appendix, we try to calculate the amount of equivalent CO_2 emissions done during the three years of this thesis. It is quite complicated to take into account every aspect of the activities done in this thesis. Thus, I do not say that this calculation is perfect, but it should at least give some order of magnitude of the different CO_2 emissions of the activities done in this thesis. The result is done as a CO_2 equivalent (CO_2e) which represents the emission of any greenhouse gases based on the global warming potential of CO_2.

As this thesis is mostly numerical, we start by listing most of the computing resources used during the thesis. They are:

- 1 000 000 *h.cpu* at the national supercomputer Jean-Zay in IDRIS
- 30 *TB* of data on the store in IDRIS
- Around 100 000 *h.cpu* on Newton (local supercomputer in Lyon)
- 5 *TB* of data on the store in Newton

In [12], they estimated the equivalent carbon footprint of 1 *h.cpu* on their local supercomputer in Grenoble. They found that on average, each cpu produced a footprint equivalent to 4.68g of CO_2 per hour. For our calculation we will do the rough estimation that the equivalent footprint for 1 *h.cpu* is the same at the supercomputer Jean-Zay in IDRIS and in the local supercomputer in Lyon called Newton. Hence the computation

has roughly produced an equivalent to 5.1t of CO_2.

The equivalent of CO_2 produced by storing data on the cloud per year have been computed in [67] in the case of the US. They found that for storing $1\,GB$ of data for one year produce an equivalent of 2kg of CO_2. We hypothesize that the data will be kept around three years (which is very gentle). This means that the storage of $35\,TB$ of data gives an equivalent of CO_2 emission of 70t of CO_2. This number is very high and is probably overestimated, as the calculation in [67] is done with the electric mix of the USA which is around five times higher than the one from France. Hence, if we suppose that most of the carbon footprint from the storage of data comes from the electricity consumption, we can estimate the CO_2 emission of the storage of $35\,TB$ of data to be around $15 tCO_2e$. Furthermore, I will probably reduce the amount of storage at the end of the thesis.

Next, we only consider the travels done for the thesis by car, train or plane. We do not consider travels by bike or by walking because they nearly do not produce any CO_2 emission. The travels done during the thesis are (round trip):

- 1 trip to San Francisco for the AGU conference (by plane)
- 9 travels to Saint-Etienne for teaching (by TER)
- 1 trip to Grenoble for an ANR meeting (by TER)
- 1 trip to les Houches for winter school (by car with 4 people)
- 1 trip to Paris for a wave turbulence workshop (by TGV)
- 1 trip to Nice for the GDR turbulence (by TGV)

Using an online calculator, I found that the trip by plane produced around an equivalent to 3 *tons* of CO_2. On the website of ouisncf (the train company), it is possible to find the footprint for 1km done in a TER train (24.81gCO_2e) or a TGV train (1.73gCO_2e). Hence, the train amount for an equivalent of 29kg of CO_2 emission. As for the travel by car an online calculator gives an equivalent of 120kg of CO_2 for 4 passengers, so 30kg of CO_2 for the travel.

Finally, we could also add the carbon footprint of the screen, the desktop computer and laptop which are estimated at an equivalent of 14.4kg per year (only for its use) in [16], so around 45kgCO_2e for the duration of the thesis. We also need to account for the emission of carbon during the manufacturing process. On Ademe's website [1] (the

French agency for ecological transition), the carbon footprint for a 21.5 inch screen is estimated to 222 kg CO_2e, the carbon footprint of a desktop computer is 169 kg CO_2e and of a laptop is 156 kg CO_2e. However, as these objects will be used around six years for the computers and ten years for the screen the carbon footprint for my thesis in the fabrication of these objects should be at 66 kg CO_2e for the screen, 75 kg CO_2e for the desktop computer and 78 kg CO_2e for the laptop computer. In the end, the carbon footprint of the items related to computers is around 264 kg CO_2e for the length of my thesis.

To conclude, I estimate this PhD thesis to produce around 23tCO_2e, mostly due to the storage of data, in a lesser measure to the cpu hours used and finally to the trip made by plane for a conference. This result can be compared with the work done in [135] who found that astronomers produced in average 37tCO_2e per year. The footprint of my thesis is smaller but this could be because I did not take into account the carbon footprint of the powering of the faculty for example, and also because the electric mix of Australia, which is the country of study in [135] use heavily coal for their production of electricity (which is known to produce a lot of CO_2e). Yet, the repartition of CO_2e is very similar in my thesis to the astronomy case because in the work done in [135], 60% of the emission was due to supercomputer usage and 15% was due to flights.

Nonetheless, the carbon footprint of this thesis remains high and very far from the objective of the "Paris agreement" which would require a net CO_2e emission of zero. To attain this objective, it is usually estimated that the average carbon footprint of a French citizen should reach 2tCO_2e per year [42]. This leads to some questions on the sustainability of such research in order to comply with the "Paris agreement".

Bibliography

[1] ADEME. Base carbone. Ademe website https://www.bilans-ges.ademe.fr/fr/basecarbone/donnees-consulter/index/siGras/1.

[2] W. Agoua, B. Favier, A. Delache, A. Briard, and W. J. T. Bos. Spontaneous generation and reversal of helicity in anisotropic turbulence. *Phys. Rev. E*, 103: L061101, Jun 2021. doi: 10.1103/PhysRevE.103.L061101.

[3] A. Alexakis and L. Biferale. Cascades and transitions in turbulent flows. *Physics Reports*, 767-769:1–101, 2018. ISSN 0370-1573. Cascades and transitions in turbulent flows.

[4] A. Alexakis, P. D. Mininni, and A. Pouquet. Shell-to-shell energy transfer in magnetohydrodynamics. I. steady state turbulence. *Phys. Rev. E*, 72:046301, Oct 2005.

[5] F. Ascani, E. Firing, J. P. McCreary, P. Brandt, and R. J. Greatbatch. The deep equatorial ocean circulation in wind-forced numerical solutions. *Journal of Physical Oceanography*, 45(6):1709–1734, 2015.

[6] Y. B. Baqui and P. A. Davidson. A phenomenological theory of rotating turbulence. *Physics of Fluids*, 27(2):025107, 2015.

[7] Y. B. Baqui, P. A. Davidson, and A. Ranjan. Are there two regimes in strongly rotating turbulence? *Physics of Fluids*, 28(4):045103, 2016.

[8] C. N. Baroud, B. B. Plapp, Z.-S. She, and H. L. Swinney. Anomalous self-similarity in a turbulent rapidly rotating fluid. *Phys. Rev. Lett.*, 88:114501, Feb 2002.

[9] P. Bartello. Geostrophic adjustment and inverse cascades in rotating stratified turbulence. *J. Atmos. Sci.*, 52(24):4410–4428, 1995.

[10] F. Bellet, F. S. Godeferd, J. F. Scott, and C. Cambon. Wave turbulence in rapidly rotating flows. *Journal of Fluid Mechanics*, 562:83–121, 2006. doi: 10.1017/S0022112006000929.

[11] D. Benielli and J. Sommeria. Excitation and breaking of internal gravity waves by parametric instability. *Journal of Fluid Mechanics*, 374:117–144, 1998. doi: 10.1017/S0022112098002602.

[12] F. Berthoud, B. Bzeznik, N. Gibelin, M. Laurens, C. Bonamy, M. Morel, and X. Schwindenhammer. Estimation de l'empreinte carbone d'une heure.coeur de calcul. Research report, UGA - Université Grenoble Alpes ; CNRS ; INP Grenoble ; INRIA, April 2020.

[13] P. Billant. Is the taylor–proudman theorem exact in unbounded domains? case study of the three-dimensional stability of a vortex pair in a rapidly rotating fluid. *Journal of Fluid Mechanics*, 920:R1, 2021. doi: 10.1017/jfm.2021.431.

[14] G. Boffetta and R. E. Ecke. Two-dimensional turbulence. *Annual Review of Fluid Mechanics*, 44(1):427–451, 2012. doi: 10.1146/annurev-fluid-120710-101240.

[15] P.-A. Bois. *Introduction à la mécanique théorique des fluides*. Ellipses, 2000.

[16] F. Bordage. Quelle est l'empreinte carbone d'un ordinateur ? Greenit https://www.greenit.fr/2011/02/10/quelle-est-l-empreinte-carbone-d-un-ordinateur/, 02 2011.

[17] L. Bourouiba and P. Bartello. The intermediate Rossby number range and two-dimensional–three-dimensional transfers in rotating decaying homogeneous turbulence. *Journal of Fluid Mechanics*, 587:139–161, 2007. doi: 10.1017/S0022112007007124.

[18] L. Bourouiba, D. N. Straub, and M. L. Waite. Non-local energy transfers in rotating turbulence at intermediate Rossby number. *Journal of Fluid Mechanics*, 690:129–147, 2012. doi: 10.1017/jfm.2011.387.

[19] G. Brethouwer, P. Billant, E. Lindborg, and J.-M. Chomaz. Scaling analysis and simulation of strongly stratified turbulent flows. *J. Fluid Mech.*, 585:343–368, 2007.

[20] C. Brouzet, E. V. Ermanyuk, S. Joubaud, I. Sibgatullin, and T. Dauxois. Energy cascade in internal-wave attractors. *Europhysics Letters*, 113(4):44001, feb 2016. doi: 10.1209/0295-5075/113/44001.

[21] M. Brunet, T. Dauxois, and P.-P. Cortet. Linear and nonlinear regimes of an inertial wave attractor. *Phys. Rev. Fluids*, 4:034801, Mar 2019. doi: 10.1103/PhysRevFluids.4.034801.

[22] M. Brunet, B. Gallet, and P.-P. Cortet. Shortcut to geostrophy in wave-driven rotating turbulence: The quartetic instability. *Phys. Rev. Lett.*, 124:124501, Mar 2020. doi: 10.1103/PhysRevLett.124.124501.

[23] M. Buzzicotti, P. Clark Di Leoni, and L. Biferale. On the inverse energy transfer in rotating turbulence. 41(11):131. ISSN 1292-895X.

[24] M. Buzzicotti, H. Aluie, L. Biferale, and M. Linkmann. Energy transfer in turbulence under rotation. *Phys. Rev. Fluids*, 3:034802, Mar 2018.

[25] C. Cambon, N. N. Mansour, and F. S. Godeferd. Energy transfer in rotating turbulence. *J. Fluid. Mech.*, 337:303–332, 1997. doi: 10.1017/S002211209700493X.

[26] A. Campagne, B. Gallet, F. Moisy, and P.-P. Cortet. Direct and inverse energy cascades in a forced rotating turbulence experiment. *Physics of Fluids*, 26(12): 125112, 2014.

[27] A. Campagne, B. Gallet, F. Moisy, and P. Cortet. Disentangling inertial waves from eddy turbulence in a forced rotating-turbulence experiment. 91(4):043016, 2015. doi: 10.1103/PhysRevE.91.043016.

[28] C. Canuto, M. Y. Hussaini, A. Quarteroni, and A. Thomas Jr. *Spectral methods in fluid dynamics*. Springer Science & Business Media, 2012.

[29] C. P. Caulfield. Layering, instabilities, and mixing in turbulent stratified flows. *Annual Review of Fluid Mechanics*, 53(1):113–145, 2021.

[30] S. Chen and R. H. Kraichnan. Sweeping decorrelation in isotropic turbulence. *Physics of Fluids A: Fluid Dynamics*, 1(12):2019–2024, 1989.

[31] J. A. Church, P. U. Clark, A. Cazenave, J. M. Gregory, S. Jevrejeva, A. Levermann, M. A. Merrifield, G. A. Milne, R. S. Nerem, P. D. Nunn, A. J. Payne, W. T. Pfeffer, D. Stammer, and A. S. Unnikrishnan. Sea Level Change. In: *Climate Change 2013: The Physical Science Basis. Contribution of Working Group I to the Fifth Assessment Report of the Intergovernmental Panel on Climate Change [T.F. Stocker, D. Qin, G.-K. Plattner, M. Tignor, S.K. Allen, J. Boschung, A. Nauels, Y. Xia, V. Bex and P.M. Midgley (eds.)].* Cambridge University Press, Cambridge, United Kingdom and New York, NY, USA, 2013.

[32] T. Colligan, J. Fowler, J. Godfrey, and C. Spangrude. Detection of stratospheric gravity waves induced by the total solar eclipse of july 2, 2019. *Scientific Reports*, 10(1), November 2020. doi: 10.1038/s41598-020-75098-2.

[33] J. M. Cusack, J. A. Brearley, A. C. Naveira Garabato, D. A. Smeed, K. L. Polzin, N. Velzeboer, and C. J. Shakespeare. Observed Eddy–Internal Wave Interactions in the Southern Ocean. *J. Phys. Ocean.*, 50(10):3043–3062, 10 2020. ISSN 0022-3670. doi: 10.1175/JPO-D-20-0001.1.

[34] T. Dauxois, C. Brouzet, E. Ermanyuk, S. Joubaud, D. Le Tourneau, and I. Sibgatullin. Energy cascade in internal wave attractors. *Procedia IUTAM*, 20:120–127, 2017. ISSN 2210-9838. 24th International Congress of Theoretical and Applied Mechanics.

[35] P. A. Davidson. *Turbulence in rotating, stratified and electrically conducting fluids*. Cambridge University Press, 2013.

[36] P. A. Davidson, P. J. Staplehurst, and S. B. Dalziel. On the evolution of eddies in a rapidly rotating system. *Journal of Fluid Mechanics*, 557:135–144, 2006. doi: 10.1017/S0022112006009827.

[37] T. de Karman and L. Howarth. On the statistical theory of isotropic turbulence. *Proceedings of the Royal Society of London. Series A - Mathematical and Physical Sciences*, 164(917):192–215, 1938. doi: 10.1098/rspa.1938.0013.

[38] A. Delache, C. Cambon, and F. S. Godeferd. Scale by scale anisotropy in freely decaying rotating turbulence. *Physics of Fluids*, 26(2):025104, 2014. doi: 10.1063/1.4864099.

[39] E. M. Dewan. Stratospheric wave spectra resembling turbulence. 204(4395): 832–835, 1979. doi: 10.1126/science.204.4395.832.

[40] P. C. Di Leoni and P. D. Mininni. Absorption of waves by large-scale winds in stratified turbulence. *Phys. Rev. E*, 91(3):033015, 2015.

[41] P. C. Di Leoni, P. J. Cobelli, and P. D. Mininni. The spatio-temporal spectrum of turbulent flows. *The European Physical Journal E*, 38(136), 2015.

[42] C. Dugast, A. Soyeux, B. Castelli, C. Cassagnaud, R. Ledoux, J.-M. Jancovici, and A. Grandjean. Faire sa part ? Pouvoir et responsabilité des individus, des entreprises et de l'état face à l'urgence climatique. Carbone4 website https://www.carbone4.com/wp-content/uploads/2019/06/Publication-Carbone-4-Faire-sa-part-pouvoir-responsabilite-climat.pdf.

[43] M. Duran-Matute, J.-B. Flór, F. S. Godeferd, and C. Jause-Labert. Turbulence and columnar vortex formation through inertial-wave focusing. *Phys. Rev. E*, 87: 041001, Apr 2013. doi: 10.1103/PhysRevE.87.041001.

[44] A. Dörnbrack. Turbulent mixing by breaking gravity waves. *J. Fluid. Mech.*, 375: 113–141, 1998. doi: 10.1017/S0022112098002833.

[45] F. Feraco, R. Marino, A. Pumir, L. Primavera, P. D. Mininni, A. Pouquet, and D. Rosenberg. Vertical drafts and mixing in stratified turbulence: Sharp transition with Froude number. *Europhysics Letters*, 123(4):44002, sep 2018.

[46] J. G. Fitzgerald and B. F. Farrell. Statistical state dynamics of vertically sheared horizontal flows in two-dimensional stratified turbulence. *Journal of Fluid Mechanics*, 854:544–590, November 2018. ISSN 0022-1120, 1469-7645. doi: 10.1017/jfm.2018.560.

[47] G. Flato, J. Marotzke, B. Abiodun, P. Braconnot, S. C. Chou, W. Collins, P. Cox, F. Driouech, S. Emori, V. Eyring, C. Forest, P. Gleckler, E. Guilyardi, C. Jakob, V. Kattsov, C. Reason, and M. Rummukainen. Evaluation of Climate Models. In: *Climate Change 2013: The Physical Science Basis. Contribution of Working Group I to the Fifth Assessment Report of the Intergovernmental Panel on Climate Change [T.F. Stocker, D. Qin, G.-K. Plattner, M. Tignor, S.K. Allen, J. Boschung, A. Nauels, Y. Xia, V. Bex and P.M. Midgley (eds.)].* Cambridge University Press, Cambridge, United Kingdom and New York, NY, USA, 2013.

[48] U. Frisch. *Turbulence: The Legacy of A. N. Kolmogorov*. Cambridge University Press, 1995. doi: 10.1017/CBO9781139170666.

[49] K. S. Gage. Evidence for a $k^{-5/3}$ law inertial range in mesoscale two-dimensional turbulence. *Journal of Atmospheric Sciences*, 36(10), 1979.

[50] M. Galmiche and J. C. R. Hunt. The formation of shear and density layers in stably stratified turbulent flows: linear processes. *Journal of Fluid Mechanics*, 455:243–262, 2002.

[51] S. Galtier. Weak inertial-wave turbulence theory. *Phys. Rev. E*, 68:015301, Jul 2003.

[52] A. Garanaik and S. K. Venayagamoorthy. On the inference of the state of turbulence and mixing efficiency in stably stratified flows. *J. Fluid. Mech.*, 867:323–333, 2019. doi: 10.1017/jfm.2019.142.

[53] C. Garrett and W. Munk. Space-time scales of internal waves. *Geophysical Fluid Dynamics*, 3(3):225–264, 1972.

[54] C. Garrett and W. Munk. Space-time scales of internal waves: A progress report. *Journal of Geophysical Research (1896-1977)*, 80(3):291–297, 1975.

[55] F. S. Godeferd and C. Cambon. Detailed investigation of energy transfers in homogeneous stratified turbulence. *Physics of Fluids*, 6(6):2084–2100, 1994.

[56] F. S. Godeferd and F. Moisy. Structure and Dynamics of Rotating Turbulence: A Review of Recent Experimental and Numerical Results. *Applied Mechanics Reviews*, 67(3), 05 2015. ISSN 0003-6900. doi: 10.1115/1.4029006. 030802.

[57] F. S. Godeferd and C. Staquet. Statistical modelling and direct numerical simulations of decaying stably stratified turbulence. Part 2. Large-scale and small-scale anisotropy. *Journal of Fluid Mechanics*, 486:115–159, June 2003. doi: 10.1017/s0022112003004531.

[58] H. P. Greenspan. *The Theory of Rotating Fluids*. Cambridge University Press, 1968.

[59] H. P. Greenspan. On the non-linear interaction of inertial modes. *Journal of Fluid Mechanics*, 36(2):257–264, 1969. doi: 10.1017/S0022112069001649.

[60] M. C. Gregg, T. B. Sanford, and D. P. Winkel. Reduced mixing from the breaking of internal waves in equatorial waters. *Nature*, 422(6931):513–515, 2003. ISSN 1476-4687. doi: 10.1038/nature01507.

[61] G. He, G. Jin, and Y. Yang. Space-time correlations and dynamic coupling in turbulent flows. *Annual Review of Fluid Mechanics*, 49(1):51–70, 2017. doi: 10.1146/annurev-fluid-010816-060309.

[62] C. Herbert, R. Marino, D. Rosenberg, and A. Pouquet. Waves and vortices in the inverse cascade regime of stratified turbulence with or without rotation. *J. Fluid. Mech.*, 806:165–204, 2016. doi: 10.1017/jfm.2016.581.

[63] J. R. Herring. Approach of axisymmetric turbulence to isotropy. *The Physics of Fluids*, 17(5):859–872, May 1974. ISSN 0031-9171.

[64] J. R. Herring and O. Métais. Numerical experiments in forced stably stratified turbulence. *J. Fluid. Mech.*, 202:97–115, 1989.

[65] C. J. Howland, J. R. Taylor, and C. P. Caulfield. Mixing in forced stratified turbulence and its dependence on large-scale forcing. *Journal of Fluid Mechanics*, 898:A7, 2020. doi: 10.1017/jfm.2020.383.

[66] C. Jause-Labert. *Simulation numérique d'écoulements turbulents en rotation, confinement et forçage à l'aide d'une méthode de pénalisation*. PhD thesis, 2012. URL https://bibli.ec-lyon.fr/exl-doc/TH_T2295_cjause.pdf.

[67] A. Justin. Carbon and the cloud. Stanford Magazine https://medium.com/stanford-magazine/carbon-and-the-cloud-d6f481b79dfe, 05 2017.

[68] H. A. Kafiabad, M. A. C. Savva, and J. Vanneste. Diffusion of inertia-gravity waves by geostrophic turbulence. *Journal of Fluid Mechanics*, 869:R7, 2019. doi: 10.1017/jfm.2019.300.

[69] Y. Kimura and J. R. Herring. Energy spectra of stably stratified turbulence. *J. Fluid. Mech.*, 698:19–50, 2012.

[70] R. H. Kraichnan and D. Montgomery. Two-dimensional turbulence. *Reports on Progress in Physics*, 43(5):547–619, may 1980. doi: 10.1088/0034-4885/43/5/001.

[71] A. Kumar, M. K. Verma, and J. Sukhatme. Phenomenology of two-dimensional stably stratified turbulence under large-scale forcing. *Journal of Turbulence*, 18 (3):219–239, 2017.

[72] H. Lam, A. Delache, and F. S. Godeferd. Partitioning Waves and Eddies in Stably Stratified Turbulence. *Atmosphere*, 11(4):420, April 2020. doi: 10.3390/atmos11040420.

[73] H. Lam, A. Delache, and F. S. Godeferd. Energy balance and mixing between waves and eddies in stably stratified turbulence. *Journal of Fluid Mechanics*, 923: A31, 2021. doi: 10.1017/jfm.2021.589.

[74] M. Le Bars. Flows driven by libration, precession, and tides in planetary cores. *Phys. Rev. Fluids*, 1:060505, Oct 2016.

[75] T. Le Reun, B. Favier, A. J. Barker, and M. Le Bars. Inertial wave turbulence driven by elliptical instability. *Phys. Rev. Let.*, 119(3), 2017. ISSN 0031-9007, 1079-7114. doi: 10.1103/PhysRevLett.119.034502.

[76] T. Le Reun, B. Favier, and M. Le Bars. Parametric instability and wave turbulence driven by tidal excitation of internal waves. *J. Fluid. Mech.*, 840:498–529, Feb 2018. ISSN 1469-7645. doi: 10.1017/jfm.2018.18.

[77] T. Le Reun, B. Favier, and M. Le Bars. Evidence of the Zakharov-Kolmogorov spectrum in numerical simulations of inertial wave turbulence. *Europhysics Letters*, 132(6):64002, dec 2020. doi: 10.1209/0295-5075/132/64002.

[78] T. Le Reun, B. Gallet, B. Favier, and M. Le Bars. Near-resonant instability of geostrophic modes: beyond greenspan's theorem. *Journal of Fluid Mechanics*, 900: R2, 2020.

[79] M.-P. Lelong and J. J. Riley. Internal wave–vortical mode interactions in strongly stratified flows. *J. Fluid. Mech.*, 232:1–19, 1991.

[80] M. Lessieur. *Turbulence in Fluids*. Springer, 2008.

[81] M. D. Levine. A Modification of the Garrett–Munk Internal Wave Spectrum. *Journal of Physical Oceanography*, 32(11):3166–3181, November 2002. doi: 10.1175/1520-0485(2002)032<3166:amotgm>2.0.co;2.

[82] M. J. Lighthill. *Waves in fluids*. Cambridge University Press, Cambridge, 2003. ISBN 978-0-521-01045-0. OCLC: 758138350.

[83] D. K. Lilly. Stratified Turbulence and the Mesoscale Variability of the Atmosphere. *J. Atmos. Sci.*, 40(3):749–761, 03 1983. ISSN 0022-4928. doi: 10.1175/1520-0469(1983)040<0749:STATMV>2.0.CO;2.

[84] E. Lindborg. The energy cascade in a strongly stratified fluid. *J. Fluid. Mech.*, 550:207–242, 2006. doi: 10.1017/S0022112005008128.

[85] E. Lindborg and G. Brethouwer. Stratified turbulence forced in rotational and divergent modes. *J. Fluid. Mech.*, 586:83, 2007.

[86] Y. V. Lvov and E. G. Tabak. Hamiltonian formalism and the Garrett-Munk spectrum of internal waves in the ocean. *Phys. Rev. Lett.*, 87:168501, Oct 2001.

[87] Y. V. Lvov, K. L. Polzin, E. G. Tabak, and N. Yokoyama. Oceanic internal-wave field: theory of scale-invariant spectra. *J. Phys. Ocean.*, 40(12):2605–2623, 2010.

[88] L. R. M. Maas, D. Benielli, J. Sommeria, and F.-P. A. Lam. Observation of an internal wave attractor in a confined, stably stratified fluid. *Nature*, 388(6642): 557–561, August 1997. doi: 10.1038/41509.

[89] A. Maffioli. Vertical spectra of stratified turbulence at large horizontal scales. *Phys. Rev. Fluids*, 2:104802, Oct 2017. doi: 10.1103/PhysRevFluids.2.104802.

[90] A. Maffioli, P. A. Davidson, S. B. Dalziel, and N. Swaminathan. The evolution of a stratified turbulent cloud. *Journal of Fluid Mechanics*, 739:229–253, 2014. doi: 10.1017/jfm.2013.612.

[91] A. Maffioli, G. Brethouwer, and E. Lindborg. Mixing efficiency in stratified turbulence. *J. Fluid. Mech.*, 794:R3, 2016. doi: 10.1017/jfm.2016.206.

[92] A. Maffioli, A. Delache, and F. S. Godeferd. Signature and energetics of internal gravity waves in stratified turbulence. *Phys. Rev. Fluids*, 5:114802, Nov 2020. doi: 10.1103/PhysRevFluids.5.114802.

[93] R. Marino, P. D. Mininni, D. Rosenberg, and A. Pouquet. Inverse cascades in rotating stratified turbulence: Fast growth of large scales. *Europhysics Letters*, 102(4):44006, may 2013.

[94] R. Marino, P. D. Mininni, D. Rosenberg, and A. Pouquet. Emergence of helicity in rotating stratified turbulence. *Phys. Rev. E*, 87:033016, Mar 2013.

[95] G. J. Marlton, P. D. Williams, and K. A. Nicoll. On the detection and attribution of gravity waves generated by the 20 march 2015 solar eclipse. *Philosophical Transactions of the Royal Society A: Mathematical, Physical and Engineering Sciences*, 374(2077):20150222, 2016. doi: 10.1098/rsta.2015.0222.

[96] A. Mashayek, H. Salehipour, D. Bouffard, C. P. Caulfield, R. Ferrari, M. Nikurashin, W. R. Peltier, and W. D. Smyth. Efficiency of turbulent mixing in the abyssal ocean circulation. *Geophys. Res. Let.*, 44(12):6296–6306, 2017. doi: https://doi.org/10.1002/2016GL072452.

[97] O. Métais, P. Bartello, E. Garnier, J.J. Riley, and M. Lesieur. Inverse cascade in stably stratified rotating turbulence. *Dyn. Atm. and Oceans*, 23(1):193 – 203, 1996. ISSN 0377-0265. Stratified flows.

[98] P. D. Mininni and A. Pouquet. Rotating helical turbulence. I. global evolution and spectral behavior. *Physics of Fluids*, 22(3):035105, 2010.

[99] P. D. Mininni, A. Alexakis, and A. Pouquet. Scale interactions and scaling laws in rotating flows at moderate Rossby numbers and large Reynolds numbers. *Physics of Fluids*, 21(1):015108, 2009.

[100] C. Morize, F. Moisy, and M. Rabaud. Decaying grid-generated turbulence in a rotating tank. *Physics of Fluids*, 17(9):095105, 2005.

[101] M. Mory and E. J. Hopfinger. Rotating turbulence evolving freely from an initial quasi 2d state. In U. Frisch, J. B. Keller, G. C. Papanicolaou, and O. Pironneau, editors, *Macroscopic Modelling of Turbulent Flows*, pages 218–236, Berlin, Heidelberg, 1985. Springer Berlin Heidelberg.

[102] F. Moulin and J.-B. Flór. Vortex–wave interaction in a rotating stratified fluid: Wkb simulations. *J. Fluid. Mech.*, 563:199–222, 2006.

[103] D. E. Mowbray and B. S. H. Rarity. A theoretical and experimental investigation of the phase configuration of internal waves of small amplitude in a density stratified liquid. *Journal of Fluid Mechanics*, 28(1):1–16, 1967. doi: 10.1017/S0022112067001867.

[104] V. Mukund and B. Hof. The critical point of the transition to turbulence in pipe flow. *Journal of Fluid Mechanics*, 839:76–94, 2018. doi: 10.1017/jfm.2017.923.

[105] P. Müller. On the diffusion of momentum and mass by internal gravity waves. *J. Fluid. Mech.*, 77(4):789–823, 1976.

[106] P. Müller, G. Holloway, F. Henyey, and N. Pomphrey. Nonlinear interactions among internal gravity waves. *Rev. Geophys.*, 24(3):493–536, 1986.

[107] J. R. Munroe and B. R. Sutherland. Generation of internal waves by sheared turbulence: experiments. *Environmental Fluid Mechanics*, 8(5-6):527–534, September 2008. doi: 10.1007/s10652-008-9094-3.

[108] W.-C. Müller and M. Thiele. Scaling and energy transfer in rotating turbulence. *Europhysics Letters*, 77(3):34003, jan 2007. doi: 10.1209/0295-5075/77/34003.

[109] G. D. Nastrom and K. S. Gage. A Climatology of Atmospheric Wavenumber Spectra of Wind and Temperature Observed by Commercial Aircraft. *J. Atm. Sci.*, 42(9):950–960, 05 1985.

[110] S. Nazarenko. *Wave Turbulence*. Springer Berlin Heidelberg, 2011. doi: 10.1007/978-3-642-15942-8.

[111] A. C. Newell. Rossby wave packet interactions. *Journal of Fluid Mechanics*, 35 (2):255–271, 1969. doi: 10.1017/S0022112069001108.

[112] D. J. Olbers. Nonlinear energy transfer and the energy balance of the internal wave field in the deep ocean. *J. Fluid. Mech.*, 74(2):375–399, 1976.

[113] T. R. Osborn. Estimates of the Local Rate of Vertical Diffusion from Dissipation Measurements. *J. Phys. Oceano.*, 10(1):83–89, 01 1980. ISSN 0022-3670. doi: 10.1175/1520-0485(1980)010<0083:EOTLRO>2.0.CO;2.

[114] R. V. Ozmidov. On the turbulent exchange in a stably stratified ocean. *Atmos. Oceanic Phys.*, 1:861–871, 1965.

[115] J. Pedlosky. *Waves in the ocean and atmosphere: introduction to wave dynamics*. Springer Science & Business Media, 2013.

[116] D. Pekurovsky. P3DFFT: A framework for parallel computations of Fourier transforms in three dimensions. *SIAM Journal on Scientific Computing*, 34(4): C192–C209, 2012.

[117] W. R. Peltier and C. P. Caulfield. Mixing efficiency in stratified shear flows. *Ann. Rev. Fluid Mech.*, 35(1):135–167, 2003. doi: 10.1146/annurev.fluid.35.101101.161144.

[118] K. L. Polzin and Y. V. Lvov. Toward regional characterizations of the oceanic internal wavefield. *Reviews of Geophysics*, 49(4), 2011.

[119] J. J. Riley, R. W. Metcalfe, and M. A. Weissman. Direct numerical simulations of homogeneous turbulence in density-stratified fluids. 76(1):79–112, 1981. ISSN 0094-243X. doi: 10.1063/1.33198.

[120] P. Sagaut and C. Cambon. *Homogeneous turbulence dynamics*, volume 10. Springer, 2008.

[121] C. Savaro, A. Campagne, M. C. Linares, P. Augier, J. Sommeria, T. Valran, S. Viboud, and N. Mordant. Generation of weakly nonlinear turbulence of internal gravity waves in the Coriolis facility. *Phys. Rev. Fluids*, 5:073801, Jul 2020. doi: 10.1103/PhysRevFluids.5.073801.

[122] M. A. C. Savva, H. A. Kafiabad, and J. Vanneste. Inertia-gravity-wave scattering by three-dimensional geostrophic turbulence. *Journal of Fluid Mechanics*, 916:A6, 2021. doi: 10.1017/jfm.2021.205.

[123] M. K. Sharma, M. K. Verma, and S. Chakraborty. On the energy spectrum of rapidly rotating forced turbulence. *Physics of Fluids*, 30(11):115102, 2018.

[124] M. K. Sharma, M. K. Verma, and S. Chakraborty. Anisotropic energy transfers in rapidly rotating turbulence. *Physics of Fluids*, 31(8):085117, 2019. doi: 10.1063/1.5109856.

[125] Siemens. Window correction factors. Siemens website https://community.sw.siemens.com/s/article/window-correction-factors, 08 2019.

[126] L. M. Smith. Numerical study of two-dimensional stratified turbulence. *Contemporary Mathematics*, 283:91–106, 2001.

[127] L. M. Smith and Y. Lee. On near resonances and symmetry breaking in forced rotating flows at moderate Rossby number. *Journal of Fluid Mechanics*, 535: 111–142, 2005.

[128] L. M. Smith and F. Waleffe. Transfer of energy to two-dimensional large scales in forced, rotating three-dimensional turbulence. *Physics of Fluids*, 11(6):1608–1622, 1999.

[129] L. M. Smith and F. Waleffe. Generation of slow large scales in forced rotating stratified turbulence. *J. Fluid. Mech.*, 451:145–168, 2002.

[130] L. M. Smith, J. R. Chasnov, and F. Waleffe. Crossover from two- to three-dimensional turbulence. *Phys. Rev. Lett.*, 77:2467–2470, Sep 1996. doi: 10.1103/PhysRevLett.77.2467.

[131] P. J. Staplehurst, P. A. Davidson, and S. B. Dalziel. Structure formation in homogeneous freely decaying rotating turbulence. *Journal of Fluid Mechanics*, 598:81–105, 2008. doi: 10.1017/S0022112007000067.

[132] C. Staquet and F. S. Godeferd. Statistical modelling and DNS of decaying stably stratified turbulence. Part 1. flow energetics. *J. Fluid. Mech.*, 360:295–340, 1998. doi: 10.1017/S0022112097008641.

[133] C. Staquet and J. Sommeria. Internal gravity waves: From instabilities to turbulence. *Annual Review of Fluid Mechanics*, 34(1):559–593, 2002.

[134] M. Stendel, J. Francis, R. White, P. D. Williams, and T. Woollings. Chapter 15 - the jet stream and climate change. In Trevor M. Letcher, editor, *Climate Change (Third Edition)*, pages 327–357. Elsevier, third edition edition, 2021. ISBN 978-0-12-821575-3. doi: https://doi.org/10.1016/B978-0-12-821575-3.00015-3.

[135] A. R. H. Stevens, S. Bellstedt, P. J. Elahi, and M. T. Murphy. The imperative to reduce carbon emissions in astronomy. *Nature Astronomy*, 4(9):843–851. ISSN 2397-3366.

[136] T. F. Stocker, G. K. C. Clarke, H. Le Treut, R. S. Lindzen, V. P. Meleshko, R. K. Mugara, T. N. Palmer, R. T. Pierrehumbert, P. J. Sellers, K. E. Trenberth, and J. Willebrand. Physical Climate Processes and Feedbacks. In: *Climate Change 2001: The Scientific Basis. Contribution of Working Group I to the Third Assessment Report of the Intergovernmental Panel on Climate Change [J.T. Houghton, Y. Ding, D.J. Griggs, M. Noguer, P.J. van der Linden, X. Dai, K. Maskell, and C.A. Johnson (eds.)]*. Cambridge University Press, Cambridge, United Kingdom and New York, NY, USA, 881pp, 2001.

[137] P. Tabeling. Two-dimensional turbulence: a physicist approach. *Physics Reports*, 362(1):1–62, 2002. ISSN 0370-1573. doi: https://doi.org/10.1016/S0370-1573(01)00064-3.

[138] B. Teaca, M. K. Verma, B. Knaepen, and D. Carati. Energy transfer in anisotropic magnetohydrodynamic turbulence. *Phys. Rev. E*, 79:046312, Apr 2009. doi: 10.1103/PhysRevE.79.046312. URL https://link.aps.org/doi/10.1103/PhysRevE.79.046312.

[139] H. Tennekes. Eulerian and Lagrangian time microscales in isotropic turbulence. *Journal of Fluid Mechanics*, 67(3):561–567, 1975. doi: 10.1017/S0022112075000468.

[140] D. Vallefuoco, F. S. Godeferd, A. Naso, and A. Delache. Anisotropic turbulent cascades in rotating homogeneous turbulence. In *Turbulent Cascades*

II, pages 133–141. Springer International Publishing, 2019. doi: 10.1007/978-3-030-12547-9_15.

[141] A. Vallgren, E. Deusebio, and E. Lindborg. Possible explanation of the atmospheric kinetic and potential energy spectra. *Phys. Rev. Lett.*, 107:268501, Dec 2011. doi: 10.1103/PhysRevLett.107.268501.

[142] M. K. Verma. *Energy Transfers in Fluid Flows: Multiscale and Spectral Perspectives*. Cambridge University Press, 2019. doi: 10.1017/9781316810019.

[143] M. K. Verma, A. Kumar, P. Kumar, S. Barman, A. G. Chatterjee, R. Samtaney, and R. A. Stepanov. Energy spectra and fluxes in dissipation range of turbulent and laminar flows. *Fluid Dynamics*, 53(6):862–873, November 2018. doi: 10.1134/s0015462818050166.

[144] M. K. Verma, A. Kumar, and A. Gupta. Hydrodynamic turbulence: sweeping effect and taylor's hypothesis via correlation function. *Transactions of the Indian National Academy of Engineering*, 5(4):649–662, September 2020. doi: 10.1007/s41403-020-00161-3.

[145] M. L. Waite and P. Bartello. Stratified turbulence dominated by vortical motion. *Journal of Fluid Mechanics*, 517:281–308, 2004. doi: 10.1017/S0022112004000977.

[146] F. Waleffe. Inertial transfers in the helical decomposition. *Physics of Fluids A: Fluid Dynamics*, 5(3):677–685, 1993. doi: 10.1063/1.858651.

[147] E. Yarom and E. Sharon. Experimental observation of steady inertial wave turbulence in deep rotating flows. *Nature Phys.*, 10(7):510–514, 2014. ISSN 1745-2481. doi: 10.1038/nphys2984.

[148] E. Yarom, Y. Vardi, and E. Sharon. Experimental quantification of inverse energy cascade in deep rotating turbulence. *Physics of Fluids*, 25(8):085105, 2013.

[149] O. Zeman. A note on the spectra and decay of rotating homogeneous turbulence. *Physics of Fluids*, 6(10):3221–3223, 1994.

[150] Q. Zhou and P. J. Diamessis. Surface manifestation of internal waves emitted by submerged localized stratified turbulence. *Journal of Fluid Mechanics*, 798:505–539, 2016. doi: 10.1017/jfm.2016.342.

[151] Y. Zhou. A phenomenological treatment of rotating turbulence. *Physics of Fluids*, 7(8):2092–2094, 1995.

Résumé (long)

Je résume en français chapitre par chapitre l'ensemble de ce manuscrit de thèse.

Introduction

Les ondes internes de gravité ont lieu dans des écoulements stablement stratifiés, un écoulement ou la densité du fluide varie avec la direction verticale, avec une couche de densité plus lourde en dessous d'une couche de densité plus légère. Les ondes internes de gravité apparaissent quand un volume de fluide évolue dans une densité différente à sa propre densité et qu'une force de flottaison fait osciller ce volume de fluide. On les retrouve dans l'atmosphère ou l'océan où elles influencent fortement leur dynamique. Elles peuvent avoir un rôle important dans le mélange et la prédiction des modèles climatiques, comme expliqué dans les rapports du GIEC [31, 47, 136].

Les ondes inertielles, ont elles lieu dans des écoulements en rotation, leur mouvement est la résultante des forces de Coriolis dans le référentiel tournant. On les retrouve dans l'océan et l'atmosphère mais aussi dans le noyau des planètes.

Les écoulements en turbulence homogène et isotrope ont fait l'objet de nombreux articles et livres [48] (malgré le fait qu'aucune solution analytique n'existe). Pour les écoulements fortement stratifiés ou fortement en rotation, il est possible de négliger le terme non linéaire et d'obtenir une solution analytique [120]. Dans ce cas, nous connaissons aussi très bien ce type d'écoulement. Le problème apparaît lorsque l'écoulement est stratifié ou en rotation mais aussi turbulent. Dans ce cas, il n'est pas possible d'ignorer le terme non linéaire, et l'écoulement possède une multitude de structures interagissant à toutes les échelles. C'est justement l'interaction entre les tourbillons et les ondes qui représente un obstacle à la compréhension de ce type d'écoulement. Dans cette thèse, nous proposons une technique de séparation des ondes et des tourbillons afin de mieux comprendre leurs interactions et comportements.

Ondes dans des écoulements

Pour commencer nous présentons les équations utilisées dans le cas stratifié et dans le cas en rotation. Les équations utilisées sont adimensionnelles. Le référentiel de Craya-Herring est défini. Il permet l'obtention des champs de vitesses et de densité de manière élégante car ce référentiel utilise l'incompressibilité du fluide pour condenser le système

d'équations en seulement trois équations dans le cas stratifié (au lieu de cinq) et deux équations dans le cas en rotation (au lieu de quatre). On montre des résultats classiques comme la relation de dispersion pour les ondes interne de gravité est définie ($\omega_r = \pm N \cos\theta$) ainsi que pour les ondes inertielles ($\omega_r = \pm 2\Omega \sin\theta$) et leurs vitesses de groupe $\mathbf{v}_g = \nabla_{\mathbf{k}}(\omega_r)$ et de phase $\mathbf{v}_\Phi = \mathbf{k}\omega_r/k^2$, où N est la fréquence de Brunt-Väisälä, 2Ω est la vitesse de rotation et θ est l'angle réalisé par le vecteur d'onde $\mathbf{k}$ avec le plan horizontal.

Une technique de représentation de la concentration d'énergie en fonction de l'angle θ et de la fréquence ω est présentée. C'est cette technique qui permet d'observer la trace des ondes (la relation de dispersion) depuis un exemple simple comme la croix de Saint André à des cas plus complexes d'écoulement turbulent. Nous observons qu'à partir d'un forçage localisé en espace et oscillant, nous retrouvons la relation de dispersion de manière numérique en traçant la concentration d'énergie en fonction de θ et ω. La technique de fenêtrage de Hann est utilisée uniquement lorsque le résultat obtenu n'est pas utilisé de manière quantitative mais de manière qualitative car cela modifie le signal, ce qui peut s'avérer gênant pour tracer des statistiques.

Puis, les effets non linéaires sur les ondes sont observés. D'abord, nous observons l'effet Doppler, le mouvement continu dans une direction d'une particule oscillante dans un écoulement au repos. Cela ne modifie pas la relation de dispersion des ondes mais uniquement la fréquence de forçage. Par la suite, l'effet du sweeping est observé. Celui-ci correspond à l'advection des ondes par un écoulement. On observe que l'effet sweeping est très bien estimé lorsque l'écoulement advectant est homogène et constant. La nouvelle relation de dispersion des ondes obtenue est $\omega_c = \omega_r + \mathbf{c} \cdot \mathbf{k}$, avec $\mathbf{c}$ la vitesse de l'écoulement advectant et $\mathbf{k}$ le vecteur d'onde. L'effet de l'échelle de l'écoulement advectant est aussi analysé mais s'avère compliqué. En effet, nous montrons que la vitesse maximale atteinte pour un écoulement de petite taille est supérieure à rms constante à un écoulement de grande taille. De plus le mode géostrophique (étudié dans les écoulements en rotation) atteint une vitesse maximale supérieure à l'écoulement cisaillé (étudié dans les écoulements stratifiés) pour une même vitesse rms. Cependant, on peut observer que l'échelle de l'écoulement advectant influence la relation de dispersion des ondes assez fortement. La fréquence de l'écoulement advectant est aussi modifiée et change significativement la relation de dispersion des ondes. Enfin, nous regardons l'effet dû à un gradient de vitesse sur les ondes. Un gradient à grande échelle a peu d'influence mais un gradient à petite échelle a beaucoup d'influence. Heureusement, les petites échelles ont généralement peu d'énergie dans les écoulements turbulents au contraire des grandes échelles. On peut donc penser qu'elles ont un effet limité sur la relation de dispersion des ondes. De plus, nous considérons plus tard uniquement les écoulements cisaillés dans le cas stratifié et le mode géostrophique dans le cas en rotation

comme source d'advection pour les ondes. Ces deux types d'écoulements ont en général une très faible fréquence temporelle.

Séparation des ondes et des tourbillons

Nous expliquons les différentes techniques pour séparer les ondes des tourbillons. Pour cela, nous faisons la transformée de Fourier en espace et en temps d'une composante de vitesse ou de flottaison noté f. A l'aide un filtre $\zeta(\mathbf{k},\omega)$, qui a pour valeur un dans la partie onde et zero dans la partie tourbillon, nous séparons les ondes et tourbillons:

$$\tilde{\mathbf{f}}^w(\mathbf{k},\omega) = \zeta(\mathbf{k},\omega)\tilde{\mathbf{f}}(\mathbf{k},\omega)$$
$$\tilde{\mathbf{f}}^e(\mathbf{k},\omega) = (1-\zeta(\mathbf{k},\omega))\tilde{\mathbf{f}}(\mathbf{k},\omega).$$

Puis la transformée inverse en temps et en espace est réalisé sur chaque composante onde et tourbillon.

Dans le cas stratifié, notre décomposition est un peu plus complexe car le terme toroidal est considéré comme ne comprenant que des tourbillons (car il ne comprend pas d'ondes dans les équations linéarisées). Ainsi, la séparation des termes en tourbillons et ondes s'écrit :

$$\tilde{\mathbf{u}}^w(\mathbf{k},\omega) = \zeta(\mathbf{k},\omega)\tilde{u}^p(\mathbf{k},\omega)\mathbf{e}^p$$
$$\tilde{\mathbf{u}}^e(\mathbf{k},\omega) = \tilde{u}^t(\mathbf{k},\omega)\mathbf{e}^t + (1-\zeta(\mathbf{k},\omega))\,\tilde{u}^p(\mathbf{k},\omega)\mathbf{e}^p$$
$$\tilde{b}^w(\mathbf{k},\omega) = \zeta(\mathbf{k},\omega)\tilde{b}(\mathbf{k},\omega), \qquad \tilde{b}^e(\mathbf{k},\omega) = (1-\zeta(\mathbf{k},\omega))\,\tilde{b}(\mathbf{k},\omega)$$

La décomposition que nous montrons est orthogonal. Les parties ondes et tourbillons sont disjoints en temps et en espace. Ainsi, pour tout nombre d'onde $\mathbf{k}$ et $\mathbf{k'}$, la moyenne temporelle du produit de deux composante $\hat{f}^i(\mathbf{k},t)$ et $\hat{g}^j(\mathbf{k'},t)$ sur un grand temps T est :

$$[\hat{f}^i(\mathbf{k},t),\hat{g}^j(\mathbf{k'},t)] \equiv \frac{1}{T}\int_T \hat{f}^i(\mathbf{k},t)\overline{\hat{g}^j(\mathbf{k'},t)}\delta_{\mathbf{k}-\mathbf{k'}}\mathrm{d}t \neq 0 \text{ seulement si } i=j \text{ et } \mathbf{k}=\mathbf{k'},$$

avec i et j pouvant être égale à la partie onde (w), tourbillon (e) ou au mode géostrophique (g).

Pour définir le filtre $\zeta(\mathbf{k},\omega)$, nous développons deux techniques distinctes :

- Une première technique explicite consiste à estimer la vitesse rms de l'écoulement advectant $\mathbf{c}$. Puis, le domaine des ondes est défini par $\zeta(\mathbf{k},\omega)=1$ lorsque $\omega_r - \mathbf{c}\cdot\mathbf{k} \leq$

$\omega \leq \omega_r + \mathbf{c} \cdot \mathbf{k}$. Les points n'appartenant pas au domaine des ondes sont considérés comme des tourbillons et $\zeta(\mathbf{k}, \omega) = 0$.

- La deuxième technique est plus raffinée. Elle permet de prendre en compte l'évolution spatiale et temporelle de l'écoulement advectant. Elle repose sur les fonctions de Green. A partir d'une série d'impulsions en temps et en espace, il est possible de montrer que la densité d'énergie atteint un pic dans le domaine $(\mathbf{k}, \omega)$ ou les ondes s'expriment. Ainsi lorsqu'un pic est observé dans l'écoulement avec impulsions advectées, cela correspond à la partie onde de la décomposition et nous avons $\zeta(\mathbf{k}, \omega) = 1$. Lorsque l'énergie au point $(\mathbf{k}, \omega)$ est basse, nous sommes dans le domaine des tourbillons et $\zeta(\mathbf{k}, \omega) = 0$.

Pour finir, la première technique explicite de séparation des ondes et tourbillons est appliquée à une croix de Saint André advectée horizontalement. Visuellement, ce test est très concluant puisque l'on voit dans la figure 3.7 que la partie onde garde l'aspect de croix, tandis que la partie tourbillon ne contient plus que le forçage.

Turbulence stratifiée

Nous appliquons la technique de séparation des ondes et tourbillons à plusieurs écoulements stratifiés. Plus particulièrement, c'est la deuxième technique, qui utilise la fonction de Green qui est utilisée. Le forçage utilisé est un forçage développé dans [89, 92]. Il permet de forcer un cylindre (dans le domaine de spatial de Fourier) avec un nombre d'onde horizontal constant et une amplitude de nombre d'ondes verticaux contraint. Il est très utile afin d'éviter des points problématiques comme l'écoulement cisaillé (nombre d'onde horizontal $k_h = 0$). De plus, afin de réduire l'écoulement cisaillé un terme de viscosité linéaire est ajouté. Les différentes simulations numériques sont réalisées avec une résolution 256^3 points et 512^3 points ce qui permet de faire varier la valeur du nombre de Froude Fr ou du Reynolds de flottaison Re_b en gardant l'autre nombre à peu près constant. Toutes les simulations sont réalisées à très faible Froude mais a des nombres de Reynolds de flottaison variable (inférieur, supérieur ou égal à un).

On vérifie que l'écoulement cisaillé extrait d'écoulements turbulent est bien convecté comme dans les cas idéalisés du chapitre 2. La relation de dispersion des ondes modifié par cet écoulement cisaillé est bien estimé par la vitesse rms du cisaillement du fluide.

L'énergie des ondes et des tourbillons est représentée en fonction du Froude et du Reynolds de flottaison. Nous montrons que la répartition des ondes et tourbillons dépend aussi quelle quantité d'énergie est regardée. En ne regardant que la composante poloidal

et de flottaison, qui contiennent toutes les deux des ondes et des tourbillons (alors que la composante toroidal ne contient que des tourbillons) la répartition ondes/tourbillons est fortement dépendante du nombre de Froude et dans une moindre mesure, du nombre de Reynolds de flottaison.

Afin d'être plus précis, nous analysons aussi des spectres d'énergie des ondes et des tourbillons en fonction du nombre d'onde k, du nombre d'onde horizontal k_h et du nombre d'onde vertical k_z. Utiliser des nombres d'ondes différents (vertical et horizontal) permet de rendre compte davantage de l'anisotropie créée par la stratification. On observe que la partie tourbillon est proche d'une pente en $-5/3$ en fonction de k et k_h. Aucune tendance particulière n'apparaît pour le spectre d'énergie des tourbillons en fonction de k_z. Le spectre d'énergie des ondes semble proche d'une pente en -3, surtout a grande stratification alors qu'à petite stratification, la pente obtenue est plus faible et se rapproche d'une pente en $-5/3$.

Nous analysons ensuite le bilan d'énergie de notre système. Grâce aux propriétés de notre technique de séparation il est possible de créer un bilan d'énergie séparé pour les ondes w et tourbillons e :

$$\begin{aligned} 0 &= T^w_{ee} + T^w_{we} - \varepsilon^w_T + P^w \\ 0 &= T^e_{ww} + T^e_{ew} - \varepsilon^e_T + P^e \end{aligned} \tag{C.1}$$

ou T^l_{ij} correspond au terme de transfert de l'advection de j par i pour prendre ou donner de l'énergie à l. P^l est le forçage dans la partie l et ε^l_T correspond à la dissipation de l'énergie par la partie l. i, j et l peuvent être égaux à la partie onde (w) et tourbillon (e) de notre décomposition. On observe qu'un large transfert existe entre la partie onde et tourbillon favorisant la dissipation d'énergie par les tourbillons. Le transfert potentielle est responsable en grande partie de cet échange d'énergie alors que le transfert cinétique est plus faible et fluctuant.

Le mélange ainsi que la dissipation dû aux ondes et tourbillons est analysé. On observe un plateau à grand Fr et grand Re_b ou le mélange dû aux tourbillons est environ quatre fois important que le mélange du aux ondes. A petit Fr et petit Re_b, c'est le mélange dû aux ondes qui domine par rapport au mélange dû aux tourbillons. Aussi, nous représentons les dissipations cinétiques et potentielles par les ondes et tourbillons. Un plateau est aussi visible à petite stratification lorsque l'on observe la dissipation potentielle et cinétique par les ondes et tourbillons. De plus la dissipation cinétique des ondes égale la dissipation potentielle des ondes.

Une analyse détaillée est faite du transfert cinétique $T^l_{u,ij}$, du transfert potentiel $T^l_{b,ij}$ et du transfert cinétique à potentiel $T^l_{u\to b,i}$. Le transfert est simplifié en quatre composantes, l'échelle moyenne de transfert positif et négatif et la valeur du transfert positif et négatif. Lorsque les nombres de Fr sont faibles c'est surtout le transfert potentiel des ondes qui domine et un peu le transfert cinétique des ondes. Lorsque les nombres de Fr et Re_b sont élevés, c'est le transfert cinétique des tourbillons qui domine, et dans une moindre mesure le transfert potentiel des tourbillons. La plupart de ces transferts participent à une cascade direct d'énergie, qui devient de plus en plus directe quand la stratification diminue. L'unique transfert qui participe à une cascade inverse d'énergie est le transfert cinétique $T^w_{u,ew}$ à forte stratification. Le transfert cinétique à potentiel est dominé par les ondes. Beaucoup d'énergie est envoyé de la partie cinétique à la partie potentielle à grande échelle par les ondes. En effet, seulement la partie cinétique est forcée, donc c'est surtout les ondes qui sont forcées dans la partie potentielle grâce au transfert d'énergie $T^w_{u\to b,w}$. En revanche, le transfert d'énergie potentielle à cinétique est surtout dû aux tourbillons et cela se réalise à petite échelle.

Finalement, des coupes 2D sont réalisés du champ de flottaison total $b(x,z)$, onde $b^w(x,z)$ et tourbillon $b^e(x,z)$. On observe que la partie onde est de plus grande échelle et les lignes d'isodensité sont lisses (on ne voit que très peu de retournement par rapport au champ de flottaison total). Au contraire, la partie tourbillonnaire est à plus petite échelle et les lignes d'isodensité se croisent beaucoup plus, signe que du mélange s'effectue. Le même genre d'analyse est réalisé pour la vitesse verticale avec des observations similaires.

Turbulence en rotation

Nous appliquons maintenant la technique de séparation des ondes et tourbillons à plusieurs écoulements en rotation avec 512^3 points ou 256^3 points. Cela permet de faire varier le nombre de Rossby (Ro) et le nombre de Reynolds inertiel (Re_I). Le forçage utilisé est le même que dans le cas stratifié et un terme de viscosité linéaire est ajouté sur le mode géostrophique (avec un nombre d'onde vertical $k_z = 0$), cependant cette viscosité additionnelle est choisie plus petite que dans le cas stratifié, ce qui permet d'avoir toujours beaucoup d'énergie dans ce mode. Le mode géostrophique est d'ailleurs considéré comme 3D car la composante verticale reste importante à nombre de Rossby élevé.

On observe aussi que l'advection de Diracs par le mode géostrophique extrait des simulations turbulentes n'est pas bien estimé par la vitesse rms du mode géostrophique.

Cela est en partie dû au fait que le mode géostrophique fluctue légèrement avec le temps et possède donc une fréquence temporelle pas tout à fait nulle.

L'énergie des ondes et tourbillons est représentée en fonction du nombre de Rossby et du nombre de Reynolds inertiel. On observe que la répartition de l'énergie entre ondes et tourbillons est fortement dépendante du nombre de Rossby. Le spectre d'énergie des ondes a une plus grande pente que le spectre d'énergie des tourbillons. Par exemple, le spectre d'énergie des ondes en fonction du nombre d'onde k est plus proche d'une pente -2 ou -3. Pour le spectre d'énergie des tourbillons, on est plus proche d'une pente en $-5/3$. Il est difficile d'observer une pente clair en fonction du nombre d'onde vertical k_z. En fonction du nombre d'onde horizontal k_h, l'énergie des ondes évolue proche d'une pente en -2 alors que celle des tourbillons est plus proche d'une pente en $-5/3$.

Toujours par les propriétés de notre séparation, nous analysons le bilan d'énergie des ondes, des tourbillons et du mode géostrophique séparément dans notre système. Le système d'équations est :

$$\begin{aligned} dE^w/dt &= T^w_{ee} + T^w_{we} + T^w_{wg} + T^w_{ge} + T^w_{eg} + \varepsilon^w + P^w \\ dE^e/dt &= T^e_{ww} + T^e_{ew} + T^e_{wg} + T^e_{gw} + T^e_{eg} + \varepsilon^e + P^e \\ dE^g/dt &= T^g_{ee} + T^g_{we} + T^g_{ww} + T^g_{ew} + \varepsilon^g \end{aligned} \tag{C.2}$$

Comme le mode géostrophique a toujours beaucoup d'énergie, celui-ci apparaît toujours dans le bilan d'énergie (avec la lettre g). On observe que ce sont les ondes qui sont presque exclusivement forcées, qu'un large transfert d'énergie des ondes aux tourbillons a lieu et que le mode géostrophique est surtout alimenté par les ondes (et un peu par les tourbillons). La répartition de la dissipation entre ondes et tourbillons dépend en grande partie du Re_I.

Pour être plus précis sur le transfert, ceux-ci sont décomposés en quatre composantes, l'échelle moyenne du transfert positif et négatif et la valeur du transfert positif et négatif. On observe que c'est le transfert qui implique uniquement les ondes $T^{+,w}_{ww}$ qui domine très largement l'écoulement, surtout à petit Ro et petit Re_I. Le transfert qui implique uniquement les tourbillons $T^{+,e}_{ee}$ devient plus important à grand Ro et grand Re_I mais son importance reste beaucoup plus faible que le transfert composé uniquement d'ondes. Lorsque seulement des ondes et tourbillons sont en interactions (sans mode géostrophique impliqué), la plupart des transferts participent à une cascade directe sauf pour le transfert T^e_{ww} qui participe à une cascade inverse à petite rotation. En revanche lorsque le mode géostrophique participe au transfert, plusieurs transferts participent à une cascade inverse à grande rotation.

Finalement, nous visualisons la séparation du champ de vitesses vertical $u_z(x,z)$ en sa partie onde $u_z(x,z)^w$ et sa partie tourbillon $u_z(x,z)^e$. La partie onde garde les grandes structure de l'écoulement alors que la partie tourbillon est à plus petite échelle. La même chose est faite à partir du champ de vitesses horizontal $u_y(x,z)$ et des observations similaires sont faite comparé au champ de vitesses vertical.

Conclusion

Pour conclure, nous avons montré comment caractériser les ondes par leurs relations de dispersion et comment la relation de dispersion pouvait être modifiée par le terme non linéaire. L'effet non linéaire prépondérant est l'effet sweeping, l'advection des ondes par un écoulement à grande échelle. Ces observations sont utilisées pour créer une technique de séparation des ondes et des tourbillons dans des écoulements turbulents en stratification ou en rotation. Pour cela nous utilisons la fonction de Green. On analyse la répartition d'énergie entre ondes et tourbillons, leurs spectres d'énergie, la dissipation et le forçage. Aussi, un accent particulier est mis sur le transfert entre ondes et tourbillons et sur la présence et force de cascade inverse ou directe.

Il reste encore beaucoup de perspectives dans la séparation des écoulements en ondes et tourbillons. Par exemple, on pourrait améliorer la technique de séparation des ondes et tourbillons, notamment dans le choix de l'écoulement advectant. On pourrait l'appliquer dans des cas stratifiés et en rotation ; un forçage différent pourrait être utilisé afin de forcer davantage les tourbillons ; de nouvelles simulations numériques avec plus de points pourraient être faites ; d'autres analyses comme la bicohérence pourrait être réalisées ...